Department of Chemistry

Single-Crystal NMR Spectroscopy – Method Development and Application to Inorganic Solids

Otto Ernst Oliver Zeman

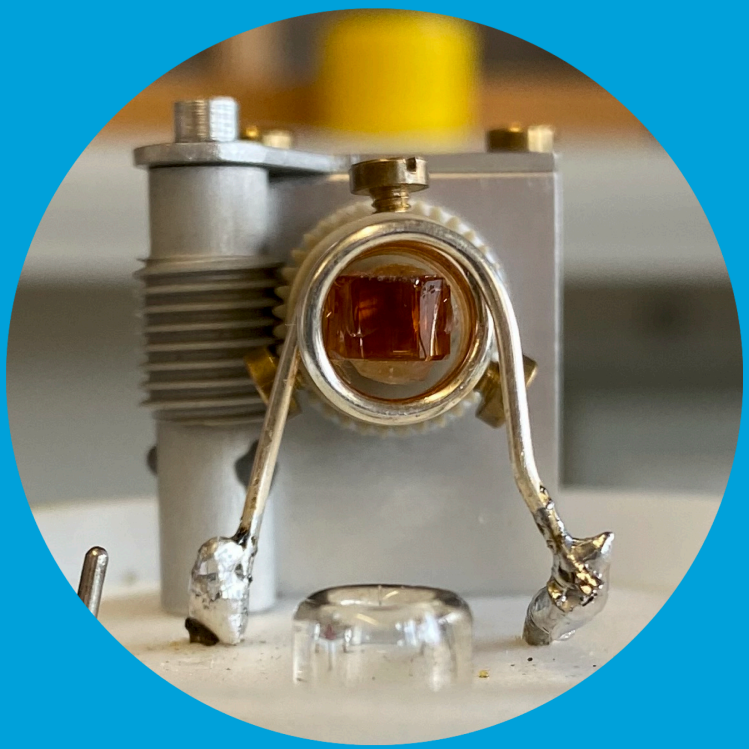

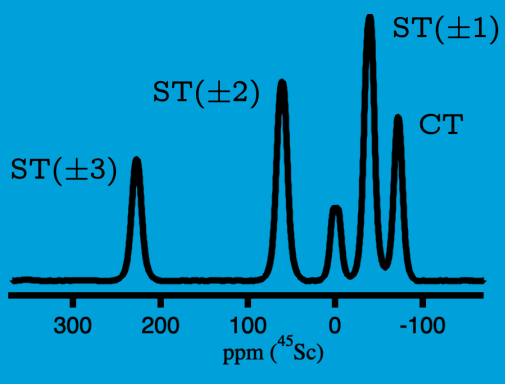

Dissertation

Dissertation zur Erlangung des Doktorgrades
der Fakultät für Chemie und Pharmazie
der Ludwig-Maximilians-Universität München

Single-Crystal NMR Spectroscopy – Method Development and Application to Inorganic Solids

Otto Ernst Oliver Zeman

aus

München, Deutschland

2020

Erklärung

Diese Dissertation wurde im Sinne von § 7 der Promotionsordnung vom 28. November 2011 von Herrn Prof. Dr. Wolfgang Schnick betreut.

Eidesstattliche Versicherung

Diese Dissertation wurde eigenständig und ohne unerlaubte Hilfe erarbeitet.

München, den 30. Juli 2020

.....

M. Sc. Otto Ernst Oliver Zeman

Dissertation eingereicht am	05.08.2020
1. Gutachter:	Prof. Dr. Wolfgang Schnick
2. Gutachter:	Prof. Dr. Konstantin Karaghiosoff
Mündliche Prüfung am	29.09.2020

Acknowledgement

An dieser Stelle möchte ich allen, die mir bei der Vorbereitung und Abfassung dieser Arbeit geholfen haben, meine größte Anerkennung aussprechen. Wenngleich ich nicht jeden Beteiligten namentlich nennen kann, so habt ihr mich alle bei der Erstellung meiner Dissertation unterstützt. Dies gilt insbesondere für meine zahlreichen Co-Autoren, mit denen ich in den letzten Jahren sehr erfolgreich publizieren durfte.

Ganz besonderer Dank geht natürlich an Dr. Thomas Bräuniger. Thomas ist als mein Lehrer und wissenschaftlicher Mentor (abgesehen von mir selbst) die Person, die den größten Beitrag zu dieser Arbeit geleistet hat! Ich bin sehr froh, ihn mittlerweile als einen engen Freund betrachten zu dürfen.

Mein aufrichtiger Dank geht auch an Professor Dr. Wolfang Schnick für seine kontinuierliche finanzielle Unterstützung. Prof. Schnick hat nicht nur meine Stelle bis zum Schluss finanziert, er hat auch die Kosten für mehrere Dienstreisen nach Stuttgart, Leipzig und zu Konferenzen in Österreich und Tschechien übernommen. Umso mehr habe ich mich gefreut, auch gemeinsam mit ihm publizieren zu können.

Mein Dank gilt auch Dr. Igor Moudrakovski für all die fruchtbaren Diskussionen, für sein großes Interesse an meiner Arbeit und für die Zeit, die wir an zahlreichen Wochenenden gemeinsam im NMR-Labor in Stuttgart verbrachten.

Letztendlich bin ich meinen wunderbaren Eltern, Otakar und Anna Zeman, sehr dankbar für all ihre Liebe, Ratschläge, finanzielle Unterstützung und überwältigende Ermutigung während meines ganzen Lebens, egal wie schwierig die Situationen gewesen sein mögen. Meine Karriere wurde durch sie möglich gemacht. Ich danke euch.

Contents

1 Introduction

For the structural characterization of periodic solids, either in single or multicrystalline form, X-ray crystallography is an invaluable tool.[1] As a complementary technique for the elucidation of structure and dynamics in solids, including amorphous ones, nuclear magnetic resonance (NMR) spectroscopy has become an established method,[2–4] to the extent that, since 2014, a "Commission on NMR Crystallography and Related Methods" exists in the International Union of Crystallography.[5] In solid-state NMR, the intrinsic orientation dependence of the resonance frequencies becomes important. Therefore, the relevant NMR parameters, i.e. the chemical shift, the dipolar (and for spin $I > 1/2$, quadrupolar) interaction are usually expressed as second-rank tensor quantities. In the context of NMR crystallography, many questions (e.g. the determination of asymmetric units, assignment of space groups) may already be answered by considering only the isotropic chemical shift δ_{iso} of the NMR-observed nuclide.[2] The deceptively simple scalar δ_{iso} is, however, the result of a contraction (of the isotropic part) of the second-rank chemical shift (CS) tensor:

$$\delta_{iso} = \frac{1}{3}\left(\delta_{11} + \delta_{22} + \delta_{33}\right) \tag{1.1}$$

Here, δ_{11}, δ_{22}, and δ_{33} are the components of the main diagonal of the CS tensor, which are the eigenvalues in its principal axes system. The full CS tensor $\boldsymbol{\delta}$ reflects the spatial distribution of electrons around the observed nucleus, which shield it from the external magnetic field to a certain extent. Therefore, a more complete picture becomes available when the full chemical shift tensor is known, which provides possible information on coordination, the influence of electron lone pairs, etc. For spin $I = 1/2$ nuclei, the eigenvalues δ_{11}, δ_{22}, and δ_{33} may be determined by measuring the NMR spectrum of a multicrystalline ('powder') sample under static conditions, as exemplified in literature.[6] It is also possible to derive these eigenvalues from the rotational side-band pattern of magic-angle spinning (MAS) spectra[7] to even higher precision.[8] In unrivalled accuracy (and for $I > 1/2$ in all cases), however, the eigenvalues of the CS tensor may be extracted from orientation-dependent measurements of single crystals.[9,10] Furthermore, the orientation of the CS tensor in the crystal structure, expressed by the corresponding eigenvectors, is unequivocally only accessible via single-crystal NMR spectroscopy. (In certain cases, indirect determination might be possible from the relative orientation of the CS tensor to the dipolar coupling tensor.[11])

The situation is similar for the quadrupole coupling tensor $\mathbf{Q}$ of nuclei with spin $I > 1/2$, where the magnitude (expressed by the quadrupolar coupling constant χ) and the eigenvalues may also be extracted from either static or MAS spectra of polycrystalline material, using specialized techniques and/or numerical simulations.[12,13] However, the full $\mathbf{Q}$ tensor and its orientation

in the crystallographic coordinate system is generally only accessible via single-crystal NMR spectroscopy. The superposition of chemical shift and quadrupolar coupling in single-crystal spectra of quadrupolar nuclei can also easily be dealt with. While, on the other hand, for static or MAS NMR data this interaction overlay further complicates the determination of the available NMR parameters and decreases precision. For characterization of a multi-component system, it is crucial to know the exact NMR-interaction parameters of the detected nuclei in the various components, in order to correctly assign and distinguish the NMR signals arising from them. In spite of these obvious advantages, single-crystal NMR is comparatively seldom employed for tensor determination. This may be traced to (at least) three problems with this method:

(*I*) Data acquisition and evaluation is rather time-consuming when compared to static or MAS NMR of polycrystalline samples;

(*II*) Tensor eigenvector determination in the crystal frame requires knowledge of the exact orientation of the crystal on the goniometer axis;

(*III*) Single crystals of sufficient size must be available because of the comparatively poor signal-to-noise ratio of NMR spectroscopy.

One purpose of this work is to show that these difficulties may be overcome in almost all cases. As for problem (*I*), the amount of necessary work can be greatly reduced by exploiting internal crystal symmetries, i.e. considering the NMR resonances of symmetry-related atoms in the unit cell as an additional dataset acquired for an independent but virtual rotation axis.[14–18] The fundamental idea behind this strategy (sometimes referred to as "single rotation method") is that symmetry-related atoms in the unit cell might still be magnetically inequivalent, giving rise to distinct signals in the NMR spectrum. If the symmetry element connecting these magnetically inequivalent atoms is known, their resonance positions in the data set gives additional information, which may allow determination of the full tensor. The same concept can be used to address problem (*II*) by calculating the exact orientation of the rotation axis from NMR data alone.[19–21] We term this extensions of the single rotation method, the "minimal rotation method", and (as will be detailed throughout this work) tensor determination by the minimal rotation method is not limited to systems with symmetry-linked atoms.[22] Regarding problem (*III*), many systems are amenable to crystal growth by methods available in a standard laboratory, and many more can be made available trough specialised growing technics (e.g. Czochralski process;[23] physical vapour deposition.[24]) In addition, natural minerals offer a great supply of single crystalline material already prepared by nature, often of sufficient size for NMR investigations.[20–22,25,26] To illustrate how to tackle the above listed problems (*I*)–(*III*), we here present the determination of

the full ^{207}Pb chemical shift tensor of a variety of lead-bearing, naturally grown minerals using single crystals from natural mineral deposits.

NMR spectroscopy of ^{207}Pb (the only stable lead isotope with a nuclear spin, namely, $I = 1/2$) is a valuable analytical tool in solid-state research. As a "heavy" nuclide, lead has a very large chemical shift range, extending over approximately 10,000 ppm, which makes ^{207}Pb a sensitive reporter of the local electronic state.[27–29] Recently, there has been intensified interest in ^{207}Pb-NMR to characterise organolead halide perovskites, which have been identified as promising materials in photovoltaics.[30–32] Frequently, ^{207}Pb NMR studies (and NMR studies in general) are augmented with quantum-mechanical calculations of chemical shifts (and for $I > 1/2$ of quadrupolar coupligs).[20,21,28,32] While, in general, such calculations have matured to the point where their results are very useful for comparison with experimental data,[33] calculations for heavy nuclei are specifically problematic, even when relativistic effects for the electrons are included.[34] Hence, another purpose of this work is to add to the comparatively small database of ^{207}Pb CS tensors available in the literature, and to provide more experimental numbers against which calculation methods may be calibrated. Finally, we go beyond mere tensor determination to further advance the use of single-crystal NMR spectroscopy as an analytical tool for structure characterisation by examining and establishing correlations between the NMR derived parameters, structural features, and crystal morphology. The initially unknown, and from our NMR experiments derived, orientations of the measured crystals can even be exploited to provide information about twinning in presumably single crystalline specimen.

Before discussing our results in detail, we briefly outline the basic principles of our main analytical technique, i.e. NMR spectroscopy of single crystals, and give a detailed explanation of the herein introduced "minimal rotation method".

2 The NMR Hamiltonians $\hat{H}_i$

The general Hamiltonian $\hat{H}_{\mathrm{NMR}}$ describing the spin evolution in solid-state NMR spectroscopy may be written as:[35–37]

$$\hat{H}_{\mathrm{NMR}} = \hat{H}_{\mathrm{Z}} + \hat{H}_{\mathrm{CS}} + \hat{H}_{\mathrm{D}} + \hat{H}_{\mathrm{J}} + \hat{H}_{\mathrm{CR}} + \left(\hat{H}_{\mathrm{Q}}\right) \tag{2.1}$$

Here, $\hat{H}_{\mathrm{Z}}$ is the nuclear Zeeman (not Zeman!) term which solely scales with the gyromagnetic ratio γ_n of the observed nuclide and the strength of the applied external magnetic field $\vec{B}_0$. $\hat{H}_{\mathrm{CS}}$ is the energy change caused by the chemical shift (CS) as a result of the interaction of the $\vec{B}_0$ field with the electrons surrounding a nuclear spin. The term $\hat{H}_{\mathrm{D}}$ describes the dipolar interactions caused by the direct and indirect couplings between the nuclear magnetic moments. The J-coupling, in which the interactions of the nuclei are transmitted throughout the bonding electrons, may be expressed by $\hat{H}_{\mathrm{J}}$, and $\hat{H}_{\mathrm{CR}}$ describes the spin-lattice interaction. For atoms with an angular momentum quantum number (spin) $I \geq 1$, a quadrupolar interaction $\hat{H}_{\mathrm{Q}}$ is observed, which has its origin in the non-spherical charge distribution in the atomic nucleus. This leads to a coupling of the nuclear quadrupole moment with the electric field gradient (EFG) caused by the asymmetric electronic environment. For the data presented in this thesis, we are going to work in a regime where the "size" of the Zeeman interaction $\hat{H}_{\mathrm{Z}}$ is much larger than the "size" of the other Hamiltonians and hence, it is convenient to treat the quadrupolar interaction as a perturbation of nth order to the Zeeman levels:[12,38,39]

$$\hat{H}_{\mathrm{Q}} = \hat{H}_{\mathrm{Q}}^{(1)} + \hat{H}_{\mathrm{Q}}^{(2)} + \hat{H}_{\mathrm{Q}}^{(3)} + ... \tag{2.2}$$

For the majority of quadrupolar nuclei measured in the strong external magnetic fields used in modern solid-state NMR spectrometer, it is more than sufficient to consider the quadrupolar term up to second-order perturbation theory. However, in some cases it may be necessary to treat the quadrupolar interaction to third order to obtain the correct NMR line shapes.

The J-coupling and the spin-lattice interaction only have a subordinate role in solid-state NMR spectroscopy, due to the comparatively low strength. While the quadrupolar interaction and the anisotropy of the chemical shift are in the range of MHz to kHz, their influence on the NMR spectra are mostly found in the region of less than hundred Hz. Since the effect of the J-coupling and the spin-lattice interaction on the spectra shown in this work only contribute to a small and unspecific line-broadening, they are negligible and not quantitatively evaluated herein. The various dipolar couplings, are discussed only in a limited context. While their interaction

strength may reach several kHz, the actual line position, i.e. the center of gravity, of a specific single-crystal NMR frequency is not affected.

A shorthand notation for the NMR interaction Hamiltonians $\hat{H}_\mathrm{i}$ in Equation 2.2 is given in Table 2.1. It may be seen, that all Hamiltonians can be described by the following general form: [37,40]

$$\hat{H}_\mathrm{i} = C_\mathrm{i}\, \hat{I}\, \underline{\underline{T_\mathrm{i}}}\, \hat{K} \tag{2.3}$$

Here C_i is a characteristic constant for the interaction i and $\hat{I}$ is a vector operator. $\hat{K}$ is either a further vector operator or the magnetic field vector of an external magnetic field $\vec{B}_0$. $\underline{\underline{T_\mathrm{i}}}$ is a second-rank Cartesian tensor that describes the orientation relation of the interactions of both vector quantities with each other and is expressed mathematically with a 3×3 matrix.

Table 2.1 – Interaction Hamiltonians describing the spin evolution in solid-state NMR spectroscopy. [37]

Interaction	**Form of the Hamiltonian**
Zeeman interaction	$\hat{H}_\mathrm{Z} = \gamma \hat{I} \cdot \underline{\underline{1}} \cdot \hat{B}_0$
Chemical shift	$\hat{H}_\mathrm{CS} = \gamma \hat{I} \cdot \underline{\underline{\delta}} \cdot \hat{B}_0$
Dipole-dipole	$\hat{H}_\mathrm{D} = \sum_{i<j} \hbar \gamma_i \gamma_j r_{ij}^{-3} \left(\hat{I}_i \cdot \hat{I}_j - \frac{3(\hat{I}_i r_{ij})(\hat{I}_j r_{ij})}{r_{ij}^2} \right)$
	$\hat{H}_\mathrm{D} = \sum_{i=j} \hat{I}_i \cdot \underline{\underline{D}} \cdot \hat{I}_j$
	$D_{\alpha\beta} = \hbar \gamma_i \gamma_j r_{ij}^{-3} (\delta_{\alpha\beta} - 3 e_\alpha e_\beta)$
	$\alpha, \beta = x, y, z; e_\alpha : \alpha-$component of the unit vector along r_{ij}
J-coupling	$\hat{H}_\mathrm{J} = \sum_{i \neq j} \hat{I}_i \cdot \underline{\underline{J}} \cdot \hat{I}_j$
Spin-rotation	$\hat{H}_\mathrm{CR} = \sum_i \hat{I}_i \cdot \underline{\underline{C_i}} \cdot \hat{J}$
Quadrupole	$\hat{H}_\mathrm{Q} = \frac{eQ}{2I(2I-1)\hbar} \hat{I} \cdot \underline{\underline{V}} \cdot \hat{I} = \frac{1}{2I(2I-1)} \hat{I} \cdot \underline{\underline{Q}} \cdot \hat{I}$
	$\underline{\underline{V}} = \{V_{\alpha\beta}\}; \alpha, \beta = x, y, z$

The main topic of this thesis is the full determination of this interaction tensor for the chemical shift ($\underline{\underline{T_\mathrm{i}}} = \boldsymbol{\delta}$) and for the quadrupolar coupling ($\underline{\underline{T_\mathrm{i}}} = \mathbf{Q}$) by means of single-crystal NMR spectroscopy and their relation to structural and electronic features of inorganic solids. As such, this Section is only meant to give an overview of the general NMR interactions present in the solid state. In the following the actual resonance frequencies measured for a specific nuclei in a solid state NMR spectra are discussed in detail. For the very principles of solid-state nuclear magnetic resonance spectroscopy, derivations of the Hamiltonians as well as the corresponding

energy levels we refer the reader to the three excellent books by Abragam,[36] Mehring,[37] and Levitt.[41]

3 Single-Crystal NMR: Signal Position

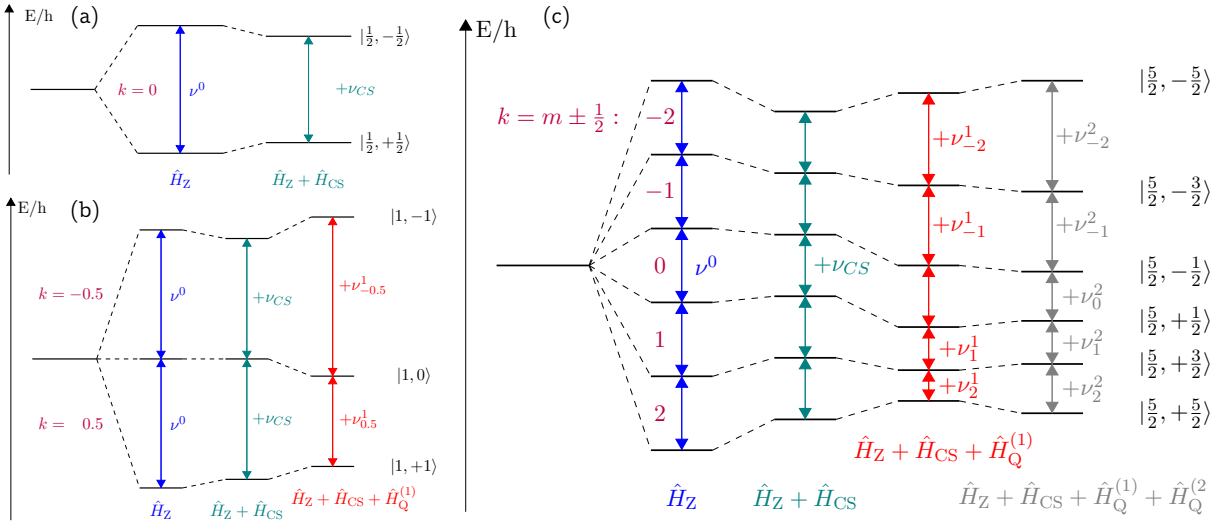

Figure 3.1 – Schematic energy levels of a spin $I = 1/2$ **(a)**, $I = 1$ **(b)**, and $I = 5/2$ **(c)** nucleus, in an external magnetic field $\vec{B}_0$, with the individual resonance frequencies designated by the parameter $k = m \pm 0.5$ (see text for details). For $I = 1/2$ only the effect of the Zeeman interaction and the chemical shift is considered. For a nucleus with spin $I = 1$, the effect of the first-order quadrupolar interaction is added. In the scheme for a nuclear spin $I = 5/2$, the quadrupolar interaction is considered up to second-order perturbation theory. The interaction strength is only qualitatively shown, since the Zeeman splitting is much larger than the quadrupolar interaction followed by the chemical shift.

For spin I in an external magnetic field, $2I$ NMR transitions exist, which are classified according to their magnetic quantum number m. With a particular transition $|m\rangle \rightarrow |m \pm 1\rangle$ designated by the parameter $k = m \pm \frac{1}{2}$,[21] the resonance frequency $\nu_{m,m\pm1}$ of this transition may be described by the following general notation:

$$\nu_{m,m\pm1}(k) = \nu_0 + \nu_{CS} + \left[\nu^{(1)}_{m,m\pm1}(k) + \nu^{(2)}_{m,m\pm1}(k^2) + \nu^{(3)}_{m,m\pm1}(k, k^3)\right] \tag{3.1}$$

For a spin $I = 1/2$ nuclei, the center of gravity of the resonance frequency is only determined by the Larmor frequency ν_0, which solely scales with the magnetic field strength for a specific nuclide and by the contribution of the chemical shift ν_{CS}. Only one NMR transition with $k = 0$ exists with the schematic energy levels shown in Figure 3.1a. For nuclides with a spin $I > 1/2$ the resonance frequency is further shifted by $\nu^{(1)}_{m,m\pm1}(k)$, $\nu^{(2)}_{m,m\pm1}(k^2)$, and $\nu^{(3)}_{m,m\pm1}(k, k^3)$, which are the effects of the quadrupolar interaction described by perturbation theory to first, second, and third order. For small quadrupolar couplings, only the first-order perturbation term needs to be considered, as is exemplary shown in Figure 3.1b for the energy scheme of a spin $I = 1$ nuclide. Here, two NMR transitions with $k = \pm 0.5$ are observable. For larger couplings, the second-order

term needs also to be considered, as is depicted in Figure 3.1c for spin $I = 5/2$. The transition $|\pm\frac{1}{2}\rangle \rightarrow |\mp\frac{1}{2}\rangle$, $k = 0$, in nuclides with half-integer spin is usually termed central transition (CT). The transitions for $k = \pm1, \pm2, \pm3$, and ±4, are referred to as the $\pm3/2, \pm5/2, \pm7/2$, and $\pm9/2$ satellite transitions (ST's). The term $\nu^{(3)}_{m,m\pm1}(k, k^3)$ in Equation 3.1 is generally small and only needs to be considered for extremely strong quadrupolar interactions at comparatively low magnetic field strength (see Section 12).

The contribution of the chemical shift ν_{CS} to the resonance frequency is gauged by the chemical shift tensor $\boldsymbol{\delta}$ and the signal position depends on the relative orientation to the external magnetic field $\vec{B}_0$. In general $\boldsymbol{\delta}$ is not necessarily symmetric. However, its antisymmetric components are practically unobservable since they contribute only in second order to the resonance frequency and hence, only the symmetric part is usually considered.[42] The CS tensor, thus, takes the following form in the laboratory coordinate system (LAB), where the $\vec{B}_0$ field vector defines the z axis of a Cartesian coordinate system (xyz):

$$\boldsymbol{\delta}^{\boldsymbol{LAB}} = \begin{pmatrix} \delta_{xx} & \delta_{xy} & \delta_{xz} \\ \delta_{xy} & \delta_{yy} & \delta_{yz} \\ \delta_{xz} & \delta_{yz} & \delta_{zz} \end{pmatrix} \tag{3.2}$$

For the NMR spectroscopy of single crystals, it is useful to define two other coordinate systems, i.e. the frame of the crystal lattice (CRY), which is the orthonormal *abc* crystal frame, and the principal axes system (PAS) of the tensor. The CS tensor may be transformed between these three coordinate systems using the Euler angles Ω_{ij} relating one frame to the other:[43,44]

$$\boldsymbol{\delta}^{\boldsymbol{LAB}} \underset{\Omega_{CL}}{\overset{\Omega_{LC}}{\rightleftharpoons}} \boldsymbol{\delta}^{\boldsymbol{CRY}} \underset{\Omega_{PC}}{\overset{\Omega_{CP}}{\rightleftharpoons}} \boldsymbol{\delta}^{\boldsymbol{PAS}} \tag{3.3}$$

Symmetric tensors take diagonal form in their own PAS, where the tensor eigenvalues $(\delta_{11}, \delta_{22}, \delta_{33})$ are the diagonal tensor elements:

$$\boldsymbol{\delta}^{\boldsymbol{PAS}} = \begin{pmatrix} \delta_{11} & 0 & 0 \\ 0 & \delta_{22} & 0 \\ 0 & 0 & \delta_{33} \end{pmatrix} = \begin{pmatrix} \delta_{iso} - \frac{\Delta\delta}{2}(1+\eta_{CS}) & 0 & 0 \\ 0 & \delta_{iso} - \frac{\Delta\delta}{2}(1-\eta_{CS}) & 0 \\ 0 & 0 & \Delta\delta + \delta_{iso} \end{pmatrix} \tag{3.4}$$

In the notation on the right-hand side, we used the definition of the isotropic chemical shift $\delta_{iso} = \frac{1}{3}(\delta_{11} + \delta_{22} + \delta_{33})$ (see also Equation 1.1), and two alternative tensor parameters according to the Haeberlen convention,[40] namely, asymmetry parameter η_{CS} and reduced anisotropy $\Delta\delta$:

$$\eta_{CS} = \frac{\delta_{22} - \delta_{11}}{\Delta\delta}; \qquad \Delta\delta = \delta_{33} - \delta_{iso} \tag{3.5}$$

For the above definitions to work properly, the eigenvalues of $\boldsymbol{\delta}$ need to be sorted according to:

$$|\delta_{33} - \delta_{iso}| \geq |\delta_{11} - \delta_{iso}| \geq |\delta_{22} - \delta_{iso}| \tag{3.6}$$

The orientation dependence of the resonance position influenced by chemical shift only (without the contribution of the quadrupolar coupling and scaled by the Larmor frequency ν_0) in the LAB frame may then be written as:[41,45]

$$\begin{aligned} \frac{\nu_{CS}}{\nu_0}\,[\text{ppm}] &= (1+\delta_{iso}) + \frac{2}{3}\left[\delta_{33} - \frac{1}{2}\left(\delta_{11}+\delta_{22}\right)\right]\left[\frac{1}{2}\left(3\cos^2\beta - 1\right) - \frac{1}{2}\eta_{CS}\cos\alpha\sin^2\beta\right] \\ &= \vec{b}_0^{\,T}\cdot\boldsymbol{\delta}\cdot\vec{b}_0 \end{aligned} \tag{3.7}$$

The azimuth angle α and the polar angle β relate the PAS frame of the chemical shift tensor to the laboratory coordinate system. The dependence of the resonance position on the relative orientation of the magnetic field vector $\vec{b}_0$ and the chemical shift tensor $\boldsymbol{\delta}$ is best seen on the second part in Equation 3.7. This shorthand notation is especially convenient to use when aiming to derive magnetic resonance frequencies in a coordinate system different from the LAB frame, as is detailed in Section 4.

Magnitude and orientation dependency of the quadrupolar interaction may be gauged by the quadrupole coupling tensor $\mathbf{Q}$.[35] Similar to the electrical field gradient (EFG) tensor $\mathbf{V}$, to which it is related by $\mathbf{Q} = (eQ/\hbar)\mathbf{V}$ with Q being the nuclear quadrupole moment, this second-rank tensor is symmetric and traceless, i.e. $Q_{ij} = Q_{ji}$ and $Q_{xx} + Q_{yy} + Q_{zz} = 0$. In an arbitrary coordinate system (x, y, z), the quadrupole coupling tensor hence takes the form:

$$\mathbf{Q} = \begin{pmatrix} Q_{xx} & Q_{xy} & Q_{xz} \\ Q_{xy} & Q_{yy} & Q_{yz} \\ Q_{xz} & Q_{yz} & -Q_{xx} - Q_{yy} \end{pmatrix} \tag{3.8}$$

In its own PAS, $\mathbf{Q}$ may be written as:

$$\boldsymbol{Q}^{PAS} = \begin{pmatrix} Q_{11} & 0 & 0 \\ 0 & Q_{22} & 0 \\ 0 & 0 & Q_{33} \end{pmatrix} = \chi \begin{pmatrix} -\frac{1}{2}\left(1-\eta_Q\right) & 0 & 0 \\ 0 & -\frac{1}{2}\left(1+\eta_Q\right) & 0 \\ 0 & 0 & 1 \end{pmatrix} \tag{3.9}$$

In the second notation of $\mathbf{Q}$, we have used the definition of the quadrupolar coupling constant,

$$\chi = C_Q = \frac{eQeq}{h} = \frac{eQ}{h}V_{33} = Q_{33} \tag{3.10}$$

and the quadrupolar asymmetry parameter

$$\eta_Q = \frac{Q_{11} - Q_{22}}{Q_{33}} \tag{3.11}$$

where the eigenvalues of $\boldsymbol{Q}^{PAS}$ are ordered according to the convention:

$$|Q_{33}| \geq |Q_{22}| \geq |Q_{11}| \tag{3.12}$$

For the notations of the quadrupolar contributions $\nu^{(n)}_{m,m\pm1}(k^n)$ in Equation 3.1 it is convenient to also define a quadrupolar frequency ν_Q in dependence of the nuclear spin I as follows:

$$\nu_Q = \frac{3eQeq}{h2I(2I-1)} = \frac{3\chi}{2I(2I-1)} \tag{3.13}$$

With this tensor notation, it is straightforward to express the orientation dependence of the resonance frequencies of quadrupolar nuclei. Similar to the contribution of the chemical shift in Equation 3.7, the quadrupolar frequency to first order depends on the relative orientation of the magnetic field vector $\vec{b}_0$ and the quadrupole coupling tensor $\mathbf{Q}$, scaled by the spin I and the respective transition k:[46]

$$\begin{aligned} \nu^{(1)}_{m,m\pm1}(k) &= -k\frac{\nu_Q}{2}\left(3\cos^2\beta - 1 + \eta_Q \cos 2\alpha \sin^2\beta\right) \\ &= \frac{3k}{2I(2I-1)}\vec{b}_0^T \cdot \mathbf{Q} \cdot \vec{b}_0 \end{aligned} \tag{3.14}$$

Here, α and β are again the Euler angles between the eigenvector with the largest eigenvalue, i.e. $Q_{33} = \chi$, and the magnetic field vector $\vec{b}_0$. As may directly be seen in Equation 3.14, the central transition (CT, $k = 0$) of a half-integer spin is unaffected by the first-order shift. The satellite transitions, on the other hand, are considerably shifted symmetrical around the CT.

The expression for the second-order perturbation term $\nu^{(2)}_{m,m\pm1}(k^2)$ has been given several times in literature.[46–52] However, some expressions are known to contain typographical errors and none have been experimentally verified by means of single-crystal NMR spectroscopy. The herein given expression (Equations 3.15–3.17) follows the results found in Wolf et al.[46] and is rewritten for easier comparison with the existing literature.

$$\nu^{(2)}_{m,m\pm1}(k^2) = -\frac{\nu_Q^2}{6\nu_0}\left[\left(I^2 + I - \frac{3}{4} - 3k^2\right) g(\alpha,\beta,\eta_Q) - 6k^2 f(\alpha,\beta,\eta_Q)\right] \tag{3.15}$$

with

$$\begin{aligned} g(\alpha,\beta,\eta_Q) &= A(\alpha,\eta_Q)\cos^4\beta + B(\alpha,\eta_Q)\cos^2\beta + C(\alpha,\eta_Q) \\ f(\alpha,\beta,\eta_Q) &= D(\alpha,\eta_Q)\cos^4\beta + E(\alpha,\eta_Q)\cos^2\beta + F(\alpha,\eta_Q) \end{aligned} \tag{3.16}$$

and

$$\begin{aligned} A &= -\tfrac{27}{8} + \tfrac{9}{4}\eta_Q\cos 2\alpha - \tfrac{3}{8}\eta_Q^2\cos^2 2\alpha & D &= -\tfrac{3}{2} + \eta_Q\cos 2\alpha - \tfrac{1}{6}\eta_Q^2\cos^2 2\alpha \\ B &= \tfrac{30}{8} - \tfrac{1}{2}\eta_Q^2 - 2\eta_Q\cos 2\alpha + \tfrac{3}{4}\eta_Q^2\cos^2 2\alpha & E &= \tfrac{3}{2} - \tfrac{1}{6}\eta_Q^2 - \eta_Q\cos 2\alpha + \tfrac{1}{3}\eta_Q^2\cos^2 2\alpha \\ C &= -\tfrac{3}{8} + \tfrac{1}{3}\eta_Q^2 - \tfrac{1}{4}\eta_Q\cos 2\alpha - \tfrac{3}{8}\eta_Q^2\cos^2 2\alpha & F &= \tfrac{1}{6}\eta_Q^2 - \tfrac{1}{6}\eta_Q^2\cos^2 2\alpha \end{aligned} \tag{3.17}$$

In the second-order approximation, also the resonance frequency of the CT is shifted and the ST's pairs ±3/2, ±5/2, ±7/2, and ±9/2, are each shifted by the same amount as a consequence of being not sign-sensitive, because of the k^2-dependency. For the central transition ($k = 0$) of a quadrupolar nuclide with half-integer spin, Equation 3.15 drastically simplifies to:

$$\nu^{(2)}_{m,m\pm1}(k^2) = -\frac{\nu_Q^2}{6\nu_0}\left(I^2 + I - \frac{3}{4} - 3k^2\right) g(\alpha,\beta,\eta_Q) \tag{3.18}$$

As will be shown in Section 9 and especially in Section 12, the above equations have been tested and proven correct (for $\eta_Q = 0$) on the single-crystal NMR response of ^{14}N and ^{27}Al in hexagonal AlN as well as for ^{45}Sc (for $\eta_Q \neq 0$) in $[(H_2O)_5Sc(\mu\text{-}OH)]_2Cl_4{\cdot}2H_2O$.

Since the quadrupolar interaction is usually only treated up to second-order, the third-order expression for the orientation dependence of the resonance frequency is rarely found in literature. In Section 12 we will prove the following expression to be correct, which again was taken from Wolf et al.[46] and is rewritten for easier comparison to the second-order term and to improve readability:

$$\begin{aligned} \nu^{(3)}_{m,m\pm1}(k,k^3) = -k\frac{\nu_Q^3}{12\nu_0^2}\Big\{ &\Big[12I\,(I+1) - 40k^2 - 17\Big]\, h(\alpha,\beta,\eta_Q) \\ &- 2\left[3I\,(I+1) - 5k^2 - \frac{19}{4}\right] l(\alpha,\beta,\eta_Q) \\ &- 3\Big[8I\,(I+1) - 20k^2 - 10\Big]\, n(\alpha,\beta,\eta_Q)\Big\} \end{aligned} \tag{3.19}$$

with

$$\begin{aligned} h(\alpha,\beta,\eta_Q) &= A'(\alpha,\eta_Q)\cos^6\beta + B'(\alpha,\eta_Q)\cos^4\beta + C'(\alpha,\eta_Q)\cos^2\beta + D'(\alpha,\eta_Q) \\ l(\alpha,\beta,\eta_Q) &= E'(\alpha,\eta_Q)\cos^6\beta + F'(\alpha,\eta_Q)\cos^4\beta + G'(\alpha,\eta_Q)\cos^2\beta + H'(\alpha,\eta_Q) \\ n(\alpha,\beta,\eta_Q) &= I'(\alpha,\eta_Q)\cos^6\beta + J'(\alpha,\eta_Q)\cos^4\beta + K'(\alpha,\eta_Q)\cos^2\beta + L'(\alpha,\eta_Q) \end{aligned} \tag{3.20}$$

and

$$\begin{aligned} A' &= -\frac{9}{4} + \frac{9}{4}\eta_Q\cos 2\alpha - \frac{3}{4}\eta_Q^2\cos^2 2\alpha + \frac{1}{12}\eta_Q^3\cos^3 2\alpha \\ B' &= 3 - \frac{1}{4}\eta_Q^2 - \frac{7}{2}\eta_Q\cos 2\alpha + \frac{1}{12}\eta_Q^3\cos 2\alpha + \frac{19}{12}\eta_Q^2\cos^2 2\alpha - \frac{1}{4}\eta_Q^3\cos^3 2\alpha \\ C' &= -\frac{3}{4} + \frac{1}{3}\eta_Q^2 + \frac{5}{4}\eta_Q\cos 2\alpha - \frac{1}{6}\eta_Q^3\cos 2\alpha - \frac{11}{12}\eta_Q^2\cos^2 2\alpha + \frac{1}{4}\eta_Q^3\cos^3 2\alpha \\ D' &= -\frac{1}{12}\eta_Q^2 + \frac{1}{12}\eta_Q^3\cos 2\alpha + \frac{1}{12}\eta_Q^2\cos^2 2\alpha - \frac{1}{12}\eta_Q^3\cos^3 2\alpha \end{aligned}$$

$$\begin{aligned} E' &= \frac{9}{16} - \frac{9}{16}\eta_Q\cos 2\alpha + \frac{3}{16}\eta_Q^2\cos^2 2\alpha - \frac{1}{48}\eta_Q^3\cos^3 2\alpha \\ F' &= -\frac{21}{16} + \frac{1}{4}\eta_Q^2 + \frac{11}{16}\eta_Q\cos 2\alpha - \frac{1}{12}\eta_Q^3\cos 2\alpha - \frac{13}{48}\eta_Q^2\cos^2 2\alpha + \frac{1}{16}\eta_Q^3\cos^3 2\alpha \\ G' &= \frac{15}{16} - \frac{1}{12}\eta_Q^2 - \frac{3}{16}\eta_Q\cos 2\alpha + \frac{1}{12}\eta_Q^3\cos 2\alpha - \frac{1}{48}\eta_Q^2\cos^2 2\alpha - \frac{1}{16}\eta_Q^3\cos^3 2\alpha \\ H' &= -\frac{3}{16} + \frac{1}{16}\eta_Q\cos 2\alpha + \frac{5}{48}\eta_Q^2\cos^2 2\alpha + \frac{1}{48}\eta_Q^3\cos^3 2\alpha \end{aligned} \tag{3.21}$$

$$\begin{aligned} I' &= \frac{3}{4} - \frac{3}{4}\eta_Q\cos 2\alpha + \frac{1}{4}\eta_Q^2\cos^2 2\alpha - \frac{1}{36}\eta_Q^3\cos^3 2\alpha \\ J' &= -\frac{3}{2} + \frac{1}{4}\eta_Q^2 + \eta_Q\cos 2\alpha - \frac{1}{12}\eta_Q^3\cos 2\alpha - \frac{5}{12}\eta_Q^2\cos^2 2\alpha + \frac{1}{12}\eta_Q^3\cos^3 2\alpha \\ K' &= \frac{3}{4} - \frac{1}{6}\eta_Q^2 - \frac{1}{4}\eta_Q\cos 2\alpha + \frac{1}{9}\eta_Q^3\cos 2\alpha + \frac{1}{12}\eta_Q^2\cos^2 2\alpha - \frac{1}{12}\eta_Q^3\cos^3 2\alpha \\ L' &= -\frac{1}{12}\eta_Q^2 - \frac{1}{36}\eta_Q^3\cos 2\alpha + \frac{1}{12}\eta_Q^2\cos^2 2\alpha + \frac{1}{36}\eta_Q^3\cos^3 2\alpha \end{aligned}$$

Just like the first-order perturbation theory term, the third order does not affect the central transition of half-integer spins ($k = 0$), and the ST's are shifted symmetrical around the CT.

At high magnetic fields, the quadrupolar interaction to third order is practically unobservable and the coupling tensor $\mathbf{Q}$ may conveniently be determined from the separations ('splittings') of the satellite transitions, since these are not affected by the chemical shift and the second-order quadrupolar interaction. Thus, the difference $\Delta\nu(k)$ of the resonance frequencies (where, from here on, we have dropped the $m, m \pm 1$ subscripts used in Equation 3.1 for brevity) is:

$$\Delta\nu(k) = \nu(+k) - \nu(-k) = \nu^{(1)}(+k)\left[+\nu^{(3)}(+k, +k^3)\right] - \nu^{(1)}(-k)\left[-\nu^{(3)}(-k, -k^3)\right] \tag{3.22}$$

If one neglects the third-order term, Equation 3.22 becomes:

$$\Delta\nu^{(1)}(k) = \nu^{(1)}(+k) - \nu^{(1)}(-k) = \frac{3\Delta k}{2I(2I-1)}\vec{b}_0^T \cdot \mathbf{Q} \cdot \vec{b}_0 \tag{3.23}$$

The coupling tensor $\mathbf{Q}$ may then be determined from the satellite splittings just like the chemical shift tensor from the resonance position of a spin $I = 1/2$ nuclei as is detailed in Section 4.

To determine the CS tensor of quadrupolar nuclei with half-integer spin it is customary to trace the orientation dependency of the central transition, i.e. the $k = 0$ transition, which is not affected by the first-, and third-order term.[53] In cases where the CT signal cannot be resolved,[54] the variation of the center of the satellite transitions (and for spin $I = 1$, the center of the doublet with $k = \pm 0.5$ in all cases) may be traced instead:

$$\nu(\Delta k/2) = \frac{\nu(+k) + \nu(-k)}{2} = \nu_0 + \nu_{CS} + \nu^{(2)}(k^2) \tag{3.24}$$

After subtracting $\nu^{(2)}(k^2)$ from the remaining frequency $\nu(\Delta k/2)$, the change of the resonance frequency from the Larmor frequency is solely due to the chemical shift and the line position again only depends on the relative orientation of the magnetic field vector $\vec{b}_0$ to the tensor $\boldsymbol{\delta}$ (see also Equation 3.7):

$$\frac{\nu(\Delta k/2) - \nu_0 - \nu^{(2)}(k^2)}{\nu_0} = \frac{\nu_{CS}}{\nu_0}\,[\text{ppm}] = \vec{b}_0^T \cdot \boldsymbol{\delta} \cdot \vec{b}_0 \tag{3.25}$$

In principle, the third-order quadrupolar interaction can be "extracted" from the experimental data points by calculating the weighted separations of the satellite splittings. As may be seen in Equation 3.22, the ST splittings are only affected by the first-, and third-order terms. The orientation dependency for the ST splittings to first-order for different satellite splittings of

the same nuclide differ only by Δk, as may be seen in Equation 3.23. Hence, by rescaling these splittings and subtracting the scaled splittings from each other, the contribution to first-order quadrupolar interaction vanishes:

$$\begin{aligned}\Delta\nu^{(1)}(k) - \frac{k}{k-n}\Delta\nu^{(1)}(k-n) &= \frac{3\Delta k}{2I(2I-1)}\vec{b}_0^T \cdot \mathbf{Q} \cdot \vec{b}_0 - \frac{k}{k-n}\frac{3\Delta(k-n)}{2I(2I-1)}\vec{b}_0^T \cdot \mathbf{Q} \cdot \vec{b}_0 \\ &= \left[\Delta k - \frac{k}{k-n}\Delta(k-n)\right]\frac{3}{2I(2I-1)}\vec{b}_0^T \cdot \mathbf{Q} \cdot \vec{b}_0 = 0 \\ &\text{with} : n = 1, 2, 3\end{aligned} \tag{3.26}$$

Here, the factor $k-n$ denotes the splitting which is subtracted from the satellite splitting Δk. For example, when calculating the separations of the 7/2 ST splitting and the 3/2 ST splitting, $k = 3$ and $n = 2$, since $k - 2 = 1$ denotes the 3/2 satellite transition. What remains in the splitting of the ST's splitting $\triangle\Delta\nu(k, k-n)$, if present at all, is a sum of third-order terms only, which can be calculated by inserting Equation 3.19 in Equation 3.27 (see Section 12, Figure 12.5b).

$$\begin{aligned}\triangle\Delta\nu(k, k-n) &= \Delta\nu(k) - \frac{k}{k-n}\Delta\nu(k-n) \\ &= \Big[\nu(+k) - \nu(-k)\Big] - \frac{k}{k-n}\Big[\nu(+k-n) - \nu(-k+n)\Big] \\ &= \Big[\nu^{(3)}(+k, +k^3) - \nu^{(3)}(-k, -k^3)\Big] \\ &\quad - \frac{k}{k-n}\Big\{\nu^{(3)}[+k-n, +(k-n)^3] - \nu^{(3)}[-k+n, -(k-n)^3]\Big\}\end{aligned} \tag{3.27}$$

4 The Minimal Rotation Method

Section 4 describes the determination of the NMR interaction tensors ($\boldsymbol{\delta}$ and $\mathbf{Q}$) from single-crystal NMR spectra by use of internal crystal symmetries and without the need for additional crystal-alignment techniques. The overall goal is to reduce the amount of analytical data to a necessary minimum. Hence, from here on, we refer to this procedure as "the minimal-rotation method".

To determine the tensor components of $\boldsymbol{\delta}$ (and $\mathbf{Q}$ from the ST splittings) from our NMR experiments, we now consider what happens when a chemical-shift tensor is rotated in the LAB frame around an axis $\vec{g}$, perpendicular to the external magnetic field $\vec{B}_0$ (described by normal vector $\vec{b}_0$ here), by an angle φ. To this end, the single crystals under investigation are fixed on a rod and installed in a goniometer mechanics, as exemplarily pictured in Figure 4.1a. The mechanics allows a defined change of rotation angle φ around the goniometer axis $\vec{g}$. For such a rotation, the orientation dependence of the resonance frequency (in units of ppm, i.e. scaled by Larmor frequency ν_0) is given by Volkoff harmonics:[9]

$$\frac{\nu_{CS}^{n}(\varphi)}{\nu_0} = \vec{b}_0^{T} \cdot \boldsymbol{\delta}^{\boldsymbol{LAB}}(\varphi) \cdot \vec{b}_0 = A^n + B^n \cos 2\varphi + C^n \sin 2\varphi \tag{4.1}$$

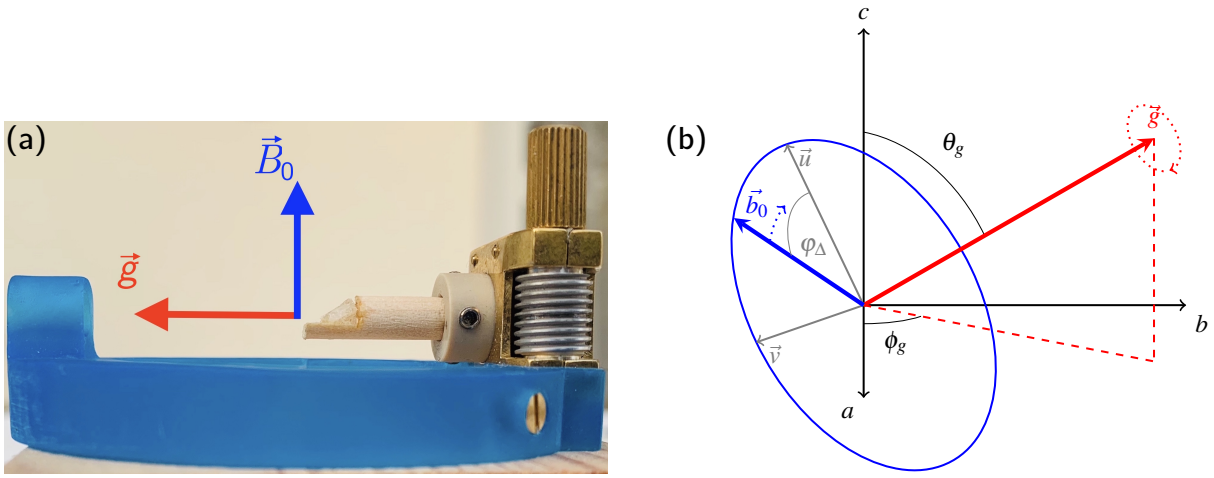

Figure 4.1 – **(a)** 'Clip-on' goniometer built by NMR Service GmbH (Erfurt, Germany) for a wide-bore Bruker static NMR probe, with an arbitrary single crystal mounted on a wooden rotation axis with 5 mm diameter. The goniometer axis (red) is perpendicular to the applied magnetic field $\vec{B}_0$ (blue). **(b)** Coordinates used for the interpretation of the rotation patterns; a, b, and c are the unit vectors of an orthonormal crystal system (CRY), $\vec{g}$ is the unit vector along the goniometer axis, θ_g and ϕ_g its polar angles in the CRY, $\vec{b}_0$ is the unit vector of the magnetic field, φ is the rotation angle, and $\vec{u}$ and $\vec{v}$ are auxiliary unit vectors necessary to define $\vec{b}_0$ perpendicular to $\vec{g}$.[Figure taken from [55]]

Plots of the resonance positions over the rotation interval of 180°, also known as "rotation patterns", are shown throughout Sections 6–12. The contribution of each magnetically inequivalent nuclide n in these rotation patterns follows the type of harmonic function shown in Equation 4.1. The factors A^n, B^n, and C^n are linear combinations of CS tensor components, their precise form depending on the relative orientation of the PAS frame to the LAB frame. In the general case, three rotation experiments about three nonparallel axes with known orientation are required to derive the full CS tensor with its six independent tensor components (see Equation 3.2).[9,10] However, instead of evaluating the rotation pattern in the LAB frame, the orthonormal *abc* crystal frame may be used to calculate $\boldsymbol{\delta^{CRY}}$ where internal crystal symmetry may be exploited to obtain more than one rotation pattern from just one physical rotation experiment.[14,16,18] The use of internal symmetry makes the CRY frame the preferred choice for carrying out all calculations needed to determine the NMR interaction tensors.

The fundamental idea behind this strategy (sometimes referred to as "single rotation method") is that symmetry-related atoms in the unit cell might still be magnetically inequivalent, giving rise to distinct signals in the NMR spectrum. While atoms related by any symmetry operation in a unit cell are crystallographically equivalent, only atomic positions related by translational or inversion symmetry are magnetically equivalent (the general requirement being that the symmetry operator commutes with the relevant spin Hamiltonian). In order to determine how two symmetry-linked tensors are related to one another, the general transformation of a second-rank tensor such as $\boldsymbol{\delta^{CRY}}$ under the rotation $R_{(i)}$ is considered:

$$\boldsymbol{\delta^{CRY}_{(i)}} = R^{-1}_{(i)} \cdot \boldsymbol{\delta^{CRY}} \cdot R_{(i)} \tag{4.2}$$

To check the influence of an inversion on the algebraic form of the tensor, we take the matrix representation for an inversion symmetry operation,

$$R_{(inv)} = R^{-1}_{(inv)} = \begin{pmatrix} -1 & 0 & 0 \\ 0 & -1 & 0 \\ 0 & 0 & -1 \end{pmatrix}, \tag{4.3}$$

and by insertion of $R^{-1}_{(inv)}$ in Equation 4.2, we find $\boldsymbol{\delta^{CRY}_{(i)}} = \boldsymbol{\delta^{CRY}}$. Hence, proving that inversion symmetry elements do not affect the NMR spectrum, and any crystallographic symmetry element acting on the chemical shift tensor can be considered as a simple rotation symmetry operator. As a consequence, one only has to distinguish between two-fold, three-fold, and four-fold symmetry elements when evaluating single-crystal NMR spectra.

The above briefly mentioned "single rotation method"[14–18] usually still requires prior knowledge of the crystal orientation before the NMR measurements begin. As a result, the goniometer of single-crystal NMR probes is usually placed inside the radio frequency (rf) coil, in order to allow precise reorientation of the sample with known rotation axis.[56–60] This always results in a non-optimal filling factor of the sample within the coil and thus in poor sensitivity. Placing the goniometer outside the rf coil and still being able to precisely reorient the crystal requires either a special coil design, which again reduces sensitivity,[61] or tilting of the goniometer axis in a way not perpendicular to the magnetic field.[62] A rotation axis non-perpendicular to the magnetic field vector, however, introduces additional harmonic terms ($D^n \cos\varphi$ and $E^n \sin\varphi$) in Equation 4.1 which reduces the precision of data evaluation especially when dealing with broad resonance frequencies and only small anisotropic interactions. One way out of this quandary is to also determine the crystal orientation, respectively the orientation of the goniometer axis in the CRY frame, from the single-crystal NMR data. The orientation of the crystal may then be arbitrarily chosen, which does not require a special goniometer probe design and no additional crystal alignment techniques are necessary.

In the CRY frame, the magnetic field vector $\vec{b}_0$ has a general orientation depending on the rotation angle φ, and the CS tensor $\boldsymbol{\delta}^{\boldsymbol{CRY}}$ is considered to be static:

$$\frac{\nu_{CS}^n(\varphi)}{\nu_0} = \vec{b}_0^T(\varphi) \cdot \boldsymbol{\delta}^{\boldsymbol{CRY}} \cdot \vec{b}_0(\varphi) \tag{4.4}$$

The components of $\vec{b}_0$ in this frame can be described in terms of the (initially unknown) orientation of the goniometer axis $\vec{g}$:

$$\vec{g} = \begin{pmatrix} \sin\theta_g \cos\phi_g \\ \sin\theta_g \sin\phi_g \\ \cos\theta_g \end{pmatrix} \tag{4.5}$$

To describe the stepwise rotation of $\vec{b}_0$ around $\vec{g}$, it is useful to define two auxiliary unit vectors, $\vec{v}$ and $\vec{u}$, in the plane perpendicular to $\vec{g}$. To unequivocally set $\vec{v}$ and $\vec{u}$, a reference vector is needed (that obviously needs to be nonparallel to $\vec{g}$), the choice of which determines the definition of offset angle φ_Δ in the plane, as shown in Figure 4.1b. For referencing along $(0, 0, 1)$, i.e. the unit vector along the crystallographic c axis, the two auxiliary unit vectors, $\vec{v}$ and $\vec{u}$ are given by:[19]

$$\begin{aligned} \vec{v} = \frac{1}{\sin\theta_g}(\vec{g} \times \vec{c})\,; \qquad \vec{u} = \vec{v} \times \vec{g} &= \frac{1}{\sin\theta_g}(\vec{g} \times \vec{c}) \times \vec{g} \\ &= \frac{1}{\sin\theta_g}(\vec{c} - \vec{g}\cos\theta_g) \end{aligned} \tag{4.6}$$

The orientation of $\vec{b}_0$ in the CRY frame may then be written as:

$$\vec{b}_0(\varphi) = \vec{v}\sin(\varphi - \varphi_\Delta) + \vec{u}\cos(\varphi - \varphi_\Delta) \tag{4.7}$$

To show, that the above expressions result in the Volkoff harmonics, we choose a simple example, where $\vec{g}$ can be assumed to be precisely aligned along one crystallographic axis, e.g. $\vec{b} = (0, 1, 0)$. It then follows from Equation 4.6 that the auxiliary unit vector $\vec{v}$ is aligned along the crystallographic a axis and $\vec{u}$ along the c axis, and Equation 4.7 reduces to:

$$\vec{b}_0(\varphi) = \begin{pmatrix}1\\0\\0\end{pmatrix}\sin(\varphi) + \begin{pmatrix}0\\0\\1\end{pmatrix}\cos(\varphi) \tag{4.8}$$

This equation and a general CS tensor (see Equation 3.2) is now inserted in Equation 4.4 which results in the following expression:

$$\frac{\nu_{CS}(\varphi)}{\nu_0} = \frac{1}{2}(\delta_{xx} + \delta_{zz}) + \frac{1}{2}(\delta_{zz} - \delta_{xx})\cos 2\varphi + \delta_{xz}\sin 2\varphi \tag{4.9}$$

If we would be in possession of experimental data for this hypothetical rotation of a crystal around the b axis, they could be fitted to the general harmonics of Equation 4.1, $A + B\cos 2\varphi + C\sin 2\varphi$ to obtain the parameters A, B and C. From this fit, the tensor elements δ_{xx}, δ_{zz} and δ_{xz} are immediately available via the relations $A = \frac{1}{2}(\delta_{xx} + \delta_{zz})$, $B = \frac{1}{2}(\delta_{zz} - \delta_{xx})$ and $C = \delta_{xz}$.

In cases where the goniometer axis $\vec{g}$ is aligned close to the reference vector, i.e. the crystallographic c axis for the expressions given in Equation 4.6, this construct does not work well for the fitting routine, which may fail to converge. Therefore, changing of the reference vector to be further away from the goniometer axis is required. In such cases, we used $\vec{b} = (0, 1, 0)$ along the crystallographic b axis as the reference vector instead, leading to the following expressions for the auxiliary vectors:

$$\begin{aligned}
\vec{v} &= \frac{1}{\sqrt{\cos^2\theta_g + \sin^2\theta_g\cos^2\phi_g}}\left(\vec{g}\times\vec{b}\right);\\
\vec{u} = \vec{v}\times\vec{g} &= \frac{1}{\sqrt{\cos^2\theta_g + \sin^2\theta_g\cos^2\phi_g}}\left(\vec{g}\times\vec{b}\right)\times\vec{g}\\
&= \frac{1}{\sqrt{\cos^2\theta_g + \sin^2\theta_g\cos^2\phi_g}}\left(\vec{b} - \vec{g}\cos\theta_g\right)
\end{aligned} \tag{4.10}$$

As may be seen in Equation 4.1, one harmonic function of a rotation pattern delivers three linear independent parameters (A^n, B^n, C^n). However, two harmonics of two symmetry-related tensors $\boldsymbol{\delta}_{(i)}^{\boldsymbol{CRY}}$ and $\boldsymbol{\delta}^{\boldsymbol{CRY}}$ are linked by a constraint and deliver only five linear independent parameters.[18] To understand this, one can think of the CS tensor in the CRY frame as a unit sphere at the systems origin. As long as the goniometer axis is placed perpendicular to the magnetic field $\vec{B}_0$, $\vec{b}_0(\varphi)$ traces out great circles on the unit sphere. The two symmetry-related tensors can be assumed to be the same unit sphere, but $\vec{b}_0(\varphi)$ traces out two different great circles on this unit sphere. Since any two great circles on a sphere with the same origin intersect, there must be an angle φ within a 180° rotation interval where the two symmetry-related tensors produce identical line positions. The two harmonics of the symmetry-related tensors $\boldsymbol{\delta}_{(i)}^{\boldsymbol{CRY}}$ and $\boldsymbol{\delta}^{\boldsymbol{CRY}}$ are hence not completely independent, but linked by one constraint. So instead of adding three linear independent parameters, only two additional parameters are available with every additional magnetically inequivalent but symmetry-linked atom. With the orientation of the goniometer axis in the CRY frame defined by the angels θ_g, ϕ_g, and φ_Δ, a total of nine linear independent parameters need to be calculated from one physical rotation pattern to determine a general CS tensor and its orientation. In order to determine all nine parameters from one rotation patter, one crystallographic site needs to be composed of four magnetically inequivalent positions. Examples of such crystal symmetries are given in Section 6 and Section 11.

Fortunately, atomic sites in a unit cell are often located at special Wyckoff positions with a higher site symmetry than $1(C_1)$. The site symmetry may impose constrains on the symmetry and orientation of the NMR interaction tensors and thereby reduces the number of independent tensor components, since the site-symmetry operator $R_{(i)}$ on the interaction tensor is self-generating:

$$\boldsymbol{\delta}_{(\boldsymbol{i})}^{\boldsymbol{CRY}} = R_{(i)}^{-1} \cdot \boldsymbol{\delta}_{(\boldsymbol{i})}^{\boldsymbol{CRY}} \cdot R_{(i)} \tag{4.11}$$

As a simple example, we assume a nucleus sitting on a mirror plane in the crystallographic ab plane, i.e. perpendicular to the c axis, the symmetry operator is then defined by:

$$R_{(mc)} = R_{(mc)}^{-1} = \begin{pmatrix} 1 & 0 & 0 \\ 0 & 1 & 0 \\ 0 & 0 & -1 \end{pmatrix} \tag{4.12}$$

Inserting in Equation 4.11 gives:

$$\begin{aligned}\begin{pmatrix}\delta_{xx} & \delta_{xy} & \delta_{xz}\\ \delta_{xy} & \delta_{yy} & \delta_{yz}\\ \delta_{xz} & \delta_{yz} & \delta_{zz}\end{pmatrix} &= \begin{pmatrix}1 & 0 & 0\\ 0 & 1 & 0\\ 0 & 0 & -1\end{pmatrix}\cdot\begin{pmatrix}\delta_{xx} & \delta_{xy} & \delta_{xz}\\ \delta_{xy} & \delta_{yy} & \delta_{yz}\\ \delta_{xz} & \delta_{yz} & \delta_{zz}\end{pmatrix}\cdot\begin{pmatrix}1 & 0 & 0\\ 0 & 1 & 0\\ 0 & 0 & -1\end{pmatrix}\\ &= \begin{pmatrix}\delta_{xx} & \delta_{xy} & -\delta_{xz}\\ \delta_{xy} & \delta_{yy} & -\delta_{yz}\\ -\delta_{xz} & -\delta_{yz} & \delta_{zz}\end{pmatrix} \Rightarrow \begin{pmatrix}\delta_{xx} & \delta_{xy} & 0\\ \delta_{xy} & \delta_{yy} & 0\\ 0 & 0 & \delta_{zz}\end{pmatrix}\end{aligned} \tag{4.13}$$

For this special position, i.e. for an atom situated on a two-fold symmetry operation, the chemical shift tensor is only defined by four linear independent tensor components since $\delta_{xz} = -\delta_{xz}$ and $\delta_{yz} = -\delta_{yz}$ is only true for $\delta_{xz} = \delta_{yz} = 0$. A comprehensive list of the site symmetry operators and their influence on the algebraic form of the NMR interaction tensor for the seven crystal classes is given by Weil et al..[63] Including the rotation axis orientation, an atom situated on a crystallographic site with a two-fold symmetry operation needs to be composed of only three magnetically inequivalent positions in order to determine all components from one rotation pattern. Examples of such crystal symmetry are given in Section 7.

In case the site symmetry of the NMR interaction tensor is a two-fold symmetry element but only two symmetry-linked atoms are generated by the crystal structure, one physical rotation pattern is insufficient, with seven fit parameters versus five independent parameters which can be derived from the experiments. The obvious solution to this problem is to acquire two rotation patterns about two different (non-parallel) rotation axis $\vec{g}_1$ and $\vec{g}_2$, and subject them to a global fit. Examples of such a global fit over two rotation pattern for tensor determination are given in Section 8 and 12.

When no symmetry linked magnetically inequivalent positions for a nuclide under investigation are present, full tensor determination from only the NMR data becomes challenging. Any rotation pattern of such a nuclide will only supply three linear independent parameters A^n, B^n, and C^n according to Equation 4.1. To determine the arbitrary rotation axes $\vec{g}_n$, three more fit parameters θ_n, ϕ_n, and $\varphi_{\Delta n}$ are needed, in effect making acquisition of additional rotation patterns a zero-sum game. When trying to avoid the application of independent, non-NMR crystal alignment techniques, a rather simple solution is to investigate a system for which the crystal morphology is well known and can be directly assigned to crystallographic planes. This is usually the case for macroscopic single crystals which where grown in controlled environments, e.g. by atomic layer deposition or physical vapor transport. Such artificially grown single crystals may be optical aligned on the goniometer axis in a known orientation, and the NMR data can

directly be fitted to the tensor elements. An example for this technique is given in Section 9 for a homoepitaxially grown AlN single crystal. For natural minerals, however, this method is impractical. Large and naturally grown single crystals not always form well defined crystal faces and even if that would be the case, precise optical alignment remains a difficult task and is prone to errors. One solution to this problem is detailed in Section 10. Here, we simultaneously acquire data of a known compound with high symmetry and Wyckoff multiplicity, which supplies additional constraints making the solution of the target compound from NMR data only possible.

The "minimal rotation method" presented in detail in this Section is not limited to the chemical shift tensor, but can also be applied to the determination of the quadrupole coupling tensor $\mathbf{Q}$. The signal position of the satellite splittings of quadrupolar nuclei under first-order perturbation theory only (see Equation 3.23) are also traced by Volkoff harmonics which for different ST splittings scale with $(3\Delta k)/[2I(2I-1)]$:

$$\Delta\nu^{(1)}(k) = \frac{3\Delta k}{2I(2I-1)}\vec{b}_0^T(\varphi)\cdot\mathbf{Q}\cdot\vec{b}_0(\varphi) = A^k + B^k\cos 2\varphi + C^k\sin 2\varphi \tag{4.14}$$

In fact, since the $\mathbf{Q}$ tensor has no isotropic component, one parameter less needs to be calculated compared to the $\boldsymbol{\delta}$ tensor, which sometimes may even further reduce data acquisition.

5 Polycrystalline NMR

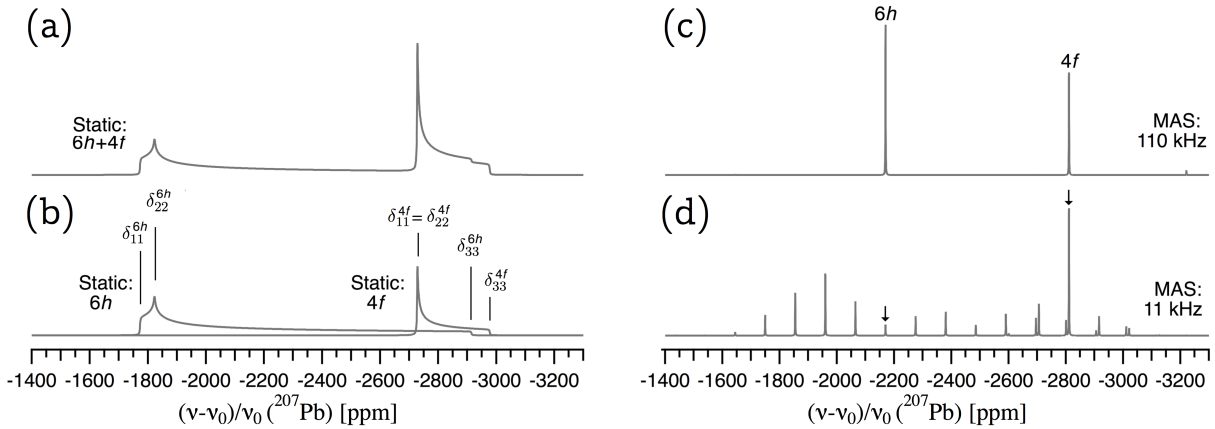

Figure 5.1 – **(a)** Simulated ^{207}Pb static powder spectra of pyromorphite with Wyckoff position $6h$ and $4f$ shown combined, and **(b)** as separate contributions with the chemical shift eigenvalues indicated. **(c)** Simulated ^{207}Pb magic-angle spinning spectra of pyromorphite at 110 kHz, and **(d)** 11 kHz spinning speed, with the isotropic bands for Wyckoff position $6h$ (-2170 ppm) and $4f$ (-2813 ppm) indicated. All spectra were calculated with the SIMPSON package,[64] using the chemical shift values from Table 7.1. (Note that static and MAS spectra are plotted on different intensity scales, since the spinning side bands in the MAS spectra contain the accumulated intensity of many powder orientations and hence have much higher signal intensity than the broad static spectra.)

Since good single crystals of a size sufficient for single-crystal NMR experiments are rare, most NMR measurements are performed on polycrystalline ("powder") samples. If the number of crystallites in such a sample is large, all orientations of the CS tensor (and for spin $I > 1/2$ the **Q** tensor) will be present simultaneously, resulting in a broad powder line shape, such as those displayed in Figure 5.1, exemplarily shown for ^{207}Pb in the natural mineral pyromorphite, $Pb_5(PO_4)_3Cl$. The static powder spectrum for ^{207}Pb of pyromorphite shows a complex powder line shape (see Figure 5.1a), resulting from the respective contributions of the two crystallographically independent lead atoms at the two Wyckoff positions $6h$ and $4f$, as shown in Figure 5.1b. This characteristic static powder line shape of spin $I = 1/2$ nuclei, such as ^{207}Pb, can, in principle, be evaluated to extract the chemical shift eigenvalues from the spectra, as indicated in Figure 5.1b. However, due to the often poor signal to noise ratio, the limited excitation length of the RF pulse, and complex overlap incase of several crystallographically independent positions, determination of chemical shift eigenvalues from static powder spectra is error prone and often impossible.

To remove the broadening and regain resolution, the magic-angle spinning (MAS) technique may be employed.[65] As shown in Section 3, the orientation dependency of an NMR interaction

includes a proportionality to the second Legendre polynomial $P_2(\theta)$:

$$P_2(\theta) = \frac{1}{2}\left(3\cos^2\theta - 1\right) \tag{5.1}$$

For $\theta = \theta_m = \arccos\left(\sqrt{1/3}\right) \approx 54.74°$, the second Legendre polynomial has a zero point. By mechanical rotation of the sample around this angle in respect to $\vec{B}_0$ the dipolar interaction, chemical shift anisotropy (see Equation 3.7) and for spin $I > 1/2$ the quadrupolar interaction to first order (see Equation 3.14) can be completely averaged out. On that account is the angle θ_m referred to as the "magic angle" and the method of spinning the sample 54.74° with respect to $\vec{B}_0$ called magic-angle spinning. For complete removal of the anisotropic interaction, the rotation frequency has to be larger than the respective interaction strength, i.e. larger than the static line width caused by anisotropy (typically tens of kHz).[65,66] In the limit of fast spinning and for spin $I = 1/2$, only one resonance line at position δ_{iso} will remain for each crystallographic inequivalent nuclide n. The highest spinning speed currently commercially available is about 110 kHz, and would be in principle sufficient to reduce the MAS spectra of pyromorphite to only the two isotropic bands with a relative intensity of 3:2 for position $6h$ and $4f$, as may be seen from Figure 5.1c.

In the more common case of incomplete averaging, a spinning side band (SSB) manifold remains which for low spinning rates traces out the shape of the powder pattern, see Figure 5.1d. Depending on the MAS frequency ω_r, the number of rotational side bands and their intensity I_N as well as the intensity of the isotropic signal I_0 changes. By acquiring MAS spectra of spin $I = 1/2$ nuclei at various spinning rates, a good estimate of the CS tensor $\boldsymbol{\delta}$ may be obtained, using the so-called Herzfeld-Berger analysis.[7] For this dimensionless analysis, one calculates contour plots of the "Herzfeld-Berger parameters" ρ and μ,

$$\rho = \frac{\delta_{11} + \delta_{33} - 2\delta_{22}}{\delta_{33} - \delta_{11}} \qquad \mu = \frac{\delta_{33} - \delta_{11}}{\omega_r}, \tag{5.2}$$

for the relativ intensities I_N/I_0 of at least two different rotational frequencies. The chemical shift eigenvalues are then calculated from the values of ρ, μ and the isotropic shift δ_{iso}. For the derivations of those contour plots and the very principles of this analysis we refer the reader to the original publication of Herzfeld and Berger.[7]

6 Four-Fold Symmetry Relation

6.1 Introduction: Phosgenite ($Pb_2Cl_2CO_3$)

In Section 6, we demonstrate the determination of both a full NMR interaction tensor and the unknown orientation of the rotation axis with the help of a four-fold symmetry element. As already described in Section 4, four symmetry-related, but magnetically inequivalent crystallographic positions yield sufficient linear independent parameters from one single rotation pattern for full tensor characterisation without prior knowledge of the rotation axis. Exemplary, we show the full chemical shift (CS) tensor determination of ^{207}Pb in the natural mineral phosgenite, $Pb_2Cl_2CO_3$, which is taken from Zeman et al. 2019 published in *Solid State Nuclear Magnetic Resonance* (Elsevier),[22] and adapted for this thesis. Phosgenite belongs to the mineral group of carbonates und nitrates, and is (as are all lead bearing minerals presented herein) a secondary mineral, occurring in the oxidized zones of lead deposits. It crystallises in tetragonal space group $P4/mbm$ (No. 127) with four formula units per unit cell, with the lead atoms occupying Wyckoff position $8k$, which generates four magnetically inequivalent ^{207}Pb in the unit cell, see also Figure 6.1b.[67]

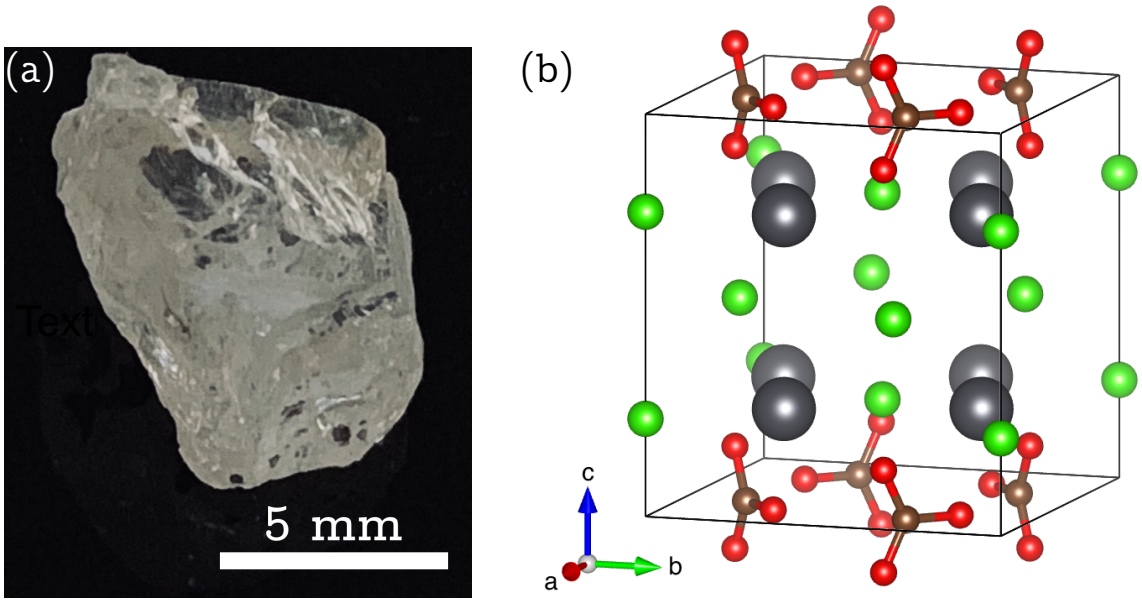

Figure 6.1 – **(a)** Single crystal of phosgenite, $Pb_2Cl_2CO_3$, from Monteponi, Sardinia/Italy (mineralogical state collection inventory no. 52634). **(b)** Unit cell of phosgenite, space group $P4/mbm$ (No. 127), according to literature.[67] The lead atoms (grey) at Wyckoff position $8k$ form two sets of four atoms related by a four-fold rotation axis parallel to the c axis, with the two sets related by an inversion center at the center of the unit cell. All lead atoms are coordinated by five nearest chlorine atoms (green) and four oxygen atoms (red).Figure taken from [22] Drawing generated with the Vesta program.[68]

6.2 Single crystal ^{207}Pb NMR

For evaluating the single-crystal NMR of phosgenite, we largely follow the procedure previously described in the literature for tetragonal γ-$LiAlO_2$.[69,70] In the unit cell of phosgenite, $Pb_2Cl_2CO_3$, the lead atoms at Wyckoff position $8k$ form two sets of four atoms, which are related by a four-fold rotation axis parallel to the c axis. These two sets are connected to each other by an inversion center at the center of the unit cell and situated on mirror planes perpendicular to the crystallographic [110] direction, as may be also seen from Figure 6.1b. Since NMR is invariant to translational elements and inversions, one can only trace four ^{207}Pb atoms in the spectra, which are related by successive 90° rotations about the crystallographic c axis:

$$\underset{(x,x+\frac{1}{2},z)}{\mathrm{Pb(1)}} \overset{90^\circ}{\leftrightarrow} \underset{(\bar{x}+\frac{1}{2},x,z)}{\mathrm{Pb(2)}} \overset{90^\circ}{\leftrightarrow} \underset{(\bar{x},\bar{x}+\frac{1}{2},z)}{\mathrm{Pb(3)}} \overset{90^\circ}{\leftrightarrow} \underset{(x+\frac{1}{2},\bar{x},z)}{\mathrm{Pb(4)}} \tag{6.1}$$

Their respective chemical shift tensors in the tetragonal crystal frame (CRY) are therefore described by only four independent tensor components P, Q, R, and S:

$$\begin{aligned} \boldsymbol{\delta}^{\boldsymbol{CRY}}_{\boldsymbol{Pb(1)}} &= \begin{pmatrix} P & Q & R \\ Q & P & -R \\ R & -R & S \end{pmatrix} \qquad \boldsymbol{\delta}^{\boldsymbol{CRY}}_{\boldsymbol{Pb(2)}} = \begin{pmatrix} P & -Q & -R \\ -Q & P & -R \\ -R & -R & S \end{pmatrix} \\ \boldsymbol{\delta}^{\boldsymbol{CRY}}_{\boldsymbol{Pb(3)}} &= \begin{pmatrix} P & Q & -R \\ Q & P & R \\ -R & R & S \end{pmatrix} \qquad \boldsymbol{\delta}^{\boldsymbol{CRY}}_{\boldsymbol{Pb(4)}} = \begin{pmatrix} P & -Q & R \\ -Q & P & R \\ R & R & S \end{pmatrix} \end{aligned} \tag{6.2}$$

To determine these NMR interaction tensors quantitatively, a single crystal of phosgenite (approximate size $4{\times}3{\times}2\,\mathrm{mm}^3$, see Figure 6.1a) was fixed on a wooden rod and installed in a goniometer probe (as depicted in Figure 4.1a) equipped with a RF coil with 6 mm inner diameter. Thus, the orientation dependence of the resonance position observed for Pb(1), scaled by the Larmor frequency ν_0, is given by insertion of Equation 6.2 into Equation 4.4:

$$\begin{aligned} \nu^{Pb(1)}(\varphi)/\nu_0 &= \vec{b}_0^{\,T}(\varphi) \cdot \boldsymbol{\delta}^{\boldsymbol{CRY}}_{\boldsymbol{Pb(1)}} \cdot \vec{b}_0(\varphi) \\ &= P(b_x b_x + b_y b_y) + Q(2b_x b_y) + R(2b_x b_z - 2b_y b_z) + S(b_z b_z) \end{aligned} \tag{6.3}$$

It can be seen from Figure 6.2 that the four magnetically inequivalent, but symmetry-linked lead atoms give rise to four resonances in the spectra for almost all recorded crystal orientations. Plotting the rotation pattern, i.e. the resonance positions over a 180° interval, as depicted in Figure 6.2b, shows that the resonances follow harmonic functions of the type

shown in Equation 4.1, and as described in Section 4 nine linear independent parameters may be obtained from one rotation pattern. The chemical shift tensor $\boldsymbol{\delta}^{CRY}$ we want to calculate according to Equation 6.2 possesses only four independent components. This fact provides sufficient free parameters to also include the orientation of the goniometer axis (described by the two angles θ, ϕ in spherical coordinates in the CRY frame), and the unknown initial orientation of $\vec{b}_0$ (expressed by the offset angle φ_Δ), into the data fit. Thus, using Equation 6.3 for Pb(1)

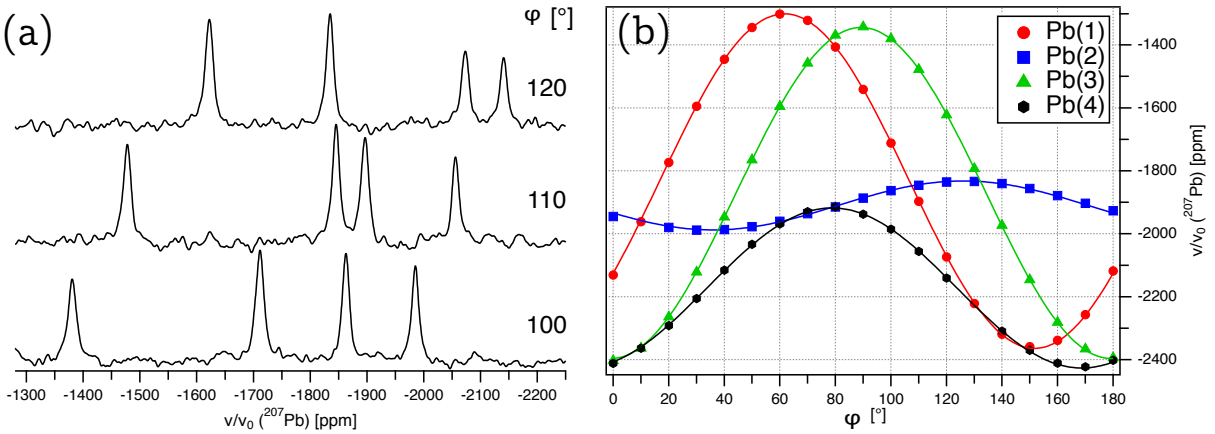

Figure 6.2 – **(a)** ^{207}Pb NMR spectra of a single crystal of phosgenite, $Pb_2Cl_2CO_3$, rotated counter-clockwise by the indicated angle φ around the rotation axis $\vec{g}$ perpendicular to the external magnetic field $\vec{B}_0$, starting from an arbitrary point $\varphi = 0$. The varying signal intensity is due to the limited excitation length of the applied echo-sequence, with an irradiation frequency offset of 1700 ppm. **(b)** Full rotation pattern over 180° for the four magnetically inequivalent ^{207}Pb at Wyckoff position $8k$, acquired by rotating the phosgenite crystal step-wise by 10° around $\vec{g}$, with the drawn lines representing the data fit results (see text for details). Figure taken from [22]

(and its symmetry-related counterparts for $n = 2 \ldots 4$), the rotation pattern in Figure 6.2b was subjected to a multi-parameter fit with the motion of the magnetic field vector in the CRY frame described by Equation 4.7 and 4.10. The fit converged on a global solution for the initial orientation of the goniometer axis $\vec{g}$ in the CRY frame at $\theta_g = (57.5 \pm 0.1)^\circ$, $\phi_g = (53.2 \pm 0.1)^\circ$, and offset angle $\varphi_\Delta = (42.2 \pm 0.1)^\circ$. The components of the chemical shift tensor for ^{207}Pb, extracted from the fit are: $P = (-1651.3 \pm 0.7)$ ppm, $Q = (-277.9 \pm 0.7)$ ppm, $R = (206.6 \pm 0.5)$ ppm, and $S = (-2481 \pm 2)$ ppm. All given uncertainties reflect the error derived from the fit residuals and are less than 0.25% for the tensor components. The lines drawn in Figure 6.2b are the pictorial representation of these fit results. Before discussing them further, we note that the comparatively high Wyckoff multiplicity for ^{207}Pb in phosgenite makes it a straightforward task to determine both CS tensor and goniometer axis orientation from a single rotation pattern, thus keeping the effort for both data acquisition and evaluation within a manageable scope.

The eigenvalues and eigenvectors of the ^{207}Pb CS tensor for phosgenite are listed in Table 6.1. The anisotropy parameter $\Delta\delta = 627$ ppm is comparatively large, despite the high symmetry of the crystal lattice, and hence indicates that the electron lone pair at the lead atoms is significantly *sp*-hybridized.[71] Also, the asymmetry parameter $\eta_{CS} = 0.995$ of the CS reflects the low symmetry of the first coordination sphere defined by the four surrounding oxygen and five chlorine atoms. The orientation of the CS tensor eigenvectors in the tetragonal unit cell of phosgenite are depicted

Table 6.1 – Chemical shift tensor of ^{207}Pb in phosgenite, $Pb_2Cl_2CO_3$. Left: Determined from single-crystal NMR experiments about one general rotation axis at room temperature. The orientation of the corresponding eigenvectors are listed in spherical coordinates (θ, ϕ) in the tetragonal *abc* crystal frame (CRY) and refer to the atom closest to the origin, i.e. Pb(1). Error values are derived from the fit residuals. Right: Determined from a Herzfeld–Berger analysis[7] of the rotational side-band pattern at $\nu_r = +22.5$ kHz magic-angle spinning (MAS) (i.e., at slightly elevated temperature), with $I_{-1}/I_0 = 1.0$, $I_{-2}/I_0 = 0.43$, and $I_{-3}/I_0 = 0.14$, leading to $\rho = -0.04 \pm 0.03$ and $\mu = 5.8 \pm 0.1$ (see Section 5). Error values of tensor components are derived from those of ρ and μ.

	Single-Crystal NMR	**MAS NMR**
δ_{11}^{PAS}	(-2553 ± 1) ppm	(-2546 ± 10) ppm[a]
δ_{22}^{PAS}	(-1929 ± 1) ppm	(-1897 ± 20) ppm
δ_{33}^{PAS}	(-1301 ± 1) ppm	(-1299 ± 10) ppm[a]
$\vec{d}_{11}$	13.9°, 135.0°	
$\vec{d}_{22}$	90.0°, 45.0°	
$\vec{d}_{33}$	76.1°, 315.0°	
$\Delta\delta$	(627 ± 2) ppm	(615 ± 20) ppm
η_{CS}	0.995 ± 0.001	1.06 ± 0.02[a]
δ_{iso}		(-1914 ± 1) ppm
	(-1928 ± 2) ppm	(-1924 ± 4) ppm[b]

[a] Strict sorting of the δ_{ii} according to Equation 3.6 has been avoided to facilitate comparison, which however leads to η_{CS} being larger than unity.
[b] Taken from shift extrapolation over squared MAS frequencies, see Figure 6.4b.

in Figure 6.3. The eigenvector orientations are in agreement with the crystal symmetry, with one eigenvector for one of the lesser tensor components ($\vec{d}_{22}$) aligning exactly along the diagonal of the *a* and *b* axis (and its symmetry equivalent directions) in the crystal frame, as may be best seen in Figure 6.3a. This is a consequence of the symmetry enforced by the mirror plane in the tetragonal unit cell at Wyckoff position 8*k*, on which the ^{207}Pb atoms are situated. The remaining eigenvectors are free to orient according to the electronic environment generated chiefly by the surrounding oxygen and chlorine atoms. Interestingly, the eigenvector with the largest

corresponding eigenvalue, i.e. $\vec{d}_{11}$, points exactly to the nearest oxygen atom, see Figure 6.3b. This peculiar alignment has previously been observed similarly for the two nearest oxygen atoms of ^{207}Pb in the natural mineral anglesite.[55]

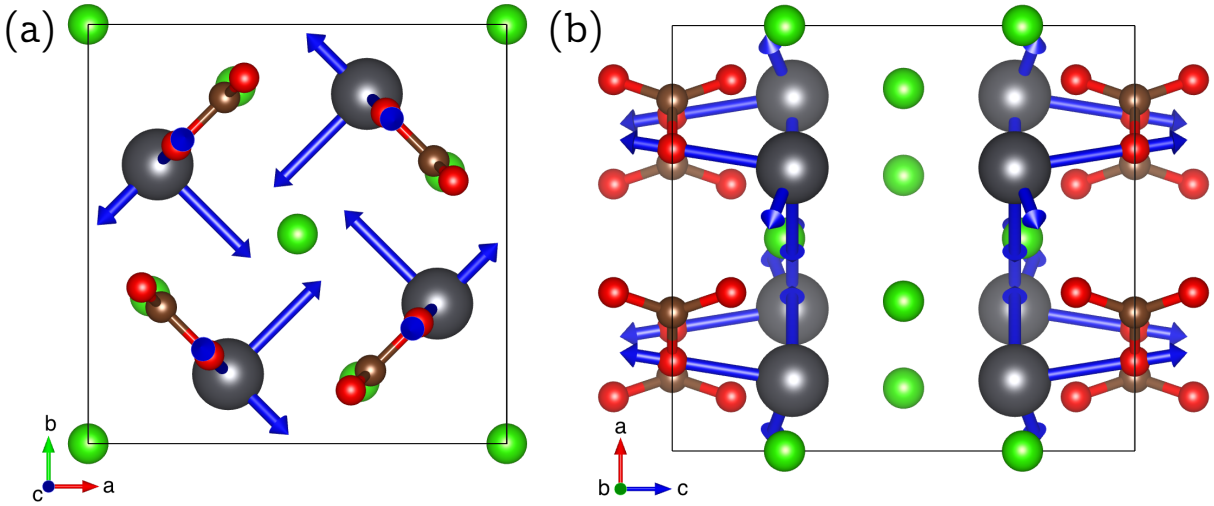

Figure 6.3 – Orientation of the experimentally determined ^{207}Pb chemical shift eigenvectors (blue) in the unit cell of phosgenite, scaled according to the magnitude of the associated eigenvalues, such that an absolute value of 750 ppm corresponds to a length of 1 Å. **(a)** Viewed down along the crystallographic c axis, with $\vec{d}_{22}$ pointing along the {110} plane normal. **(b)** Viewed down along the crystallographic b axis, with the largest eigenvector, $\vec{d}_{11}$, pointing exactly to the next-nearest oxygen atom.Figure taken from [22]

6.3 Polycrystalline ^{207}Pb NMR

Information about the magnitude of the CS tensor, i.e. the eigenvalues and the isotropic chemical shift derived from them, may also be obtained from a polycrystalline sample, using either static or magic-angle spinning (MAS) NMR spectroscopy. As a useful comparison to our single crystal data, ^{207}Pb-NMR spectra of a sample of phosgenite crushed into a powder were acquired at various MAS spinning speeds, ranging from 12.5 kHz to 22.5 kHz, with the latter shown in Figure 6.4a. The isotropic shift derived from this spectrum is −1914.5 ppm, differing significantly from the value of our single-crystal experiments ($\delta_{iso} = -1928$ ppm). It is however well known that ^{207}Pb chemical shifts may vary strongly with temperature, so that even the friction heating from fast MAS frequencies can lead to a noticeable change in δ_{iso}.[6,72,73] Extrapolating the isotropic shift over the squared MAS frequency allows the determination of the MAS isotropic shift at room temperature, as shown in Figure 6.4b, giving $\delta_{iso}^{MAS} = -(1924 \pm 4)$ ppm, which is in good agreement with our single-crystal NMR value. To also extract the three eigenvalues of the CS tensor, we have performed a Herzfeld-Berger analysis[7] of the MAS spectrum at 22.5 kHz.

The results are given in Table 6.1, showing that the magnitude of the MAS-derived eigenvalues are in very good agreement with the single-crystal values, especially taking into account that discrepancies may arise from the temperature difference between static single-crystal and MAS experiments.

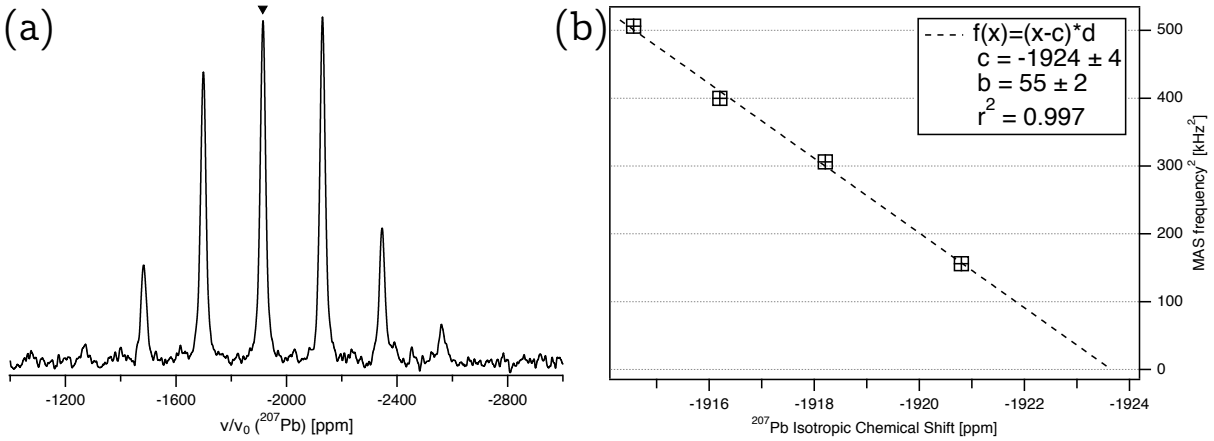

Figure 6.4 – **(a)** ^{207}Pb magic-angle spinning NMR spectrum of polycrystalline phosgenite, acquired in a magnetic field of $\vec{B}_0 = 11.7$ T at 22.5 kHz spinning speed, with the isotropic band indicated at -1914.5 ppm. **(b)** ^{207}Pb isotropic chemical shift of phosgenite versus squared MAS frequency, with the linear fit given by the dashed line. An extrapolation to zero spinning frequency results in an isotropic chemical shift of -1924 ± 4 ppm.Figure taken from [22]

6.4 Experimental details

^{207}Pb NMR spectra were acquired on a Bruker Avance-III 500 Spectrometer at LMU Munich, with Larmor frequency $\nu_0(^{207}\mathrm{Pb}) = 104.63$ MHz, using echo acquisition with 2/4 μs pulse duration to minimize base line roll,[74] and a recycle delay of 60 s. The angular dependent single-crystal spectra were acquired at room temperature (about 20°C) with a clip-on goniometer build by NMR Service GmbH (Erfurt, Germany). This goniometer was installed on a wide-bore Bruker static NMR probe equipped with a home-made solenoid coil with 6 mm inner diameter. For the MAS spectra, a polycrystalline sample was prepared by crushing single crystals of phosgenite with an agate mortar, and measured using a 2.5 mm rotor. All spectra were referenced indirectly to ^{1}H in 100% TMS at -0.1240 ppm, which is equivalent to the common $Pb(NO_3)_2$-powder referencing at $\delta_{iso} = -3492$ ppm. The global fit of the rotation pattern, including the orientation of the magnetic field vector $\vec{b}_0$ in the CRY frame, was performed with the program Igor Pro 7 from WaveMatrics Inc., which delivers excellent non-linear fitting performance.

7 Three-Fold Symmetry Relation

7.1 Introduction: Vanadinite, Pyromorphite, Mimetite [$Pb_5(AO_4)_3Cl$]

In Section 7, we demonstrate the determination of both a full NMR interaction tensor and the unknown orientation of the rotation axis with the help of a three-fold symmetry element. Three symmetry-related, but magnetically inequivalent crystallographic positions yield only sufficient linear independent parameters from one single rotation pattern, if the tensor is constraint by the crystallographic site symmetry (see Section 4).

Recently, we have conducted NMR studies of ^{207}Pb on naturally grown single crystals of pyromorphite,[20] and vanadinite,[21] determining both the full chemical shift tensor and the isotropic shift. In this Section, we also include NMR results of mimetite, which is taken from Zeman et al. 2020 published in *American Mineralogist* (MSA),[75] and adapted for this thesis. All three compounds are secondary minerals, occurring in the oxidized zones of lead deposits, and have recently attracted attention for their ability to immobilize heavy metal ions (see for example, Epp et al. 2019,[76] and references therein). The general formula of the minerals, all of which belong to the apatite supergroup and crystallize in space group $P6_3/m$ (No. 176),[77] may be written as $[Pb(4f)]_2[Pb(6h)]_3(AO_4)_3Cl$, with Z = 2, and A = V (vanadinite), P (pyromorphite), and As (mimetite). In all crystal structures, the lead atom at Wyckoff position $4f$ is located on a 6_3 screw axis parallel to the c axis with two pairs of magnetically inequivalent ^{207}Pb sites, whereas lead at position $6h$ is located on a mirror plane perpendicular to c, giving three pairs of magnetically inequivalent but symmetry-linked ^{207}Pb sites per unit cell. Beside mere tensor determination, when comparing our NMR results for these three isostructural minerals, we found an expected relation of the isotropic shift to the unit cell volume within this mineral family. Also, a linear correlation between the isotropic shift and the Cl–Pb–Cl angle (for Wyckoff position $6h$) could be established. In contrast to pyromorphite and vanadinite, we did however not succeed in determining the full chemical shift tensor for mimetite using the established methodology of single-crystal NMR spectroscopy. This was due to the morphology of the available minerals: even very tiny specimen, which under the microscope appeared to be single crystals, were actually composed of multiple crystals, with their relative orientations showing a variation much greater than those expected from mosaicity effects. This prompted us to re-examine our data on vanadinite and pyromorphite, and in particular an orientation-dependent line broadening we had observed in the NMR spectra of the latter. As described in the second part of Section 7, a clear trend in crystal morphology of the three isostructural minerals may be discerned, and partly even quantitatively estimated, from single-crystal NMR experiments:

Whereas our vanadinite specimens show a high degree of crystallinity, pronounced mosaicity effects are present in pyromorphite, while the high variability of domain orientations goes beyond mere mosaicity in mimetite. To some extent, these findings are mirrored in the appearance of the minerals. While crystals of vanadinite mostly occur with well-defined hexagonal crystal faces

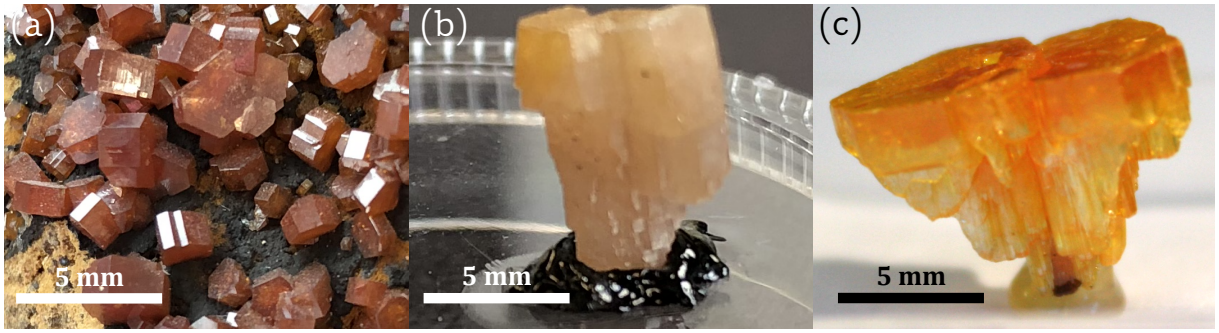

Figure 7.1 – **(a)** Crystals of vanadinite, $Pb_5(VO_4)_3Cl$, from Mibladen, Morocco. **(b)** Crystals of pyromorphite, $Pb_5(PO_4)_3Cl$,l from Grube Friedrichssegen near Bad Ems, Germany (mineralogical state collection inventory no. 3013). **(c)** Crystals of mimetite, $Pb_5(AsO_4)_3Cl$, from China.[Figure taken from [75]]

and in uniform red color (see Figure 7.1a), pyromorphite (see Figure 7.1b), and mimetite (see Figure 7.1c) can be found in crystals with widely varying morphology and color. Thus, in this Section, we also aim to show that the benefits of single-crystal NMR may extend beyond the mere determination of NMR interaction parameters, but in certain cases also supply information about internal structure and morphology of the studied crystals.

7.2 ^{207}Pb CS Tensor in Pyromorphite

To understand the number of resonances present in the ^{207}Pb NMR spectra of vanadinite and pyromorphite, as shown in Figure 7.2, one has to specify the number of crystallographically and magnetically inequivalent lead atoms in the crystal structure. Since only atoms related by translational or inversion symmetry are magnetically equivalent (see Section 4), the 6_3 screw axis along the crystallographic c axis generates three magnetically inequivalent ^{207}Pb at Wyckoff position $6h$, while the mirror planes parallel to the crystallographic ab plane generate two magnetically inequivalent ^{207}Pb at position $4f$:

$$\begin{array}{ccccc} & & \mathrm{Pb(1)}_{(\frac{1}{3},\frac{2}{3},z)} & \overset{180^\circ}{\leftrightarrow} & \mathrm{Pb(2)}_{(\frac{2}{3},\frac{1}{3},z+\frac{1}{2})} \\ \mathrm{Pb(5)}_{(\bar{x}+y,\bar{x},\frac{1}{4})} & \overset{-120^\circ}{\leftrightarrow} & \mathrm{Pb(3)}_{(x,y,\frac{1}{4})} & \overset{+120^\circ}{\leftrightarrow} & \mathrm{Pb(4)}_{(\bar{y},x-y,\frac{1}{4})} \end{array} \tag{7.1}$$

Their respective chemical shift tensors in the a^*bc CRY frame of the hexagonal unit cell are therefore described by only seven independent tensor components T, U, and V, for ^{207}Pb at Wyckoff position $4f$, and P, Q, R, and S for ^{207}Pb at Wyckoff position $6h$:

$$\boldsymbol{\delta}^{\boldsymbol{CRY}}_{\boldsymbol{Pb(1)}} = \begin{pmatrix} T & U & 0 \\ U & T & 0 \\ 0 & 0 & V \end{pmatrix} \qquad \boldsymbol{\delta}^{\boldsymbol{CRY}}_{\boldsymbol{Pb(2)}} = \begin{pmatrix} T & -U & 0 \\ -U & T & 0 \\ 0 & 0 & V \end{pmatrix} \qquad \boldsymbol{\delta}^{\boldsymbol{CRY}}_{\boldsymbol{Pb(3)}} = \begin{pmatrix} P & Q & 0 \\ Q & R & 0 \\ 0 & 0 & S \end{pmatrix} \tag{7.2}$$

$$\boldsymbol{\delta}^{\boldsymbol{CRY}}_{\boldsymbol{Pb(4)}} = \begin{pmatrix} \frac{P-2\sqrt{3}Q+3R}{4} & \frac{\sqrt{3}P-2Q-\sqrt{3}R}{4} & 0 \\ \frac{\sqrt{3}P-2Q-\sqrt{3}R}{4} & \frac{P+2\sqrt{3}Q+R}{4} & 0 \\ 0 & 0 & S \end{pmatrix} \boldsymbol{\delta}^{\boldsymbol{CRY}}_{\boldsymbol{Pb(5)}} = \begin{pmatrix} \frac{P+2\sqrt{3}Q+3R}{4} & \frac{-\sqrt{3}P-2Q+\sqrt{3}R}{4} & 0 \\ \frac{-\sqrt{3}P-2Q+\sqrt{3}R}{4} & \frac{P-2\sqrt{3}Q+R}{4} & 0 \\ 0 & 0 & S \end{pmatrix}$$

In summary, we expect to have a maximum of five signals in the respective ^{207}Pb NMR spectra. For the rotation axes chosen by us, however, both vanadinite and pyromorphite show four resolved resonances at most (see Figure 7.2), albeit one with double intensity, belonging to the two ^{207}Pb at Wyckoff position $4f$.

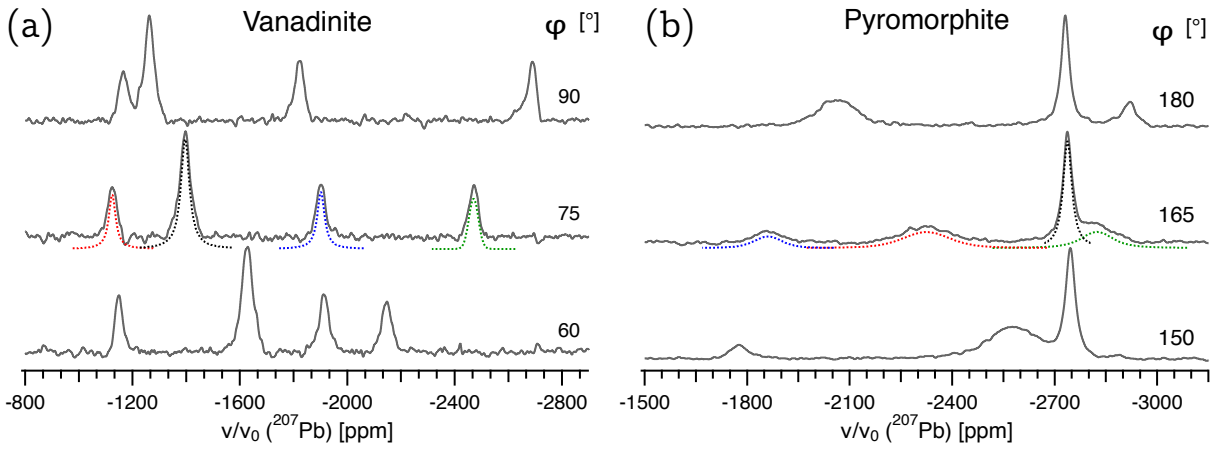

Figure 7.2 – **(a)** ^{207}Pb NMR spectra of a single crystal of vanadinite, $Pb_5(VO_4)_3Cl$, rotated counter-clockwise by the indicated angle φ around a rotation axis perpendicular to the external magnetic field $\vec{B}_0$. **(b)** ^{207}Pb NMR spectra of a single crystal of pyromorphite, $Pb_5(PO_4)_3Cl$, acquired by the same procedure. For the orientations of 75/165 degrees, the dashed lines show the deconvolution of each signal with a Lorentzian fit. The colors of the Lorentzian fits correspond to those of the harmonics in Figure 7.3.[Figure taken from [75]]

By making use of the known symmetry relation between the lead atoms at positions $6h$ and $4f$ respectively, it is now possible to fit the full ^{207}Pb CS tensors, as well as the initially unknown orientation of the rotation axis from only one rotation pattern. Thus, the full rotation pattern of pyromorphite shown in Figure 7.3 (together with the previously published rotation pattern [20])

was subjected to a multi-parameter fit according to Equation 4.4 with the chemical shift tensors given in Equation 7.2 and the motion of the magnetic field vector in the CRY frame described by Equation 4.7 and 4.6. The fit converged on a global solution for the initial orientation of the goniometer axis $\vec{g}$ in the CRY frame at $\theta_g = (22.7 \pm 0.5)^\circ$, $\phi_g = (0 \pm 0.1)^\circ$, and offset angle $\varphi_\Delta = (94.8 \pm 0.1)^\circ$. The components of the chemical shift tensor for ^{207}Pb at Wyckoff position $4f$, extracted from the fit are: $T = (-2730 \pm 5)$ ppm, $U = (12 \pm 4)$ ppm, $V = (-2980 \pm 0.7)$ ppm, and for ^{207}Pb at Wyckoff position $6h$: $P = (-2822 \pm 6)$ ppm, $Q = (-315 \pm 4)$ ppm, $R = (-1866 \pm 5)$ ppm, and $S = (-1821 \pm 5)$. The error values reflect the fit residuals only.

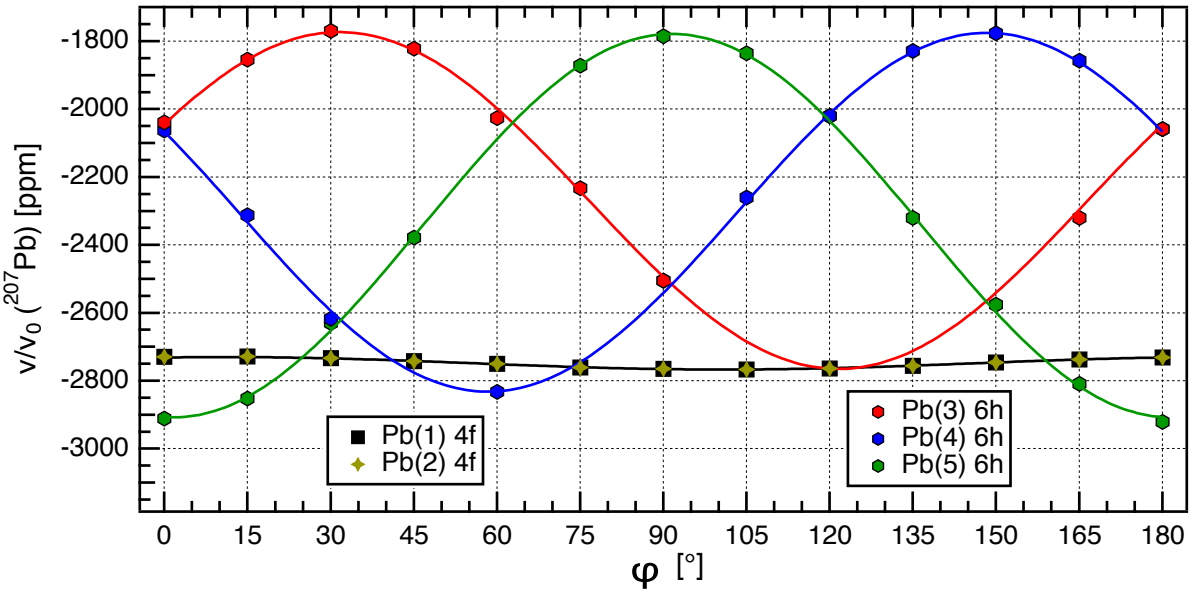

Figure 7.3 – Full rotation pattern over 180° of pyromorphite, $Pb_5(PO_4)_3Cl$, for the 3 magnetically inequivalent ^{207}Pb at Wyckoff position $6h$, and 2 (unresolved) inequivalent ^{207}Pb at position $4f$. The pyromorphite crystal is rotated step-wise by 15° around an axis perpendicular to the external magnetic field $\vec{B}_0$. Figure taken from [75]

Although we need the data set shown in Figure 7.3 primarily for discussing crystal morphology effects (see below Section 7.4), we also re-determine the ^{207}Pb CS tensors for pyromorphite from it. The re-determined tensors can be considered more precise than those reported in our original publication (Zeman et al. 2017 [20]) for three reasons: (i) The current simultaneous fit also includes the previously published rotation pattern (Zeman et al. 2017 [20]), leading to overall higher accuracy. (ii) The current fit was performed in the CRY frame, i.e. extracting the tensor in the form given in Equation 7.2. (iii) When the CS tensor is determined in the CRY frame, the orientation of all eigenvectors in the unit cell is obtained directly by tensor diagonalisation. The ^{207}Pb CS tensor eigenvalues and their corresponding eigenvectors are listed in Table 7.1.

These values are practically identical with those previously reported (Zeman et al. 2017 [20]) for ^{207}Pb at position $6h$, while those for the $4f$ position differ by up to 2%. Considering that the $4f$ are never resolved in the individual rotation patterns, the accuracy of their tensor determination especially benefits from the simultaneous fit over two rotation patterns presented here. The eigenvector orientations are in agreement with the crystal symmetry, with one eigenvector for one of the lesser tensor components ($\vec{d}_{22}$) of ^{207}Pb at position $6h$ aligning exactly along the c axis the crystal frame, as may be best seen in Figure 6.3a. This is a consequence of the symmetry enforced by the mirror plane in the hexagonal unit cell parallel to the ab plane, on which the ^{207}Pb atoms are situated. In the orthogonal a^*bc coordinate system, the calculated eigenvectors of ^{207}Pb at position $4f$ point exactly along the coordinate axes, which is enforced by the symmetry of the 6_3 screw axis along the crystallographic c axis, on which the $4f$ lead atoms are situated.

Table 7.1 – Chemical shift tensor of ^{207}Pb at Wyckoff position $6h$ and $4f$ in the pyromorphite structure, as determined from single-crystal NMR experiments including two rotation patterns (one in Figure 7.3 and one published in Zeman et al. 2017 [20]). The orientation of the corresponding eigenvectors are listed in spherical coordinates (θ, ϕ) in the a^*bc coordinate system of the hexagonal unit cell and refer to the atoms closest to the origin for each crystallographic orbit. Error values are derived from the fit residuals.

	^{207}Pb at $6h$	**^{207}Pb at $4f$**
δ_{11}^{PAS}	(-1772 ± 4) ppm	(-2730 ± 5) ppm
δ_{22}^{PAS}	(-1822 ± 4) ppm	(-2730 ± 5) ppm
δ_{33}^{PAS}	(-2917 ± 6) ppm	(-2980 ± 5) ppm
$\vec{d}_{11}$	90.0°, 106.7°	90.0°, 0.0°
$\vec{d}_{22}$	0.0°, 0.0°	90.0°, 90.0°
$\vec{d}_{33}$	90.0°, 16.7°	0.0°, 0.0°

7.3 Relation of the chemical shift to crystal morphology

Referring back to Figure 7.2, we note that the line widths of the ^{207}Pb NMR signals, in each spectrum, differ significantly between pyromorphite and vanadinite. While vanadinite exhibits comparatively narrow, and constant line widths with a full width at half-maximum intensity ($FWHM$) of approximately 30 ppm, the ^{207}Pb NMR signals in pyromorphite are inherently broader and are different for magnetically inequivalent ^{207}Pb atoms. Interestingly, for pyromorphite, the observed broadening also depends on the crystal orientation, as can be seen from the plots of $FWHM$ vs. rotation angle in Figure 7.4. By deconvoluting all resonances in a spectrum (see

dotted lines in Figure 7.2), *FWHM* was found to vary between 50 to 250 ppm for position $6h$ and between 28 to 42 ppm for position $4f$. This variation of line width even appears to be systematically orientation-dependent, most obviously in the top left plot of Figure 7.4. There are several factors influencing the line width of NMR spectra, starting with inherent transverse relaxation, and continuing with inhomogeneities of the static and the radiofrequency magnetic field, all of which however result in a constant line width in good approximation. It is different for broadening caused by spin couplings (see Section 2), which does contain orientation dependent terms.[36,37] However, the coupling pattern of ^{207}Pb in the apatite structure, being surrounded in the first coordination sphere by chlorine and oxygen only, is practically identical for vanadinite and pyromorphite, and cannot cause the large line width variation observed for the latter. We therefore attribute the orientation-dependent *FWHM* change shown in Figure 7.4 to effects caused by macroscopic crystal imperfections, i.e. the well-documented mosaicity of single crystals (see, for example, Vinet et al. 2011[78]).

The obvious question arising now is whether some quantitative information about the nature of this mosaicity may be derived from our NMR data. Mosaicity may be defined as an ensemble of small crystallites, which all have small deviations from a main orientation, which can be described as the average of all crystallite orientations. For a simple first estimate of this effect in pyromorphite, this alignment deviation was assumed to follow a Gaussian distribution with a standard deviation angle σ along one of the crystallographic axes. The line width for a full rotation pattern was then calculated as the difference between the frequencies $\nu^n(+\sigma)$ and $\nu^n(-\sigma)$, and adding a constant isotropic line width lw for each magnetically inequivalent lead atom:[1]

$$FWHM(\varphi) = |\nu^n(\varphi, \sigma) - \nu^n(\varphi, \sigma) + lw| \tag{7.3}$$

Comparing the resulting line widths to the experimental results for each magnetically inequivalent ^{207}Pb atom, we found the best agreement for a distribution along the c axis, with a standard deviation angle of $\sigma = 5^{\circ}$. For at least one lead site (top left plot of Figure 7.4), the agreement between the prediction of this relatively crude model and the experimental data is remarkably good. It is also obvious from Figure 7.4, however, that our simple model fails to completely reproduce the experimental results of all five lead sites. This can be easily understood by considering that mosaicity may also exist along other directions than just along the c axis. Therefore, while the full complexity of the actual disorder in our pyromorphite crystals could not

[1] A similar model has been used to quantify orientation-dependent line broadening in ^{2}H-NMR spectra of specifically deuterated azulene ($C_{10}H_6D_2$). For such alignment disorder in a molecular crystal, the assumption of a Gaussian distribution worked very well.[79]

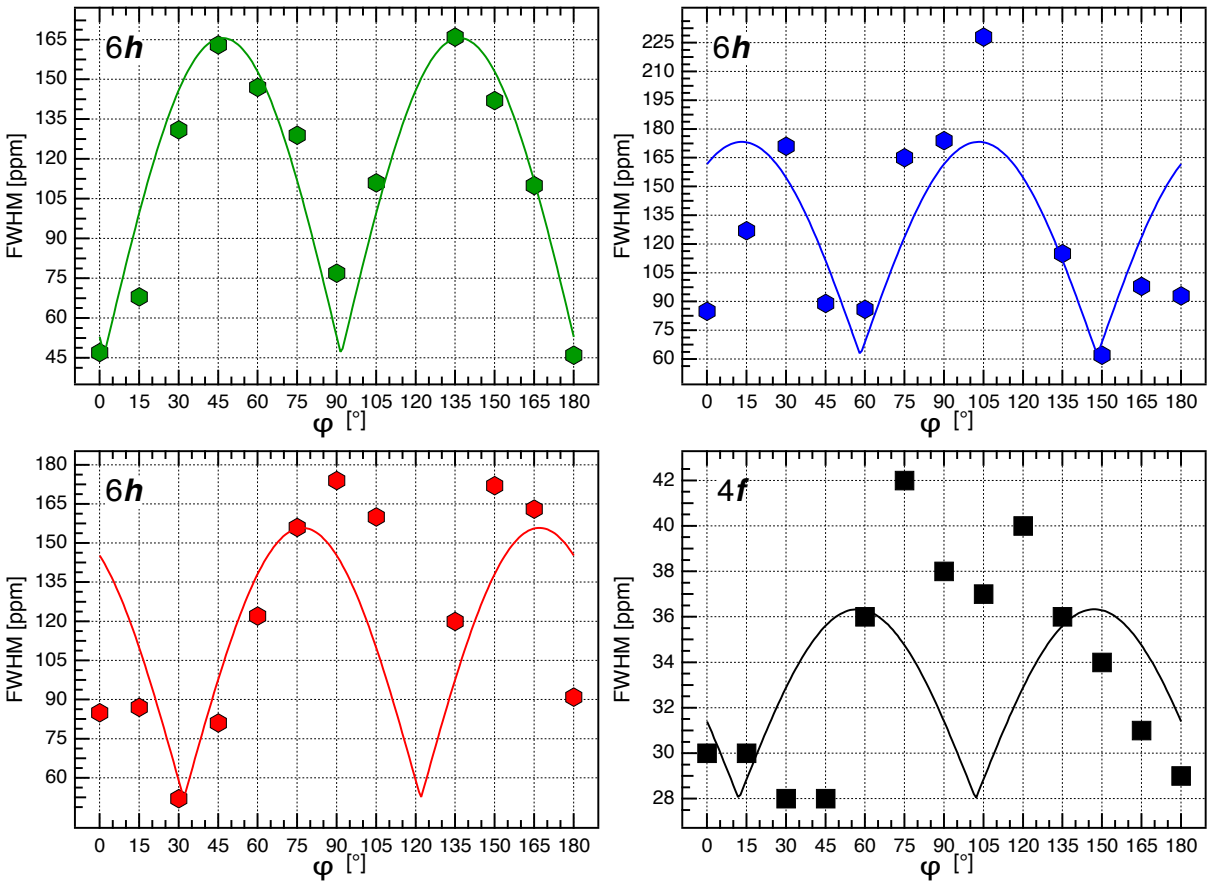

Figure 7.4 – Experimental full width at half-maximum intensities (*FWHM*) for the full rotation pattern over 180° of pyromorphite, $Pb_5(PO_4)_3Cl$, for the 3 magnetically inequivalent ^{207}Pb at Wyckoff position $6h$ (hexagons), and 2 (non-resolved) inequivalent ^{207}Pb at position $4f$ (squares). The solid lines were calculated for a Gaussian distribution of crystal domains about the c axis with $\sigma = 5°$, see text for details.[Figure taken from [75]]

be fully resolved here, the general approach shows the potential usefulness of NMR investigations for obtaining information about the geometry of multi-crystalline growth in minerals.

This usefulness of single-crystal NMR for characterization of crystal morphology can be further illustrated by the case of mimetite. In Figure 7.5, the ^{207}Pb-NMR spectra of two naturally grown crystals of mimetite are shown, which from optical inspection by polarizing microscope were assumed to be single crystals. One originates from China (Figure 7.5b; Mimetite A) with a size of approx. $8 \times 5 \times 4$ mm^3, the other from Namibia (Figure 7.5d; Mimetite B) with a size of approx. $1.3 \times 1 \times 1$ mm^3. Contrary to expectation, both spectra show more than the five ^{207}Pb signals, which are the maximum allowed for a single crystal. At the same time, the observed spectra are markedly different from what would be expected from a polycrystalline powder sample

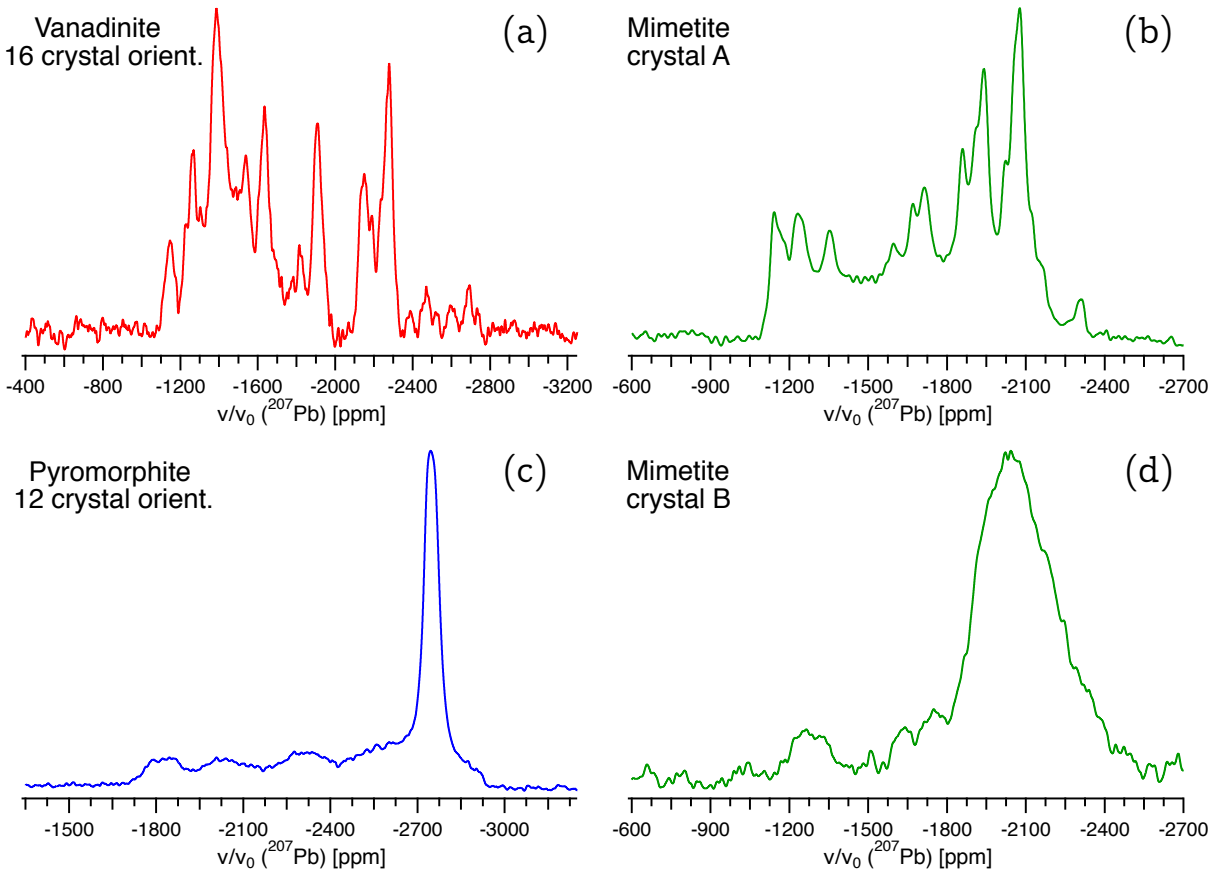

Figure 7.5 – **(a)** Added up ^{207}Pb NMR signals of the full rotation pattern of vanadinite, presented by Zeman et al. 2018.[21] **(b)** ^{207}Pb NMR spectra of a supposed single crystal of mimetite (crystal A) from China. **(c)** Added up ^{207}Pb NMR signals of the full rotation pattern of pyromorphite (Figure 7.3). **(d)** ^{207}Pb NMR spectra of a supposed single crystal of mimetite (crystal B) from Tsumeb, Namibia (mineralogical state collection inventory no. 4770).Figure taken from [75]

representing all orientations, such as those shown in Figure 5.1. Rather, the mimetite ^{207}Pb spectra arise from a large, but "countable" number of differently oriented sub-crystals within the macroscopic agglomerates. Interestingly, from the fact that a higher number of resonances are resolved in the spectra of crystal A, it can be concluded that the actual number of crystallites in A is smaller, although its outer dimensions are much bigger than those of crystal B. In order to rationalize the appearance of the spectra of crystals A and B, we took the rotation patterns from our vanadinite specimen (which shows truly single crystalline behavior in terms of NMR) and pyromorphite (single crystalline, but with mosaicity effects on the NMR line width), and combined the ^{207}Pb spectra for each orientation of the rotation pattern, which is equivalent to measuring 16 respectively 12 crystals in varying orientations simultaneously. The combined spectra (Figure 7.5a; rotation spectra taken from Zeman et al. 2018,[21] Figure 7.5c; rotation

spectra from Figure 7.3) look remarkably similar to the experimental ^{207}Pb-NMR spectra of mimetite. This encourages the assumption that our crystal specimens of mimetite are condensed agglomerates of the order of 10 (crystal A) and 20 to 30 (crystal B) truly single crystalline domains, with more or less arbitrary orientation relative to each other. Thus, "sub-crystal counting" in multi-crystalline samples is in principle possible by solid-state NMR spectroscopy, which, if quantitatively accomplished, could give additional information about the inner morphology of mineral agglomerates. The NMR approach is especially useful for large crystals with high absorption coefficents, such as present in lead-bearing minerals, where analysis of inner domain structure by X-ray diffractometry is practically impossible.

7.4 Relation of the isotropic chemical shift to the crystal structure

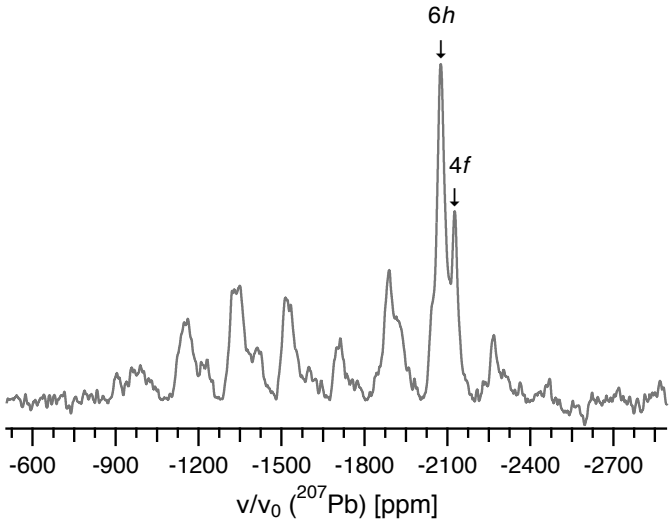

Figure 7.6 – Magic-angle spinning ^{207}Pb-NMR of polycrystalline mimetite, $Pb_5(AsO_4)_3Cl$, at 20 kHz spinning speed, with the isotropic bands for Wyckoff position $6h$ (-2074 ppm) and $4f$ (-2124 ppm) indicated. The spectrum was acquired in a magnetic field of $\vec{B}_0 = 11.7$ T with 2160 scans and a recycle delay of 60 s.[Figure taken from [75]]

For both pyromorphite and vanadinite, we have determined the isotropic shifts of ^{207}Pb by single-crystal experiments, and used the values from MAS spectra only for verification.[20,21] Because of the multi-domain structure of its crystals, single-crystal NMR is not feasible for mimetite, $Pb_5(AsO_4)_3Cl$, as is discussed in more detail above. The hitherto unknown ^{207}Pb isotropic shifts of mimetite were therefore derived from MAS spectra only, such as the one displayed in Figure 7.6. (Note that the severe overlap of the $6h$ and $4f$ signals in the SSB manifold prevented us from estimating the full tensor by Herzfeld-Berger analysis.)

Table 7.2 – Isotropic chemical shift of ^{207}Pb at the position $6h$ and $4f$ in the apatite structure of vanadinite (from single-crystal NMR, Zeman et al. 2018),[21] pyromorphite (from single-crystal NMR, this work) and mimetite (from MAS spectra, this work).

δ_{iso}	Vanadinite	Pyromorphite	Mimetite
$6h$	(-1729 ± 9) ppm	(-2170 ± 5) ppm	(-2074 ± 3) ppm
$4f$	(-1619 ± 2) ppm	(-2813 ± 5) ppm	(-2124 ± 3) ppm

The ^{207}Pb isotropic chemical shifts of the three isostructural minerals $Pb_5(AO_4)_3Cl$ with A = V, P, and As, determined from either single-crystal or MAS NMR experiments, are listed in Table 7.2. We can now proceed to test whether δ_{iso} can be correlated to structural parameters within this mineral family. Such correlations have previously shown to be useful for deducing coordination numbers from chemical shift values. Usually, the chemical shift decreases with higher coordination, i.e. higher electron density, which translates into higher shielding values.[50] Indeed we find a similar trend for our apatite minerals when plotting the chemical shift versus the ratio of the unique c axis to the a axis. As may be seen from Figure 7.7, the chemical shift

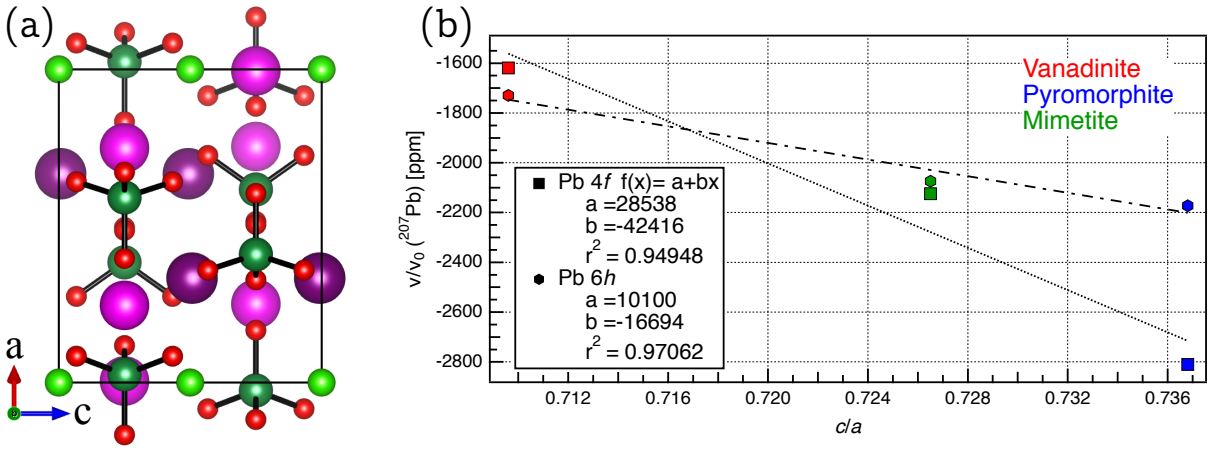

Figure 7.7 – **(a)** Unit cell of mimetite according to Okudera 2013,[77] viewed down the b axis to illustrate the c/a ratio. The chlorine atoms are shown in green, the Pb atoms at Wyckoff position $4f$ in dark purple, Pb atoms at position $6h$ in purple, and the As atoms in dark green tetrahedrally coordinated by oxygen (red). **(b)** ^{207}Pb NMR isotropic chemical shifts of vanadinite (red), pyromorphite (blue), and mimetite (green) versus the respective c/a ratio, with the least-square fit (dashed line) showing good linear correlation. Lead atoms at position $6h$ are shown as hexagons and as squares at position $4f$. Figure taken from [75] Drawing generated with the Vesta program.[68]

decreases when reducing the c/a ratio, which is equivalent to shrinking the unit cell volume and

hence increasing the electron density.[2] This is true for both ^{207}Pb on Wyckoff position 6*h* and 4*f*, regardless of the widely differing coordination sphere of both positions.

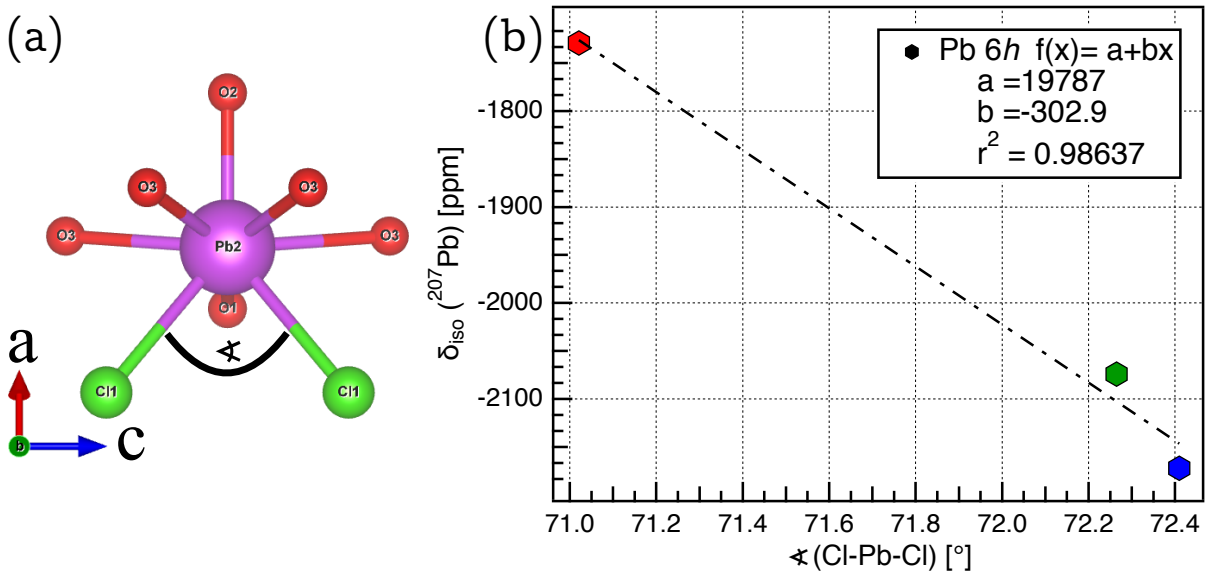

Figure 7.8 – **(a)** First coordination sphere of the lead atoms (purple) on Wyckoff position 6*h* in mimetite according to literature,[77] viewed down along the *b* axis. The lead atoms are coordinated by six oxygen atoms (red) and two chlorine atoms (green), with the Cl-Pb-Cl angle highlighted in black. **(b)** ^{207}Pb NMR isotropic chemical shifts on position 6*h* of vanadinite (red), pyromorphite (blue), and mimetite (green) versus the respective Cl-Pb-Cl angle. Drawing generated with the Vesta program.[68]

While lead on the 4*f* site is coordinated by nine oxygen anions, ^{207}Pb on Wyckoff position 6*h* is coordinated by six oxygen anions and two chlorine anions. The two differing coordination spheres suggest that there might exist linear correlations between shift and structure which are valid for only one Wyckoff position. Indeed, looking at Figure 7.8b, the isotropic shift of ^{207}Pb shows a good linear correlation with the Cl-Pb-Cl angle, which of course only applies for the 6*h* position, since 4*f* is solely coordinated by oxygen. For such Pb^{2+} ions solely coordinated by oxygen, there has been an attempt to correlate the ^{207}Pb isotropic shift to the mean distance of all oxygen atoms in the coordination sphere of the lead atom.[27] It will, however, be shown in Section 8.4 that use of the shortest Pb-O distance results in a better correlation, while also avoiding the pitfalls associated with defining the exact coordination sphere around an atom in a periodic structure.[55] The determined value of δ_{iso} for the 4*f* lead atoms in mimetite, vanadinite, and pyromorphite also fits well into this correlation (see Figure 8.5). One can even envisage a useful application for the correlations within the chloroapatite mineral family. Vanadinite, pyromorphite, and mimetite are capable of forming almost continuous solid solutions

[2] In this argument, we do not take into account the different electron contributions of the central atom (V, P, or As) of the AO_4 anion, since this atom is effectively screened by the surrounding oxygen atoms.

by substituting V or As atoms with phosphorus.[77,80] This substitution will result in changes of both structural parameters and ^{207}Pb chemical shift values. While in X-ray crystallography, it is notoriously difficult to resolve mixed site occupancy, those structural changes might be traceable by measuring the ^{207}Pb MAS NMR spectra and taking into account the correlations presented above.

7.5 Experimental details

Single-crystal NMR spectra were acquired with a Bruker Avance-III 400 spectrometer at MPI-FKF Stuttgart, with the Larmor frequency being $\nu_0(^{207}\mathrm{Pb}) = 83.71$ MHz. The spectra were recorded with echo acquisition to minimize base line roll,[74] using a recycle delay of 60 s, and referenced to $Pb(NO_3)_2$ powder at -3487.5 ppm. The goniometer probe with solenoid coil was built by NMR Service GmbH (Erfurt, Germany). For the MAS spectra, a polycrystalline sample was created by crushing macroscopic crystals of mimetite with an agate mortar. The MAS spectra were acquired on a Bruker Avance-III 500 spectrometer at LMU Munich, using a 2.5 mm rotor for lead with $\nu_0(^{207}\mathrm{Pb}) = 104.63$ MHz. The global fit of the rotation pattern data for the chemical shift tensor of ^{207}Pb in pyromorphite, and the deconvolution of the static ^{207}Pb NMR spectra, was performed using the program Igor Pro 7.08 from WaveMetrics Inc.

8 Two-Fold Symmetry Relation

8.1 Introduction: Anglesite ($PbSO_4$)

Throughout Section 8, we demonstrate the determination of both a full NMR interaction tensor and the unknown orientation of the rotation axis with the help of a two-fold symmetry element. Two symmetry-related, but magnetically inequivalent crystallographic positions generally do not yield sufficient linear independent parameters from one single rotation pattern, even if the tensor is constraint by the crystallographic site symmetry (see Section 4). In the first half of this Section, we present the determination of the full ^{207}Pb chemical shift tensor of anglesite, $PbSO_4$, (which is taken from Zeman et al. 2019 published in *Crystals* (MDPI),[55] and adapted for this thesis) using a single crystal from a natural mineral deposit, as pictured in Figure 8.1a. Anglesite crystallises in the orthorhombic space group *Pbnm* (No. 62),[81] with the location of the ^{207}Pb in the unit cell (shown in Figure 8.1b) given rise to two magnetically inequivalent but crystallographically identical lead positions. To further advance the use of ^{207}Pb-NMR as an

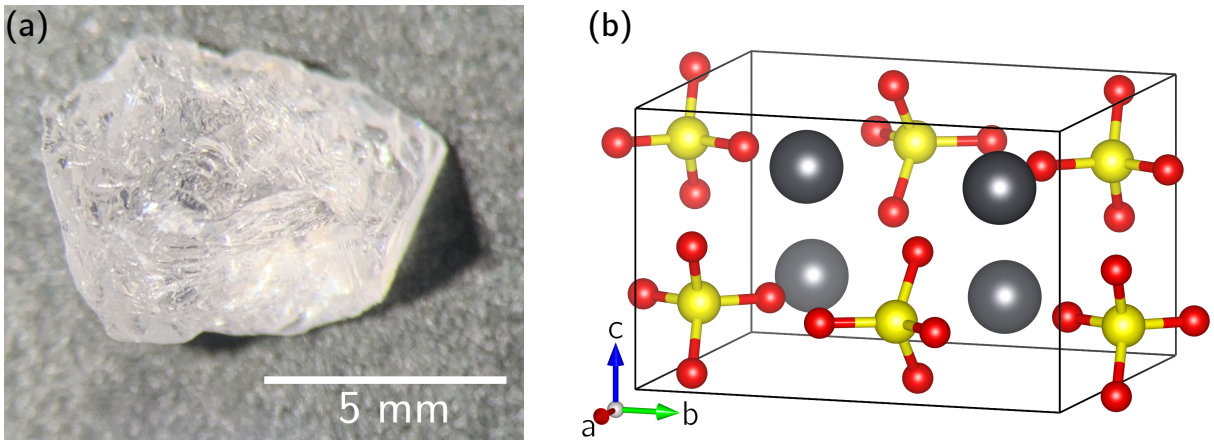

Figure 8.1 – **(a)** Single crystal of anglesite, $PbSO_4$, from Monteponi Mine, Iglesias, Sardinia/Italy (Mineralogical State Collection, Munich inventory MSM 6140). **(b)** Unit cell of anglesite according to Literature.[81] The lead atoms (gray, located at Wyckoff position 4*c*) are related by glides $(x\frac{1}{4}z)$, $(x\frac{3}{4}z)$ and $(\frac{1}{4}yz)$, $(\frac{3}{4}yz)$, and are coordinated by the ten nearest oxygen atoms (red). The sulfur atoms (yellow) are located in the $(xy\frac{1}{4})$ and $(xy\frac{3}{4})$ planes, with their covalent bonds to oxygen in tetrahedral coordination also shown.Figure taken from [55] Drawing generated with the Vesta program.[68]

analytical tool for structure characterisation, we examine an earlier attempt to correlate ^{207}Pb isotropic shift δ_{iso} to interatomic distances between lead and the coordinating oxygen atoms,[27] as already briefly mentioned in Section 7.4. In this previous work, a connection was proposed between δ_{iso} and the average distance of all oxygens in a coordination sphere, which, however, is

not unequivocally defined. Here, we suggest to instead use the shortest distance between lead and oxygen, which is not only a well-defined parameter, but also improves the observed correlation.

8.2 ^{207}Pb single-crystal NMR of Anglesite

The lead atoms in anglesite occupy Wyckoff position $4c$ in the crystal structure, which means that they are located on mirror planes parallel to ab, and generated by glides parallel to ac and bc (see also Figure 8.1b). Since translational elements and inversion do not affect NMR spectra, the four symmetry-related lead atoms in the unit cell form two groups of magnetically inequivalent ^{207}Pb, which can be considered to be related by a 180° rotation about the crystallographic b axis:

$$\underset{(x,\frac{1}{4},z)}{\mathrm{Pb(1)}} \overset{180^\circ}{\longleftrightarrow} \underset{(x+\frac{1}{2},\frac{1}{4},\bar{z}+\frac{1}{2})}{\mathrm{Pb(2)}} \tag{8.1}$$

Their respective CS tensors in the orthorhombic CRY frame are therefore described by only four independent tensor components, P, Q, R, and S:

$$\boldsymbol{\delta}^{\boldsymbol{CRY}}_{\boldsymbol{Pb(1)}} = \begin{pmatrix} P & Q & 0 \\ Q & R & 0 \\ 0 & 0 & S \end{pmatrix} \qquad \boldsymbol{\delta}^{\boldsymbol{CRY}}_{\boldsymbol{Pb(2)}} = \begin{pmatrix} P & -Q & 0 \\ -Q & R & 0 \\ 0 & 0 & S \end{pmatrix} \tag{8.2}$$

To determine these NMR interaction tensors quantitatively, a single crystal of anglesite with approximate size $3{\times}3{\times}2\,\mathrm{mm}^3$ was fixed on a wooden rod and installed in a goniometer probe (as depicted in Figure 4.1a) equipped with a 6 mm coil. Thus, the orientation dependence of the resonance position observed for Pb(1), scaled by the Larmor frequency ν_0, is given by insertion of Equation 8.2 in Equation 4.4:

$$\begin{aligned} \nu^{Pb(1)}(\varphi)/\nu_0 &= \vec{b}_0^T(\varphi) \cdot \boldsymbol{\delta}^{\boldsymbol{CRY}}_{\boldsymbol{Pb(1)}} \cdot \vec{b}_0(\varphi) \\ &= Pb_x^2 + Rb_y^2 + Sb_z^2 + Q2b_xb_y \end{aligned} \tag{8.3}$$

From fitting the experimental line positions in Figure 8.2, we obtained two sets of prefactors (A^1, B^1, C^1 and A^2, B^2, C^2) from the Volkoff harmonics, see Equation 4.1. Since the rotation was carried out around one physical goniometer axis $\vec{g}$, the two harmonics of the magnetically inequivalent lead atoms are linked by one constraint (see Section 4), and only five linear independent parameters may be extracted from one rotation pattern. The chemical shift tensor $\boldsymbol{\delta}^{\boldsymbol{CRY}}$, which we want to calculate from the rotation pattern, possesses four independent tensor

elements (Equation 8.2) due to constraints imposed by crystal symmetry. With the three parameters $\theta, \phi, \varphi_\Delta$ defining the rotation axis, overall, therefore, our system is underdetermined, with seven fit parameters versus five experimental ones.

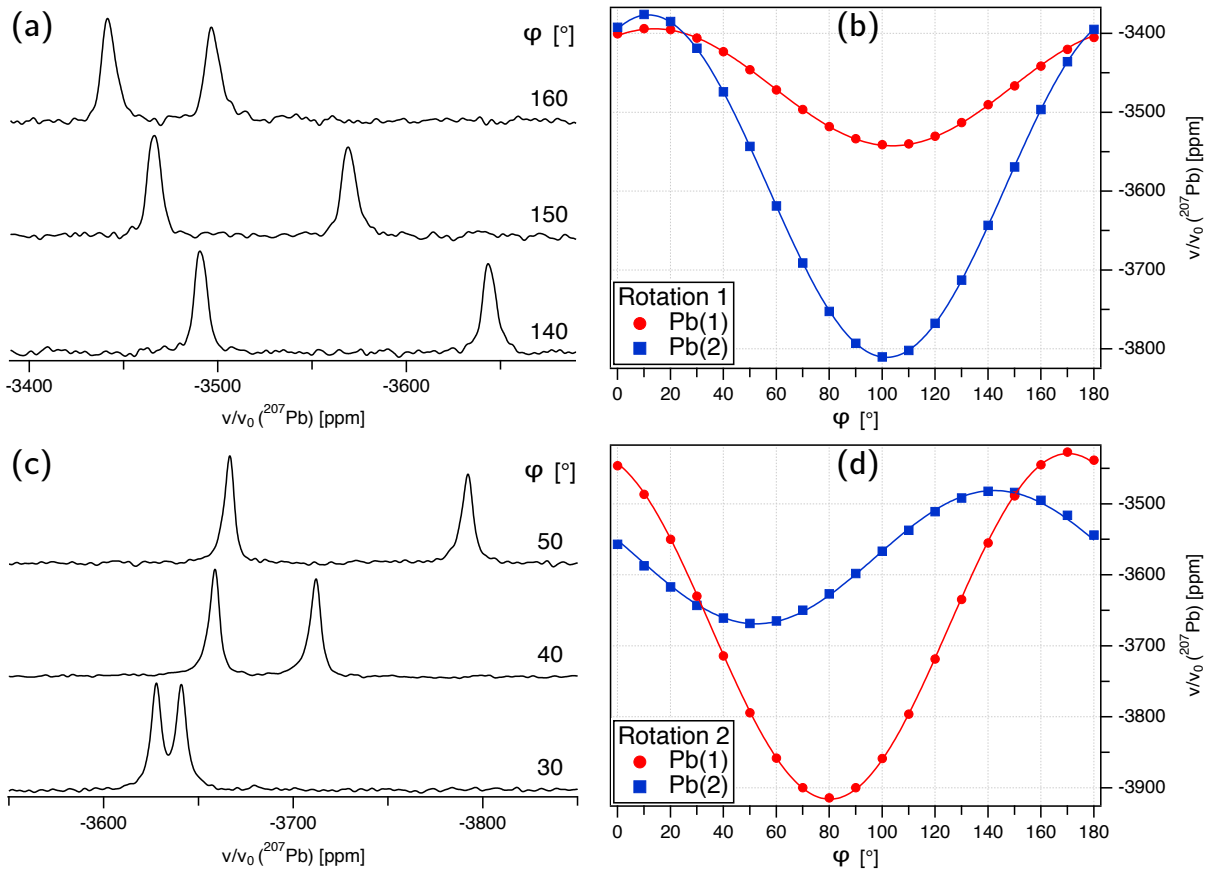

Figure 8.2 – ^{207}Pb NMR spectra of a single crystal of anglesite, $PbSO_4$, rotated counterclockwise by the indicated angle φ around rotation axes $\vec{g}_1$ **(a)** and $\vec{g}_2$ **(c)**, both perpendicular to the external magnetic field $\vec{B}_0$ (varying signal intensity is due to the limited excitation width of the used spin-echo sequence). Full rotation pattern over 180° for the two magnetically inequivalent ^{207}Pb at WYCKOFF position 4*c*, acquired by rotating the anglesite crystal stepwise by 10° around $\vec{g}_1$ (**b**) and $\vec{g}_2$ **(d)**. Lines represent the fit of the experimental points to the CS tensor elements (see main text for details).[Figure taken from [55]]

The obvious solution to this problem is to acquire two rotation patterns about two different rotation axes, $\vec{g}_1$ (Figure 8.2b) and $\vec{g}_2$ (Figure 8.2d), yielding enough free parameters (10) to also include the orientations of $\vec{g}_1$ and $\vec{g}_2$ into the fit. Thus, the two rotation patterns were simultaneously fitted according to Equation 8.3 (and its symmetry-related counterpart), with the motion of field vector $\vec{b}_0$ in the CRY frame described by Equation 4.7 and 4.6. The fit converged on a global solution with the following values for the ten parameters (the errors reflect the fit

residuals):

$$\begin{array}{lllll} \vec{g}_1: & \theta_g = (76.8 \pm 0.4)^{\circ} & \phi_g = (149.8 \pm 0.2)^{\circ} & \varphi_\Delta = (17.5 \pm 0.2)^{\circ} & \\ \vec{g}_2: & \theta_g = (126.6 \pm 0.2)^{\circ} & \phi_g = (228.3 \pm 0.7)^{\circ} & \varphi_\Delta = (178.4 \pm 0.6)^{\circ} & (8.4) \\ P = (-3873 \pm 4)\,\text{ppm} & Q = (152.0 \pm 0.5)\,\text{ppm} & R = (-3607 \pm 3)\,\text{ppm} & S = (-3365 \pm 1)\,\text{ppm} & \end{array}$$

The diagonalization of the CS tensor defined by the P, Q, R, S values listed above transforms it to its own PAS frame, giving the eigenvalues and eigenvectors shown in Table 8.1. Inspecting the properties of $\boldsymbol{\delta^{CRY}}$, we find the anisotropy of the CS tensor ($\Delta\delta = -327$ ppm) to be comparatively small, which indicates that the electron lone pair at the lead atoms has predominantly *s*-character.[71] The asymmetry parameter $\eta_{CS} = 0.529$, on the other hand, reflects the comparatively low symmetry of the polyhedron defined by the surrounding oxygens, with the coordination number being 10 (see Section 8.4 below). Both derived tensor parameters agree reasonably well with those previously reported from static spectra of a polycrystalline sample: $\Delta\delta = -320$ ppm and $\eta_{CS} = 0.545$.[6]

Table 8.1 – Chemical shift tensor $\boldsymbol{\delta^{CRY}}$ of ^{207}Pb in the anglesite structure. Left: Determined from single-crystal NMR experiments about two rotation axes at room temperature. The orientations of the corresponding eigenvectors are listed in spherical coordinates (θ, ϕ) in the orthorhombic *abc* crystal system CRY and refer to the atom closest to the origin, i.e. Pb(1). Error values are derived from the fit residuals. Right: Determined from a Herzfeld-Berger analysis[7] of the rotational side-band pattern at $\nu_r = +12.5$ kHz magic-angle spinning (MAS) (i.e. at slightly elevated temperature), with $I_{-1}/I_0 = 0.52$, $I_{-2}/I_0 = 0.24$, and $I_{-3}/I_0 = 0.054$, leading to $\rho = -0.3 \pm 0.04$ and $\mu = 4.5 \pm 0.3$ (see Section 5). The error values of the tensor components are derived from those of ρ and μ.

	Single-Crystal NMR	**MAS NMR**
δ_{11}^{PAS}	(-3365 ± 3) ppm	(-3369 ± 15) ppm
δ_{22}^{PAS}	(-3538 ± 3) ppm	(-3557 ± 10) ppm
δ_{33}^{PAS}	(-3942 ± 4) ppm	(-3907 ± 30) ppm
$\vec{d}_{11}$	0.00°, 0.00°	
$\vec{d}_{22}$	90.00°, 65.59°	
$\vec{d}_{33}$	90.00°, 155.59°	
$\Delta\delta$	(-327 ± 4) ppm	(-296 ± 30) ppm
η_{CS}	0.529 ± 0.002	0.64 ± 0.06
δ_{iso}		(-3611 ± 4) ppm
	(-3615 ± 3) ppm	(-3614 ± 3) ppm [a]

[a] From extrapolation of MAS spectra to zero spinning, see Figure 8.4b.

The orientation of the scaled eigenvectors of the CS tensor in the unit cell of anglesite, as listed in Table 8.1, may be visualised from Figure 8.3. These orientations are in agreement with the crystal symmetry, with the eigenvector of one of the lesser tensor components (δ_{11}^{PAS}) aligning exactly along the c axis in the crystal frame. This is a consequence of the symmetry enforced by the mirror plane in the orthorhombic unit cell at Wyckoff position $4c$, on which the ^{207}Pb atoms are situated. This generates CS tensors of the shape shown in Equation 8.2, where the principal component S does not change when transforming from the CRY to the PAS frame. The eigenvectors belonging to the two other principal components are free to orient according to the electronic environment, generated chiefly by the surrounding oxygen atoms. The eigenvector with the second largest corresponding eigenvalue, i.e. $\vec{d}_{22}$, points exactly along the bisector of the next two nearest oxygen atoms with the same Pb-O distance, as may be best seen in the lower-left corner of Figure 8.3b.

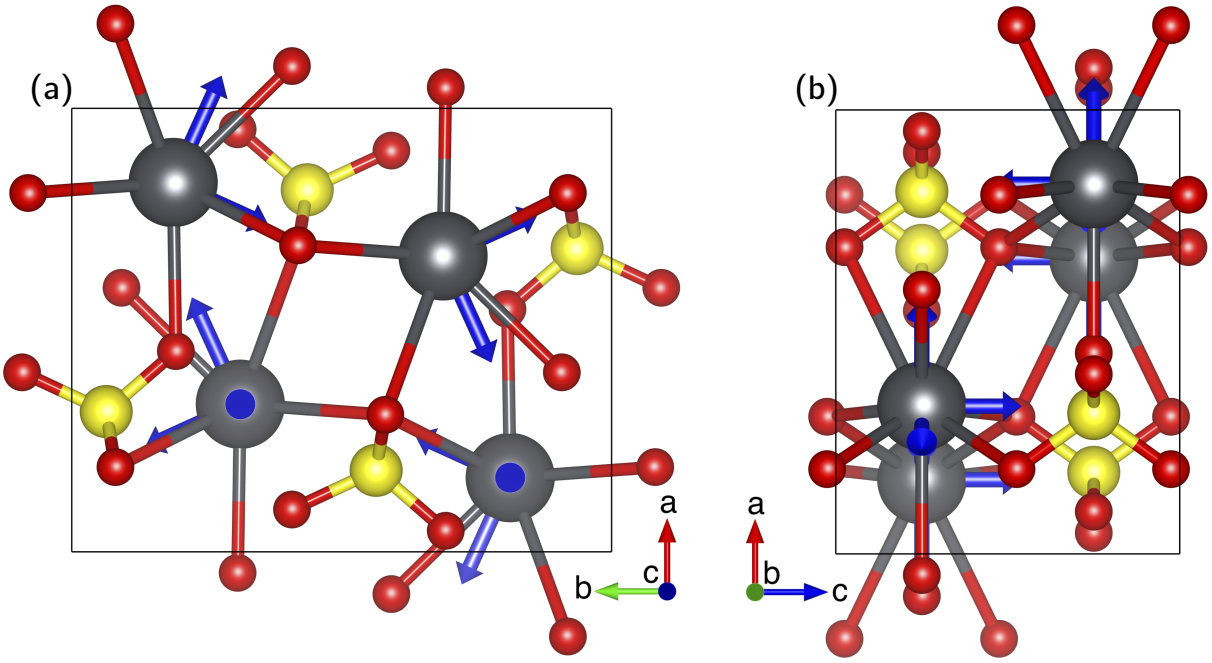

Figure 8.3 – Orientation of the experimentally determined ^{207}Pb chemical shift eigenvectors (blue) in the unit cell of anglesite, scaled according to the magnitude of the associated eigenvalues, such that an absolute value of 750 ppm corresponds to a length of 1 Å, with the lead atoms (gray) shown with their coordination to ten oxygen atoms (red): **(a)** View down the c axis; **(b)** view down the b axis.[Figure taken from [55]] Drawing generated with the Vesta program.[68]

8.3 ^{207}Pb polycrystalline NMR of Anglesite

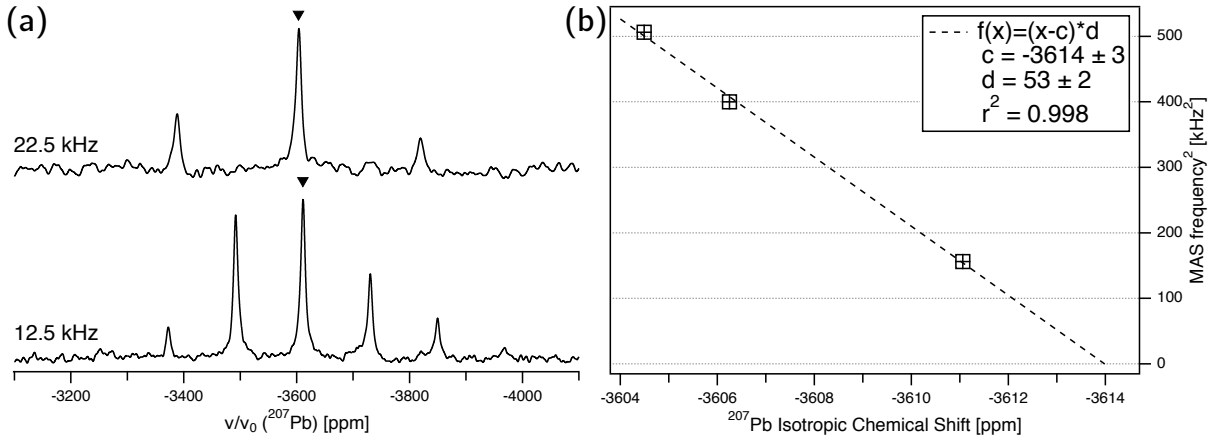

Figure 8.4 – **(a)** ^{207}Pb magic-angle spinning NMR spectra of polycrystalline anglesite, acquired at the indicated MAS frequencies, with isotropic bands marked by a triangle. **(b)** Plot of the ^{207}Pb isotropic chemical shift of anglesite versus the squared MAS frequency, with the linear fit given by the dashed line. An extrapolation to zero spinning speed results in an isotropic chemical shift of -3614 ± 3 ppm.Figure taken from [55]

For the single-crystal NMR experiments, the isotropic chemical shift is computed from the diagonal elements of $\boldsymbol{\delta}$ to $\delta_{iso} = -3615$ ppm. As a useful comparison, δ_{iso} may also be obtained from MAS NMR spectroscopy. To this end, we acquired the NMR spectra of a polycrystalline sample (prepared by crushing larger anglesite crystals in a mortar) at various spinning speeds, ranging from 22.5 to 12.5 kHz. The ^{207}Pb MAS NMR spectrum at 22.5 kHz spinning speed, shown in Figure 8.4a, shows the isotropic band at -3604.5 ppm, deviating significantly from the single-crystal value. It is, however, well known that for many lead-containing compounds, the ^{207}Pb chemical shift markedly varies with temperature (see also Section 6.3), to the extent that lead nitrate is routinely used for temperature calibration of NMR probes.[72,73,82] Our anglesite sample also already showed a noticeable change in δ_{iso} within the comparatively small temperature deviations produced by friction effects of the MAS technique. In order to be able to compare the isotropic shift derived from our single-crystal experiments at static (and therefore room-temperature) conditions, we extrapolated the temperature dependence of the isotropic shift to zero spinning speed, taking into account that the resonance position quadratically varies with MAS frequency.[6] The fit (see Figure 8.4b) resulted in an 'static' isotropic chemical shift of -3614 ± 3 ppm, in near perfect agreement with the single-crystal NMR value. Our δ_{iso} for anglesite is also in good agreement with the value of -3613 ppm, published in 1997.[27] Curiously, the isotropic shift determined from a static polycrystalline sample[6] is significantly different at -3505 ppm. All principal tensor components given in that work are about +110 ppm off ours,

so that δ_{iso} is strongly affected, but derived parameters $\Delta\delta$ and η_{CS} are not (see above). Since the obvious pitfall of referencing can be ruled out, we currently have no convincing explanation for this large difference in tensor values.

As already mentioned in Section 6.3 it is also possible to extract all three eigenvalues of the CS tensor from the rotational side-band pattern of MAS spectra. We have performed a Herzfeld-Berger analysis [7] on our MAS spectrum measured at the slowest speed (12.5 kHz). The results are listed in Table 8.1, and agree remarkably well with the single-crystal values.

8.4 Correlation of ^{207}Pb isotropic shifts and Pb-O distances

In the context of NMR crystallography, the aspiration is always to find connections between NMR parameters and structural features of the compounds under investigation. As already mentioned in the introduction, it has previously been attempted to correlate the ^{207}Pb isotropic shift δ_{iso} to interatomic distances between lead and oxygen for compounds where lead occurs solely in oxygen coordination. In this work by Fayon et al. in 1997,[27] a connection was proposed between δ_{iso} and the mean Pb-O distance in a given coordination sphere. However, this average distance is obviously strongly dependent on the chosen coordination sphere and the coordination number (CN) following from it. In fact, the question of how to define a coordination sphere around a given atom in a periodic structure is complex,[83] and still a matter of debate among inorganic chemists. When checking the suggested correlation [27] for our anglesite data, classical counting within the coordination polyhedra gives CN = 10 for ^{207}Pb, whereas the more convoluted concept of effective coordination number (eCoN) according to Hoppe [83] produces the almost identical value of 9.8. Thus, for lead in $PbSO_4$, the coordination sphere is comparatively well-defined, and the calculation of a mean Pb-O distance from the atomic coordinates is a straightforward task. However, when we tried to reproduce the plot of Reference [27], we encountered many compounds where the definition of the coordination sphere was more ambiguous. For a number of those, our best effort at determining the coordination number, and the average distance following from it, gave a result that deviated from the earlier work. The CN's and corresponding Pb-O distances of our assessment are listed in Table 8.2, where we restricted ourselves to lead compounds that also occur as natural minerals, with the respective mineral names specified. The plot of δ_{iso} versus mean Pb-O distance is shown in Figure 8.5a, evidently correlating these two parameters only poorly.

However, we found that using the shortest Pb-O distance, which, in contrast to the mean distance, can be established unequivocally, results in much improved correlation with the ^{207}Pb

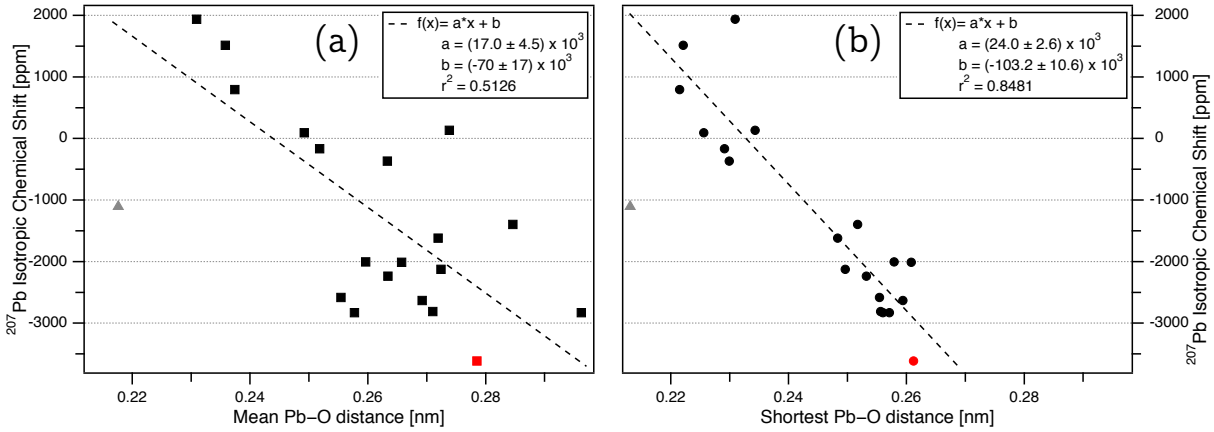

Figure 8.5 – **(a)** Evolution of ^{207}Pb isotropic chemical shift (δ_{iso}) versus mean Pb-O distance for compounds where lead occurs solely in oxygen co-ordination, with anglesite shown in red. **(b)** δ_{iso} versus the shortest Pb-O distance. All data given in Table 8.2. (Dashed lines show the least-squares linear fit, with fit parameters and their errors given in the upper-right corners. The data point for Pb^{4+}(1) in Pb_3O_4 (minium) is shown as a gray triangle and was not included in the least-square fits, as the correlation was restricted to only Pb^{2+}).[adapted from [55]]

isotropic chemical shift, as shown in Figure 8.5b. Thus, the evolution of δ_{iso} with the shortest Pb-O distance in the coordination sphere, d_{short}, may be described by:

$$\delta_{iso}[\mathrm{ppm}] = 23925 - 102780 \cdot d_{\mathrm{short}}[\mathrm{nm}] \tag{8.5}$$

Here, it should be emphasised that the above correlation only applies to Pb^{2+}. The absence of the lone pair in Pb^{4+} obviously strongly changes the electronic surrounding of the ^{207}Pb nucleus. As one example, we included the Pb^{4+} at the Pb(1) site of the mixed-valence oxide Pb_3O_4 (minium), which clearly lies far away from the suggested correlation lines in both plots of Figure 8.5. Regarding the well-documented temperature dependence of the ^{207}Pb isotropic shift (see above), all δ_{iso} values in Table 8.2 were reported at "room temperature". While this specification is obviously somewhat vague, we note that the possible errors introduced by temperature deviations of a few degrees Celsius are so small that the error bars would be inside the size of the symbols used in the plots of Figure 8.5.

Furthermore, in the plot using the shortest Pb-O distances, the data points seem to appear in two clusters. Broadly, this clustering follows chemical intuition in the sense that shorter Pb-O distances are possible for the compounds with lower coordination number (for higher coordination, the "crowding" of oxygen around lead makes close contact difficult). There are, however, exceptions to that rule of thumb, in particular for changbaiite, $PbNb_2O_6$. Compounds

with CN = 6 also show up in either cluster. It can therefore not be decided from the currently available database whether the observed clustering is a real effect or purely coincidental.

8.5 Experimental details for Anglesite

^{207}Pb NMR spectra were acquired on a Bruker Avance-III 500 ($\vec{B}_0 = 11.7$ T) spectrometer at LMU Munich, with a Larmor frequency of $\nu_0(^{207}\mathrm{Pb}) = 104.63$ MHz. A spin–echo sequence was employed to minimise baseline roll.[74] A recycle delay of 60 s was used for both single-crystal and MAS spectra. The rotation pattern of Figure 8.2b was acquired with 8 scans for each spectrum, the pattern in Figure 8.2d mostly with 16 scans (one exception is the spectrum at 40 degrees shown in Figure 8.2c, for which 60 scans were added). The orientation change of the single crystal was realised by a goniometer mechanics build by NMR Service GmbH (Erfurt, Germany), which was 'clipped on' (see Figure 4.1a) a wide-bore Bruker static NMR probe with a home-built 6 mm solenoid coil. For the MAS spectra, a polycrystalline sample was prepared by crushing single crystals of anglesite with an agate mortar and measured using a 2.5 mm rotor. All spectra were indirectly referenced to ^{1}H in 100% TMS at -0.1240 ppm. According to our measurements, this is equivalent to the commonly used reference of a static $Pb(NO_3)_2$ powder spectrum at room temperature, with $\delta_{iso} = -3492$ ppm, or -3474 ppm at the highest point of the line shape, both in good agreement with previously reported values.[6] The global fit of the two rotation patterns was performed with the program Igor Pro7 from WaveMatrics Inc..

Table 8.2 – Crystallographic data and ^{207}Pb isotropic chemical shifts δ_{iso} of lead-bearing minerals. First coordination sphere of at least one lead side for each compound is solely determined by the next neighbouring oxygen atoms.

Mineral	**Space Group (Ref.)**	**Pb Coord. No.**	**Pb–O Mean Bond Length [nm]**	**Pb–O Shortest Bond Length [nm]**	$\boldsymbol{\delta_{iso}}$ **[ppm]**	**NMR Ref.**
red PbO [Litharge]	$P4/nmm$ [84]	4	0.2309	0.2309	1939 ± 5	[27]
yellow PbO [Massicot]	$Pbcm$ [85]	4	0.2358	0.2221	1515 ± 5	[27]
$PbSiO_3$: Pb(1)	$P2/n$ [86]	5	0.2518	0.2291	−166 ± 5	[27]
[Alamosite] Pb(2)		5	0.2492	0.2256	93 ± 5	[27]
Pb(3)		6	0.2633	0.2299	−366 ± 5	[27]
Pb_3O_4: Pb^{4+}(1)	$P4_2/mbc$ [87]	6	0.2176	0.2131	−1105 ± 1	[27]
[Minium] Pb(2)		4	0.2374	0.2215	795 ± 2	[27]
$PbTiO_3$ [Macedonite]	$P4mm$ [88]	12 (8+4)	0.2846	0.2517	−1395.1 ± 8.4	[6]
$Pb_5(VO_4)_3Cl$: Pb(1)	$P6_3/m$ [77]	9	0.2719	0.2483	−1619 ± 2	[21]
[Vanadinite] Pb(2)[a]		6	0.2664	0.2324	−1729 ± 9	[21]
$PbWO_4$ [Stolzite]	$I4_1/a$ [89]	8	0.2596	0.2579	−2003	[90]
$PbMoO_4$ [Wulfenite]	$I4_1/a$ [91]	8	0.2657	0.2608	−2009 ± 2	[27]
$Pb_5(AsO_4)_3Cl$: Pb(1) [Mimetite]	$P6_3/m$ [77]	9	0.2724	0.2496	−2124 ± 3	this
Pb(2) [a]		6	0.2680	0.2583	−2074 ± 3	work
$PbCrO_4$ [Crocoite]	$P2_1/n$ [92]	8	0.2634	0.2532	−2236.2 ± 2.9	[6]
$PbSb_2O_6$ [Rosiaite]	$P\bar{3}m$ [93]	6	0.2554	0.2554	−2581 ± 3	[94]
$PbCO_3$ [Cerussite]	$Pmcn$ [95]	9	0.2692	0.2594	−2630 ± 2	[27]
$Pb_5(PO_4)_3Cl$: Pb(1)	$P6_3/m$ [77]	9	0.2710	0.2556	−2810 ± 14	[20]
[Pyromorphite] Pb(2) [a]		6	0.2671	0.2353	−2172 ± 11	[20]
$PbNb_2O_6$: Pb(1)	$R3m$ [96]	6				
		6	0.2577	0.2560	−2829	[97]
[Changbaiite] Pb(2)		(3+3)	0.2962	0.2571	−2829	[97]
Pb(3)		12 (6+6)	0.2738	0.2343	134	[97]
$PbSO_4$ [Anglesite]	$Pbnm$ [81]	10	0.2785	0.2612	−3615 ± 3	[55]

[a] Pb(2) is located on Wyckoff position 6*h* in vanadinite, pyromorphite, and mimetite, and is not included into the Pb-O distance correlation due to chlorine also being in the first coordination sphere.

8.6 Introduction: Cerussite ($PbCO_3$)

In this second half of Section 8, we use ^{207}Pb NMR spectroscopy to study the natural lead-bearing carbonate cerussite, $PbCO_3$, of which a single crystal is shown in Figure 8.6a. Cerussite crystallises in space group *Pmcn* (No. 62), and contains one crystallographically independent atomic site for lead in the asymmetric unit. This atom is occupying Wyckoff position 4*c*, which generates four lead sites in the unit cell (which may be referred to as crystallographically equivalent), as shown in Figure 8.6b.

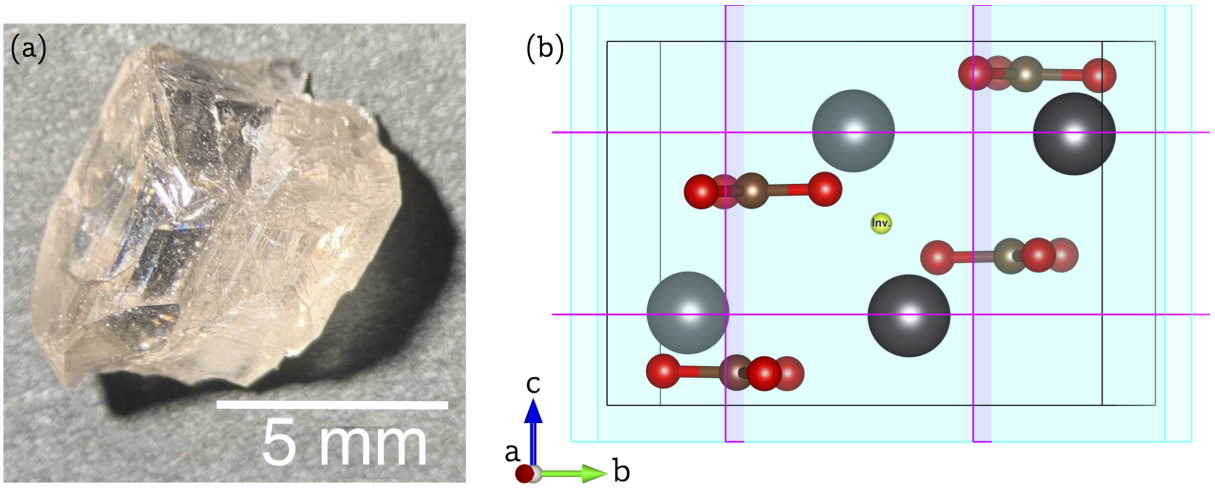

Figure 8.6 – **(a)** Single crystal of cerussite, $PbCO_3$, from Tsumeb, Namibia (Mineralogical state collection, Munich inventory MSM. 34393). **(b)** Unit cell of cerussite in a projection along *a*, according Table 8.5. The four lead atoms (gray, located at Wyckoff position 4*c*) are situated on mirror planes at $(\frac{1}{4}yz)$ and $(\frac{3}{4}yz)$ (light blue) and are related by glide planes *c* at $(x\frac{1}{4}z)$, $(x\frac{3}{4}z)$ and glide planes *n* at $(xy\frac{1}{4})$, $(xy\frac{3}{4})$ (purple). The carbon atoms (grey) are located on mirror planes at $\frac{1}{4}yz$, and $\frac{3}{4}yz$, with their covalent bonds to oxygen (red) in trigonal-planar coordination also shown. Drawing generated with the Vesta program.[68]

To establish the number of crystallographic independent lead atoms by NMR, a ^{207}Pb NMR spectrum of a polycrystalline sample of $PbCO_3$ under static conditions may be acquired, such as the one shown in Figure 8.7a. The spectrum is consistent with the existence of only one crystallographically independent lead atom in the unit cell of cerussite, in agreement with the findings of XRD studies. NMR spectra of static powders become, however, difficult to analyze when the asymmetric unit contains several sites for one nuclide, and their respective spectral contributions overlap. This lack of resolution can be alleviated by application of the magic-angle spinning (MAS) technique,[65] with a ^{207}Pb NMR spectrum of a powder sample of cerussite under MAS displayed in Figure 8.7b. Here, the MAS is not fast enough to fully average the large chemical shift anisotropy of ^{207}Pb, and consequently, a manifold of so-called spinning side bands

(SSB's) appears in the spectrum. For cerussite, this SSB manifold contains only one isotropic peak, again consistent with the XRD result that there is a single lead atom in the asymmetric unit.

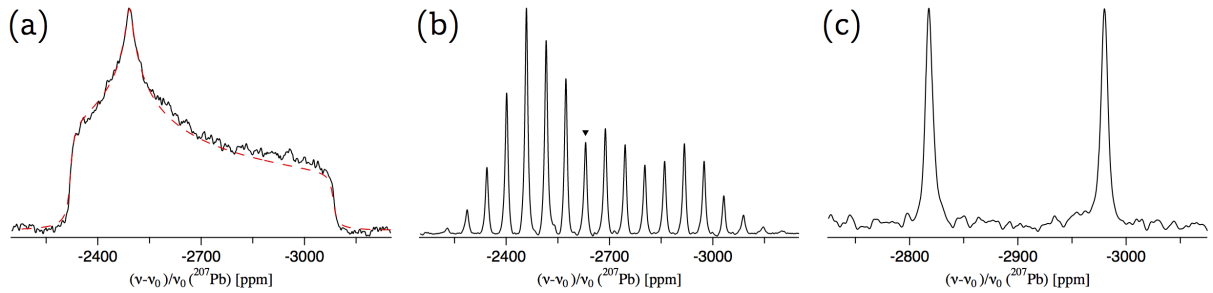

Figure 8.7 – **(a)** ^{207}Pb static powder spectrum of cerussite, showing one crystallographic lead position. Due to the limited excitation length of the applied echo-sequence, the shown spectra is a combination of two spectra with the irradiation frequency offset located at the two edges of the static powder line, i.e. at -2320 ppm and -3090 ppm. The dashed line was calculated with the Simpson package,[64] using the chemical shift values listed in Table 8.4(right). **(b)** ^{207}Pb magic-angle spinning NMR spectrum of polycrystalline cerussite, acquired at 6 kHz spinning speed, with the isotropic band indicated at -2630.4 ppm corresponding to one crystallographic lead position. **(c)** Static ^{207}Pb NMR spectrum of a single crystal of cerussite, $PbCO_3$, with two magnetically inequivalent lead positions. All spectra were acquired in a magnetic field of $\vec{B}_0 = 11.7$ T, and are plotted with the same maximum intensity, hence do not represent the true intensity variation between those three measurement conditions.

The situation is significantly different when taking the NMR spectrum of a single crystal. In Figure 8.7c, it may be seen that the ^{207}Pb NMR spectrum of cerussite shows two comparatively narrow resonances, similarly to the single-crystal spectra of anglesite shown in Section 8.2. To establish whether the presence of two ^{207}Pb resonances in a single crystal of cerussite is compatible with the proposed crystal structure, we need to evaluate the structure model derived from XRD in more detail. The inorganic crystal structure database (ICSD) contains seven entries on the crystal structure of $PbCO_3$, determined between 1928 and 2012.[95,98–103] As will be discussed in detail below, the crucial difference in their refinement of atomic coordinates concerns the positioning of the lead atom, namely whether it is placed exactly on a glide plane,[98–100] or just next to it.[95,101–103] For the first structure model, only one resonance is expected in the ^{207}Pb NMR spectrum, for the second, two. Obviously, the number of resonances may also be influenced by crystal twinning, especially for natural minerals where twinning frequently occurs. However, in Section 8.8, a genuine twin crystal of cerussite is investigated and found to display four resonances. By assessing the relative intensities of the ^{207}Pb NMR resonances, the contribution of the respective twins can be separated, and by fitting the two data sets, the twinning geometry can even be quantified as most likely being a {130}-contact twin.

Thus, by excluding twinning, and evaluating the crystallographic and magnetic equivalence for different XRD structure models, the correct crystal structure with respect to the lead position in cerussite can be resolved by single-crystal NMR. The ^{207}Pb NMR spectrum is compatible only with the structure model where the lead atoms are slightly displaced from the glide plane,[95,101–103] and this model is also supported by our own single-crystal XRD data, as given in Section 8.10.

8.7 Clarification of crystal structure from single-crystal NMR

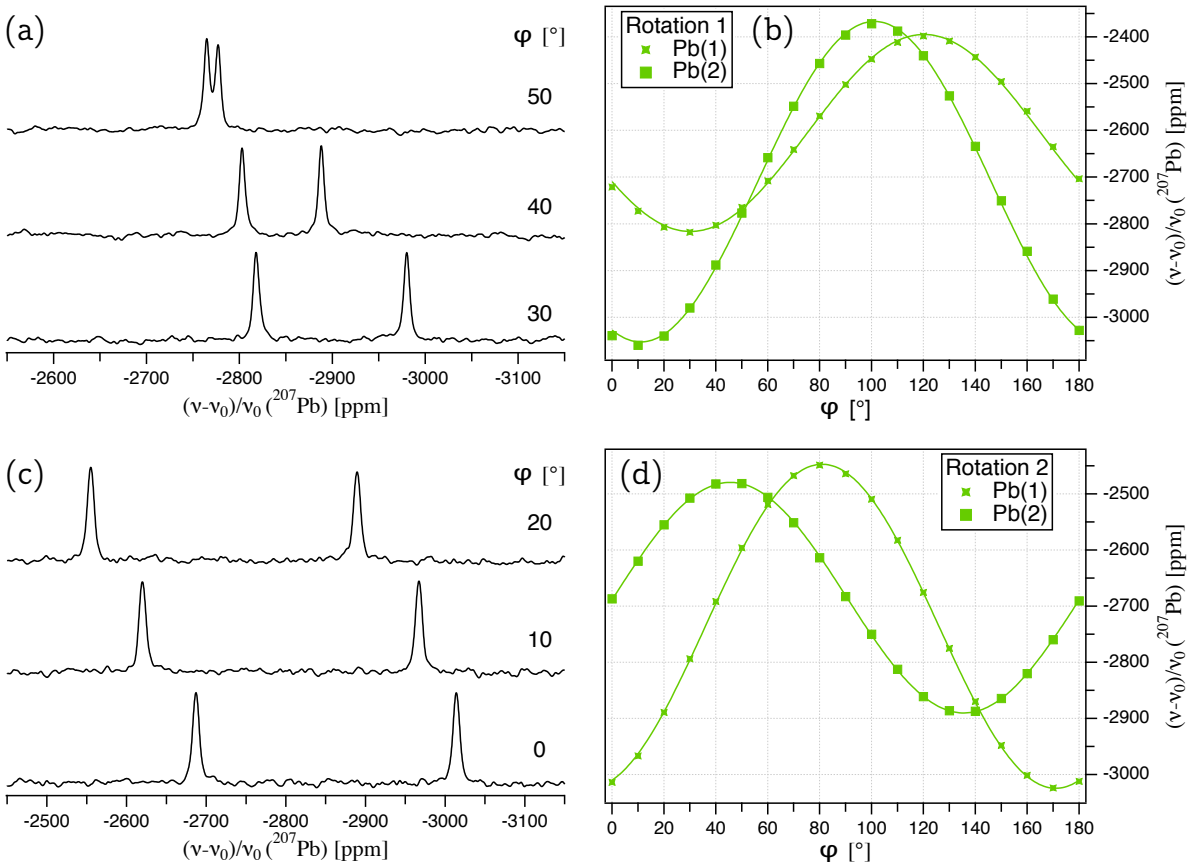

Figure 8.8 – ^{207}Pb NMR spectra of a single crystal of cerussite, $PbCO_3$, rotated counter-clockwise by the indicated angle φ around the rotation axis $\vec{g}_1$ **(a)** and $\vec{g}_2$ **(c)**, both perpendicular to the external magnetic field $\vec{B}_0$. Full rotation pattern over 180° for the two magnetically inequivalent ^{207}Pb at Wyckoff position 4*c*, acquired by rotating the cerussite crystal step-wise by 10° around two goniometer axis $\vec{g}_1$ **(b)** and $\vec{g}_2$ **(d)**. The lines represent the fit of the experimental points to the CS tensor elements and axis orientation (see main text for details).

^{207}Pb NMR spectra of the cerussite crystal depicted in Figure 8.6a are displayed on the left in Figure 8.8 for a limited number of crystal orientations in the external magnetic field $\vec{B}_0$. These orientations are defined by the rotation angle φ around a given axis, which is perpendicular to $\vec{B}_0$, due to the architecture of the goniometer probe. All spectra are composed of two ^{207}Pb resonances with identical shape and intensity, with the resonance position markedly dependent on the crystal orientation. Plots of the full rotation pattern for $\varphi = 0^{\circ} \ldots 180^{\circ}$ are shown on the right of Figure 8.8 for the rotation axes $\vec{g}_1$ (Figure 8.8b) and $\vec{g}_2$ (Figure 8.8d). In the current context, only the number of ^{207}Pb NMR resonances in the single crystal spectra of cerussite is of interest, in order to address the question whether the presence of two resonances is in agreement with the structure models derived from XRD studies.[95,98–103] All previously reported structure refinements of cerussite agree that it crystallises in the orthorhombic crystal frame *Pmcn* (No. 62) of aragonite-type carbonates, with four formula units per unit cell. The fact that only one lead atom is found in the asymmetric unit seems to be at odds with the existence of two ^{207}Pb resonances in the NMR spectra. However, as already explained in Section 4, for single-crystal NMR, one has to distinguish between crystallographically and magnetically equivalent nuclei, where inversions and translational elements do not affect NMR spectra. The single crystallographic site of lead in cerussite is at Wyckoff position 4*c*, which generates four lead atoms in the unit cell. Two of those atoms are situated on a mirror plane located at $\frac{1}{4}yz$, and two on a mirror plane at $\frac{3}{4}yz$. As may be seen from Figure 8.6b, those two pairs are connected to each other by an inversion center at the middle of the unit cell and are generated by glide planes at $x\frac{1}{4}z$ and $x\frac{3}{4}z$. The available crystal structure refinements differ in their placement of the lead atoms relative to the glide planes at $xy\frac{1}{4}$ and $xy\frac{3}{4}$. According to three XRD studies,[98–100] the two pairs of lead atoms are situated exactly on these glide planes, whereas four structure determinations[95,101–103] place the atoms just next to them. Since positions on glide planes, as opposed to mirror planes, are not special positions for crystallography, the placement of the lead atoms exactly on, or slightly off the glide plane *n* does not impose symmetry restrictions and hence impacts the quality of the XRD structure refinement only marginally. In contrast, for NMR spectra, the mirror and glide planes effectively reduce to two-fold rotations, since the inversion operation renders the pairs magnetically equivalent. Thus, the four symmetry-related lead atoms in the unit cell are all magnetically equivalent when positioned exactly on the glide planes. Alternatively, when placed slightly off the glide planes, the four lead atoms form two groups of magnetically inequivalent ^{207}Pb sites, which are generated by the glide planes at $xy\frac{1}{4}$ and $xy\frac{3}{4}$. The first possibility results in only one ^{207}Pb NMR signal for a single crystal, the second in two. From the existence of two ^{207}Pb NMR resonances of equal intensity in the spectra shown in Figure 8.8, it can be concluded that the lead atoms are not exactly positioned on the glide planes at $xy\frac{1}{4}$ and $xy\frac{3}{4}$, in accordance with four previous XRD studies.[95,101–103]

However, there exists one effect which could also produce two ^{207}Pb NMR signals with equal intensity in a presumed single crystal, and that is intrinsic twinning. The probably best-known system exhibiting this effect is the mineral cinnabar, HgS.[104] As described in the following, both an investigation of a genuine cerussite twin by single-crystal NMR spectroscopy and a re-determination of the crystal structure by XRD show that intrinsic twinning does not occur in our samples, so that the clarification of crystal structure outlined here is valid.

8.8 Elucidation of macroscopic twinning by single-crystal NMR

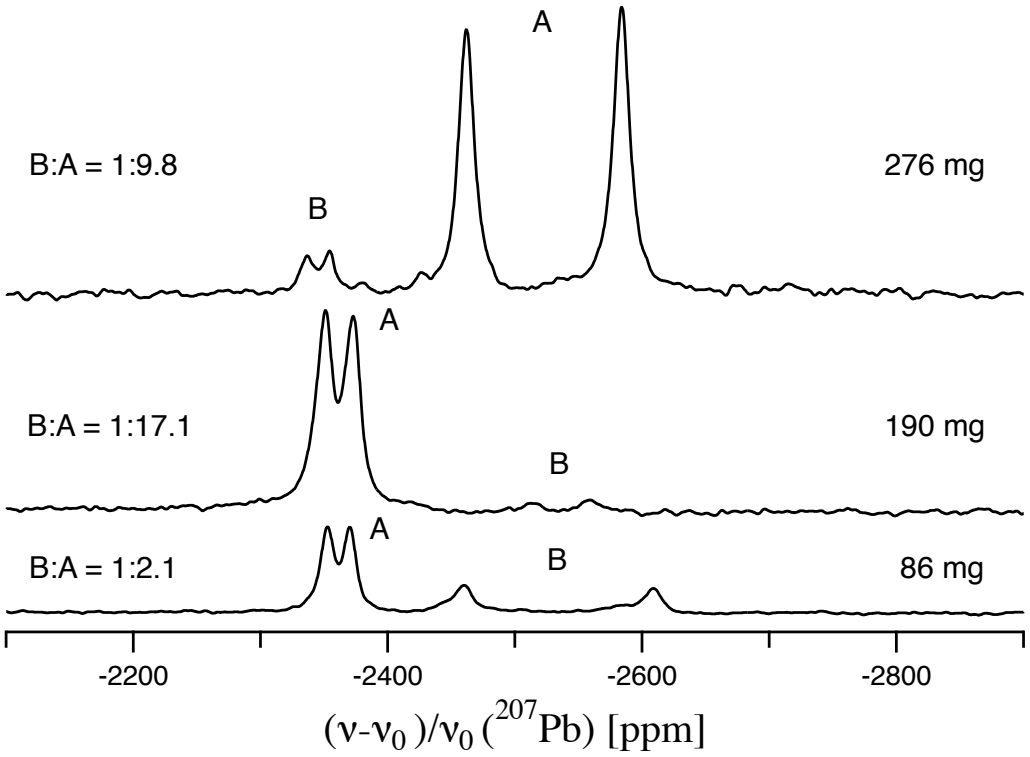

Figure 8.9 – Static ^{207}Pb NMR spectrum of a twinned crystal of cerussite (top). Spectra after cutting the original crystal into a larger (middle) and smaller piece (bottom), with the respective weights of all crystals listed on the right. On the left of the spectra the relative spectral contributions of the two twin domains *A* and *B* are indicated, showing that the ratio of *A* to *B* is changing. The spectra have been acquired with a differing number of scans, with the plotted intensity scaled according to crystal weight. For all spectra, the orientation of the crystals in the magnetic field are non-specific, but chosen to resolve all four resonances.

In the course of the NMR measurements for this study, we chanced upon a macroscopically twinned cerussite crystal. It is a different specimen from the one depicted in Figure 8.6a, but

originates from the same location in Tsumeb, Namibia. In Figure 8.9, a ^{207}Pb NMR spectrum taken of this twin crystal is shown, before cutting it into a larger and smaller piece, the spectra of which are also depicted. In each spectrum, there are four signals forming two pairs of equal intensity corresponding to one twin domain, cerussite twin A and B, respectively. The upper spectrum in Figure 8.9 belongs to the original twin crystal (weighing 276 mg), where the ^{207}Pb NMR intensity ratio of $B : A = 1 : 9.8$ gives a good estimate of the relative twin domain sizes. The middle spectrum in Figure 8.9 belongs to the larger piece after cutting, with a remaining weight of 190 mg, the bottom spectrum to the smaller piece weighing 86 mg. In both these spectra, the ratio of $B : A$ is significantly changed in comparison to the original twin, with the larger crystal containing mostly domain A, with $B : A = 1 : 17.1$, and the smaller piece having a higher proportion of domain B, with $B : A = 1 : 2.1$. Such changes in relative domain sizes induced by cutting can only occur for macroscopic twin crystals, since for intrinsic twinning, the relative contributions of the two domains would be identical for any chosen part of the crystal.

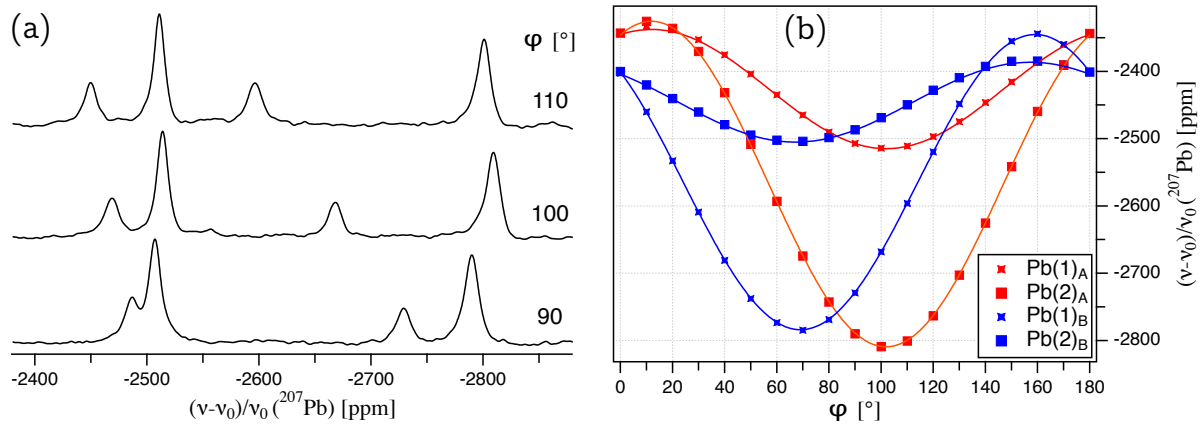

Figure 8.10 – **(a)** ^{207}Pb NMR spectra of a twinned cerussite crystal rotated counter-clockwise by the indicated angle φ around a rotation axis perpendicular to the external magnetic field $\vec{B}_0$. **(b)** Full rotation pattern over 180° for the two magnetically inequivalent ^{207}Pb at Wyckoff position 4*c* in each twin-crystal domain A (red) and B (blue), acquired by rotating the cerussite twin step-wise by 10° around one goniometer axis. The lines represent the fit of the experimental points to the CS tensor elements and axis orientation (see main text for details).

For the twin crystal with a weight of 86 mg, the resonances of the smaller B domain are clearly discernible in the ^{207}Pb NMR spectrum, and they can easily be separated from the A domain signals by their smaller signal intensity, as may be seen in Figure 8.10a. A full rotation pattern of this twin crystal was acquired, shown in Figure 8.10b, by glueing the crystal on a rod, which was oriented perpendicular to the external field, and rotated step-wise by the goniometer mechanics. As it turns out, this rotation pattern also contains information

about the relative orientation of the A and B domains, which allows the elucidation of the twinning geometry of the investigated crystal. Data of the type shown in Figure 8.10b are used to extract NMR interaction tensors in a given reference frame. This frame is usually defined by the (if necessary, orthonormalized) vectors along the crystallographic axes *abc*, since tensors expressed in the CRY frame have a direct relation to the electron distribution in the unit cell. For the tensor determination procedure, it is essential to know the orientation of the rotation axis in the CRY frame, or in other words, to know the precise way in which the macroscopic crystal is glued onto the goniometer axis (for details see Section 4). For the data of the cerussite twin shown in Figure 8.10, this fit delivers the orientation of the goniometer axis vector $\vec{g}_A$ for domain A, and similarly $\vec{g}_B$ for domain B, with the actual numbers derived and listed in Section 8.9 (see below). In the common crystal frame CRY, the vectors $\vec{g}_A$ and $\vec{g}_B$ possess different directions, since they belong to two distinct crystal domains of the twin. By switching the point of view to the frame of the goniometer (often referred to as laboratory frame LAB), where only one physical rotation axis exists, it can be understood that the difference in directions of $\vec{g}_A$ and $\vec{g}_B$ actually represents the orientation difference of the two crystal frames belonging to the domains A and B, which is the twinning geometry we seek. Unfortunately, to relate one twin frame to another, three Euler angles (or directional cosines) are needed,[105] and the difference of two vectors provides only two of those. Fortunately, it is known that the most common type of twinning in cerussite is contact twinning, predominantly occurring in the form of {110} and {130} twins.[106–109] In case of a simple contact twin, the contact plane of the two twin domains is fully defined by the bisector of the two goniometer axes and the crystallographic c axis in the CRY frame. For our cerussite crystal, the bisector between $\vec{g}_A$ and $\vec{g}_B$ points along $(1\,3\,0)^T$ with a deviation of 3.5°. It is therefore highly likely that the investigated twin crystal of cerussite is a {130}–contact twin, a type of twin well known to collectors of natural minerals.[106] A large specimen of such a cerussite twin (with several cm in diameter, depicted in Figure 8.11) is also exhibited in the Mineralogical state

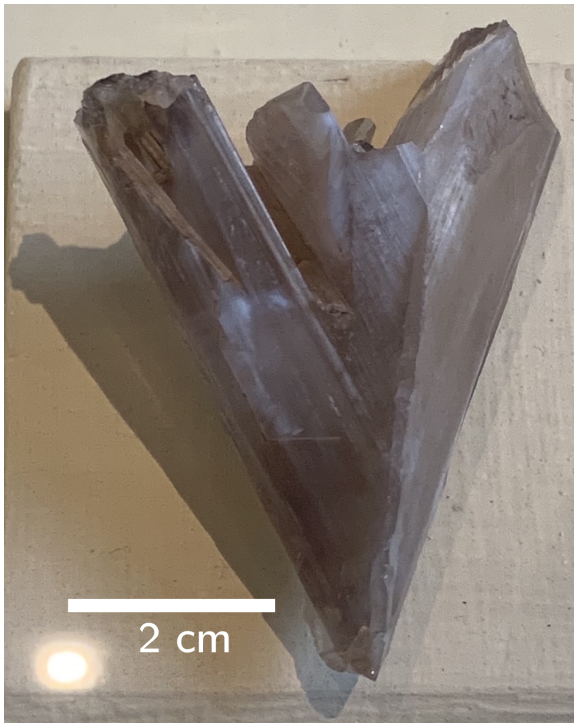

Figure 8.11 – {130}–contact twin of cerussite, $PbCO_3$, from Touissit, Morocco (Mineralogical state collection, 'Museum für Naturkunde' Berlin).

collection of the 'Museum für Naturkunde' in Berlin, Germany. It should however be noted that due to the bisector deviation of 3.5°, our NMR results do not allow us to unambiguously distinguish between {130} and very similar twinning planes, e.g. the {270} plane.

8.9 ^{207}Pb chemical shift tensor determination of Cerussite

The systematic recording of the orientation dependence of the ^{207}Pb NMR resonances allows the determination of the full ^{207}Pb chemical shift (CS) tensor in cerussite in the same way it has been shown for anglesite ($PbSO_4$) in the first half of Section 8. The rotation patterns of $PbCO_3$ shown in Figures 8.8 and 8.10 are clearly described by Volkoff harmonics according to Equation 4.1. The two magnetically inequivalent lead sites in space group *Pmcn* of cerussite can be considered to be related by a 180° rotation about the crystallographic *c* axis and are situated on mirror planes parallel to the *bc* plane. These symmetry requirements affect the structure of the ^{207}Pb chemical shift tensors in the *CRY* frame (again very similar to anglesite), which are hence given by:

$$\underset{(x,\frac{1}{4},z)}{\boldsymbol{\delta}^{\boldsymbol{CRY}}_{\boldsymbol{Pb(1)}}} = \begin{pmatrix} P & 0 & 0 \\ 0 & Q & R \\ 0 & R & S \end{pmatrix} \quad \overset{180^o_c}{\longleftrightarrow} \quad \underset{(\bar{x}+\frac{1}{2},\frac{3}{4},z+\frac{1}{2})}{\boldsymbol{\delta}^{\boldsymbol{CRY}}_{\boldsymbol{Pb(2)}}} = \begin{pmatrix} P & 0 & 0 \\ 0 & Q & -R \\ 0 & -R & S \end{pmatrix} \tag{8.6}$$

To determine the tensor components P, Q, R, and S and the orientation of the rotation axis from the respective rotation patterns in Figures 8.8 and 8.10, we follow the approach extensively described above in the first half of Section 8 for orthorhombic $PbSO_4$.[55] Thus, the two rotation patterns for the cerussite single crystal with the rotation axis $\vec{g}_1$ (Figure 8.8b) and $\vec{g}_2$ (Figure 8.8d), as well as the rotation pattern of the twinned cerussite (Figure 8.10b) with rotation axis $\vec{g}_A$ and $\vec{g}_B$, corresponding to an individual rotation of each twin domain, were simultaneously fitted according to Equation 4.4 with the chemical shift tensors given in Equation 8.6 and the motion of the magnetic field vector in the *CRY* frame described by Equation 4.7 and 4.6. The fit converged on a global solution, with the resulting rotation (goniometer) axes listed in Table 8.3, and the following ^{207}Pb chemical shift tensor components, with the errors reflecting the fit residuals:

$$P = (-2315 \pm 1) \text{ ppm} \quad Q = (-3012 \pm 3) \text{ ppm}$$
$$R = (173.1 \pm 0.5) \text{ ppm} \quad S = (-2550 \pm 1) \text{ ppm}$$

Table 8.3 – Orientation of the various goniometer axes $\vec{g}_i$ used for the determination of the ^{207}Pb CS tensor of cerussite, $PbCO_3$, from a global fit of the indicated rotation patterns. The directions of the $\vec{g}_i$ are given in spherical coordinates (θ_g, ϕ_g) of the CRY frame, with the errors reflecting the fit residuals. The φ_Δ parameters define the starting point of each rotation, see Section 4 for details.

Goniometer axis (rotation pattern)	θ_g	ϕ_g	φ_Δ
$\vec{g}_1$ (Figure 8.8b)	$(136.3 \pm 0.3)^o$	$(142.6 \pm 0.3)^o$	$(142.4 \pm 0.2)^o$
$\vec{g}_2$ (Figure 8.8d)	$(112.2 \pm 0.4)^o$	$(205.1 \pm 0.3)^o$	$(51.6 \pm 0.1)^o$
$\vec{g}_A$ (Figure 8.10b)	$(118.5 \pm 0.2)^o$	$(78.5 \pm 0.4)^o$	$(113.4 \pm 0.4)^o$
$\vec{g}_B$ (Figure 8.10b)	$(66.3 \pm 0.1)^o$	$(70.0 \pm 0.2)^o$	$(48.7 \pm 0.3)^o$

The CS tensor defined by the P, Q, R, S values in the CRY frame can be transformed into its principal axes system (PAS) by diagonalization, resulting in the eigenvalues and eigenvectors listed in Table 8.4(left). The eigenvalues agree well with those previously reported from static spectra of a polycrystalline sample: $\delta_{11} = -2311$ ppm, $\delta_{22} = -2481$ ppm, and $\delta_{33} = -3075$ ppm.[6] From our ^{207}Pb CS tensor values for cerussite, the isotropic shift computes to $\delta_{iso} = -2626$ ppm. We find the anisotropy in cerussite to be moderately large with -445 ppm, which indicates that the electron lone pair at the lead atoms is significantly *sp*-hybridized.[71] The orientation of the CS tensor eigenvectors in the orthorhombic unit cell, scaled according to the associated eigenvalues, are depicted in Figure 8.12. As a consequence of the symmetry enforced by the mirror planes parallel to the *bc* plane, the eigenvector of one of the lesser tensor components, i.e. δ_{11}^{PAS}, aligns exactly along the crystallographic *a* axis. The remaining two eigenvectors belonging to the other principal components are free to orient according to the electronic surroundings, generated chiefly by the surrounding carbonyl ions. Interestingly, the eigenvector with the largest corresponding eigenvalue (δ_{33}^{PAS}) points exactly to the next nearest carbon atom, as may be best seen in the upper right corner of Figure 8.12a.

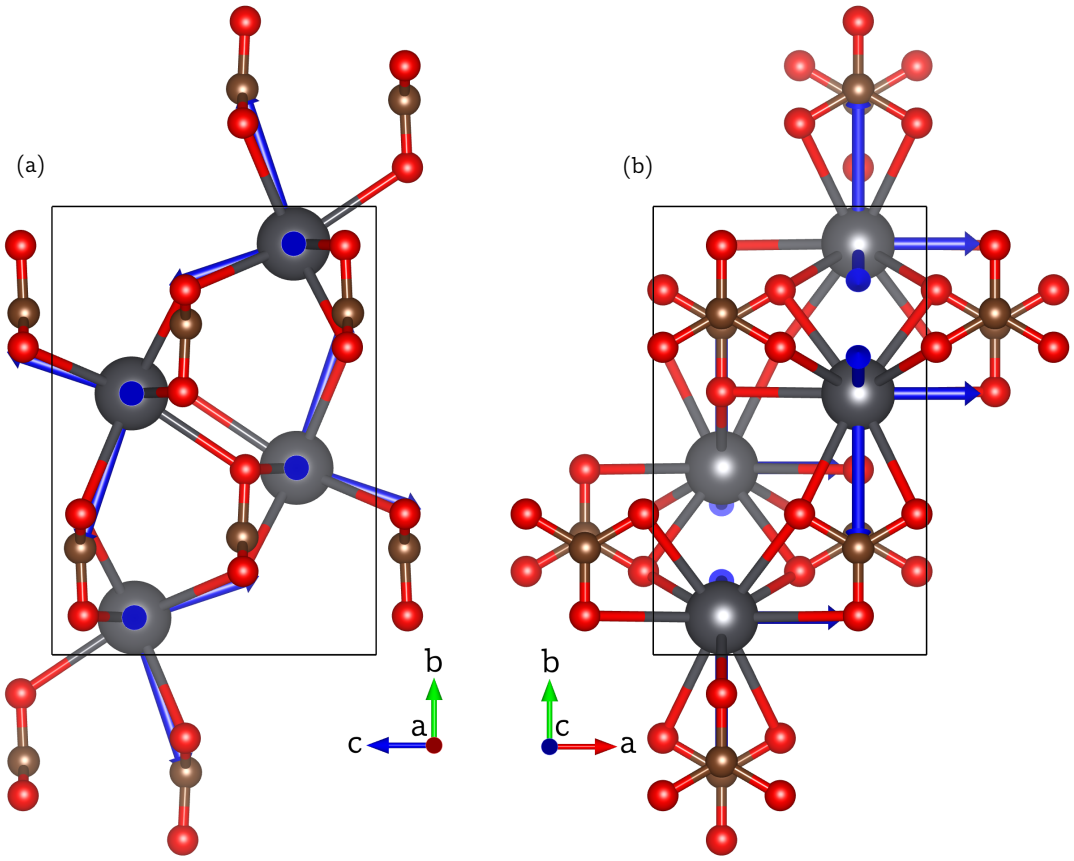

Figure 8.12 – Orientation of the experimentally determined ^{207}Pb chemical shift eigenvectors (blue) in the unit cell of cerussite (space group *Pmcn*), scaled according to the magnitude of the associated eigenvalues, such that an absolute value of 750 ppm corresponds to a length of 1 Å, with the lead atoms (gray) shown with their coordination to nine oxygen atoms (red); **(a)** Viewed down along the crystallographic *a* axis. **(b)** Viewed down along the crystallographic *c* axis. Drawing generated with the Vesta program.[68]

As already mentioned in Section 5, it is also possible to extract information about the magnitude of the CS tensor, i.e. the eigenvalues and the isotropic chemical shift, from a polycrystalline sample, using either static or magic-angle spinning (MAS) NMR spectroscopy. As a useful comparison to our single crystal data, ^{207}Pb NMR spectra of a sample of cerussite crushed into a powder were acquired at three different MAS spinning speeds, 10 kHz, 8 kHz, and 6 kHz, with the latter shown in Figure 8.7b. It is well known that ^{207}Pb chemical shifts vary strongly with temperature for many inorganic compounds,[72,73,82] so that even friction heating from MAS can lead to a noticeable change in the isotropic chemical shift (see also MAS-NMR measurements for anglesite above). Extrapolating δ_{iso} over the squared MAS frequency, as shown in Figure 8.13, allows the determination of the isotropic shift at room temperature to $\delta_{iso}^{MAS} = (-2632 \pm 5)$ ppm. Within error limits, this is identical with the value derived from single-crystal NMR. To also extract

the three eigenvalues of the CS tensor, the weighted sum of which constitutes δ_{iso}, a Herzfeld-Berger analysis[7] of the MAS spectrum at 6 kHz was performed using the *hba 1.7.5* program.[110] The results are given in Table 8.4(middle), showing that the magnitude of the MAS-derived eigenvalues are in good agreement with the single-crystal values, especially taking into account that discrepancies may arise from the temperature difference between static single-crystal and MAS experiments. Finally, the chemical shift eigenvalues were also estimated from the static ^{207}Pb powder spectrum shown in Figure 8.7a. This spectrum was compared to various spectra calculated with the Simpson package,[64] with the best agreement between the experiment and simulation found for the eigenvalues listed in Table 8.4(right). These eigenvalues are very similar to those derived from MAS NMR and agree well with the single-crystal values.

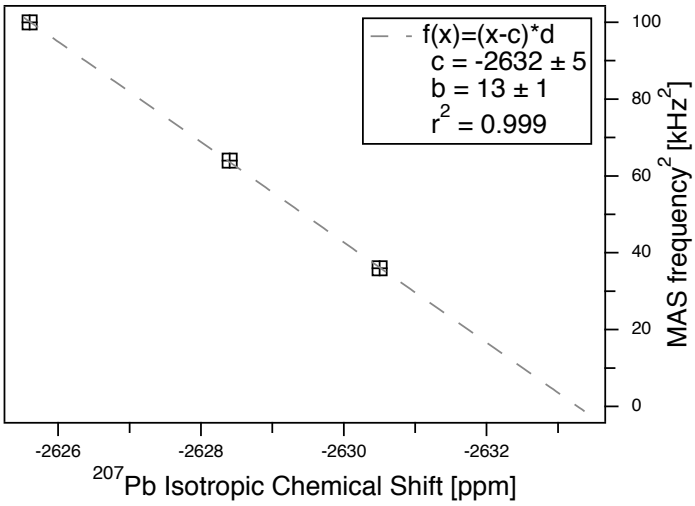

Figure 8.13 – Plot of the ^{207}Pb isotropic chemical shift of cerussite versus the squared MAS frequency, with the linear fit given by the dashed line. An extrapolation to zero spinning speed results in an isotropic chemical shift of -2632 ± 5 ppm.

Table 8.4 – ^{207}Pb chemical shift tensor $\boldsymbol{\delta^{CRY}}$ of cerussite, $PbCO_3$. Left: Determined from room temperature single-crystal NMR experiments about the four rotation axes listed in Table 8.3. The orientation of the corresponding eigenvectors are given in spherical coordinates (θ, ϕ) in the orthorhombic *abc* crystal system *Pmcn*, and refer to the atom closest to the origin, i.e. Pb(1). The error values are derived from the fit residuals. Middle: Determined from a Herzfeld-Berger analysis [7] of the rotational side band pattern at $\nu_r = +6$ kHz MAS (i.e. at slightly elevated temperature), using the *hba 1.7.5* program [110], leading to $\rho = 0.58 \pm 0.01$ and $\mu = 13.2 \pm 0.1$ (see Section 5). The error values of the tensor components are derived from those of ρ and μ. Right: Determined from a static polycrystalline powder sample at room temperature. Error values of tensor components are derived from a Simpson simulation. [64]

	Single-Crystal NMR	**MAS NMR**	**static powder NMR**
δ_{11}^{PAS}	(-2315 ± 1) ppm	(-2324 ± 4) ppm	(-2320 ± 7) ppm
δ_{22}^{PAS}	(-2492 ± 3) ppm	(-2485 ± 3) ppm	(-2492 ± 4) ppm
δ_{33}^{PAS}	(-3071 ± 3) ppm	(-3082 ± 3) ppm	(-3084 ± 10) ppm
$\vec{d}_{11}$	90.0°, 0.0°		
$\vec{d}_{22}$	18.4°, 90.0°		
$\vec{d}_{33}$	71.6°, 270.0°		
δ_{iso}		(-2630 ± 3) ppm	
	(-2626 ± 3) ppm	(-2632 ± 5) ppm[a]	(-2632 ± 7) ppm

[a] From extrapolation of squared MAS frequencies to zero spinning, see Figure 8.13.

8.10 Re-determination of cerussite structure from single-crystal XRD

To corroborate the structure model of cerussite derived from NMR data, we also re-determined the crystal structure from single-crystal XRD, using specimens from the same mineral source as were used for the NMR measurements discussed above. A small xenomorphic fragment was broken off the crystal depicted in Figure8.6a and glued on top of a glass fibre. The diffraction data were carefully corrected for absorption effects on the basis of indexed crystal faces. [111,112] In order to cope with the high absorption and to achieve high precision by collecting high-angle reflections with significant intensities, data collection was performed in Ag-K_α radiation. The orthorhombic metric together with the extinction conditions ($0kl$ only observed for $k+l = 2n$, $hk0$ only observed for $h = 2n$, $h00$ only observed for $h = 2n$, $0k0$ only observed for $k = 2n$ and $00l$ only observed for $l = 2n$) and the statistics over $E^2 - 1$ unambiguously pointed towards the aragonite structure type (space group *Pmcn*, No. 62), and structure solution and refinement showed this to be correct. Crystallographic details and results of the single-crystal structure refinement are compiled in Tables 8.5-8.7.

The cerussite structure model could be refined to a very high precision, allowing for precise statements with respect for fractional atomic coordinates. This is important with regard to the NMR spectroscopic measurements, especially for the atomic position of lead which is slightly but significantly shifted from the glide plane. The single crystal specimen chosen for the X-ray diffraction experiments was tested for the twin laws known to occur in the aragonite structure family but no significant twin domain volume fractions could be detected.

Table 8.5 – Standardized fractional atomic coordinates[115] and equivalent isotropic displacement parameters (U_{equiv}) in Å^2 for cerussite, $PbCO_3$. The equivalent isotropic displacement parameter is defined as 1/3 of the trace of the anisotropic displacement tensor. All standard deviations are given in parentheses in units of the last digit.

Standard setting *Pnma* with crystal lattice *abc*						
Atom	Wyck.	Symm.	x	y	z	U_{equiv}
Pb1	4*c*	.*m*.	0.24494(7)	1/4	0.58284(4)	0.01057(14)
C1	4*c*	.*m*.	0.0864(16)	1/4	0.2393(14)	0.0120(16)
O1	4*c*	.*m*.	0.0961(14)	1/4	0.0866(10)	0.0163(15)
O2	8*d*	1	0.0892(10)	0.0346(12)	0.3140(7)	0.0167(11)
Non-standard setting *Pmcn* with crystal lattice *bca*						
Pb1	4*c*	*m*..	1/4	0.58284(4)	0.24494(7)	0.01057(14)
C1	4*c*	*m*..	1/4	0.2393(14)	0.0864(16)	0.0120(16)
O1	4*c*	*m*..	1/4	0.0866(10)	0.0961(14)	0.0163(15)
O2	8*d*	1	0.0346(12)	0.3140(7)	0.0892(10)	0.0167(11)

Table 8.6 – Coefficients U_{ij} of the anisotropic displacement tensor (Å^2) for cerussite, $PbCO_3$, given for the standard setting *Pnma*. U_{ij} is defined as $U_{ij} = exp\{-2\pi^2[U_{11}(ha^*)^2 + ... + 2U_{21}hka^*b^*]\}$. All standard deviations are given in parentheses in units of the last digit.

Atom	U_{11}	U_{22}	U_{33}	U_{23}	U_{13}	U_{12}
Pb1	0.01135(17)	0.01097(18)	0.00938(16)	0	0.00042(19)	0
C1	0.013(4)	0.012(4)	0.010(4)	0	-0.003(3)	0
O1	0.025(3)	0.008(2)	0.017(3)	0.003(2)	0.002(2)	-0.001(2)
O2	0.022(3)	0.018(4)	0.009(3)	0	0.001(3)	0

Table 8.7 – Crystallographic data and details on single-crystal data collection, structure solution and refinement for $PbCO_3$. Data collection was performed at room temperature. All standard deviations are given in parentheses in units of the last digit. For comparison with literature the cell is given for both, the standard setting of the space group *Pnma* and for the non-standard setting *Pmcn*, which is the preferred choice for existing literature. The index range refers to the standard setting *Pnma*.

Composition		$PbCO_3$
Crystal system		orthorhombic
Space group		*Pnma*, (Nr. 62)
Lattice parameters / Å	a	6.1329(8)
	b	5.1744(7)
	c	8.4819(9)
Non-standard setting **bca**		*Pmcn*
Lattice parameters / Å	a'	5.1744(7)
	b'	8.4819(9)
	c'	6.1329(8)
V / Å^3		269.17(6)
Z		4
Data collection temperature / K		293(1)
Density (X-ray) ρ / g·cm^{-3}		6.84
Structure factor $F(000)$		467
Absorption coefficient / mm^{-1}		34.32
Radiation, wavelength / Å		Ag-K$_\alpha$, 0.56086
Diffraction angle range 2ϑ / ^{o}		7.3 – 50.0
Index range	h	−9 – +9
	k	−7 – +7
	l	−12 – +12
Diffractometer		Stoe IPDS1
Corrections		Polarization, Lorentz, absorption effects[111–113]
Structure refinement		full-matrix least-squares on F^2 [114]
No. of collected reflections		6559
No. of independent reflections		529
No. of independent reflections ($I \geq 2\sigma(I)$)		479
No. of least-squares parameters		29
R_{int}		0.0543
R_σ		0.0184
$R1$ for $I \geq 2\sigma(I)$		0.0399
$wR2$ for $I \geq 2\sigma(I)$		0.0472
$R1$ (all I)		0.0476
$wR2$ (all I)		0.0484
GooF		1.642
Residual ρ(e$^-$) max/min / e$^-$·Å^{-3}		+1.74 / −2.44

8.11 Experimental details for Cerussite

For the single-crystal XRD data collection, the xenomorphic single crystal of cerussite, $PbCO_3$, was centered on the one-circle goniometer of a diffractometer system IPDS 1 (Stoe & Cie., Darmstadt, Germany) equipped with graphite-monochromatised Ag-K_α radiation (fine-focus X-ray tube) and imaging plate detector. Data collection was performed in φ scans from the accessible part of an entire Ewald sphere, and corrected for Lorentz and polarisation effects with the diffractometer software packages.[113,116] Absorption corrections were performed carefully on the basis of optimised indexed crystal faces,[111,112] and structure solution was performed with direct methods[114] in space group *Pnma* as indicated by extinction conditions together with statistics on $E^2 - 1$. Structure refinement was performed with full-matrix least-squares cycles[114] on F^2. All atoms were treated with anisotropic displacement tensors.

All NMR spectra were acquired on a Bruke Avance-III 500 Spectrometer at LMU Munich, with the Larmor frequency being $\nu_0(^{207}\mathrm{Pb}) = 104.63$ MHz, using echo acquisition to minimize base line roll,[74] and a recycle delay of 16 s. Single-crystal ^{207}Pb-NMR spectra were acquired at room temperature on a commercial wide-bore Bruker static NMR probe, equipped with an home-build 6 mm solenoid coil, using echo pulses of 2/4 μs duration. Orientation change was realized with a clip-on goniometer build by NMR Service GmbH (Erfurt, Germany), which allows for defined rotations in steps of 10°. A polycrystalline sample was prepared by crushing single crystals of cerussite with an agate mortar, and measured using a 4 mm rotor under both MAS and static conditions, employing echo pulse durations of 5.25/10.5 μs. All spectra were referenced indirectly to ^{1}H in 100% TMS at -0.1240 ppm, which is equivalent to the common $Pb(NO_3)_2$-powder referencing at -3487.5 ppm. The global fit of the rotation pattern, including the orientation of the magnetic field vector $\vec{b}_0$ in the crystal frame, was performed with the WaveMetrics Inc. program Igor Pro 7.08.

9 No Symmetry Relation: Known Morphology

9.1 Introduction: Aluminum Nitride (AlN)

In cases where all equivalent crystallographic positions are also magnetically equivalent, interaction-tensor determination and simultaneous rotation axes determination from NMR data only is not a straightforward task (as is detailed in Section 4). In Section 9, we demonstrate the determination of the quadrupole coupling tensor and the chemical shift tensor with prior knowledge of the chosen rotation axis, which allows to overcome the lack of symmetry-linked but magnetically inequivalent sides. To this end, we present the determination of the full $\boldsymbol{\delta}$ tensor and $\mathbf{Q}$ tensor for ^{27}Al ($I = 5/2$) and ^{14}N ($I = 1$) in hexagonal aluminum nitride, which is taken from Zeman et al. 2020 published in *Molecules* (MDPI),[117] and adapted for this thesis. This is made possible

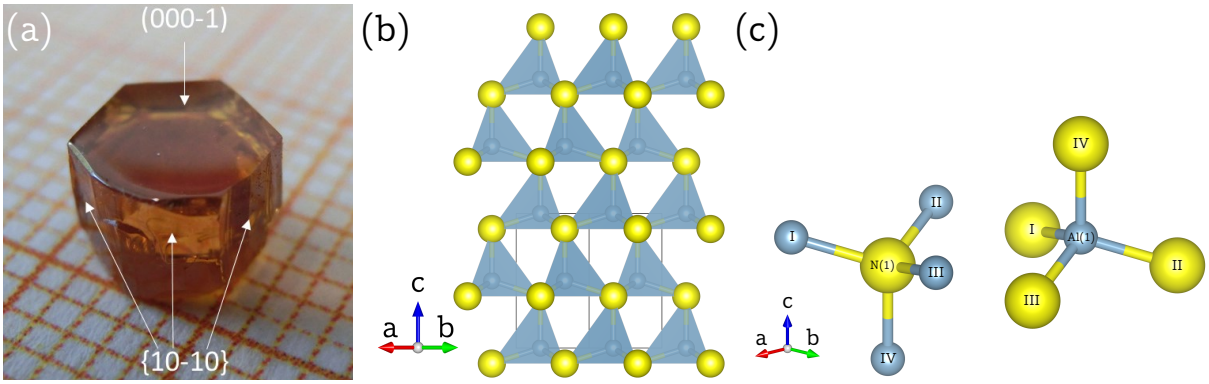

Figure 9.1 – **(a)** Single crystal of aluminum nitride, AlN, with the synthesis described in Literature.[24] The crystallographic c axis and the ab plane are indicated by arrows. **(b)** Wurtzite structure of AlN, according to Reference,[118] viewed down the crystallographic [11-20] direction. The aluminum atoms (blue-grey) and the nitrogen atoms (yellow), both located at Wyckoff position $2b$, are tetrahedrally coordinated by each other with one Al-N bond directed parallel to the crystallographic c axis. **(c)** Individual, tetrahedrally coordinated, aluminum and nitrogen atom in the crystal structure of AlN, in which the three equal, shorter, bonds Al/N—I/II/III with 1.8891(8) Å and the longer bond Al/N—IV with 1.9029(16) Åalong the three-fold rotation axis are highlighted.Figure taken from [117] Drawing generated with the Vesta program.[68]

by the successful preparation of a macroscopic single crystal of AlN (shown in Figure 9.1a) using a bulk growth process on a native AlN seed.[24] Aluminum nitride commonly occurs in the hexagonal wurtzite structure, depicted in Figure 9.1b, with space group $P6_3mc$ (No. 186) and two formula units per unit cell.[118]. The aluminum as well as the nitrogen atoms are located at Wyckoff position $2b$ on a three-fold rotation axis parallel to the crystallographic c axis. Aluminum is tetrahedrally coordinated by nitrogen and vice versa, with one slightly elongated Al-N bond directed along the three-fold rotation axis, and the other three bonds found in equivalent positions

around this axis, as may be seen in Figure 9.1c. These symmetry constraints have a direct impact on the structure of the NMR tensors and therefore the CRY and the PAS frames for ^{14}N and ^{27}Al are identical. In their PAS frame, symmetric tensors take diagonal form (see Section 3). This has the consequence that the tensors cannot change when the two formula units are generated by the symmetry elements of Wyckoff position 2*b*. Therefore, the two ^{14}N and ^{27}Al atoms in the AlN unit cell are practically pairwise magnetically equivalent, even though they do not fulfill the strict equivalence criterion of being connected by either inversion or translation. The **Q** tensor for both nuclides is hence uniaxial ($\eta_Q = 0$), and solely defined by the quadrupolar coupling constant $\chi = C_Q = Q_{33}$:

$$\mathbf{Q^{PAS}} = \mathbf{Q^{CRY}} = \begin{pmatrix} -\frac{\chi}{2} & 0 & 0 \\ 0 & -\frac{\chi}{2} & 0 \\ 0 & 0 & \chi \end{pmatrix} \tag{9.1}$$

Also, due to the high symmetry of the crystal lattice, the quadrupolar interaction is expected to be moderate and, hence, only needs to be considerate to maximum second order (See Section 3). Taking into account the same symmetry arguments as for the **Q** tensor above, the chemical shift (CS) tensor $\boldsymbol{\delta}$ for ^{14}N and ^{27}Al in AlN is given by:

$$\boldsymbol{\delta}^{PAS} = \boldsymbol{\delta}^{CRY} = \begin{pmatrix} P & 0 & 0 \\ 0 & P & 0 \\ 0 & 0 & R \end{pmatrix} \tag{9.2}$$

9.2 ^{27}Al quadrupole coupling tensor

A single crystal of aluminum nitride with approximate dimensions of $5 \times 5 \times 4$ mm^3 was used for the single-crystal NMR experiments. Since the crystal was grown by a homoepitaxial growth process,[24] it is possible to assign the crystal faces to crystallographic planes, as indicated in Figure 9.1a. It was therefore possible to fix the crystal into in a specific orientation by gluing it with its (10-10) face onto the goniometer axis, which itself is perpendicular to the external magnetic field $\vec{b}_0$. The crystal was then rotated until the [000-1] direction was parallel to $\vec{b}_0$. Both orienting procedures involve small misalignments, which can however be quantified by the data analysis, as described below. Representative ^{27}Al NMR spectra are shown in Figure 9.2a, with the full rotation pattern over 180° shown in Figure 9.2b, which was obtained by rotating the crystal counterclockwise in steps of 15° using the goniometer gear. The satellite pairs for $k = \pm 2$, in the following denoted as ST(5/2), and $k = \pm 1$, in the following denoted as ST(3/2), are symmetrically positioned around the central transition. All ^{27}Al resonance lines are fairly

broad, with a full width at half-maximum $FWHM \approx 9$ kHz, caused by hetero- and homonuclear dipolar interactions between aluminum and nitrogen atoms in the structure.[119]

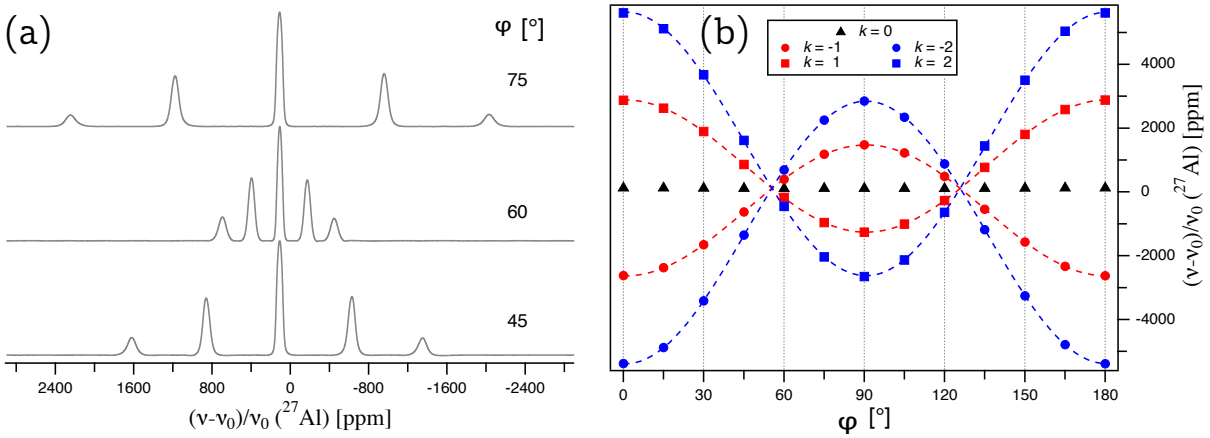

Figure 9.2 – **(a)** ^{27}Al NMR spectra of a single crystal of aluminum nitride, AlN, with the indicated rotation angles φ referring to the full rotation pattern on the right. **(b)** Full rotation pattern over 180° for ^{27}Al at Wyckoff position 2*b*, acquired by rotating the AlN crystal counterclockwise by 15° around a rotation axis which is perpendicular to the external magnetic field $\vec{b}_0$, and situated in the crystallographic *ab* plane of AlN. The zero point of the rotation, $\varphi = 0$, deviates by $\varphi_\Delta = 0.65°$ from the ideal position where $\vec{b}_0$ is parallel to the [000-1] direction (see text for details). Figure taken from [117]

The experimentally determined satellite splittings of the ST(5/2) and ST(3/2) doublets in kHz are plotted over the rotation angle φ in Figure 9.3a. The rotation patterns in both Figure 9.2b and Figure 9.3a are mirrored at a position very close to 90°, with the mirror defining the rotation angle for which $\vec{b}_0$ is situated in the crystallographic *ab* plane. The deviation φ_Δ of the mirror from 90° quantifies the original misalignment of the [000-1] direction to $\vec{b}_0$. From the way the crystal is glued on the goniometer axis, we know that the rotation axis must be in the crystallographic *ab* plane. Also, the above considerations of the effects of crystal symmetry on the tensor structure imply that the eigenvector with the largest eigenvalue ($Q_{33} = \chi$) must point along the three-fold rotation axis, i.e. along the crystallographic *c* axis, which we attempted to align along $\vec{b}_0$ for the starting point of our rotation pattern. For this situation, the polar angle β in Equation 3.14 can be replaced by $\beta \to \varphi - \varphi_\Delta$, and (neglecting quadrupolar contributions to third order) the magnitude of the satellite splittings can be expressed by inserting Equation 3.14 in Equation 3.23 with $\eta_Q = 0$:

$$\Delta\nu^{(1)}(k) = \frac{3\chi\Delta k}{2I(2I-1)} \frac{3\cos^2(\varphi - \varphi_\Delta) - 1}{2} \tag{9.3}$$

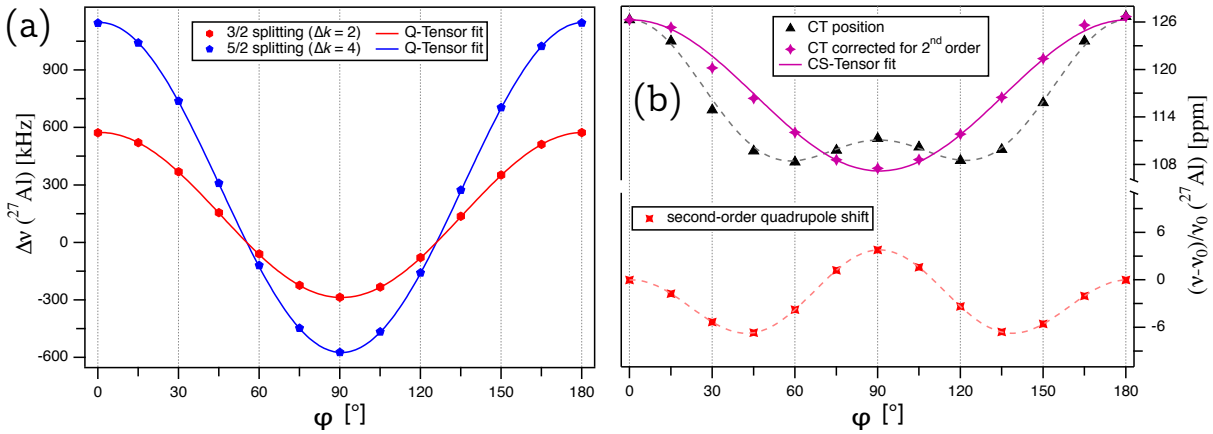

Figure 9.3 – **(a)** Plot of the splittings $\Delta\nu^{(1)}(k) = \nu(+k) - \nu(-k)$ for the ST(3/2) ($\Delta k = 2$; red) and ST(5/2) ($\Delta k = 4$; blue) doublets for ^{27}Al in the unit cell of the AlN single crystal. The lines represent the fit of the quadrupole coupling tensor according to Equation 9.3. **(b)** Plot of the experimentally determined central transition for ^{27}Al ($k = 0$; black), the contribution of the quadrupolar interaction according to Equation 3.15 (red), and the central transition after subtracting the quadrupolar second-order shift from the experimental data points (purple). The solid purple line represents the fit of the chemical shift tensor according to Equation 9.4. Figure taken from [117]

To determine the quadrupole coupling tensor $\mathbf{Q_{Al}}$ of ^{27}Al, the satellite splittings were simultaneously fitted according to Equation (9.3) with $\Delta k = 2$ for the ST(3/2) and $\Delta k = 4$ for the ST(5/2) splittings. The fit converged on a global solution, giving $\chi = (1.914 \pm 0.001)$ MHz and $\varphi_\Delta = (0.65 \pm 0.04)°$. The quadrupolar coupling constant determined from our single-crystal NMR experiments is in perfect agreement with the previously reported value of $\chi = 1.913$ MHz, determined from a static polycrystalline powder sample of AlN.[120] The full $\mathbf{Q_{Al}}$ tensor, with the eigenvalues and corresponding eigenvectors in the PAS frame (Equation 9.1), is summarized in Table 9.1. The quadrupolar asymmetry parameter $\eta_Q = 0$, and the orientation of the eigenvectors are a consequence of the crystal symmetry, with $\vec{q}_{33}$ aligned exactly along the c axis and $\vec{q}_{11}$, $\vec{q}_{22}$ placed in the ab plane.

9.3 ^{27}Al chemical shift tensor

As is detailed in Section 3, to determine the chemical shift tensor $\boldsymbol{\delta}_{Al}$ of ^{27}Al, the contribution of the second-order quadrupolar interaction must be subtracted from the central transition ($k = 0$) line position. In Figure 9.3b, the ^{27}Al CT is plotted over φ, and the data points clearly show the presence of the quadrupolar-induced shift, which according to Equation 3.15, contains harmonic terms depending on both $\cos^4(\beta)$ and $\cos^2(\beta)$. Using the results obtained from evaluating the splittings ($\chi = 1.914$ MHz and $\varphi_\Delta = 0.65°$), this second-order quadrupole shift can be calculated

Table 9.1 – Quadrupole coupling tensor $\mathbf{Q_{Al}}$ (left), and chemical shift tensor $\boldsymbol{\delta}_{Al}$ (right) of ^{27}Al in the wurtzite structure of AlN, as determined from single-crystal NMR experiments. The orientation of the corresponding eigenvectors are listed in spherical coordinates (θ, ϕ) in the hexagonal *abc* crystal frame *CRY*. The errors of the experimental values reflect those delivered by the fitting routine.

NMR-Interaction Tensors of ^{27}Al in Aluminum Nitride			
Q_{11}^{PAS}	-0.957 ± 0.001 MHz	δ_{11}^{PAS}	107.2 ± 0.3 ppm
Q_{22}^{PAS}	-0.957 ± 0.001 MHz	δ_{22}^{PAS}	107.2 ± 0.3 ppm
$Q_{33}^{PAS} = \chi$	1.914 ± 0.001 MHz	δ_{33}^{PAS}	126.3 ± 0.3 ppm
$\vec{q}_{11}$	90°, γ^a	$\vec{d}_{11}$	90°, γ^a
$\vec{q}_{22}$	90°, γ^a + 90°	$\vec{d}_{22}$	90°, γ^a + 90°
$\vec{q}_{33}$	0°, 0°	$\vec{d}_{33}$	0°, 0°
		δ_{iso}	113.6 ± 0.3 ppm
		$\Delta\delta$	12.7 ± 0.6 ppm
η_Q	0	η_{CS}	0

[a] Indeterminate in the *ab* plane because of the cylindrical symmetry of the tensor. This situation also makes it impractical to visualize the tensors by plotting the eigenvectors in the unit cell, as has been done before for similar systems.[21,54,121]

for each crystal orientation according to Equation 3.15 with $\beta = \varphi - \varphi_\Delta, \eta_Q = 0$, and $k = 0$, see red points in Figure 9.3b. After subtracting the quadrupole contribution from the experimental points, the remaining variation in CT line position (Figure 9.3b, purple) is solely caused by the chemical shift tensor, which can be determined from it. Due to the cylindrical symmetry of the tensor and the fact that its *PAS* and *CRY* frame are identical (see Equation 9.2), the exact orientation of the rotation axis in the crystallographic *ab* plane of AlN is indeterminate. For simplicity, the rotation axis can be assumed to be parallel to the *b* axis (which is equal to the example given in Section 4), and the orientation of the magnetic field vector in the *CRY* frame for each rotation angle φ can be expressed by Equation 4.8. Inserting this (and Equation 9.2) into Equation 3.25, we obtain the expression necessary for fitting the data in Figure 9.3b:

$$\frac{\nu_{CS}}{\nu_0}[ppm] = \frac{1}{2}(P + R) + \frac{1}{2}(R - P)\cos[2(\varphi - \varphi_\Delta)] \tag{9.4}$$

For this fit, φ_Δ was kept fixed at the value derived from fitting $\mathbf{Q_{Al}}$, and the components of the chemical shift tensor of ^{27}Al determined thereby are $P = (107.2 \pm 0.3)$ ppm and $R = (126.3 \pm 0.3)$ ppm, with the full tensor listed in Table 9.1. The isotropic chemical shift of $\delta_{iso} = (113.6 \pm 0.3)$ ppm is in good agreement with a previously reported value,[122] which was

determined from a polycrystalline sample of AlN under magic-angle spinning (MAS), and after correcting for the second-order quadrupole shift,[3] comes out to $\delta_{iso} = 114.2$ ppm. The chemical shift asymmetry parameter $\eta_{CS} = 0$ and the orientation of the chemical shift eigenvectors follow the same symmetry restrictions as for the quadrupole coupling tensor described above.

9.4 ^{14}N quadrupole coupling tensor

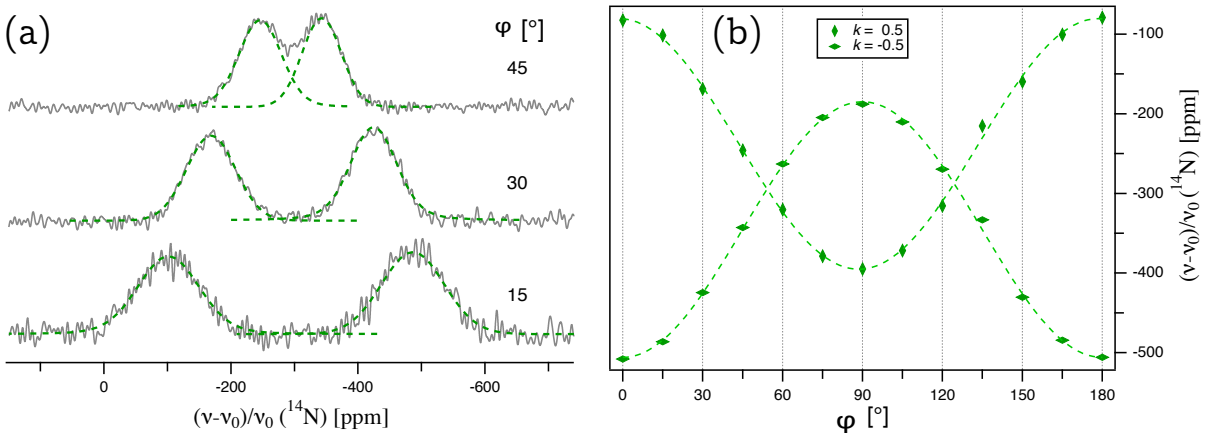

Figure 9.4 – **(a)** ^{14}N NMR spectra of an AlN single crystal, acquired under the same conditions as listed in the caption of Figure 9.2. The green, dashed lines show the deconvolution of each signal with a Voigt profile, the maxima of which give the line positions plotted on the right. **(b)** Full 180° rotation pattern for ^{14}N at Wyckoff position 2*b* in AlN crystal. The point $\varphi = 0$ deviates by $\varphi_\Delta = -0.74°$ from the ideal position where $\vec{b}_0$ is parallel to the [000-1] direction (see text for details). Figure taken from [117]

For the determination of the quadrupole coupling tensor $\mathbf{Q_N}$ and the chemical shift tensor $\boldsymbol{\delta}_N$ of ^{14}N in aluminum nitride, the same AlN crystal (Figure 9.1a) and goniometer axis as for ^{27}Al was used. Since a change of the solenoid coil was necessary to go from the resonance frequency of ^{27}Al to ^{14}N, the offset angle φ_Δ is slightly different and needs to be determined from the data fit again. Representative ^{14}N NMR spectra are depicted in Figure 9.4a, and at first glance, appear to show much broader lines than the ^{27}Al spectra. In fact, with $FWHM \approx 3$ kHz, the resonance lines are only about one third as broad as those of ^{27}Al, since the gyromagnetic ratio of ^{14}N is 3.5 times smaller than that of aluminum, which scales down the homonuclear contribution of the dipolar coupling. The impression of broad lines for ^{14}N is chiefly because the shifts of its $k = \pm 0.5$ resonances caused by the quadrupolar interaction (≈ 300 ppm) are much smaller than those of ^{27}Al (≈ 8000 ppm), since these shifts scale with the quadrupolar moment of the nucleus, which is 20.44 mb for ^{14}N, but 146.6 mb for ^{27}Al.[123] The broad resonance lines

[3] From the reported line position of 113.3 ppm at a 600 MHz spectrometer,[122] the correction of $\nu_{ai}^{(2)} = -(3/500)(\chi^2/\nu_0) \approx -0.9$ ppm needs to be subtracted.

of the ^{14}N spectra, combined with the relatively poor signal-to-noise ratio (due to the long relaxation time of $T_1 = 1080$ s[120]) make it difficult to precisely derive the line positions from the spectra. Therefore, all ^{14}N NMR spectra were deconvoluted, assuming combined Lorentz-Gauss functions (so-called Voigt profiles), to reliably obtain the line positions.

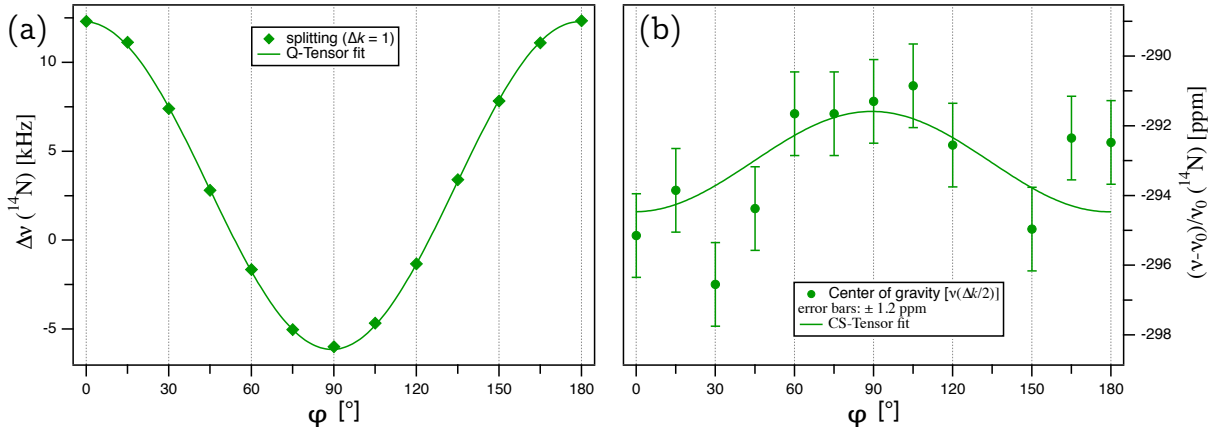

Figure 9.5 – **(a)** Plot of the splittings $\Delta\nu^{(1)}(k) = \nu(+0.5) - \nu(-0.5)$ for ^{14}N from an AlN single crystal. The lines represent the fit of the quadrupole coupling tensor according to Equation 9.3. **(b)** Plot of the center $\nu(\Delta k/2) = [\nu(0.5) + \nu(-0.5)]/2$ for ^{14}N, with the error bars (± 1.2 ppm) taken from the Voigt profile fit for each individual signal. The solid green line represents the fit of the chemical shift tensor according to Equation 9.4. Figure taken from [117]

The splittings of the thus deconvoluted ^{14}N doublets are plotted over the rotation angle φ in Figure 9.5a. The quadrupole coupling tensor was determined by a fit of these splittings according to Equation 9.3 with $\Delta k = 1$, giving the quadrupolar coupling constant $\chi = (8.19 \pm 0.02)$ kHz and an offset angle of $\varphi_\Delta = -(0.74 \pm 0.13)°$. The full quadrupole coupling tensor, with the eigenvalues and corresponding eigenvectors in the PAS frame (Equation 9.1), is summarized in Table 9.2. The quadrupolar asymmetry parameter $\eta_Q = 0$, and the orientation of the eigenvectors are identical to the **Q** tensor of ^{27}Al. So far, only an upper limit of the quadrupolar coupling constant of ^{14}N in AlN was available in the literature, namely $\chi < 10$kHz determined from a polycrystalline powder sample.[120]

9.5 ^{14}N chemical shift tensor

The chemical shift tensor of ^{14}N can be calculated from the evolution of the center of the doublet with $k = \pm 0.5$ over the rotation angle, as plotted in Figure 9.5b. Fitting the data in Figure 9.5b according to Equation 9.4, with the offset angle kept fixed at the value derived from the quadrupole coupling tensor fit ($\varphi_\Delta = -0.74$ ppm), gives $P = -(291.6 \pm 0.7)$ ppm and

Table 9.2 – Quadrupole coupling tensor $\mathbf{Q_N}$ (left), and chemical shift tensor $\boldsymbol{\delta}_N$ (right) of ^{14}N in the wurtzite structure of AlN, as determined from single-crystal NMR experiments. The orientation of the corresponding eigenvectors are listed in spherical coordinates (θ, ϕ) in the hexagonal *abc* crystal frame *CRY*. The errors of the experimental values reflect those delivered by the fitting routine.

NMR-Interaction Tensors of ^{14}N in Aluminum Nitride			
Q_{11}^{PAS}	-4.096 ± 0.009 kHz	δ_{11}^{PAS}	-291.6 ± 0.7 ppm
Q_{22}^{PAS}	-4.096 ± 0.009 kHz	δ_{22}^{PAS}	-291.6 ± 0.7 ppm
$Q_{33}^{PAS} = \chi$	8.192 ± 0.020 kHz	δ_{33}^{PAS}	-294.5 ± 0.6 ppm
$\vec{q}_{11}$	90°, γ^a	$\vec{d}_{11}$	90°, γ^a
$\vec{q}_{22}$	90°, γ^a + 90°	$\vec{d}_{22}$	90°, γ^a + 90°
$\vec{q}_{33}$	0°, 0°	$\vec{d}_{33}$	0°, 0°
		δ_{iso}	-292.6 ± 0.6 ppm
		$\Delta\delta$	-1.9 ± 1.1 ppm
η_Q	0	η_{CS}	0

[a] Indeterminate in the *ab* plane because of the cylindrical symmetry of the tensor.

$R = -(294.5 \pm 0.6)$ ppm, with the full tensor listed in Table 9.2. The data in Figure 9.5b exhibit quite some scatter; however, it has to be kept in mind that for tracing the anisotropy of the ^{14}N chemical shift in aluminum nitride, we are attempting to extract variations of the order of ≈ 90 Hz from resonance lines with $FWHM \approx 3$ kHz. Despite the scatter, about two thirds of all data points belong to the CS tensor fit function within the error margins of ± 1.2 ppm. The resulting isotropic chemical shift $\delta_{iso} = -(292.6 \pm 0.6)$ ppm is in good agreement with the previously reported value of $\delta_{iso} = 64.7$ ppm,[122] determined from a polycrystalline powder sample under MAS and referenced to an aqueous $(NH_4)_2SO_4$ solution, with a 'NH_4^+' solution resonance shifted -355 ppm relative to the 'NO_3^-' solution used here.[124] Similar to the quadrupole coupling tensor, the asymmetry of the CS tensor with $\eta_{CS} = 0$, as well as the eigenvector orientation follow the symmetry restrictions of the crystal lattice.

9.6 ^{14}N and ^{27}Al DFT calculations

It has become customary within the solid-state NMR community to augment experimental results by comparing them to predictions derived from calculations using density functional theory (DFT) methods employing periodic plane waves.[33] To check how the quadrupolar coupling constants for ^{27}Al and ^{14}N derived from our precise single-crystal results compare to DFT predictions, we have performed such calculations for aluminum nitride, using the Castep code,

see Section 9.7 for computational details. Table 9.3 shows the quadrupolar coupling constants χ_{calc} determined by DFT calculations using the coordinates from X-ray diffraction data reported in the inorganic crystal structure database (ICSD) for a selection of different database entries. The variation of these entries concerns mostly the unit cell dimensions (see also below about geometry optimization), which is reflected in the varying unit cell volumes V_{cell} listed in the table. On the left of Table 9.3, the calculation results are given from directly using the ICSD coordinates, the so-called single-point energy (SPE). We note that for this calculation mode, the DFT algorithm returns χ_{calc} values within a wide scatter, mirrored by standard deviations of 37% for ^{27}Al and 73% for ^{14}N. Whereas a single structure might accidentally give numbers for χ_{calc} that are practically identical to the experiment, as structure ICSD 34475 does here for AlN, a more systematic exploration would demand to take the arithmetic mean of the eight different structures. These mean values, $\chi_{\mathrm{calc}}(^{27}\mathrm{Al}) = 3.288$ MHz and $\chi_{\mathrm{calc}}(^{14}\mathrm{N}) = -26.4$ kHz are very far from the experimentally determined values of $\chi(^{27}\mathrm{Al}) = (1.914 \pm 0.001)$ MHz and $\chi(^{14}\mathrm{N}) = (8.19 \pm 0.02)$ kHz, with the absolute sign of χ not being available from the experiments.

Table 9.3 – Quadrupolar coupling constant χ_{calc} for ^{27}Al and ^{14}N in aluminum nitride, as determined from DFT calculations with the Castep code. Calculations were run using the atomic coordinates of the reported crystal structures directly (single-point energy—SPE), and after geometry optimization (GO) of the unit cell.

ICSD	**Ref.**	V_{cell}	χ_{calc} **from SPE**		χ_{calc} **from GO**	
		[Å^3]	^{27}Al [MHz]	^{14}N [kHz]	^{27}Al [MHz]	^{14}N [kHz]
34475	[118]	41.714	1.984	−8.0	1.791	−16.0
34236	[125]	41.724	4.478	43.0	1.791	−22.0
54697	[126]	41.774	4.023	34.0	1.791	−20.0
183638	[127]	41.919	1.836	−12.0	1.795	−16.0
257810	[128]	41.738	3.007	9.0	1.788	−23.0
230434	[129]	41.684	2.101	−12.0	1.788	−24.0
602459	[130]	41.689	4.967	60.0	1.795	−16.0
602460	[130]	41.747	3.910	33.0	1.791	−19.0
$\bar{X}$			3.288	−26.4[a]	1.791	−19.5
σ			1.222 (37%)	19.1 (73%)	0.003 (0.1%)	3.3 (17%)

[a] To form the mean, the signs of all individual values were assumed to be negative.

It is however well documented in the literature that in order to obtain good agreement between DFT and experimental results, a geometry optimization (GO) of the crystal structure is usually necessary.[131–133] This was also done for AlN, taking the coordinates of the previously

used ICSD database entries as a starting point. It should be noted that for AlN, only the unit cell parameters a, b, c may be geometry optimized, since both aluminum and nitrogen atoms are situated on a crystallographic special position, Wyckoff position 2*b*. As may be seen from the entries on the right in Table 9.3, the χ_{calc} values are practically independent from the starting point after energy optimization, with a mean of $\overline{\chi}_{\mathrm{calc}}(^{27}\mathrm{Al}) = 1.7913$ MHz and $\overline{\chi}_{\mathrm{calc}}(^{14}\mathrm{N}) = -19.5$ kHz. This leads to small standard deviations (0.1% for ^{27}Al and 17% for ^{14}N), which seem to imply a high accuracy of the DFT results. However, the small standard deviations of the GO calculations reflect only on a high precision of the computational algorithm. The accuracy of calculation results is defined by comparison to the experiment,[134] and is therefore quite low, since both experimental values (especially that of ^{14}N) are outside the standard deviation of the high-precision $\overline{\chi}_{\mathrm{calc}}$ values.

9.7 Experimental details

The single crystal of aluminum nitride shown in Figure 9.1a was grown at IKZ, using physical vapor transport of bulk AlN in a TaC crucible with radio frequency induction heating. Further details may be found in Reference.[24]

Single-crystal NMR spectra were acquired on a Bruker Avance-III 400 spectrometer at MPI-FKF Stuttgart, at a Larmor frequency of $\nu_0(^{27}\mathrm{Al}) = 104.263$ MHz, and $\nu_0(^{14}\mathrm{N}) = 28.905$ MHz, using a goniometer probe with a 6 mm solenoid coil, built by NMR Service GmbH (Erfurt, Germany). The ^{27}Al spectra were recorded with single-pulse acquisition, four scans and a relaxation delay of 20 s. For the ^{14}N spectra a spin–echo sequence[74] was employed to minimize baseline roll and the spectra were recorded with 16 scans and a relaxation delay of 300 s. All spectra were referenced to a dilute $Al(NO_3)_3$ solution at 0 ppm. The fit of the rotation pattern and deconvolution of the ^{14}N spectra were performed with the program Igor Pro 7 from WaveMetrics Inc..

All calculations were run with the Castep density functional theory (DFT) code[135] integrated within the Biovia Materials Studio 2017 suite, using the Gipaw algorithm.[136] The computations use the generalized gradient approximation (GCA) and Perdew–Burke–Ernzerhof (PBE) functional,[137] with the core-valence interactions described by ultra-soft pseudopotentials.[136] Integrations over the Brillouin zone were done using a Monkhorst–Pack grid[138] of $16 \times 16 \times 8$, with a reciprocal spacing of at least 0.025 Å^{-1}. The convergence of the calculated NMR parameters was tested for both the size of a Monkhorst–Pack k-grid and a basis set cut-off energy, with the cut-off energy being 1500 eV. Also, the possible contribution of pairwise disper-

sion interactions was checked by using the Tkatchenko–Scheffler method[139] as implemented in Castep, but no improvements were observed. The calculation results reported here therefore do not include dispersion interaction.

Geometry optimization (GO) calculations were performed using the Broyden–Fletcher-Goldfarb–Shanno (BFGS) algorithm,[140] with the same functional, k-grid spacings and cut-off energies as in the single-point energy (SPE) calculations. Convergence tolerance parameters for geometry optimization were as follows: maximum energy 2.0×10^{-5} eV/atom, maximum force 0.001 eV/Å, maximum stress 0.01 GPa/atom, and maximum displacement in a step 0.002 Å. Crystallographic data used in the calculations were taken from literature listed in Table 9.3.

10 No Symmetry Relation: Unknown Morphology

10.1 Introduction: Wulfenite ($PbMoO_4$)

As is detailed in Section 9, one way to overcome the lack of symmetry-linked magnetically inequivalent crystallographic positions for NMR interaction-tensor determination, can be to investigate a system with well known crystal morphology. For such a single crystals with well defined crystal faces, the chosen rotation axis may be known from optical alignment of the crystal prior to the NMR measurements.[117] Obviously, this method is error prone and restricted to a few selected systems where crystal growth under controlled conditions is well established. In Section 10, a general approach for the determination of the NMR tensors and crystal orientation is presented, which is widely applicable for systems without symmetry linked atoms. Exemplary, we show the full chemical shift tensor determination of ^{207}Pb in the natural mineral wulfenite, $PbMoO_4$ (see Figure 10.1a), which is taken from Zeman et al. 2019 published in *Solid State Nuclear Magnetic Resonance* (Elsevier),[22] and adapted for this thesis.

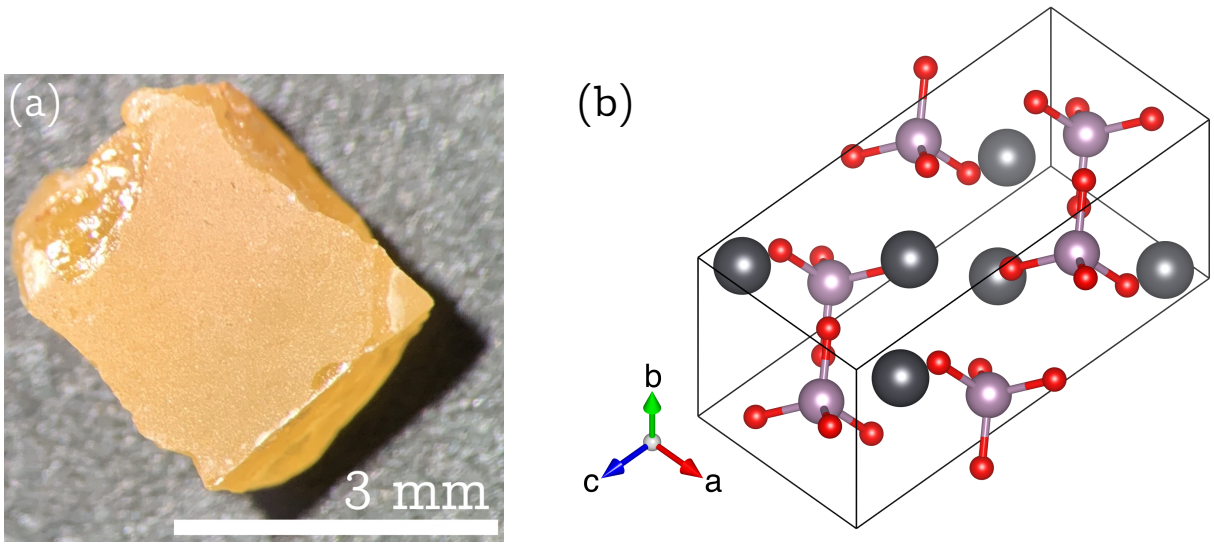

Figure 10.1 – **(a)** Single crystal of wulfenite, $PbMoO_4$, from Bleiberg, Carinthia/Austria (inventory no. 52435). **(b)** Unit cell of wulfenite, space group $I4_1/a$ (No. 88), according to literature.[91] The lead atoms (grey) at Wyckoff position $4a$, situated on four-fold screw axes parallel to the c axis, are coordinated by eight oxygen atoms (red). The molybdenum atoms (purple) are tetrahedrally coordinated by oxygen. Figure taken from [22] Drawing generated with the Vesta program.[68]

Wulfenite crystallises in tetragonal space group $I4_1/a$ (No. 88), with the lead atoms occupying Wyckoff position $4a$, which generates only one magnetically inequivalent ^{207}Pb, see also Figure 10.1b.[91] As is detailed in Section 4, the single ^{207}Pb resonance leaves one with a

system of equations that is underdetermined, no matter how many rotation patterns we would record. The solution to this quandary, which we demonstrate in this Section, is to measure the compound with low symmetry and/or Wyckoff multiplicity (here: wulfenite) simultaneously with a compound with high symmetry and Wyckoff multiplicity (here: phosgenite, see Section 6), around two different rotation axes. The straightforward analysis of the phosgenite data supplies us with the relative orientation of the two axes. The knowledge of this orientation difference can be carried over to the wulfenite system, supplying an additional fit constraint, which turns out to be sufficient for a successful determination of the ^{207}Pb CS tensor in the wulfenite structure. The approach presented herein for determination of the full chemical shift tensor in compounds with arbitrary crystal lattice symmetry and Wyckoff multiplicity is, of course, not limited to ^{207}Pb NMR, but may be applied to any nucleus with spin $I = 1/2$. It can also easily be adapted to determine the quadrupole coupling tensor $\mathbf{Q}$ for nuclei with spin $I > 1/2$, thus expanding the capabilities of the "minimal rotation method".

10.2 ^{207}Pb NMR of Wulfenite: Single crystal

As already outlined in the Introduction, the crystal structure of wulfenite, $PbMoO_4$, does not provide more than one magnetically inequivalent ^{207}Pb. The four lead atoms in the tetragonal unit cell occupy Wyckoff position $4a$,[91] and may be viewed as being generated by a series of inversion operations, to which NMR is invariant. All ^{207}Pb atoms in the unit cell are positioned on four-fold screw axes parallel to the crystallographic c axis, which causes the ^{207}Pb chemical shift tensor to be uniaxial ($\eta_{CS} = 0$), and the off-diagonal elements to be zero, so that the CRY frame is the principal axis system of the tensor, $\boldsymbol{\delta}^{\boldsymbol{CRY}} = \boldsymbol{\delta}^{\boldsymbol{PAS}}$. Therefore, the CS tensor of wulfenite is described by only two independent tensor components T and U, making it the simplest possible non-isotropic tensor (just as is the case for the CS tensors in hexagonal AlN; see Section 9):

$$\boldsymbol{\delta}_{\boldsymbol{Pb}}^{\boldsymbol{CRY}} = \boldsymbol{\delta}_{\boldsymbol{Pb}}^{\boldsymbol{PAS}} = \begin{pmatrix} T & 0 & 0 \\ 0 & T & 0 \\ 0 & 0 & U \end{pmatrix} \tag{10.1}$$

Accordingly, compared to phosgenite (Section 6 Equation 6.3), the expression describing the resonance position is significantly simplified:[4]

$$\begin{aligned}\nu^{Pb}(\varphi)/\nu_0 &= \vec{b}_0^T(\varphi) \cdot \boldsymbol{\delta}_{\boldsymbol{Pb}}^{\boldsymbol{CRY}} \cdot \vec{b}_0(\varphi) \\ &= 2Tb_x^2 + Ub_z^2\end{aligned} \tag{10.2}$$

To extract the ^{207}Pb CS tensor for wulfenite from one rotation pattern using Equation 10.2, five linear independent parameters are required: tensor components T and U, and axis parameters θ, ϕ and φ_Δ. Yet, any rotation pattern of wulfenite will only supply a single harmonic function with the three linear independent parameters A, B, and C according to Equation 4.1. The seemingly obvious solution to this problem, i.e. acquisition of an additional rotation pattern with a different rotation axis $\vec{g}_2$, does not work here (such a solution for tensor determination is detailed in Section 8). Although this would supply a new harmonic function with parameters A_2, B_2, and C_2, also three new fit parameters θ_2, ϕ_2 and $\varphi_{\Delta 2}$ are added, in effect making acquisition of additional rotation patterns a zero-sum game.

One possible way out of this quandary is to acquire two rotation patterns of wulfenite, while simultaneously measuring a single crystal of phosgenite. Evaluation of the phosgenite data then provides independent information about the two (randomly chosen) rotation axes, and thereby reduces the amount of fit variables. To this end, a single crystal of wulfenite (approximate size 1.5×5×3 mm^3) and a single crystal of phosgenite (approximate size 2.5×3×2 mm^3) were glued an a 5 mm × 5 mm teflon support with dual-component adhesive, as depicted in Figure 10.2. This allowed the reorientation of the effective rotation axis from $\vec{g}_1$ to $\vec{g}_2$, without changing the relative orientation of both crystals. ^{207}Pb-NMR spectra resulting from this setup are shown in Figure 10.3, where

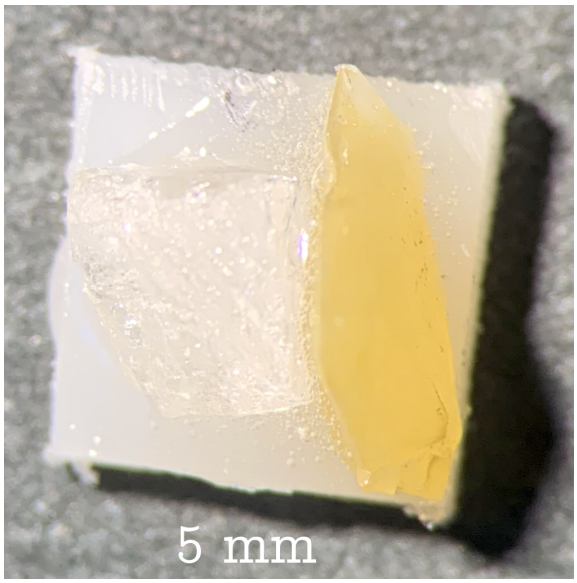

Figure 10.2 – Single crystal of wulfenite, $PbMoO_4$, (yellow) and phosgenite, $Pb_2Cl_2CO_3$, (translucent) glued together on a teflon support with dimensions 5 mm × 5 mm using dual-component adhesive.

[4] It should be noted that the strong reduction of independent tensor elements by the crystal symmetries in our test system wulfenite is a coincidence – the general strategy of tensor determination outlined here does not depend on it.

the four equally intense ^{207}Pb signals of phosgenite can be clearly distinguished from the single, narrow wulfenite signal with much higher intensity. Using the known CS tensor of phosgenite listed in Section 6, Table 6.1, the only free parameters in the data fit were θ, ϕ and φ_Δ for both $\vec{g}_1(p)$ and $\vec{g}_2(p)$ in the CRY frame of the phosgenite structure. These could precisely be determined from fitting the rotation patterns in Figure 10.3 to:

$$\begin{aligned}
\vec{g}_1(p): &\quad \theta_1 = (17.5 \pm 0.1)^\circ \quad \phi_1 = (36.0 \pm 0.1)^\circ \quad \varphi_{\Delta 1} = (30.4 \pm 0.1)^\circ \\
\vec{g}_2(p): &\quad \theta_2 = (96.9 \pm 0.1)^\circ \quad \phi_2 = (120.1 \pm 0.1)^\circ \quad \varphi_{\Delta 2} = (153.8 \pm 0.1)^\circ \\
\Delta\vec{g}(p): &\quad \Delta\theta = (79.4 \pm 0.2)^\circ \quad \Delta\phi = (84.1 \pm 0.2)^\circ \quad \Delta\varphi_\Delta = (123.4 \pm 0.2)^\circ
\end{aligned} \tag{10.3}$$

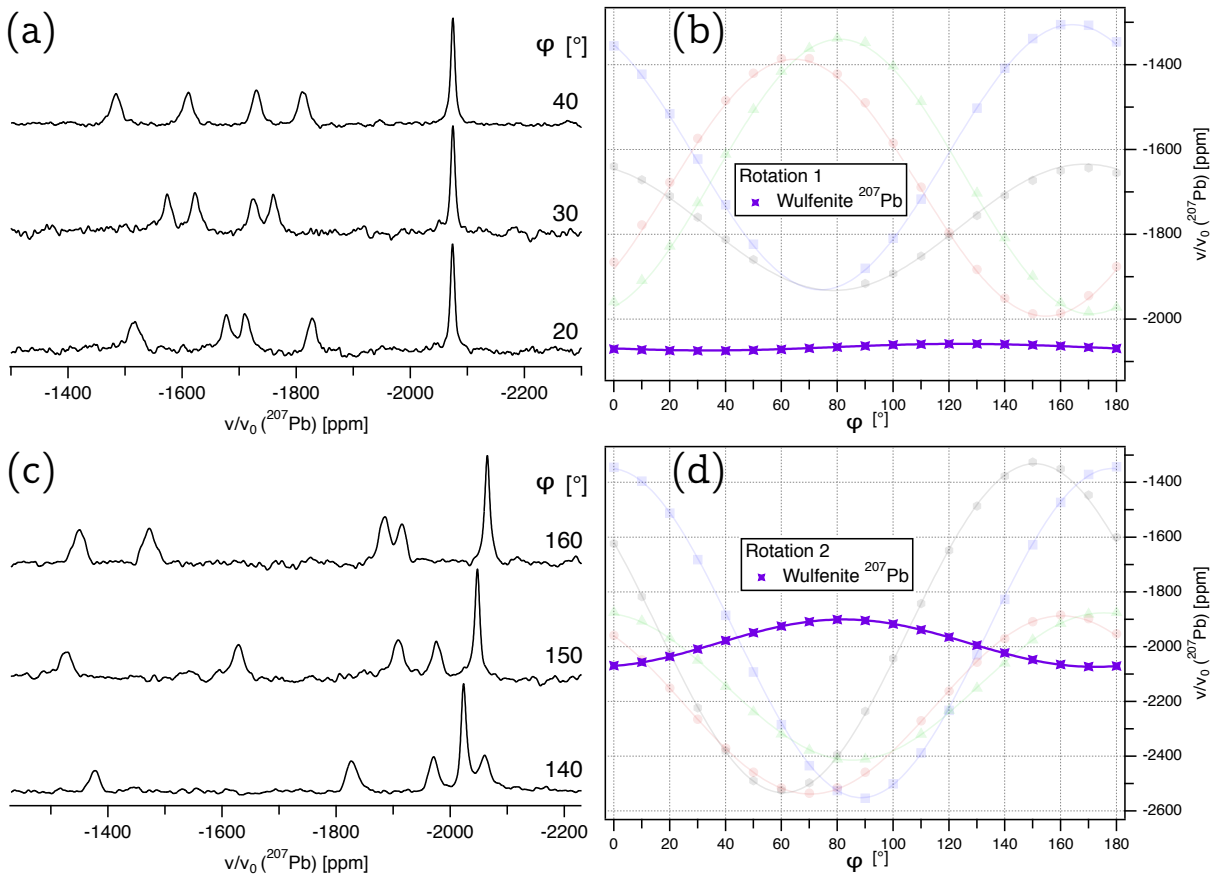

Figure 10.3 – ^{207}Pb NMR spectra of single crystals of wulfenite, $PbMoO_4$, and phosgenite, $Pb_2Cl_2CO_3$, glued together on a teflon support and rotated counter-clockwise around the axis **(a)** $\vec{g}_1$ and **(c)** $\vec{g}_2$. The strong signal belongs to wulfenite, while the four equally intense signals are those of the phosgenite single crystal. Full rotation pattern over 180° for ^{207}Pb at Wyckoff position $4a$ in the wulfenite structure (purple), acquired by rotating the crystals step-wise by 10° around **(b)** $\vec{g}_1$ and **(d)** $\vec{g}_2$. The attenuated background shows the full rotation pattern of the simultaneously measured ^{207}Pb in phosgenite. Figure taken from [22]

The two rotation measurements on the two glued crystals are hence linked by the known difference of goniometer axis orientation $\Delta\vec{g}(p) = \vec{g}_2(p) - \vec{g}_1(p)$ and offset angles $\Delta\varphi_\Delta$. While we do not know anything yet about the absolute orientation of the two goniometer axes $\vec{g}_1(w)$ and $\vec{g}_2(w)$ in the unit cell of wulfenite, we do know that the *difference* must be the same as for phosgenite, $\Delta\vec{g}(w) = \Delta\vec{g}(p)$. Therefore, the motion of the field vector $\vec{b}_0$ in the CRY frame of wulfenite of the second rotation pattern (Figure 10.3d) can be related back to the first rotation pattern (Figure 10.3b) by $\theta_2 = \theta_1 + \Delta\theta$, $\phi_2 = \phi_1 + \Delta\phi$, and $\varphi_{\Delta 2} = \varphi_{\Delta 1} + \Delta\varphi_\Delta$. This reduces the amount of free fit parameters from eight to exactly the five that are needed to define the system. Therefore, it is now possible to simultaneously fit the two rotation patterns according to Equation 10.2 with the motion of the magnetic field vector described by Equation 4.7 and Equation 4.10, and to obtain both $\boldsymbol{\delta}_{\boldsymbol{Pb}}^{\boldsymbol{CRY}}$ and $\vec{g}_1(w)$, $\vec{g}_2(w)$. The fit converged on a global solution, giving the CS tensor elements to $T = (-2074 \pm 1)$ ppm and $U = (-1898 \pm 1)$ ppm, plus the orientations of the two goniometer axes (the errors reflect the fit residuals and the uncertainties in $\Delta\vec{g}(p)$ determined from the phosgenite rotation patterns):

$$\begin{aligned} \vec{g}_1(w): &\quad \theta_1 = (17.3 \pm 0.2)^\circ \quad \phi_1 = (153.5 \pm 0.7)^\circ \quad \varphi_{\Delta 1} = (59.2 \pm 0.4)^\circ \\ \vec{g}_2(w): &\quad \theta_2 = (96.7 \pm 0.4)^\circ \quad \phi_2 = (237.6 \pm 0.9)^\circ \quad \varphi_{\Delta 2} = (2.6 \pm 0.6)^\circ \end{aligned} \tag{10.4}$$

It may be noted that the error margins on the orientations of the goniometer axes are much smaller for the phosgenite system than for the wulfenite. We attribute this to the fact that the free fit parameters for phosgenite are heavily overdetermined (especially with the tensor components fixed), whereas for wulfenite, the number of free parameters exactly matches the data supplied by the experiment, as explained above. These small errors further illustrate the suitability of the phosgenite system for determination of goniometer axes orientation.[5]

The CS tensor of wulfenite is also listed in Table 10.1. In contrast to phosgenite, we find the anisotropy of $\boldsymbol{\delta}^{\boldsymbol{PAS}}$ in the wulfenite structure to be small ($\Delta\delta = 117\,\text{ppm}$), which indicates that the electron lone pair at the lead atoms has predominantly s-character.[71] The asymmetry parameter $\eta_{CS} = 0$, and the orientation of the eigenvectors are a consequence of the crystal symmetry, with $\vec{d}_{33}$ aligning exactly along the c axis and $\vec{d}_{11}$, $\vec{d}_{22}$ placed in the ab plane. The tensor parameters agree reasonably well with those previously reported from static powder spectra of polycrystalline wulfenite: $\delta_{11}^{PAS} = \delta_{22}^{PAS} = -2067\,\text{ppm}$, $\delta_{33}^{PAS} = -1880\,\text{ppm}$, and $\Delta\delta = 123\,\text{ppm}$.[6]

[5] Samples of single-crystalline phosgenite suitable for aiding in tensor determination through single-crystal NMR spectroscopy may be available from Bräuniger T. and Zeman O.E.O. at LMU Munich.

Table 10.1 – Chemical shift tensor of ^{207}Pb in wulfenite, $PbMoO_4$. Left: Determined from single-crystal NMR experiments about two rotation axes at room temperature. The orientation of the corresponding eigenvectors is listed in spherical coordinates (θ, ϕ) in the tetragonal *abc* crystal system CRY. Error values are derived from the fit residuals and uncertainties in $\Delta\vec{g}$ determined from the phosgenite rotation patterns (Equation 10.3). Right: Determined from a static polycrystalline powder sample at room temperature. Error values of tensor components are derived from a Simpson [64] simulation.

	Single-Crystal NMR	**Polycrystalline-Powder NMR**
δ_{11}^{PAS}	(-2074 ± 1) ppm	(-2079 ± 5) ppm
δ_{22}^{PAS}	(-2074 ± 1) ppm	(-2079 ± 5) ppm
δ_{33}^{PAS}	(-1898 ± 1) ppm	(-1887 ± 10) ppm
$\vec{d}_{11}$	90.0°, β [a]	
$\vec{d}_{22}$	90.0°, $\beta + 90.0°$ [a]	
$\vec{d}_{33}$	0.0°, 0.0°	
$\Delta\delta$	(117 ± 3) ppm	(128 ± 20) ppm
η_{CS}	0	0
δ_{iso}		(-2015 ± 10) ppm
	(-2015 ± 1) ppm	(-2015 ± 2) ppm [b]

[a] Indeterminate in the *ab* plane because of the cylindrical symmetry of the tensor.
[b] Taken from shift extrapolation over squared MAS frequencies, see Figure 10.4b.

10.3 ^{207}Pb NMR of Wulfenite: Polycrystalline

To compare the isotropic chemical shift calculated from the single-crystal NMR experiments ($\delta_{iso} = -2015$ ppm) to MAS experiments, NMR spectra of a polycrystalline sample of crushed wulfenite were acquired at spinning speeds from 10 kHz to 22.5 kHz. The ^{207}Pb chemical shift of wulfenite is known to exhibit a significant change with increasing temperature. [28] Accordingly, the ^{207}Pb MAS NMR spectra at 22.5 kHz spinning speed (Figure 10.4a) shows the isotropic band at -2006.6 ppm, while the extrapolation of the squared spinning frequency to zero spinning shown in Figure 10.4b results in an isotropic shift of $\delta_{iso} = -2015$ ppm, in perfect agreement with the single-crystal NMR values. The absence of a noticeable rotational sideband pattern (due to the small anisotropy of the ^{207}Pb CS tensor) precludes CS tensor eigenvalue determination using a Herzfeld–Berger analysis. [7] Instead, the eigenvalues were estimated from a static ^{207}Pb spectra of polycrystalline wulfenite, shown in Figure 10.4c. To this end, the recorded spectra was compared to various spectra calculated with the Simpson package. [64] The best agreement between the experimental and computed spectra was found using the eigenvalues given in Table 10.1(right).

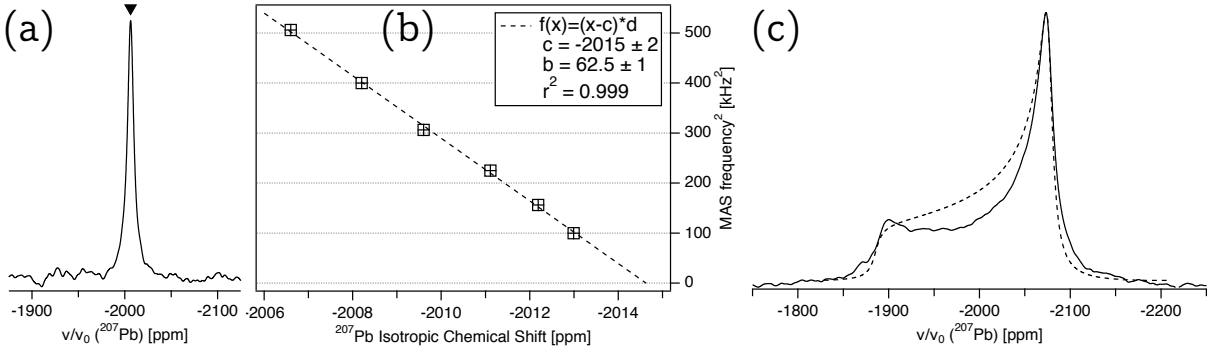

Figure 10.4 – **(a)** ^{207}Pb magic-angle spinning NMR spectrum of polycrystalline wulfenite, acquired in a magnetic field of $\vec{B}_0 = 11.7\,\mathrm{T}$ at 22.5 kHz spinning frequency, with the isotropic band indicated at -2006.6 ppm. **(b)** ^{207}Pb isotropic chemical shift of wulfenite versus squared MAS frequency, with the linear fit given by the dashed line. An extrapolation to zero spinning results in an isotropic chemical shift of -2015 ± 2 ppm. **(c)** ^{207}Pb static powder spectrum of wulfenite, acquired in a magnetic field of $\vec{B}_0 = 11.7\,\mathrm{T}$. The dashed line was calculated with the Simpson package[64], using the chemical shift values listed in Table 10.1(right). Figure taken from [22]

While these eigenvalues are very similar to those derived from single-crystal NMR, their error margins are much larger, confirming again that NMR of single crystals is the "gold standard" [141] for tensor determination.

10.4 Experimental details

For the experimental details on ^{207}Pb NMR of wulfenite, $PbMoO_4$, see Section 6.4.

11 Losing Resolution: Overcoming Broad Signals

11.1 Introduction: LDP (LiH_2PO_4)

Broad single-crystal resonance lines, which may result from dynamics, disorder and/or strong dipolar couplings in the crystal lattice, can significantly increase the effort necessary for NMR-tensor determination. As long as only minor overlap of resonances in one single-crystal spectra appear, the broad signals can be deconvoluted, assuming combined Lorentz-Gauss functions (so-called Voigt profiles), to reliably obtain the line positions. There is therefore no need to collect additional data, as is shown in Section 9.4. When many, significantly broadened, resonance frequencies overlap in most single-crystal spectra for one rotation pattern, more than just the minimum amount of rotation pattern necessary for precise tensor determination have to be recorded.

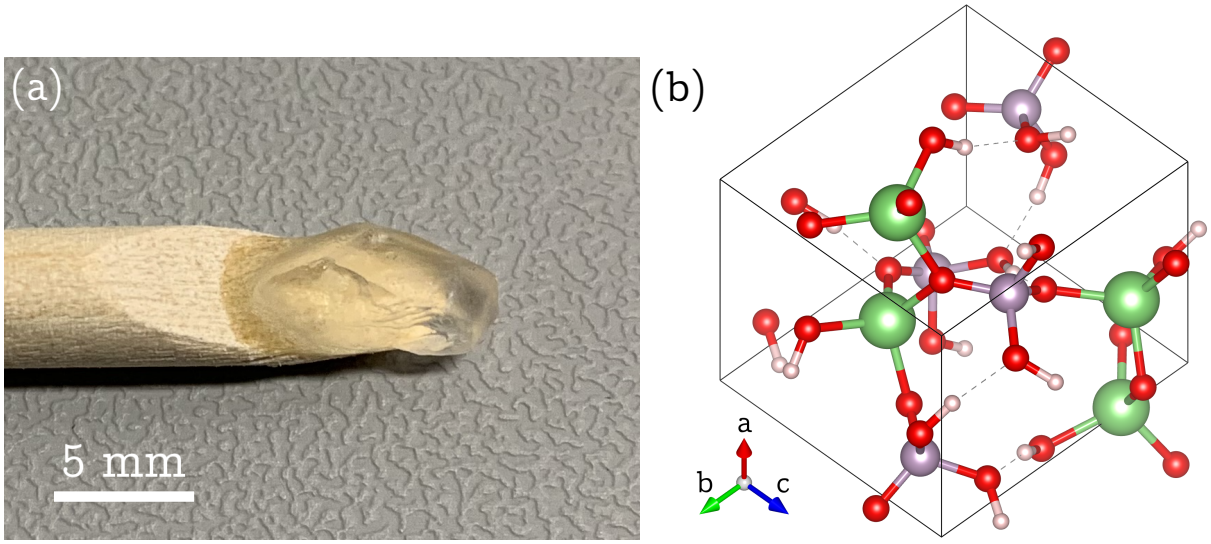

Figure 11.1 – **(a)** LiH_2PO_4 (LDP) single crystal, synthesised according to literature[147] and fixed on a wooden rotation axis using dual-component adhesive. **(b)** Orthorhombic structure of LDP (space group $Pna2_1$, No. 33), according to Reference,[146] with the chosen view down the crystallographic [111] direction. All atoms in the unit cell are located at Wyckoff position 4*a*, with the lithium atoms (green) and the phosphorus atoms (purple) both tetrahedrally coordinated by oxygen (red). The hydrogen atoms (ivory) stabilize the crystal structure by forming hydrogen bonds (dotted lines) between the PO_4 and LiO_4 tetrahedra.Figure taken from [142] Drawing generated with the Vesta program.[68]

In Section 11, we will demonstrate such a case, were strong dipolar interaction lead to sever line broadening, which can be dealt with by acquiring additional rotation pattern. Thereby the full chemical shift tensor of ^{31}P and the quadrupole coupling tensor of ^{7}Li in lithium dihydrogen phosphate (LDP), LiH_2PO_4, is precisely determined, which is taken from Zeman et al. 2020

published in *Crystals* (MDPI),[142] and adapted for this thesis. LDP exhibits a conductivity of the order of $10^{-4}\Omega^{-1}\text{cm}^{-1}$, which is exceptionally high for a solid at room temperature. This conductivity is predominantly attributed to fast proton movements in the crystal lattice of LDP.[143] This, and the fact that LDP is widely available, makes it a promising material for fuel cell or rechargeable battery applications and hence precise structural and electronic characterization of this material is of great interest. Recently, the mechanism of the protonic conductivity of LDP has been investigated by ^{1}H NMR spectroscopy of powder samples under magic-angle spinning (MAS).[144,145] However, not much attention has been paid to the electronic surroundings of the phosphorus and lithium atoms, which despite their light mass have been found to be quite immobile in the crystal structure at room temperature.[146] Since relatively large single crystals of LDP with several mm in diameter can be grown from aqueous solution,[147] a good method to analyze the local surroundings of these nuclei is NMR of single crystals.

LiH_2PO_4 crystallizes in orthorhombic space group $Pna2_1$ (No. 33), depicted in Figure 11.1b, with four formula units per unit cell.[146] The PO_4 tetrahedra build a three-dimensional framework connected by two different types of hydrogen bonds. The LiO_4 coordination tetrahedra are linked by their vertices forming [100] isolated chains and share each edge with the PO_4 units. All atoms in the unit cell are located at Wyckoff position $4a$ with the general site symmetry $1 - C_1$.[147] As a result, no symmetry constraints affect the algebraic form of the NMR interaction tensors, as detailed below and shown in Equation 11.2 and 11.5.

11.2 ^{31}P NMR of LDP

In the orthorhombic unit cell of LDP, the four phosphorus (and lithium) atoms at Wyckoff position $4a$ are related by a two-fold rotation axis parallel to the crystallographic c axis and two glides parallel to the ac, and bc plane. Since NMR is invariant to translational elements and inversions, one can trace four ^{31}P atoms in the single-crystal spectra (see Figure 11.1c), which are related by 180° rotations about the three crystallographic abc axes, starting from the atom closest to the unit cell origin, P(1):

$$\begin{array}{ccccc} \underset{(\bar{x},\bar{y},z+\frac{1}{2})}{\text{P(2)}} & \xleftrightarrow{180^\circ(c)} & \underset{(x,y,z)}{\text{P(1)}} & \xleftrightarrow{180^\circ(b)} & \underset{(x+\frac{1}{2},\bar{y}+\frac{1}{2},z)}{\text{P(3)}} \\ & & \Big\updownarrow{\scriptstyle 180^\circ(a)} & & \\ & & \underset{(\bar{x}+\frac{1}{2},y+\frac{1}{2},z+\frac{1}{2})}{\text{P(4)}} & & \end{array} \tag{11.1}$$

Their respective CS tensors in the orthorhombic CRY frame are therefore described by six independent tensor components which differ only by sign for each ^{31}P position:

$$\boldsymbol{\delta}^{CRY}_{P(1)} = \begin{pmatrix} P & R & S \\ R & T & U \\ S & U & V \end{pmatrix} \qquad \boldsymbol{\delta}^{CRY}_{P(2)} = \begin{pmatrix} P & R & -S \\ R & T & -U \\ -S & -U & V \end{pmatrix}$$
$$\boldsymbol{\delta}^{CRY}_{P(3)} = \begin{pmatrix} P & -R & S \\ -R & T & -U \\ S & -U & V \end{pmatrix} \qquad \boldsymbol{\delta}^{CRY}_{P(4)} = \begin{pmatrix} P & -R & -S \\ -R & T & U \\ -S & U & V \end{pmatrix} \tag{11.2}$$

To quantitatively determine these chemical shift tensors, a single crystal of LDP with approximate dimensions of $9 \times 5 \times 4$ mm^3 grown from solution (see Section 11.4) was fixed on a wooden rotation axis as depicted in Figure 11.1a. In the goniometer setup, this rotation axis is oriented perpendicular to the external magnetic field $\vec{B}_0$ (following the procedure described in Section 4), and ^{31}P-NMR spectra of the LDP crystal were recorded in steps of 10°, some of which are shown in Figure 11.2a. The full rotation pattern over a 180° interval is depicted in Figure 11.2b. As already detailed in Section 4 and experimentally shown in Section 6, the four harmonics in the ^{31}P rotation pattern result in $4 \times 3 - 3 = 9$ linear independent parameters which may be extracted from fitting the data of one rotation pattern. The chemical shift tensor we want to obtain possesses six independent components according to Equation 11.2. Adding the two angles θ_g and ϕ_g defining the orientation of the rotation axis in the CRY frame, and the offset angle φ_Δ, a total of nine fit parameters need to be extracted from the NMR data. Thus, in principle, one rotation pattern (such as the one shown in Figure 11.2b) encapsulates sufficient information to determine the ^{31}P CS tensor in LDP, together with the orientation of the rotation axis and the offset angle.

However, as may be seen in the single-crystal spectra depicted in Figure 11.2a, their resolution is comparatively poor. All resonance lines are extremely broad, with a full width at half-maximum $FWHM \approx 20$ppm ≈ 4 kHz, leading to extensive overlap in many spectra. We attribute this line broadening to the strong homo- and heteronuclear dipolar interactions between phosphorus and lithium atoms in the structure. For $NH_4H_2PO_4$, a ^{31}P–^{31}P dipolar coupling constant of 270 Hz was shown to lead to an observed maximum line broadening in the ^{31}P single-crystal spectra of $FWHM \approx 1.6$ kHz.[148] The dipolar coupling constants in LDP, calculated from the atomic distances, are 200 Hz (average of the four closest ^{31}P), and −630 Hz (average of the four closest ^{7}Li), which means that the ratio of the largest coupling constants and the $FWHM$'s in $NH_4H_2PO_4$ and LiH_2PO_4 are very similar. Thus, with high certainty, dipolar

broadening can be identified as the only factor for the observed line broadening. While additional broadening mechanisms such as orientational disorder or lattice defects cannot be ruled out completely, their extent must be small, in accordance with the findings of a neutron diffraction study.[146]

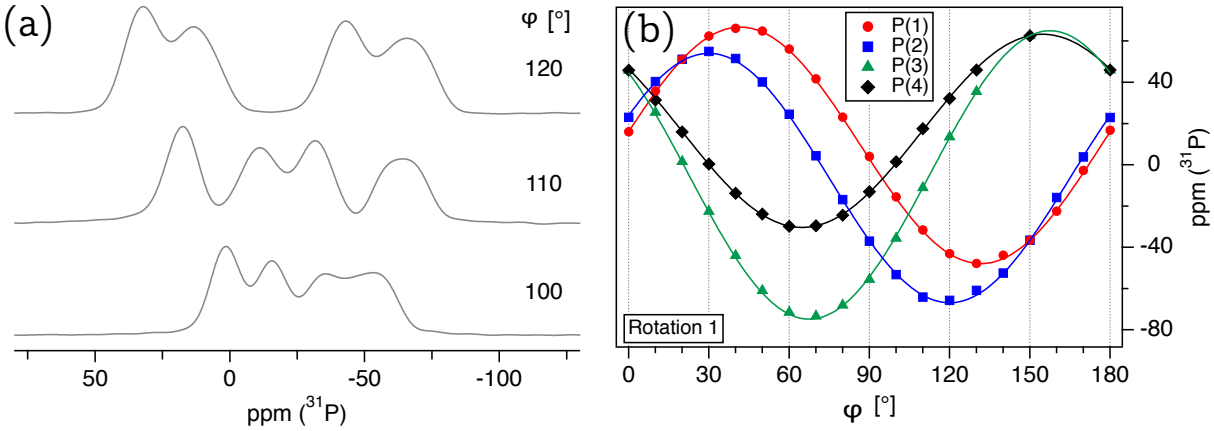

Figure 11.2 – **(a)** ^{31}P NMR spectra of the LDP single crystal, with the indicated rotation angles φ referring to the full rotation pattern on the right. **(b)** Full rotation pattern over 180° for the four magnetically inequivalent ^{31}P at Wyckoff position 4*a*, acquired by rotating the LDP crystal counter-clockwise by 10° around the goniometer axis $\vec{g}_1$. The lines represent the fit of the experimental points to the CS tensor elements and axis orientation (see text for details). Figure taken from [142]

The variation of the ^{31}P chemical shift in LDP we are attempting to extract from resonance lines with $FWHM \approx 20$ ppm is of the order of ≈ 140 ppm. Consequently, precise localization of the four resonance positions in each spectrum of the rotation pattern is challenging and error-prone. To increase the accuracy for the determined tensors (especially of the quadrupole coupling tensor of ^{7}Li, as will be discussed below in Section 11.3), we acquired three full rotation patterns over three non-orthogonal (and non-parallel) rotation axes $\vec{g}_1$ (Figure 11.2b), $\vec{g}_2$ (Figure 11.3a), and $\vec{g}_3$ (Figure 11.3b). The three rotation patterns were then subjected to a multi-parameter fit according to Equation 4.4, with the motion of the field vector $\vec{b}_0(\varphi)$ described by Equations 4.7 and 4.6, and the chemical shift tensors given in Equation 11.2. To enhance the accuracy of the determined crystal orientation (expressed by the rotation axis orientation and offset angle) for each rotation pattern, we simultaneously fitted the quadrupole coupling tensor of ^{7}Li according to Equation 11.6 and detailed in Section 11.3, as the orientation of the LDP single crystal for the measurements of both nuclides is identical. The fit converged on a global solution with the following rotation axes and ^{31}P chemical shift tensor components (the error values reflect the fit

residuals):

$$\begin{array}{lccc}
\vec{g}_1: & \theta_g = (17.1 \pm 0.4)^{\circ} & \phi_g = (53.9 \pm 0.9)^{\circ} & \varphi_\Delta = (60.0 \pm 0.9)^{\circ} \\
\vec{g}_2: & \theta_g = (30.0 \pm 0.4)^{\circ} & \phi_g = (31.2 \pm 0.5)^{\circ} & \varphi_\Delta = (28.9 \pm 0.5)^{\circ} \\
\vec{g}_3: & \theta_g = (158.8 \pm 0.4)^{\circ} & \phi_g = (105.7 \pm 0.8)^{\circ} & \varphi_\Delta = (114.9 \pm 0.8)^{\circ} \\
& P = (34.5 \pm 0.3)\ \text{ppm} & R = (52.1 \pm 0.3)\ \text{ppm} & S = (8.3 \pm 0.4)\ \text{ppm} \\
& T = (-27.3 \pm 0.3)\ \text{ppm} & U = (-41.0 \pm 0.6)\ \text{ppm} & V = (-5.0 \pm 1.9)\ \text{ppm}
\end{array} \tag{11.3}$$

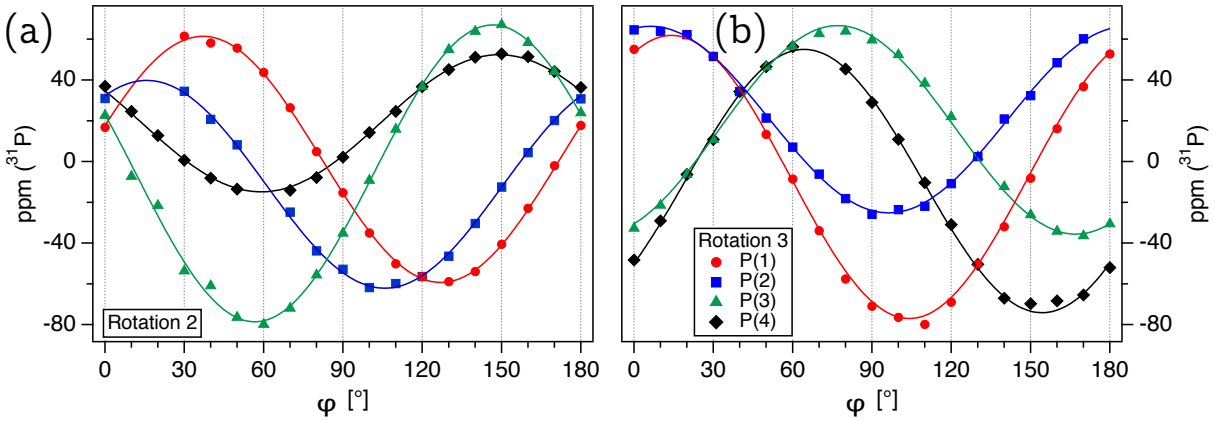

Figure 11.3 – Full rotation pattern for the four magnetically inequivalent ^{31}P in LDP at Wyckoff position $4a$, acquired by rotating the crystal counter-clockwise in steps of 10° around the goniometer axes $\vec{g}_2$ **(a)**, and $\vec{g}_3$ **(b)**. The lines represent the fit of the experimental points to the CS tensor elements and axes orientation (see text for details).[Figure taken from [142]]

The eigenvalues and eigenvectors of the ^{31}P CS tensor for LDP are listed in Table 11.1(left). The CS tensor is clearly biaxial, with the asymmetry parameter $\eta_{CS} = 0.67$ reflecting the low site symmetry of Wyckoff site $4a$.[147] The orientation of the CS tensor eigenvectors in the orthorhombic unit cell of LDP for P(1), scaled according to the associated eigenvalues, are depicted in Figure 11.7. The eigenvector orientations are free to orient according to the electronic environment generated predominantly by the surrounding oxygen atoms.

As a useful comparison to our single-crystal data, a ^{31}P-NMR spectrum of a sample of LDP crushed into a powder was acquired at 5 kHz MAS spinning speed, shown in Figure 11.4. The isotropic chemical shift $\delta_{iso}^{MAS} = -1.7$ ppm extracted from this spectrum is in reasonable agreement with the value $\delta_{iso} = (0.7 \pm 1)$ ppm derived from single-crystal NMR and identical with the previously reported value from a powder sample under MAS.[145] To also extract the three eigenvalues of the CS tensor, a Herzfeld–Berger analysis[7] of the MAS spectrum was performed using the *hba 1.7.5* program.[110] The results are given in Table 11.1(right), showing that the magnitude

of the MAS-derived eigenvalues are in good agreement with the single-crystal values. The error values of the Herzfeld–Berger quantities ρ, and μ are estimated from the contour plots generated by the *hba 1.7.5* program. Due to the steep slope of the contour lines in this plot, the error values of $\rho = 0.15\ ^{+15}_{-12}$ are estimated to be larger than those of $\mu = 6.2 \pm 0.5$ and are unsymmetric, resulting in different upper and lower error margins for the CS eigenvalues. The narrow signal at 10.5 ppm in Figure 11.4 is attributed to the ^{31}P chemical shift in aqueous LiH_2PO_4 solution, which is formed over time by the hygroscopic LDP powder with residual moisture in the MAS rotor.

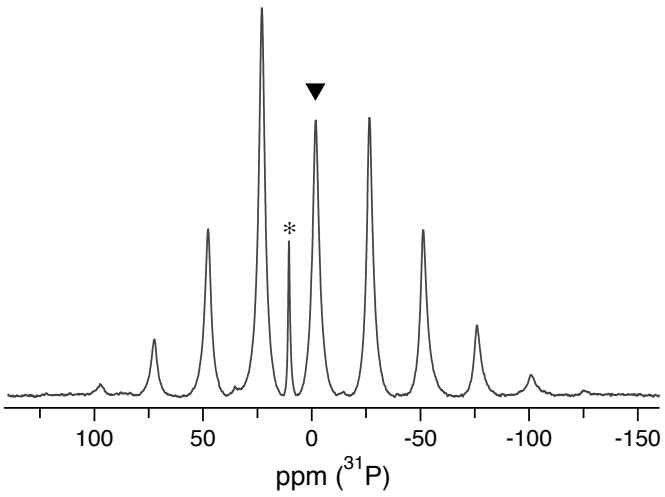

Figure 11.4 – ^{31}P-NMR spectrum of polycrystalline LDP, acquired at a MAS rate of 5 kHz. The black triangle indicates the isotropic resonance at −1.7 ppm. The signal at 10.5 ppm (∗) is attributed to the ^{31}P chemical shift in aqueous LiH_2PO_4 solution.[Figure taken from [142]]

Table 11.1 – Chemical shift (CS) tensor of ^{31}P in LDP, LiH_2PO_4, at room temperature. Left: From single-crystal NMR rotation patterns, acquired for three different rotation axes. Eigenvector orientations are listed in spherical coordinates (θ, ϕ) in the orthorhombic *abc* crystal CRY frame and refer to the atom closest to the origin, i.e. P(1). Error values are derived from the fit residuals. Right: Determined from a Herzfeld–Berger analysis[7] of the rotational side-band pattern at $\nu_r = +5$ kHz magic-angle spinning (MAS), using the *hba 1.7.5* program.[110] The error values of the tensor components are derived from those of ρ and μ.

	Single-Crystal NMR	**MAS NMR**
δ_{11}^{PAS}	(67.0 ± 0.6) ppm	$(71\ ^{+7}_{-6})$ ppm
δ_{22}^{PAS}	(13.9 ± 1.5) ppm	$(6\ ^{+8}_{-6})$ ppm
δ_{33}^{PAS}	(-78.7 ± 0.9) ppm	$(-82\ ^{+6}_{-7})$ ppm
$\vec{d}_{11}$	77.6°, 213.8°	
$\vec{d}_{22}$	31.6°, 325.0°	
$\vec{d}_{33}$	61.3°, 116.8°	
$\Delta\delta$	(-79.4 ± 1.9) ppm	(-81 ± 7) ppm
η_{CS}	0.67 ± 0.03	0.8 ± 0.2
δ_{iso}	(0.7 ± 1) ppm	(-1.7 ± 0.1) ppm

In order to extend the potential of NMR spectroscopy as an analytical tool for inorganic solids, constant efforts are being made trying to relate NMR parameters to structural features of the studied compounds. One example is the correlation of the isotropic chemical shift of ^{207}Pb in lead-bearing minerals to the distance of oxygen atoms in the lead coordination sphere.[55] However, for ^{31}P in phosphates, where the first coordination sphere is always formed by covalently bound oxygen atoms, it is notoriously difficult to establish such relations.[149] One structural parameter that is promising in this context is the dimensionless distortion index (DDI) of the O–P–O bond angles in the PO_4 tetrahedra, i.e. their deviation from the ideal tetrahedral angle, 109.47°. According to Baur,[150] the DDI is defined by:

$$DDI = \frac{\sum_{n=1}^{6} |\angle\mathrm{OPO} - 109.47^{\circ}|}{6 \cdot 109.47^{\circ}} \tag{11.4}$$

A distortion of PO_4 tetrahedra leads to a non-zero value of the DDI, and is expected to have an effect on the anisotropy of the chemical shift, which in the convention used here,[40] is quantified by the parameter $\Delta\delta = \delta_{33} - \delta_{iso}$. For LDP, we find $DDI = 0.0323$ from the X-ray structure,[146] showing a comparatively strong distortion.[150] The ^{31}P CS anisotropy of $\Delta\delta = -79.4$ ppm (see Table 11.1) is also large, which conforms to expectation. For comparison, the phosphate groups in the mineral pyromorphite, $Pb_5(PO_4)_3Cl$, (see Section 7) exhibit a smaller distortion with $DDI = 0.0146$, and accordingly also a smaller CS anisotropy of $\Delta\delta = 20.2$ ppm.[20] However, this apparent correlation between the distortion of the tetrahedral geometry and the anisotropy of the ^{31}P chemical tensor has only limited validity.[149]

11.3 ^{7}Li NMR of LDP

^{7}Li is a quadrupolar nucleus, and hence the quadrupolar coupling between the non-symmetric charge distribution of the nucleus and its electronic surroundings also needs to be considered (see Section 3). For the three transitions of ^{7}Li with $I = 3/2$, the values for k (see Figure 3.1 and Equation 3.1) are $k = 0$ for the central transition, and $k = \pm 1$ for the two satellite transitions (ST's). Representative ^{7}Li single-crystal NMR spectra of LDP are shown in Figure 11.5a, with the satellite pairs for $k = \pm 1$ symmetrically positioned around the non-resolved central transitions of the four independent lithium atoms in the crystal structure. All ^{7}Li resonance lines are fairly broad with $FWHM \approx 5.5$ kHz, and hence overlap in almost every spectrum. As discussed in detail above (Section 11.2) for ^{31}P, strong homo- and heteronuclear dipolar coupling is assumed to be the dominating effect of line broadening. With similar ^{7}Li line widths encountered in other inorganic compounds,[69] no additional broadening mechanism needs to be invoked. Taking into

account the same symmetry arguments as for the CS tensor $\boldsymbol{\delta}$ of ^{31}P at Wyckoff position $4a$ given in Equations 11.1 and 11.2, the $\mathbf{Q}^{CRY}$ tensors for ^{7}Li in the orthorhombic crystal frame of LDP are given by:

$$\mathbf{Q}^{CRY}_{Li(1)} = \begin{pmatrix} E & F & G \\ F & H & I \\ G & I & -E-H \end{pmatrix} \qquad \mathbf{Q}^{CRY}_{Li(2)} = \begin{pmatrix} E & F & -G \\ F & H & -I \\ -G & -I & -E-H \end{pmatrix}$$
$$\mathbf{Q}^{CRY}_{Li(2)} = \begin{pmatrix} E & -F & G \\ -F & H & -I \\ G & -I & -E-H \end{pmatrix} \qquad \mathbf{Q}^{CRY}_{Li(2)} = \begin{pmatrix} E & -F & -G \\ -F & H & I \\ -G & I & -E-H \end{pmatrix} \tag{11.5}$$

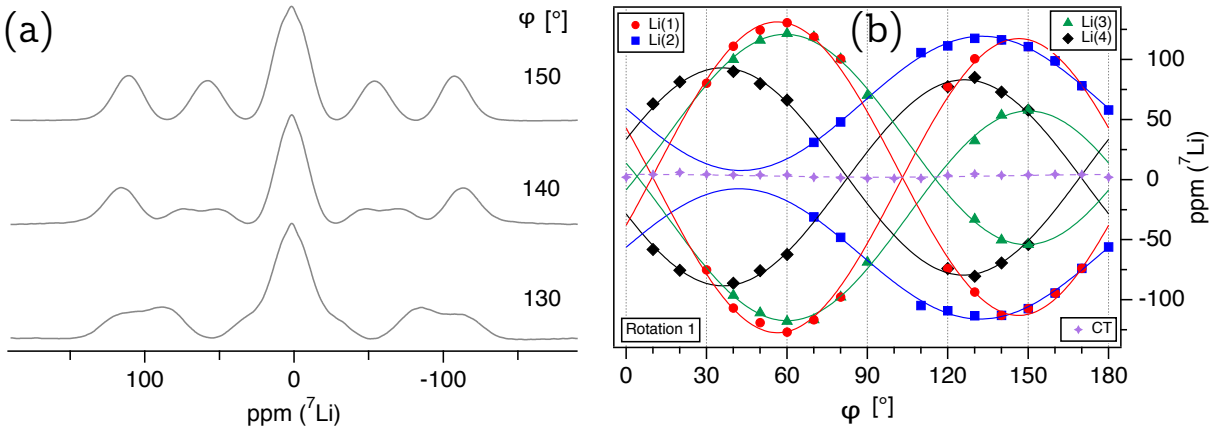

Figure 11.5 – **(a)** ^{7}Li NMR spectra of the LDP single crystal, with the indicated rotation angles φ referring to the full rotation pattern on the right. **(b)** Full rotation pattern over 180° for the four magnetically inequivalent ^{7}Li at Wyckoff position $4a$, acquired by rotating the LDP crystal counter-clockwise by 10° around the goniometer axis $\vec{g}_1$. The lines represent the fit of the experimental points to the quadrupole coupling tensor elements and axis orientation (see text for details). Figure taken from [142]

As detailed in Section 3 and shown in Section 9, these tensors are conveniently determined from the separations ('splittings') of the satellite transitions (ST's) with $k = \pm 1$ for ^{7}Li, since these are not affected by either the second-order quadrupolar interaction or the chemical shift. Also, at the applied magnetic field strength of $\vec{B}_0 = 11.74$ T the quadrupolar interaction to third-order for ^{7}Li is practically zero. Thus, the difference $\Delta\nu^{(1)}(k)$ of the resonance frequencies in dependents of the $\mathbf{Q}^{CRY}$ tensor for ^{7}Li according to Equation 3.23 with $\Delta k = 2$ and $I = 3/2$ is:

$$\Delta\nu^{(1)}(k) = \nu(+k) - \nu(-k) = \vec{b}_0^{T}(\varphi) \cdot \mathbf{Q}^{CRY} \cdot \vec{b}_0(\varphi) \tag{11.6}$$

The experimentally determined satellite splittings for $\Delta k = 2$ are plotted over the rotation angle φ for the three rotation axes $\vec{g}_1$ (Figure 11.6a), $\vec{g}_2$ (Figure 11.6b), and $\vec{g}_3$ (Figure 11.6c) and show a number of comparatively ill-defined data points. However, it has to be kept in mind that for determining the ^{7}Li ST splittings in LDP, we need to trace the eight satellite resonances with a $FWHM \approx 5.5$ kHz in a limited spectral range of maximum ≈ 61 kHz. Here, the spectral range is defined as the difference between the position of the two outermost satellite transitions. In fact, the average spectral range (calculated over 49 ^{7}Li spectra and three rotation patterns) is only ≈ 41 kHz and the always overlapping central transitions reduce the localizable range for the ST's further by their $FWHM \approx 7$ kHz.

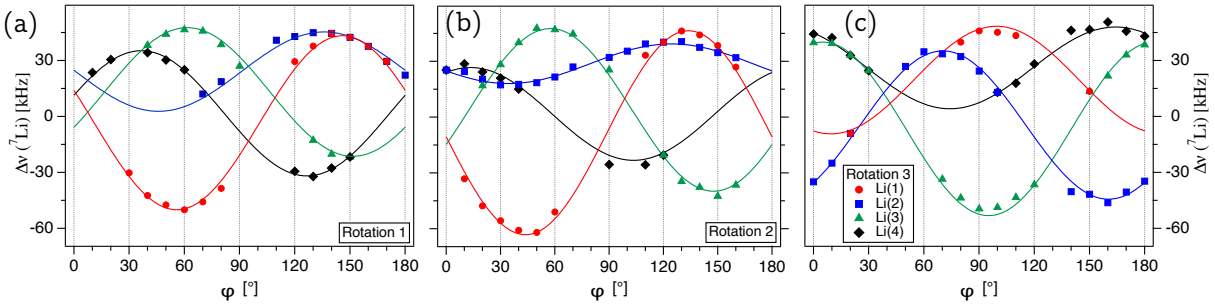

Figure 11.6 – Plot of the satellite splittings over 180° for the four magnetically inequivalent ^{7}Li at Wyckoff position 4*a*, acquired by rotating the LDP crystal counter-clockwise by 10° around the three goniometer axes $\vec{g}_1$ **(a)**, $\vec{g}_2$ **(b)**, and $\vec{g}_3$ **(c)**. The lines represent the fit of the experimental points to the quadrupole coupling tensor elements and axes orientation (see text for details).[Figure taken from [142]]

The quadrupole coupling tensors in Equation 11.5 were determined by a multi-parameter fit of the experimental splittings according to Equation 11.6 with the motion of the field vector $\vec{b}_0(\varphi)$ described by Equations 4.7 and 4.6, with the fit being coupled to the CS tensor fit of ^{31}P to improve accuracy. The rotation axes extracted thereby are given in Equation 11.3 and the components of the quadrupole coupling tensor for ^{7}Li are (the error values reflect the fit residuals): $E = (12.3 \pm 0.4)$ kHz, $F = (-33.2 \pm 0.3)$ kHz, $G = (23.6 \pm 0.5)$ kHz, $H = (8.8 \pm 0.4)$ kHz, and $I = (43.8 \pm 0.7)$ kHz. The eigenvalues and the corresponding eigenvectors in the PAS frame of the ^{7}Li **Q** tensor are listed in Table 11.2. The quadrupolar coupling constant derived is $\chi = -71$ kHz and the asymmetry parameter $\eta = 0.37$ confirms a biaxial symmetric tensor, as might be expected for Wyckoff position 4*a* with the low site symmetry, $1 - C_1$. The orientation of the eigenvectors for Li(1), scaled according to the length of the associated eigenvalue are depicted in Figure 11.7.

Table 11.2 – Quadrupole coupling tensor $\mathbf{Q_{Li}}$ (left), and isotropic chemical shift δ_{iso} of ^{7}Li in LDP, LiH_2PO_4, from single-crystal NMR rotation patterns and magic-angle spinning (MAS) NMR. Eigenvector orientations are listed in spherical coordinates (θ, ϕ) in the orthorhombic *abc* crystal frame *CRY*. The errors of the experimental values reflect those delivered by the fitting routine.

	Single-Crystal NMR	**MAS NMR**
Q_{11}^{PAS}	(22.3 ± 0.9) kHz	
Q_{22}^{PAS}	(48.4 ± 0.8) kHz	
$Q_{33}^{PAS} = \chi$	(-71 ± 1) kHz	
$\vec{q}_{11}$	50.8°, 16.8°	
$\vec{q}_{22}$	71.1°, 123.1°	
$\vec{q}_{33}$	45.2°, 233.0°	
η_Q	0.37 ± 0.02	
δ_{iso}		(-0.2 ± 0.1) ppm

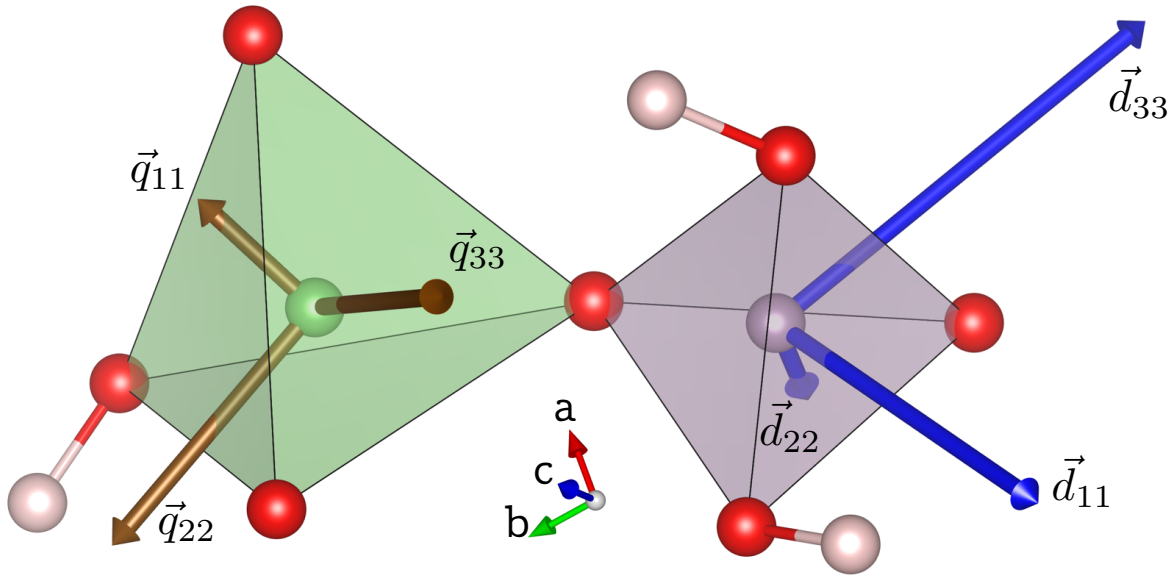

Figure 11.7 – LiO_4 and PO_4 polyhedra with related hydrogen atoms in the LDP crystal structure (colour scheme identical to that in Figure 11.1b). The bold arrows show the principal axes of the ^{7}Li **Q** tensor (brown) and ^{31}P CS tensor (blue), scaled according to the magnitude of the associated eigenvalues, such that an absolute value of 10 kHz (for ^{7}Li) and 10 ppm (for ^{31}P) corresponds to a length of 0.4 Å. Figure taken from [142] Drawing generated with the Vesta program. [68]

Having determined the size of the quadrupolar coupling, we can now estimate the extent to which the resonance frequency given in Equation 3.1 is affected by the second-order quadrupolar interaction, i.e. the relative magnitude of $\nu^{(2)}_{m,m\pm1}(k^2)$. The angle-independent part of the second-order quadrupolar induced shift $\nu^{(2)}_{ai}$ provides a quantitative measure for the second-order effect. For the CT ($k = 0$) of a spin $I = 3/2$ nuclide at a Larmor frequency of $\nu_0(^7\mathrm{Li}) = 194.416$ MHz, this calculates to:[49]

$$\nu^{(2)}_{ai} = -\frac{1}{40}\frac{\chi^2}{\nu_0}\left(1+\frac{\eta^2}{3}\right) = -0.7 \text{ Hz} \approx -4\times10^{-3} \text{ ppm} \tag{11.7}$$

Obviously, the effects of the quadrupolar interaction to second order for ^{7}Li in LDP are negligibly small, especially taking into account the very broad resonance lines.[6] Accordingly, it should now be possible to determine its chemical shift tensor by tracing the variation of the center of the satellite transitions without correcting for second order effects.[21] However, the chemical shift anisotropy of lithium atoms is generally very small (in the range of 5 ppm),[50] making detection of anisotropic effects from resonance lines with a *FWHM* $\approx$ 28 ppm practically impossible. The isotropic chemical shift was, nevertheless, determined from a sample of LDP crushed into a powder and measured at 10 kHz MAS spinning speed. The isotropic shift $\delta_{iso} = -0.2$ ppm extracted thereby is in good agreement with the previously reported value $\delta_{iso} \approx 0$ ppm derived from a polycrystalline powder sample under MAS.[145]

11.4 Experimental details

The single crystal of LiH_2PO_4 shown in Figure 11.1a was grown according to literature[147] by slow evaporation technique at 38°C from a saturated aqueous solution of LDP powder (Sigma Aldrich, St. Louis, MO, USA, 99%). Since LDP is extremely hygroscopic (having a solubility in liquid water of 160 g/100 g H_2O at 0 °C),[151] the single crystals had to be rinsed by ethanol (C_2H_5OH) upon recovering from the saturated solution. The resulting large single crystals are practically unaffected by ambient humidity, because of the much smaller surface-to-volume ratio compared to polycrystalline samples.

NMR spectra were acquired on a Bruker Avance-III 500 spectrometer at LMU Munich, at a Larmor frequency of $\nu_0(^{31}\mathrm{P}) = 202.505$ MHz, and $\nu_0(^7\mathrm{Li}) = 194.416$ MHz. The angular dependent single-crystal spectra were acquired at room temperature with a 6 mm solenoid coil and a clip-on goniometer build by NMR Service GmbH (Erfurt, Germany) using one scan and a

[6] Since the quadrupolar interaction to second order already proofs negligible, third-oder quadrupolar effects are effectively zero, as already stated above.

recycle delay of 3200 s. For the magic-angle spinning (MAS) spectra, a polycrystalline sample was prepared by crushing single crystals of LDP in an argon-filled glovebox (Unilab, MBraun, Garching, Germany, $H_2O < 1$ ppm) with an agate mortar, and measured using a 4 mm rotor by accumulating eight scans with a recycle delay of 9000 s. The ^{31}P spectra were recorded under ^{1}H decoupling using sweep-frequency two-pulse phase modulation (SW_f-TPPM)[152] with a linear sweep profile.[153] Since the ^{7}Li–^{1}H distances in the crystal structure of LDP are significantly longer than the ^{31}P–^{1}H distances, the ^{7}Li spectra did not improve under ^{1}H decoupling, and hence were recorded with single-pulse acquisition. All spectra were referenced indirectly to ^{1}H in 100% TMS at −0.1240 ppm. The simultaneous fit of the ^{31}P rotation pattern and the ^{7}Li splittings was performed with the program Igor Pro 7 from WaveMetrics Inc.

12 Quantifying The Quadrupolar Interactions

12.1 Introduction: $[(H_2O)_5Sc(\mu\text{-}OH)]_2Cl_4{\cdot}2H_2O$

As outlined in Section 2, as long as the "size" of the fundamental Zeeman interaction dominates the appearance of an NMR spectrum, it is customary to treat the quadrupolar interaction of $I > 1/2$ nuclei as a perturbation to the Zeeman levels. The contribution to the resonance frequency in Equation 3.1 for the first-order quadrupolar interaction follows a rather simple expression (Equation 3.14), is well known and experimentally proven for both, single crystal and polycrystalline NMR spectroscopy. However, the second-, and third-order perturbation terms have only been verified by polycrystalline ("powder") NMR spectroscopy. While one finds several, slightly differing, expressions for the second-order term $\nu^{(2)}_{m,m\pm1}(k^2)$ in the literature,[46–52] only one may be found for the third-order term $\nu^{(3)}_{m,m\pm1}(k,k^3)$.[46] For a powder sample, the presence of the quadrupolar coupling leads to severe line broadening and the intrinsic orientation dependency partially degenerates. Exact quantification of the first-, second-, and third-order perturbation theory terms of the quadrupolar interaction can thus only be verified by NMR spectroscopy of single crystals.

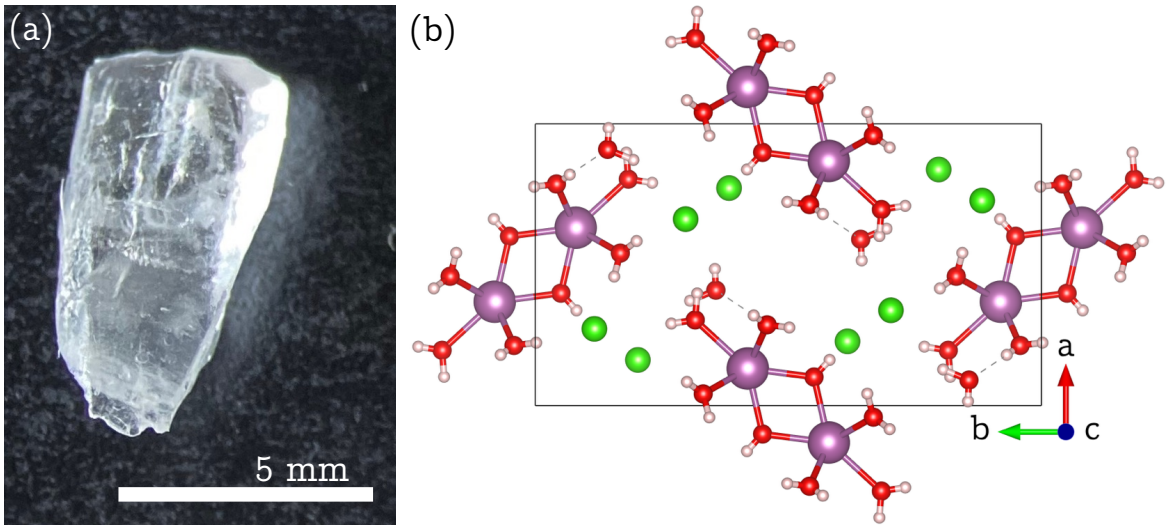

Figure 12.1 – **(a)** Single crystal of scandium hydroxy chloride hydrate, $[(H_2O)_5Sc(\mu\text{-}OH)]_2Cl_4{\cdot}2H_2O$, grown from an aqueous solution of $ScCl_3{\cdot}6H_2O$ at 38°C. **(b)** Unit cell of scandium hydroxy chloride hydrate, space group *Pnnm* (No. 58), according to literature[154] and viewed down along the crystallographic *c* axis. The scandium atoms (purple) at Wyckoff position 4*g* are situated on mirror planes parallel to the *ab* plane. Each Sc atom is coordinated by five H_2O molecules (oxygen: red; hydrogen: ivory) and bridged by two hydroxides to one other Sc atom, resulting in two $[(H_2O)_5Sc(\mu\text{-}OH)]_2{}^{4+}$ clusters per unit cell. Four chlorine atoms (green) and two H_2O molecules reside between those dinuclear moieties in the unit cell. Drawing generated with the Vesta program.[68]

The nuclide ^{45}Sc ($I = 7/2$) occurs in 100% natural abundance, has a resonance frequency close to ^{13}C, and a large quadrupole moment,[123] making it the ideal candidate to precisely determine the magnitude of the quadrupolar interaction. In Section 12, we will verify the expressions for the quadrupolar interaction treated as a perturbation to the Zeeman-levels given in Section 3 right, by acquiring orientation-dependent ^{45}Sc NMR spectra of a single crystal of scandium hydroxy chloride hydrate, $[(H_2O)_5Sc(\mu\text{-}OH)]_2Cl_4{\cdot}2H_2O$ (depicted in Figure 12.1a), which can easily be grown from an aqueous solution of $ScCl_3{\cdot}6H_2O$. $[(H_2O)_5Sc(\mu\text{-}OH)]_2Cl_4{\cdot}2H_2O$, in the following denoted as 'ScOHCl', crystallises in orthorhombic space groupe *Pnnm* (No. 58) with two formula units per unit cell, as depicted in Figure 12.1b. Each scandium atom, located at Wyckoff position 4*g*, is coordinated by five H_2O molecules and bridged to one other Sc atom by two hydroxide anions, resulting in heptacoordination with a capped trigonal prismatic geometry. The two $[(H_2O)_5Sc(\mu\text{-}OH)]_2{}^{4+}$ clusters per unit cell are linked by hydrogen bonds via the crystallisation water molecules, forming chains along the crystallographic *a* axis.[154] The Sc atoms bridged in those dimers are related to each other through an inversion center at the center of this cluster and the two dimers in the orthorhombic unit cell are related by glides parallel to the crystallographic *ac* and *bc* plane. Since inversion and translational elements do not affect NMR, the two symmetry-related scandium clusters in the unit cell form two groups of magnetically inequivalent ^{45}Sc, which can be considered to be related by a 180° rotation about the crystallographic *a* (or *b*) axis:

$$\underset{(x,y,0)}{\text{Sc}(1)} \overset{180^{\circ}}{\longleftrightarrow} \underset{(\bar{x}+\frac{1}{2},y+\frac{1}{2},\frac{1}{2})}{\text{Sc}(2)} \tag{12.1}$$

Since all ^{45}Sc atoms at Wyckoff position 4*g* are situated on mirror planes parallel to the *ab* plane, their respective quadrupole coupling tensors in the orthorhombic *CRY* frame are described by only three independent tensor components, *E*, *F*, and *G*, with the quadrupolar coupling constant defined by $\chi = -E - G$:

$$\mathbf{Q}^{\mathbf{CRY}}_{\mathbf{Sc(1)}} = \begin{pmatrix} E & F & 0 \\ F & G & 0 \\ 0 & 0 & \chi = -E-G \end{pmatrix} \qquad \mathbf{Q}^{\mathbf{CRY}}_{\mathbf{Sc(2)}} = \begin{pmatrix} E & -F & 0 \\ -F & G & 0 \\ 0 & 0 & \chi = -E-G \end{pmatrix} \tag{12.2}$$

12.2 1st-Order Quadrupolar Interaction

A single crystal of scandium hydroxy chloride hydrate, 'ScOHCl', with approximate dimensions of $3 \times 3 \times 7$ mm^3, grown from at aqueous solution and depicted in Figure 12.1a, was used for the single-crystal NMR experiments. In order to compare the experimental ^{45}Sc signal position in

scandium hydroxy chloride hydrate to the calculated ones using the expressions given in Section 3, the precise quadrupole coupling tensor of ^{45}Sc in Equation 12.2 needs to be determined first. From one rotation pattern of the two symmetry-linked ^{45}Sc in 'ScOHCl', five linear independent parameters may be extracted. The **Q** tensor, which we need to calculate posses three independent tensor components, and with the three parameters $\theta, \phi, \varphi_\Delta$ defining the rotation axis, we need to acquire two rotation pattern (see also Section 8). Two full rotation pattern over 180° for the two

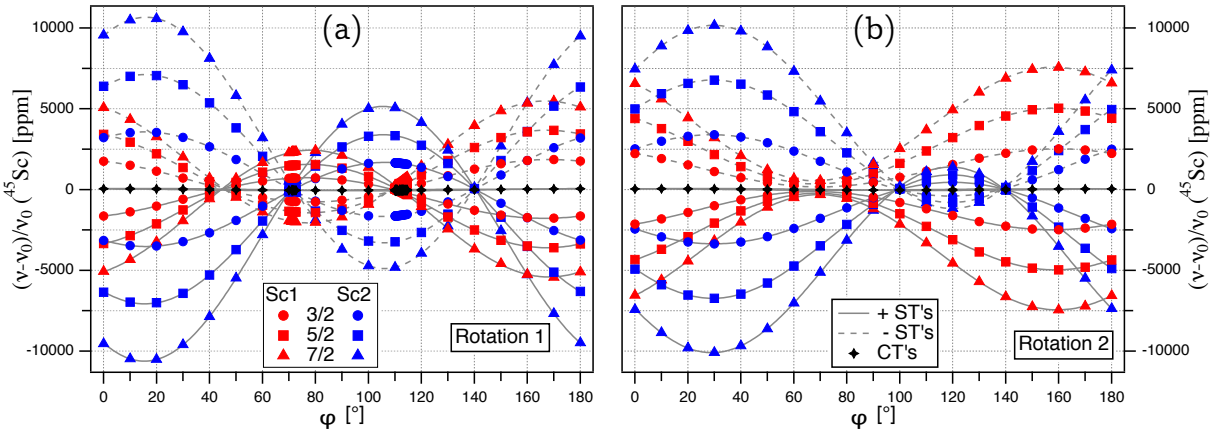

Figure 12.2 – Full rotation pattern over 180° for the two magnetically inequivalent ^{45}Sc at Wyckoff position $4g$, acquired by rotating the $[(H_2O)_5Sc(\mu\text{-}OH)]_2Cl_4{\cdot}2H_2O$ crystal stepwise by 10° around $\vec{g}_1$ **(a)** and $\vec{g}_2$ **(b)**, both perpendicular to the external magnetic field $\vec{B}_0 = 17.6$ T. At $\varphi = 70°$ and $\varphi = 110°$ for goniometer axis $\vec{g}_1$, the crystal was further rotated stepwise by 5′.

magnetically inequivalent ^{45}Sc are shown in Figure 12.2, which were obtained by rotation the crystal counterclockwise in steps of 10° about the two rotation axes, $\vec{g}_1$ (Figure 12.2a) and $\vec{g}_2$ (Figure 12.2b). To avoid quadrupolar effects to third order in these rotation pattern, which is necessary to determine the coupling tensor from the satellite splittings using Equation 3.23, all spectra were recorded at the high magnetic field strength of $\vec{B}_0 = 17.6$ T. The satellite pairs for $k = \pm 3$, in the following denoted as ST(7/2), $k = \pm 2$, in the following denoted as ST(5/2), and $k = \pm 1$, in the following denoted as ST(3/2), are (almost) symmetrically positioned around the central transition. Both rotation pattern show a large spectral range of maximum ≈ 4 MHz.[7] In order to trace all ST's for both ^{45}Sc in such a large spectral range, several spectral windows with varying irradiation frequency offsets have to be recorded. As the quadrupolar interaction to second order depends on the nutation frequency ν_0 (see Equation 3.15), also the signal position slightly changes with differing irradiation frequency offsets. To increase the accuracy of the determined **Q** tensor, only the ST(3/2) resonance frequencies are evaluated, since they are all

[7] Here, the spectral range is defined as the difference between the position of the two outermost satellite transitions.

fairly close to the central transition for each rotation angle φ. Hence, they can be recorded with an irradiation frequency offsets placed at the actual nutation frequency ν_0, i.e. at zero ppm.

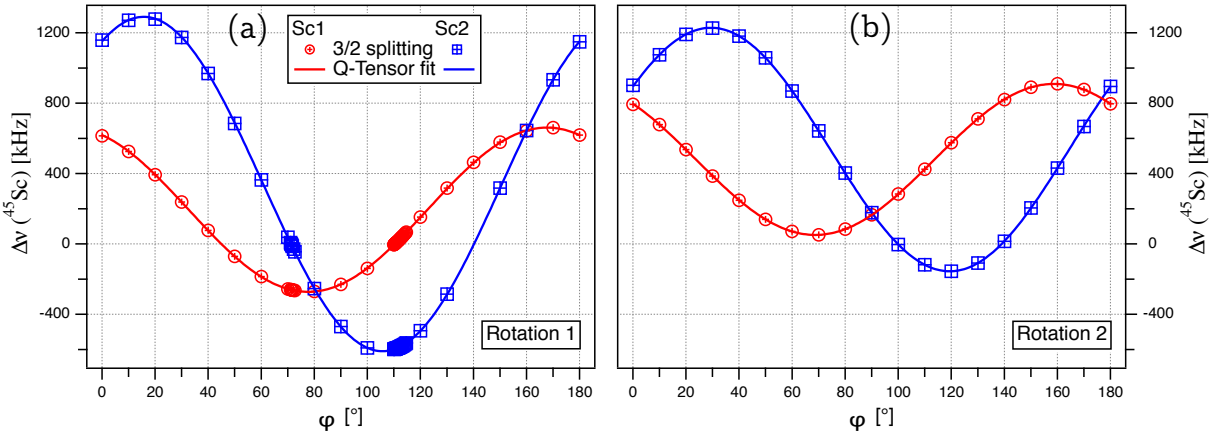

Figure 12.3 – Plot of the splittings $\Delta\nu^{(1)}(k) = \nu(+k) - \nu(-k)$ for the ST(3/2) ($\Delta k = 2$) doublets for ^{45}Sc in the unit cell of the $[(H_2O)_5Sc(\mu\text{-}OH)]_2Cl_4{\cdot}2H_2O$ single crystal, determined from the full rotation pattern in Figure 12.2. **(a)** rotated about the goniometer axis $\vec{g}_1$, and **(b)** rotated about $\vec{g}_2$. The lines represent the fit of the quadrupole coupling tensor and axes orientation according to Equation 4.14 (see main text for details).

The experimentally determined satellite splittings of the ST(3/2) doublets in kHz are plotted over the rotation angle for both rotation axes in Figure 12.3. To determine the quadrupole coupling tensor $\mathbf{Q}$ for ^{45}Sc given by Equation 12.2, the satellite splittings were then fitted according to Equation 4.14, with $\Delta k = 2$, $I = 7/2$, and the motion of the magnetic field vector $\vec{b}_0(\varphi)$ described by Equations 4.7 and 4.6. The fit converged on a global solution with the following values for the nine parameters (the errors reflect the fit residuals):

$$\begin{array}{lccc} \vec{g}_1: & \theta_g = (43.5 \pm 0.1)^\circ & \phi_g = (287.5 \pm 0.1)^\circ & \varphi_\Delta = (93.5 \pm 0.1)^\circ \\ \vec{g}_2: & \theta_g = (34.7 \pm 0.1)^\circ & \phi_g = (279.5 \pm 0.1)^\circ & \varphi_\Delta = (98.3 \pm 0.1)^\circ \\ E = (6.065 \pm 0.003)\,\text{MHz} & F = (-3.752 \pm 0.002)\,\text{MHz} & G = (8.548 \pm 0.003)\,\text{MHz} & \end{array} \quad (12.3)$$

The diagonalization of the quadrupole coupling tensor defined by the E, F, G values listed above transforms it to its own PAS frame, giving the eigenvalues and eigenvectors shown in Table 12.1. Inspecting the properties of $\mathbf{Q}^{PAS}$, we find the quadrupolar coupling constant ($\chi = -14.613$ MHz) to be comparatively large, which indicates that the magnitude of the quadrupolar interaction to second order is also fairly large, as discussed below. Also, by lowering the external magnetic field strength, one can hope to observed third-order effects, as will be discussed in Section 12.4. The quadrupolar asymmetry parameter $\eta_Q = 0.5409 \pm 0.0004$ clearly indicates a biaxial symmetric tensor, and the orientation of the eigenvectors are a consequence

of the crystal symmetry, with $\vec{q}_{33}$ aligned exactly along the crystallographic c axis and $\vec{q}_{11}$, $\vec{q}_{22}$ placed in the ab plane.

Table 12.1 – Quadrupole coupling (**Q**) tensor of ^{45}Sc in $[(H_2O)_5Sc(\mu\text{-}OH)]_2Cl_4{\cdot}2H_2O$. The corresponding eigenvector orientations are listed in spherical coordinates (θ, ϕ) in the orthorhombic *abc* crystal frame *CRY* and refer to the atom closest to the origin, i.e. Sc(1). The listed error values reflect those delivered by the fitting routine.

Q Tensor of ^{45}Sc in $[(H_2O)_5Sc(\mu\text{-}OH)]_2Cl_4{\cdot}2H_2O$			
Q_{11}^{PAS}	(3.355 ± 0.001) MHz	$\vec{q}_{11}$	90.0°, 35.8°
Q_{22}^{PAS}	(11.259 ± 0.004) MHz	$\vec{q}_{22}$	90.0°, 125.8°
$Q_{33}^{PAS} = \chi$	(-14.613 ± 0.006) MHz	$\vec{q}_{33}$	0.0°, 0.0°
η_Q	0.5409 ± 0.0004		

12.3 2^{nd}-Order Quadrupolar Interaction

As the orientation dependency of the first-, and second-order perturbation theory term of the quadrupolar interaction given by Equations 3.14–3.17 differ, the second-order term can best be verified in spectral regions with small satellite splittings. The magnitude of the ST's splittings is dominated by the first-order term and hence, small splittings correspond to regions where this interaction is small. For the first rotation pattern of ^{45}Sc in 'ScOHCl' at around $\varphi \approx 110^{o}$, displayed in Figure 12.2a, the satellite transitions of Sc(1) are crossing its central transition, resulting in zero splitting for at least one crystal orientation, and the splittings for Sc(2) are also comparatively small. Hence, to closer observe the positions of the resonance frequency for this crystal orientation, we acquired an inset of the rotation pattern for rotation axis $\vec{g}_1$, starting at $\varphi = 110^{o}$ and rotated stepwise by only $5'$. Figure 12.4a shows the thus obtained single-crystal spectra, with the satellite transitions for Sc(1) highlighted, and the rotation pattern inset is shown in Figure 12.4b.

At first sight, the recorded spectra look astonishing, with all satellite transitions of Sc(1) "ordered" pairwise and asymmetric on one side of the central transition of Sc(1). The ST's of Sc(2) are located outside of the spectral window and its CT is located at ≈ 0 ppm.[8] To understand the appearance of those spectra, and thereby verify the quadrupolar expressions in Section 3, we now calculate the individual contribution of the quadrupolar interaction to first $\nu^{(1)}(k)$, and second

[8]The CT of Sc(2) in this region of the rotation pattern is split into a doublet as a result of homonuclear dipolar couplings between ^{45}Sc in the crystal structure, the center of gravity of the resonance frequency is not affected. Details can be found in Section 12.6.

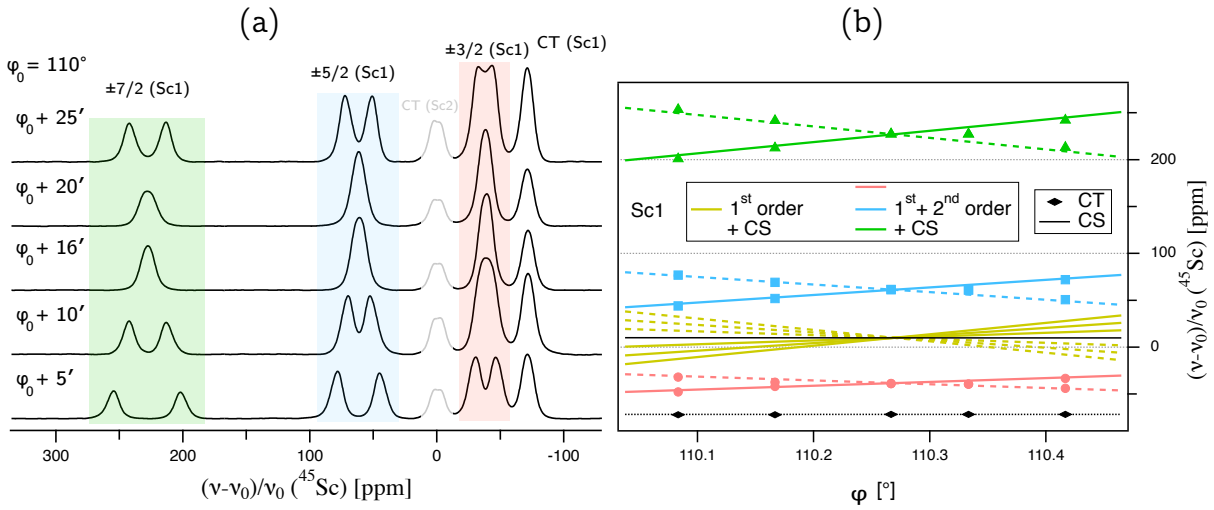

Figure 12.4 – **(a)** ^{45}Sc NMR spectra of a single crystal of $[(H_2O)_5Sc(\mu\text{-}OH)]_2Cl_4{\cdot}2H_2O$, with the indicated rotation angle φ referring to the rotation pattern inset on the right and to the full rotation pattern in Figure 12.2a. All satellite transitions of Sc(1), with the ST(7/2) (green), ST(5/2) (blue), ST(3/2) (red), are positioned to the left of the CT (black) of Sc(1). The CT of Sc(2) (grey) is located between the ST(3/2) and ST(5/2) of Sc(1) at ≈ 0 ppm. **(b)** Inset of the full rotation pattern shown in Figure 12.2a, acquired by rotating the single crystal counterclockwise by 5′ around $\vec{g}_1$ starting from $\varphi = 110°$. The yellow lines represent the contribution of the quadrupolar interaction to first order according to Equation 3.14 and the chemical shift. The red, blue, and green lines also include the contribution of the quadrupolar interaction to second order according to Equations 3.15–3.17 for the ST(3/2), ST(5/2) and ST(7/2) of Sc(1), respectively.

order $\nu^{(2)}(k^2)$ to the measured resonance frequency $\nu(k)$ described by Equation 3.1. First, we need to determine the Euler angles β and α between the eigenvector with the largest eigenvalue, i.e. $Q_{33} = \chi$, and the magnetic field vector $\vec{b}_0$. As we already determined the orientation of the goniometer axis, respectively the magnetic field vector, in the CRY frame, we only need to transform θ_g and ϕ_g in Equation 12.3 into the PAS frame to do so. The eigenvector of the quadrupolar coupling constant $\vec{q}_{33}$, aligns exactly along the c axis in the crystal frame, which is a consequence of the symmetry enforced by the mirror plane at Wyckoff position $4g$. This generates a **Q** tensor of the shape shown in Equation 12.2, where the principal component Q_{33} does not change when transforming from the CRY to the PAS frame and hence, $\theta_g^{CRY} = \theta_g^{PAS}$ for both magnetically inequivalent ^{45}Sc. The azimuthal angle ϕ_g of the goniometer axis in the CRY frame now only needs to be aligned along $\vec{q}_{11}$ for a complete transformation into the PAS. Hence, according to Table 12.1 for Sc(1), $\phi_g^{PAS} = \phi_g^{CRY} - 35.8°$. The motion of the magnetic field vector $\vec{b}_0^{PAS}(\varphi) = (b_x, b_y, b_z)$ in the PAS frame of the quadrupole coupling tensor is then defined by inserting the transformed goniometer axis $\vec{g}^{PAS}$ in Equations 4.7 and 4.6, and the

Euler angles β and α are simply calculated according to the relation:

$$\beta = \arccos\left[b_z\right] \qquad \alpha = \text{atan2}\ \left[b_y, b_x\right] \tag{12.4}$$

The contribution of the quadrupolar interaction to first order according to Equation 3.14 and including the second-order shift according to Equations 3.15–3.17 for the inset of the rotation pattern is shown in Figure 12.4b. For a better comparison between the calculated and measured line positions, the chemical shift ν_{CS} of ^{45}Sc given in Table 12.2 (see details in Section 12.5) is also added to all calculated line positions. Inspecting the course of the lines under the influence of first-order quadrupolar perturbation one finds, as expected, all ST's symmetrically positioned around the theoretical CT (after subtracting the second-order contribution) which is only shifted by the chemical shift. The pairwise "ordering" of all satellite transitions asymmetrically to the central transition is clearly caused by the second-order quadrupolar shift. Interestingly, for Sc(1) at $\varphi = 110^{\circ}16'$ the first-order contribution is zero, and the signal position is only determined by the second-order shift (and the chemical shift). As may be seen in Figure 12.4, the $k = \pm 3, \pm 2, \pm 1$ ST's hence superimpose and the resulting single transition for each ST pair is shifted differently from the CT. Following the quadrupolar interaction to second order given by Equations 3.15–3.17 the CT and ST(3/2) are shifted to smaller values ("upfield") with a stronger shift for the CT, and the ST(5/2) and ST(7/2) are shifted to higher values ("downfield") with a stronger shift for the ST(7/2). The calculated signal positions including the second-order shift agree well with all measured signal positions and thus, verifies the second-order terms given in Section 3, and quantitatively explains the rather unusual appearance of the ^{45}Sc single-crystal spectra.

12.4 3rd-Order Quadrupolar Interaction

When searching for effects of the quadrupolar interaction treated to third-order perturbation theory $\nu^{(3)}(k, k^3)$ (see Equation 3.1), the above discussed ^{45}Sc data acquired at a magnetic field strength of $\vec{B}_0 = 17.6$ T are unsuitable, since those effect are negligible small. Hence, a full rotation pattern of ^{45}Sc of the 'ScOHCl' single crystal (which was still mounted on rotation axis $\vec{g}_2$) was acquired at a magnetic field strength of $\vec{B}_0 = 9.4$ T. As the quadrupolar interaction to third order scales with $1/\nu_0^2$ (see Equation 3.19), the effects to third order increase thereby by a factor of ≈ 3.5. Figure 12.5a shows the thus obtained rotation pattern for Sc(2). Since a change of NMR spectrometer and goniometer probe was necessary to go from $\vec{B}_0 = 17.6$ T to $\vec{B}_0 = 9.4$ T, the rotation axis slightly differs from $\vec{g}_2$ (see Equation 12.3) which was determined from the rotation pattern in Figure 12.2b. The precise rotation axis was thus determined using

the known **Q** tensor of 'ScOHCl' listed in Table 12.1, by fitting the full rotation pattern acquired at $\vec{B}_0 = 9.4$ T to:

$$\vec{g}_2^*: \qquad \theta_g = (35.2 \pm 0.1)^o \quad \phi_g = (282.3 \pm 0.1)^o \quad \varphi_\Delta = (103.2 \pm 0.1)^o \tag{12.5}$$

As detailed in Section 3, the third-order shift can be "extracted" from the experimental data points by calculating the weighted separations of the satellite splittings according to Equation 3.27, since these are not affected by the chemical shift, first-, and second-order contributions. Accordingly, Figure 12.5b shows the experimentally determined splittings of the ST splittings $\triangle\Delta\nu(k, k-n)$ and the calculated ones by inserting Equations 3.19–3.21 in Equation 3.27 for Sc(2) and for $\Delta\nu(3) - 3\Delta\nu(1)$, $\Delta\nu(3) - 1.5\Delta\nu(2)$, and $1.5\Delta\nu(2) - 3\Delta\nu(1)$. The Euler angles β and α, necessary to calculate the individual contribution of the quadrupolar interaction to third order are calculated according to Equation 12.4 with $\theta_g^{PAS} = 35.2^o$ and $\phi_g^{PAS} = 282.3^o + 35.8^o$ (see Section 12.3 for details) and the **Q** tensor of 'ScOHCl' was taken from Table 12.1. The calculated and the experimental splittings of the ST splittings agree well, especially taking into account that the variation of the accumulated third-order terms is in the same range as the *FWHM* ≈ 4.5 kHz of each individual single-crystal resonance frequency.

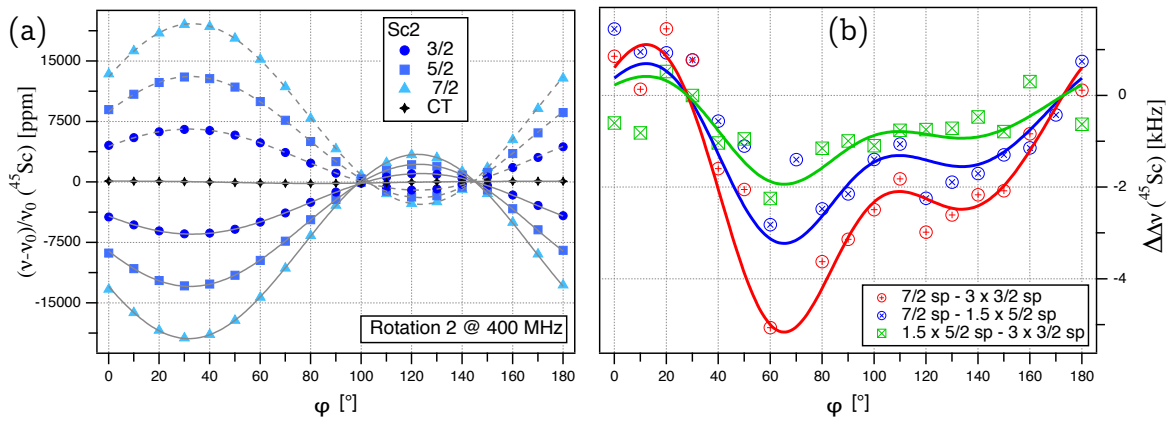

Figure 12.5 – **(a)** Full Rotation pattern over 180° for ^{45}Sc(2) acquired by rotating the $[(H_2O)_5Sc(\mu\text{-}OH)]_2Cl_4{\cdot}2H_2O$ crystal stepwise by 10° around $\vec{g}_2^*$ at an external magnetic field $\vec{B}_0 = 9.4$ T. **(b)** Plot of the splittings of the ST splittings $\triangle\Delta\nu(k, k-n)$ for the full rotation pattern of Sc(2) on the left with $\Delta\nu(3) - 3\Delta\nu(1)$ (red), $\Delta\nu(3) - 1.5\Delta\nu(2)$ (blue), and $1.5\Delta\nu(2) - 3\Delta\nu(1)$ (green). The lines represent the calculated splittings of the ST splittings according to Equation 3.27 with the third-order contribution given by Equations 3.19–3.21.

12.5 ^{45}Sc chemical shift tensor

The contribution of the chemical shift, already included in the calculated line positions in Figure 12.4b, is defined by its chemical shift tensor. Taking into account the same symmetry arguments as for the **Q** tensor given in Section 12.1, the CS tensor $\boldsymbol{\delta}$ for the two magnetically inequivalent ^{45}Sc in the CRY frame of 'ScOHCl' is given by:

$$\boldsymbol{\delta}^{\boldsymbol{CRY}}_{\boldsymbol{Sc(1)}} = \begin{pmatrix} P & R & 0 \\ R & S & 0 \\ 0 & 0 & T \end{pmatrix} \qquad \boldsymbol{\delta}^{\boldsymbol{CRY}}_{\boldsymbol{Sc(2)}} = \begin{pmatrix} P & -R & 0 \\ -R & S & 0 \\ 0 & 0 & T \end{pmatrix} \tag{12.6}$$

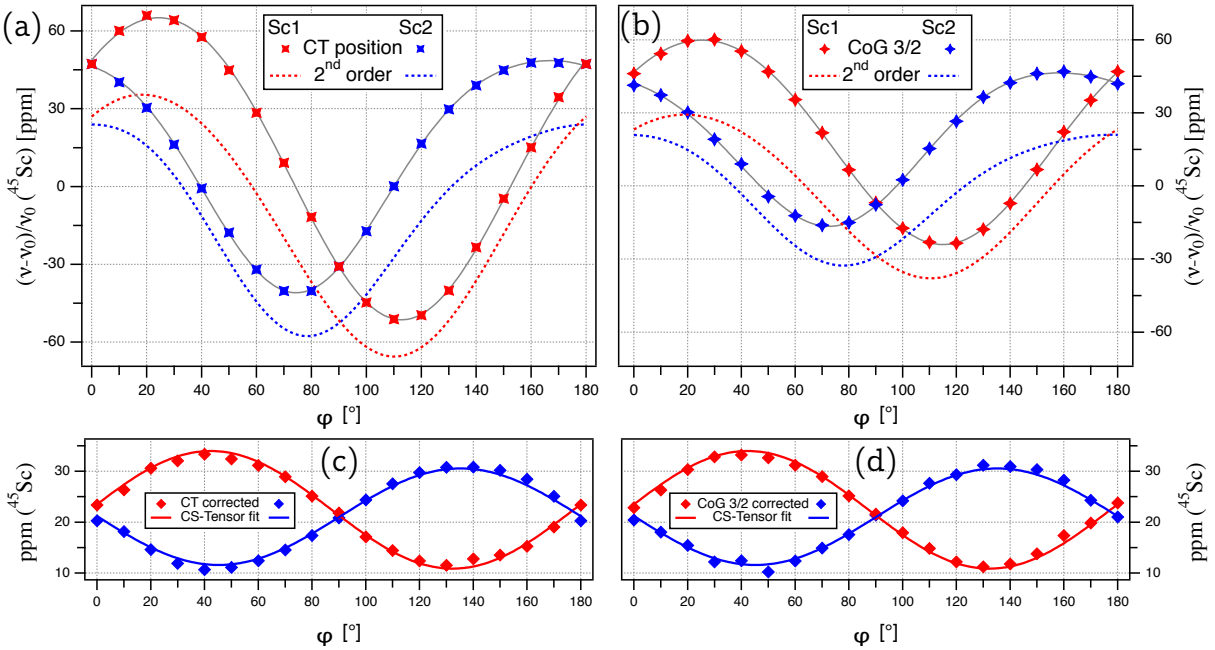

Figure 12.6 – Plot of the experimentally determined central transition for ^{45}Sc ($k = 0$) **(a)** and center of gravity (CoG) for the ST(3/2) ($\Delta k/2 = 1$) **(b)** for the full rotation pattern in Figure 12.2b (Sc(1) red; Sc(2) blue). The contribution of the quadrupolar interaction according to Equations 3.15–3.17 is shown as dotted lines. The central transition **(c)** and the CoG for the ST(3/2) **(d)** after subtracting the quadrupolar second-order shift from the experimental data points, with the solid lines representing the fit of the chemical shift tensor (see text for details).

To determine $\boldsymbol{\delta}$, the contribution of the second-order quadrupolar interaction must be subtracted from the central transition ($k = 0$) line position or from the center of gravity of the satellite transitions ($\Delta k/2$) (see Section 3 for details). Since the chemical shift (in Hz) increases with increasing magnetic field strength, the CT's and the ST(3/2) of both rotation pattern in Figure 12.2, which were acquired at a field strength of $\vec{B}_0 = 17.6$ T, were used for tensor

determination. As already outlined in Section 12.2, the ST(5/2) and ST(7/2) were omitted for data evaluation to avoid inaccuracies which arise from the different irradiation frequency offsets during data acquisition. Exemplarily, in Figure 12.6a and b, the ^{45}Sc CT's and the center of gravity (CoG) of the ST(3/2), respectively, for the rotation axis $\vec{g}_2$ are plotted over the rotation angle φ. The dotted lines show the calculated second-order quadrupole shift according to Equations 3.14–3.17 for each crystal orientation using the results obtained from evaluating the splittings in Figure 12.3 and the Euler angles discussed in Section 12.3. It should be noted, that the second-order shift for the CT's for all crystal orientations is larger than for the ST(3/2), as was already indicated in Figure 12.4. After subtracting the quadrupolar contribution from the experimental points, the remaining variation in line position is solely caused by the chemical shift tensor. As may be seen in Figure 12.6c and d the quadrupolar corrected CT positions and the corrected ST(3/2) CoG's are identical, again proving the expressions given by Equations 3.14–3.17 correct. The quadrupolar corrected line positions were then subject to a multi-parameter fit according to Equation 4.4, with the chemical shift tensor given by Equation 12.6 and the motion of the magnetic field vector in the CRY frame described by Equations 4.6 and 4.7. For this fit, the rotation axis $\vec{g_1}$ and $\vec{g_2}$ were kept fixed at the value derived from fitting the quadrupole coupling tensor (Equation 12.3), and the components of the chemical shift tensor for ^{45}Sc determined thereby are $P = (22.2 \pm 0.2)$ ppm, $R = (12.7 \pm 0.2)$ ppm, $S = (28.4 \pm 0.6)$ ppm, and $T = (5.6 \pm 0.9)$ ppm (the error values reflect the fit residuals).

Table 12.2 – Chemical shift ($\boldsymbol{\delta}$) tensor of ^{45}Sc in $[(H_2O)_5Sc(\mu\text{-}OH)]_2Cl_4{\cdot}2H_2O$. The corresponding eigenvector orientations are listed in spherical coordinates (θ, ϕ) in the orthorhombic *abc* crystal frame CRY and refer to the atom closest to the origin, i.e. Sc(1). The listed error values reflect those delivered by the fitting routine.

$\boldsymbol{\delta}$ Tensor of ^{45}Sc in $[(H_2O)_5Sc(\mu\text{-}OH)]_2Cl_4{\cdot}2H_2O$			
δ_{11}^{PAS}	(5.6 ± 1) ppm	$\vec{d}_{11}$	0.0°, 0.0°
δ_{22}^{PAS}	(12.4 ± 0.9) ppm	$\vec{d}_{22}$	90.0°, 141.6°
δ_{33}^{PAS}	(38.5 ± 0.9) ppm	$\vec{d}_{33}$	90.0°, 51.6°
δ_{iso}	(18.8 ± 1) ppm	$\Delta\delta$	(19.7 ± 1) ppm
η_{CS}	0.35 ± 0.03		

The diagonalization of the CS tensor transforms it to its own PAS frame, giving the eigenvalues and eigenvectors listed in Table 12.2. Just as for the **Q** tensor of ^{45}Sc, we find a biaxial symmetric CS tensor with an asymmetry parameter $\eta_{CS} = 0.35 \pm 0.03$. The isotropic chemical shift $\delta_{iso} = (18.8 \pm 1)$ ppm as well as the anisotropy of the CS tensor $\Delta\delta = (19.7 \pm 1)$ ppm are comparatively small for ^{45}Sc in inorganic solids.[155–157] The orientation of the chemical

shift eigenvectors are in agreement with the crystal symmetry on Wyckoff position $4g$ on which all scandium atoms are situated, with one eigenvector of one of the lesser tensor components (δ_{11}^{PAS}) aligning a exactly along the c axis in the CRY frame. The eigenvector of the largest corresponding eigenvalue, i.e. δ_{33}^{PAS}, is aligned 15.8° from the eigenvector $\vec{q}_{11}$ of the quadrupole coupling tensor in the crystallographic ab plane.

12.6 Dipolar couplings of ^{45}Sc

For some orientations of the 'ScOHCl' crystal, the ^{45}Sc single-crystal resonances are split into doublets, as is shown in Figure 12.4a for the central transition of Sc(2). This splitting (and the fairly large line broadening of $FWHM \approx 4.5$ kHz) is an effect of direct homonuclear ^{45}Sc–^{45}Sc dipolar interaction. In the crystal structure of 'ScOHCl' the two magnetically equivalent ^{45}Sc bridged by hydroxide ions in the $[(H_2O)_5Sc(\mu\text{-}OH)]_2^{4+}$ clusters are separated by ≈ 3.4 Å.[154] At this separation, the ^{45}Sc–^{45}Sc direct dipolar coupling constant, d_{II}, is 180 Hz, where d_{II} is defined by (all symbols are standard):[148]

$$d_{II} = \frac{\mu_0 \hbar}{8\pi^2} \frac{\gamma_{Sc}^2}{r_{Sc,Sc}^3} \tag{12.7}$$

As ^{45}Sc is a spin $I = 7/2$ nuclide, each ^{45}Sc resonance frequency is split into an octet by this strong direct coupling present between the two scandium atoms in the dinuclear moiety. In the crystal structure of 'ScOHCl', those ^{45}Sc atoms are further surrounded by eight ^{45}Sc with an average distance of ≈ 7.0 Å, which calculates to an coupling constant $d_{II} \approx 20$ Hz. Those various couplings again split the octet for each ^{45}Sc resonance frequency and results in a rather complicated coupling pattern. As detailed in Section 2, the dipolar interactions are orientation dependent, and the homonucelar coupling pattern of ^{45}Sc in 'ScOHCl' either results in resonance frequencies which are split into a doublet or inherently broadened, depending on the orientation of the crystal in respect to the magnetic field $\vec{B}_0$. A quantitative evaluation of the dipolar interactions in 'ScOHCl' by means of single-crystal NMR spectroscopy is outside the scope of this work, since only little information can be obtained from such complex coupling patterns.[148] Important for the evaluation of the single crystal data is, that the center of gravity of the individual ^{45}Sc CT's and ST's, which are used for the calculations discussed above, are not significantly shifted by the various dipolar interactions.

12.7 Experimental details

Scandium hydroxy chloride hydrate ('ScOHCl'), $[(H_2O)_5Sc(\mu\text{-}OH)]_2Cl_4{\cdot}2H_2O$, was synthesized according to literature starting from Sc_2O_3 (ABCR GmbH, 99%).[158] To this end, 1.9 g of Sc_2O_3 was added to a round bottom flask with 34 mL of distilled water and 16 mL HCl (37%). The mixture was then refluxed for 2 hours at 150°C, cooled down to room temperature, and filtered to remove excess Sc_2O_3. The filtrate was dried in a rotation evaporator, resulting in a yellowish powder of 'ScOHCl', which was recrystallised from water for purification until a white crystalline powder was obtained. The single-crystals of 'ScOHCl' with several mm in diameter were grown by slow evaporation technique at 38°C from a saturated aqueous solution of the white 'ScOHCl' powder.

Single-crystal NMR spectra were acquired on a Bruker Avance-750 ($\vec{B}_0 = 17.6$ T) spectrometer at University of Leipzig, and Bruker Avance-III 400 ($\vec{B}_0 = 9.4$ T) spectrometer at MPI-FKF Stuttgart, at a Larmor frequency of $\nu_0(^{45}\text{Sc}) = 181.826$ MHz, and $\nu_0(^{45}\text{Sc}) = 97.199$ MHz, respectively. For the measurements at $\vec{B}_0 = 17.6$ T a goniometer probe built by Bruker Corporation (Billerica, USA), and for the measurements at $\vec{B}_0 = 9.4$ T a goniometer probe built by NMR Service GmbH (Erfurt, Germany) was used, both equipped with a 6 mm solenoid coil. The ^{45}Sc spectra were recorded with single-pulse acquisition, 160 scans and a relaxation delay of 0.5 s. All spectra were referenced to a 0.001 M $ScCl_3$ solution at 0 ppm. The fit of the rotation pattern, as well as the calculations of the quadrupolar interactions, were performed with the program Igor Pro 7 from WaveMetrics Inc..

13 Summary

In this work, the full ^{207}Pb chemical shift tensor in the crystal structure of the five lead-bearing minerals phosgenite ($Pb_2Cl_2CO_3$), pyromorphite [$Pb_5(PO_4)_3Cl$], anglesite ($PbSO_4$), cerussite ($PbCO_3$), and wulfenite ($PbMoO_4$) has been determined using orientation-dependent NMR measurements on naturally grown single crystals. With this study, we also attempted to demonstrate that problems usually associated with single-crystal NMR, i.e. problems (*I*)–(*III*) listed in the Introduction, may be overcome:

(*I*) The presumed extensive effort for data acquisition and evaluation is clearly manageable for all lead-bearing minerals. Despite the relatively low natural abundance of ^{207}Pb of 22.1%, the spectra for one rotation pattern of all minerals were acquired with an average of only eight scans and 60 s recycle delay, meaning the absolute measurement time was only about 2.5 hours. It can be seen from the various single-crystal spectra shown, that the signal-to-noise ratio is satisfactory under these conditions. In contrast to static spectra of polycrystalline material (see, for example, Reference [6]), spectral intensity is focused on only few resonance lines, making detection less demanding. Our total experimental time was, of course, longer than 2.5 hours, with reorientation of the crystals and especially the subsequent necessary tuning and matching of the probe causing additional delays (the procedure of reorient/tune/match, however, may in principle be automated, considerably lessening the work load of the operator).[159] To further improve the efficiency of both data acquisition and processing, we utilised crystallographic symmetry relations[63] between crystallographically equivalent but magnetically inequivalent ^{207}Pb atoms, reducing the necessary data for determining the full CS tensor to a maximum of two full rotation patterns, about two nonparallel rotation axes. It took an average of three hours to record the MAS spectrum of a polycrystalline sample for each mineral, yet, for ^{207}Pb spectra of systems with large $\Delta\delta$, two such MAS spectra are usually required to unequivocally assign the isotropic peak. Additionally, the isotropic shift δ_{iso} of ^{207}Pb has been proven temperature dependent in almost all compounds, which requires recording of several MAS spectra with differing rotation frequency to determine its room temperature value. In terms of pure experimental time, therefore, single-crystal NMR compares not unfavourably to MAS NMR, although the necessary effort for data processing and evaluation is obviously more extensive. At the end of this process, however, the full CS tensor is gained, and not only the value of δ_{iso} available from fast MAS experiments.

(*II*) The necessity to know the orientation of the rotation axis in the crystal frame is generally solvable in a number of ways, including optical orientation using well-developed crystal

faces as demonstrated in Section 9 for hexagonal AlN. One precise method is certainly the use of X-ray diffraction on the mounted crystal on which NMR measurements are to be performed. However, the large crystals needed for NMR tend to absorb most of the X-ray beam, in particular when compounds with high lead content, such as lead-bearing minerals, are being investigated. For these systems, resolving the orientation of the rotation axis by relying only on NMR data is a very useful and precise approach, as shown throughout this work. In compounds with several magnetically inequivalent but symmetry linked atomic positions, this approach is rather straight forward as is described in detail for a four-fold (phosgenite), three-fold (pyromorphite), and two-fold (anglesite and cerussite) symmetry relation between the positions. We have even outlined a strategy to determine NMR interaction tensors and rotation axis orientation from single crystals of compounds with low symmetry and/or Wyckoff multiplicity, which leaves a system of equations underdetermined for such a fit. To obtain additional information on the rotation axes orientations, we acquired two full rotation patterns of the test system (wulfenite), while simultaneously measuring a single crystal of phosgenite. In the phosgenite structure, four magnetically inequivalent ^{207}Pb are generated by the Wyckoff multiplicity, allowing the determination of both ^{207}Pb CS tensor and axis orientation from a single rotation pattern. Use of the previously determined CS tensor of phosgenite made it feasible to resolve the relative orientation of the two rotation axes for the simultaneous measurements of the two mineral crystals. This orientation difference could be applied as an additional fit constraint for the data fit of wulfenite, making the determination of the full ^{207}Pb CS tensor possible, without using other crystal alignment techniques.

(*III*) For the scarce availability of single crystals of sufficient size for NMR experiments, no general solution appears to exist. For the area of ^{207}Pb-NMR, however, a considerable number of compounds also occur as natural minerals (see Table 8.2). For many lead compounds, comparatively large single crystals are therefore available from mineral collections. In addition, single crystals of soluble substances can be grown fairly easy and with dimensions of several mm from aqueous solutions, as has been done during this work for lithium dihydrogen phosphate, LiH_2PO_4, and scandium hydroxy chloride hydrate, $[(H_2O)_5Sc(\mu\text{-}OH)]_2Cl_4{\cdot}2H_2O$. Many more single crystals in sufficient size are amenable by well established crystal-growth techniques, such as shown for hexagonal aluminum nitride, AlN, single crystals grown via physical vapour deposition.

The approach presented herein for determination of the full chemical shift tensor in compounds with arbitrary crystal lattice symmetry and Wyckoff multiplicity is, of course, not limited to ^{207}Pb NMR, but may be applied to any nucleus with spin $I = 1/2$. As has been shown, it

can also easily be adapted to determine the quadrupole coupling tensor **Q** for nuclei with spin $I > 1/2$, thus considerably expanding the capabilities of single-crystal NMR spectroscopy.

Furthermore, in the context of establishing connections between NMR parameters and crystal structure, we here have reported on a linear correlation between ^{207}Pb isotropic chemical shift and the shortest Pb–O distance in the coordination sphere, for compounds with Pb^{2+} solely surrounded by oxygen. This correlation appears to work better than the previously suggested connection between δ_{iso} and an average distance of all oxygens in a coordination sphere,[27] in particular because the precise definition of this sphere is debatable. Our results for ^{207}Pb in vanadinite ($[Pb_5(AO_4)_3Cl]$; A = V), pyromorphite (A = P), and mimetite (A = As) also suggest that single crystal NMR spectroscopy provides not only information about the relevant NMR interaction tensors, i.e. the chemical shift, but also information about local coordination geometry and crystal microstructure. Regarding the relation between ^{207}Pb chemical shift and crystal structure parameters, the correlations to both unit cell volume and bond angle shown here could possibly be extended to other lead bearing minerals and/or apatites. This could result in the establishment of more reliable and widely applicable correlations between NMR interaction parameters and structural features. Similarly, the information on crystal morphology available via NMR spectroscopy, as discussed herein, opens an alternative venue to X-ray diffraction to study effects such as mosaicity and multi-crystalline structures. A systematic rather than a random pattern of misorientation in the crystal microstructure is represented by twinning. To characterize twinning in macroscopic crystals by means of NMR spectroscopy, a genuine twin crystal of cerussite was investigated and found to display four resonances in the static ^{207}Pb-NMR spectra. By assessing the relative intensities of the ^{207}Pb-NMR resonances, the contribution of the respective twins can be separated, and by fitting the two data sets, the twinning geometry could even be quantified as most likely being a {130}-contact twin.

We have also determined the full ^{31}P chemical shift tensor and ^{7}Li quadrupole coupling tensor of the ionic conductor lithium dihydrogen phosphate (LDP), LiH_2PO_4, at room temperature by single-crystal NMR spectroscopy. To this end, orientation-dependent NMR spectra of a LDP single crystal were acquired about three different and initially unknown rotation axes. This allowed tensor determination to good precision, despite the broad resonance lines of the ^{31}P and ^{7}Li spectra caused by strong homo- and heteronuclear dipolar couplings. The overdetermination of the equation system, caused by the symmetry relation between the four crystallographic equivalent but magnetically inequivalent phosphorus and lithium atoms in the unit cell, made it possible to make the orientation of all three crystal rotation axes free parameters of the data fit. This again evidences the usefulness of NMR spectroscopy as a complementary analytical tool for investigation of solid electrolytes. The ^{7}Li and ^{31}P NMR interaction tensors determined

provide a good starting point for temperature dependent single-crystal NMR of LDP, which possibly could reveal new insights about the diffusion mechanism of the lithium atoms in the crystal structure.

In order to demonstrate tensor determination from crystals with well defined crystal faces, both the chemical shift and quadrupole coupling tensors for ^{27}Al and ^{14}N in aluminum nitride have been determined to high precision by single-crystal NMR spectroscopy. To this end, a homoepitaxially grown AlN single crystal with known morphology was used, which allowed the rotation axis to be determined by optical alignment. Because of the high symmetry of wurtzite-type AlN, one full rotation pattern was sufficient to determine the NMR-interaction tensors in the crystal frame. The three-fold rotation axis on which both atom types are located enforces colinearity of the tensor eigenvectors with the crystallographic coordinate system, which simplifies data analysis. To extract the chemical shift tensor for ^{27}Al, the evolution of the central transition over the crystal rotation was tracked, and the contribution of the second-order quadrupolar shift was subtracted according to the previously determined quadrupolar coupling tensor. Due to the small quadrupolar coupling of ^{14}N, its second-order quadrupolar shift in AlN is negligible, and the chemical shift tensor was directly fitted from the evolution of the ^{14}N doublet centers over the rotation angle. For comparison, the quadrupolar coupling parameters of ^{14}N and ^{27}Al were also calculated using the Castep DFT code for a variety of previously reported X-ray structures. For both calculation strategies, i.e. single-point energy (SPE, where the coordinates are directly taken from XRD), and structures which were geometry optimized (GO) by the DFT code, agreement with the experimental values was relatively poor, leaving room for further improvement of these computational methods.

Utilizing the high precision inherent in single-crystal NMR spectroscopy, the expressions given in this work for the quadrupolar interactions to second-, and third-order perturbation theory have been verified for the first time for nuclei with half-integer spins. To this end, a single crystal of scandium hydroxy chloride hydrate, $[(H_2O)_5Sc(\mu\text{-}OH)]_2Cl_4{\cdot}2H_2O$, ('ScOHCl') grown from an aqueous solution was used. The large quadrupole coupling of ^{45}Sc in 'ScOHCl' results in pronounced quadrupole shifts of the resonance frequencies and hence, makes it a precise probe for these interactions. The full ^{45}Sc quadrupole coupling tensor and chemical shift tensor has thereby been determined from two full rotation pattern acquired at a magnetic field strength of $\vec{B}_0 = 17.6$ T. At this field strength, the quadrupolar interaction needs only to be treated to second order. To also trace third-order effects, we acquired another ^{45}Sc rotation pattern at a field strength of $\vec{B}_0 = 9.4$ T, which enabled us to visualize the shift caused by the quadrupolar interaction to third order. Thus, contributing to an even better understanding of NMR spectroscopy of quadrupolar nuclei.

References

[1] Ewald, P.P. Fifty Years of X-ray Diffraction. International Union of Crystallography. 1999. Available online: `http://www.iucr.org/publ/50yearsofxraydiffraction` (accessed on 15 June 2020).

[2] Harris, R.K. NMR crystallography: The use of chemical shifts. *Solid State Sci.* **2004**, *6*, 1025–1037, doi:10.1016/j.solidstatesciences.2004.03.040.

[3] Martineau, C.; Senker, J.; Taulelle, F. NMR Crystallography. *Ann. Rep. NMR Spectrosc.* **2014**, *82*, 1–57, doi:10.1016/B978-0-12-800184-4.00001-1.

[4] Bryce, D.L. NMR crystallography: Structure and properties of materials from solid-state nuclear magnetic resonance observables. *IUCrJ* **2017**, *4*, 350–359, doi:10.1107/S2052252517006042.

[5] Available online: `https://www.iucr.org/iucr/commissions/nmr-crystallography` (accessed on 15 June 2020).

[6] Neue, G.; Dybowski, C.; Smith, M.L.; Hepp, M.A.; Perry, D.L. Determination of $^{207}Pb^{2+}$ chemical shift tensors from precise powder lineshape analysis. *Solid State Nucl. Magn. Reson.* **1995**, *6*, 241–250, doi:10.1016/0926-2040(95)01225-7.

[7] Herzfeld, J.; Berger, A.E. Sideband intensities in NMR spectra of samples spinning at the magic angle. *J. Chem. Phys.* **1980**, *73*, 6021–6030, doi:10.1063/1.440136.

[8] Hodgkinson, P.; Emsley, L. The reliability of the determination of tensor parameters by solid-state nuclear magnetic resonance. *J. Chem. Phys.* **1997**, *107*, 4808–4816, doi:10.1063/1.474844.

[9] Volkoff, G.M.; Petch, H.E.; Smellie, D.W.L. Nuclear electric quadrupole interactions in single crystals. *Can. J. Phys.* **1952**, *30*, 270–289, doi:10.1139/p52-026.

[10] Vosegaard, T.; Hald, E.; Langer, V.; Skov, H.J.; Daugaard, P.; Bildsøe, H.; Jakobsen, H.J. Improved hardware and software for single-crystal NMR spectroscopy. *J. Magn. Reson.* **1998**, *135*, 126–132, doi:10.1006/jmre.1998.1551.

[11] Hou, G.; Paramasivam, S.; Byeon, I.J.L.; Gronenborn, A.M.; Polenova, T. Determination of relative tensor orientations by γ-encoded chemical shift anisotropy/heteronuclear dipolar coupling 3D NMR spectroscopy in biological solids. *Phys. Chem. Chem. Phys.* **2010**, *12*, 14873–14883, doi:10.1039/c0cp00795a.

[12] Vega, A.J. Quadrupolar nuclei in solids, in *Encyclopedia of Nucl. Magn. Reson.*; Grant, D.M.; Harris, R.K. (Eds.), Vol. 6; John Wiley & Sons: Chichester, UK, 1996; p. 3869.

[13] Frydman, L.; Harwood, J.S. Isotropic spectra of half-integer quadrupolar spins from bidimensional magic-angle spinning NMR. *J. Am. Chem. Soc.* **1995**, *117*, 5367–5368, doi:10.1021/ja00124a023

[14] Weil, J.A. Use of symmetry-related crystal sites for measuring tensor properties in magnetic resonance. *J. Magn. Reson.* **1973**, *10*, 391–393, doi:10.1016/0022-2364(73)90260-6.

[15] El Saffar, Z.M. The determination of the quadrupole coupling tensor using nuclear magnetic resonance. *J. Magn. Reson.* **1975**, *19*, 233–239, doi:10.1016/0022-2364(75)90069-4.

[16] Berglund, B.; Tegenfeldt, J. The determination of quadrupole coupling tensors from single-crystal NMR data. *J. Magn. Reson.* **1978**, *30*, 451–455, doi:10.1016/0022-2364(78)90270-6.

[17] Kind, R. Exploring crystal symmetry for the determination of EFG-tensors from NMR-NQR rotation patterns. *Z. Naturforsch* **1986**, *41a*, 122–128, doi:10.1515/zna-1986-1-218.

[18] Tesche, B.; Zimmermann, H.; Poupko, R.; Haeberlen, U. The Single-Rotation Method of Determining Quadrupole Coupling Tensors in Monoclinic Crystals. Error Analysis and Application to Bullvalene. *J. Magn. Reson. Ser. A* **1993**, *140*, 68–77, doi:10.1006/jmra.1993.1189.

[19] Bräuniger, T.; Poupko, R.; Luz, Z.; Zimmermann, H.; Haeberlen, U. Quantification of the orientational disorder in ortho-dichlorotetramethylbenzene: A single crystal deuterium nuclear magnetic resonance and x-ray study of the site populations. *J. Chem. Phys.* **2001**, *115*, 8049–8059, doi:10.1063/1.1407840.

[20] Zeman, O.E.O.; Moudrakovski, I.L.; Hoch, C.; Hochleitner, R.; Schmahl, W.W.; Karaghiosoff, K.; Bräuniger, T. Determination of the ^{31}P and ^{207}Pb Chemical Shift Tensors in Pyromorphite, $Pb_5(PO_4)_3Cl$, by Single-Crystal NMR Measurements and DFT calculations. *Z. Anorg. Allg. Chem.* **2017**, *643*, 1635–1641, doi:10.1002/zaac.201700261.

[21] Zeman, O.E.O.; Hoch, C.; Hochleitner, R.; Bräuniger, T. NMR interaction tensors of ^{51}V and ^{207}Pb in vanadinite, $Pb_5(VO_4)_3Cl$, determined from DFT calculations and single-crystal NMR measurements, using only one general rotation axis. *Solid State Nucl. Magn. Reson.* **2018**, *89*, 11–20, doi:10.1016/j.ssnmr.2017.12.002.

[22] Zeman, O.E.O.; Steinadler, J.; Hochleitner, R.; Bräuniger, T. Single-crystal ^{207}Pb-NMR of wulfenite, $PbMoO_4$, aided by simultaneous measurement of phosgenite, $Pb_2Cl_2CO_3$. *Solid State Nucl. Magn. Reson.* **2019**, *103*, 17–24, doi:10.1016/j.ssnmr.2019.101620.

[23] Czochralski, J. Ein neues Verfahren zur Messung der Kristallisationsgeschwindigkeit der Metalle. *Z. Phys. Chem.* **1918**, *92*, 219–221, doi:10.1515/zpch-1918-9212.

[24] Hartmann, C.; Wollweber, J.; Sintonen, S.; Dittmar, A.; Kirste, L.; Kollowa, S.; Irmscher, K.; Bickermann, M. Preparation of deep UV transparent AlN substrates with high structural perfection for optoelectronic devices. *CrystEngComm.* **2016**, *18*, 3488–3497, doi:10.1039/c6ce00622a.

[25] Hafner, S.; Raymond, M. The nuclear quadrupole coupling tensors of Al^{27} in kyanite. *Am. Mineral.* **1967**, *52*, 1632–1642.

[26] Bryant, P.L.; Harwell, C.R.; Wu, K.; Fronczek, F.R.; Hall, R.W.; Butler, L.G. Single-crystal ^{27}Al NMR of andalusite and calculated electric field gradients: The first complete NMR assignment for a 5-coordinated aluminum site. *J. Phys. Chem. A* **1999**, *103*, 5246–5252, doi:10.1021/jp990374i.

[27] Fayon, F.; Farnan, I.; Bessada, C.; Coutures, J.; Massiot, D.; Coutures, J. P. Empirical correlations between ^{207}Pb NMR chemical shifts and structure in solids. *J. Am. Chem. Soc.* **1997**, *119*, 6837–6843, doi:10.1021/ja963593f.

[28] Dmitrenko, O.; Bai, S.; Beckmann, P.A.; van Bramer, S.; Vega, A.J.; Dybowski, C. The Relationship between ^{207}Pb NMR Chemical Shift and Solid-State Structure in Pb(II) Compounds. *J. Phys. Chem. A* **2008**, *112*, 3046–3052, doi:10.1021/jp711182z.

[29] Mason, H.E.; Hirner, J.J.; Xu, W.; Parise, J.B.; Phillips, B.L. Solid-state NMR spectroscopy of Pb-rich apatite. *Magn. Reson. Chem.* **2009**, *47*, 1062–1070, doi:10.1002/mrc.2514.

[30] Senocrate, A.; Moudrakovski, I.; Kim, G.Y.; Yang, T.Y.; Gregori, G.; Grätzler, M.; Maier, J. The Nature of Ion Conduction in Methylammonium Lead Iodide: A Multimethod Approach. *Angew. Chem. Int. Ed.* **2017**, *56*, 7755–7759, doi:10.1002/anie.201701724.

[31] Hanrahan, M.P.; Men, L.; Rosales, B.A.; Vela, J.; Rossini, A.J. Sensitivity-Enhanced ^{207}Pb Solid-State NMR Spectroscopy for the Rapid, Non-Destructive Characterization of Organolead Halide Perovskites. *Chem. Mater.* **2018**, *30*, 7005–7015, doi:10.1021/acs.chemmater.8b01899.

[32] Senocrate, A.; Moudrakovski, I.; Maier, J. Short-range ion dynamics in methylammonium lead iodide by multinuclear solid state NMR and ^{127}I NQR. *Phys. Chem. Chem. Phys.* **2018**, *20*, 20043–20055, doi:10.1039/C8CP01535J.

[33] Charpentier, T. The PAW/GIPAW approach for computing NMR parameters: A new dimension added to NMR study of solids. *Solid State Nucl. Magn. Reson.* **2011**, *40*, 1–20, doi:10.1016/j.ssnmr.2011.04.006.

[34] Alkan, F.; Dybowski, C. Chemical-shift tensors of heavy nuclei in network solids: A DFT/ZORA investigation of ^{207}Pb chemical-shift tensors using the bond-valence method. *Phys. Chem. Chem. Phys.* **2015**, *17*, 25014–25026, doi:10.1039/C5CP03348A.

[35] Cohen, M.H.; Reif, F. Quadrupole effects in nuclear magnetic resonance studies of solids, in *Solid State Physics Advances in Research and Applications*; Seitz, F.; Turnbull, D. (Eds.), Vol. 5; Academic Press: New York, NY, USA, 1957; p. 327438.

[36] Abragam, A. *Principles of Nuclear Magnetism*; Clarendon Press: Oxford, UK, 1961; ISBN 0-198-52014-X.

[37] Mehring, M. *Principles of High Resolution NMR in Solids*; Springer-Verlag: New York, NY, USA, 1983; ISBN 3-540-11852-7.

[38] Freude, D.; Haase, J. Quadrupole effects in solid-state nuclear magnetic resonance, in *NMR Basic Principles and Progress*; Diehl, P.; Fluck, E.; Günther, H.; Kasfeld, R.; Seelig, J. (Eds.), Vol. 29; Springer-Verlag: Berlin, DE, 1993; p. 1.

[39] Jerschow, A. From nuclear structure to the quadrupolar NMR interaction and high-resolution spectroscopy. *Prog. Nucl. Magn. Reson. Spectrosc.* **2005**, *46*, 63–78, doi:10.1016/j.pnmrs.2004.12.001.

[40] Haeberlen, U. High Resolution NMR in Solids: Selective Averaging, In *Advances in Magnetic Resonance*; Waugh, J., (Ed.); Academic Press: New York, NY, USA, 1976; ISBN 0-12-025561-8.

[41] Levitt, M.H. *Spin Dynamics: Basic of Nuclear Magnetic Resonance*; John Wiley & Sons: Chichester, UK, 2008; ISBN 978-0-470-51117-6.

[42] Anet, F.A.L.; O'Leary, D.J. The shielding tensor. Part I: Understanding its symmetry properties. *Concepts Magn. Reson.* **1991**, *3*, 193–214, doi:10.1002/cmr.1820030403.

[43] Rose, M. E. *Elementary Theory of Angular Momentum*; John Wiley & Sons: New York, USA, 1957; ISBN 0-486-68480-6.

[44] Millot, Y.; Man, P.P. Active and passive rotations with Euler angles in NMR. *Concepts Magn. Reson.* **2012**, *40A*, 215–252, doi:10.1002/cmr.a.21242.

[45] Weil, J.A.; Anderson, J.H. Determination of the g Tensor in Paramagnetic Resonance. *J. Chem. Phys.* **1958**, *28*, 864–866, doi:10.1063/1.1744284.

[46] Wolf, F.; Kline, D.; Story, H.S. ^{93}Nb and ^{23}Na NMR in Polycrystalline Sodium Niobate. *J. Chem. Phys.* **1970**, *53*, 3538–3543, doi:10.1063/1.1674529.

[47] Narita, K.; Umeda, J.-I.; Kusumoto, H. Nuclear Magnetic Resonance Powder Patterns of the Second-Order Nuclear Quadrupole Interaction in Solids with Asymmetric Field Gradient. *J. Chem. Phys.* **1966**, *44*, 2719–2723, doi:10.1063/1.1727118.

[48] Baugher, J.F.; Taylor, P.C.; Oja, T.; Bray, J. Nuclear Magnetic Resonance Powder Patterns in the Presence of Completely Asymmetric Quadrupole and Chemical Shift Effects: Application to Metavanadates. *J. Chem. Phys.* **1969**, *50*, 4914–4925, doi:10.1063/1.1670988.

[49] Samoson, A. Satellite Transition High-Resolution NMR of Quadrupolar Nuclei In Powders. *Chem. Phys. Lett.* **1985**, *119*, 29–32, doi:10.1016/0009-2614(85)85414-2.

[50] MacKenzie, K.J.D.; Smith, M.E. Multinuclear Solid-State NMR of Inorganic Materials, In *Pergamon Materials Series*; Cahn, R.W., (Ed.); Elsevier Science: Oxford, UK, 2002; ISBN 0-08-043787-7.

[51] Pascal, P.P. Quadrupolar Interactions, in *Encyclopedia of Magnetic Resonance*; John Wiley & Sons: Chichester, UK, 2011; p. 3838, doi:10.1002/9780470034590.emrstm0429.pub2.

[52] Freude, D.; Haase, J. `www.quad-nmr.de` (2013–2019), (accessed on 15 June 2020).

[53] Vosegaard, T.; Jakobsen, H.J. ^{27}Al Chemical Shielding Anisotropy. *J. Magn. Reson.* **1997**, *128*, 135–137, doi:10.1006/jmre.1997.1236.

[54] Bräuniger, T.; Groh, B.; Moudrakovski, I.L.; Indris, S. Local Electronic Structure in γ-$LiAlO_2$ Studied by Single-Crystal ^{27}Al NMR and DFT Calculations. *J. Phys. Chem. A* **2016**, *120*, 7839–7846, doi:10.1021/acs.jpca.6b07286.

[55] Zeman, O.E.O.; Steinadler, J.; Hochleitner, R.; Bräuniger, T. Determination of the Full ^{207}Pb Chemical Shift Tensor of Anglesite, $PbSO_4$, and Correlation of the Isotropic Shift to Lead-Oxygen Distance in Natural Minerals. *Crystals* **2019**, *9*, 43, doi:10.3390/cryst9010043.

[56] Pines, A.; Chang, J.J.; Griffin, R.G. Carbon?13 nuclear magnetic resonance in solid ammonium tartrate. *J. Chem. Phys.* **1973**, *61*, 1021–1030, doi:10.1063/1.1681970.

[57] Pausak, S.; Tegenfeldt, J.; Waugh, J.S. ^{13}C chemical shielding tensors in polyalkylbenzenes. *J. Chem. Phys.* **1974**, *61*, 1338–1344, doi:10.1063/1.1682057.

[58] Veeman, W.S. ^{13}C chemical shift tensors in organic single crystals. *Phil. Trans. R. Soc. Lond. A* **1981**, *299*, 629–641, doi:10.1098/rsta.1981.0039.

[59] Honkonen, R.S.; Doty, F.D.; Ellis, P.D. Cadmium-113 Shielding Tensors of Cadmium-Oxo Compounds. 1. Single-Crystal Studies on $Cd(NO_3)_2{\cdot}4H_2O$ and $3CdSO_4{\cdot}8H_2O$. *J. Am. Chem. Soc.* **1983**, *105*, 4163–4168, doi:10.1021/ja00351a007.

[60] Vosegaard, T.; Langer, V.; Daugaard, P.; Hald, E.; Bildsøe, H.; Jakobsen, H. J. A new goniometer design for single-crystal nuclear magnetic resonance spectroscopy. *Rev. Sci. Instrum.* **1996**, *67*, 2130–2133, doi:10.1063/1.1147026.

[61] Hauser, H.; Radloff, C.; Ernst, R.R.; Sundell, S.: Pascher, I. The ^{31}P Chemical Shielding Tensor in Phospholipids. *J. Am. Chem. Soc.* **1988**, *110*, 1054–1058, doi:10.1021/ja00212a009.

[62] Vosegaard, T.; Hald, E.; Daugaard, P.; Jakobsen H.J. A two-axis goniometer for sensitivity enhancement in single-crystal nuclear magnetic resonance spectroscopy. *Rev. Sci. Instrum.* **1999**, *70*, 1771–1779, doi:10.1063/1.1149667.

[63] Weil, J.A.; Buch, T.; Clapp, J.E. Crystal Point Group Symmetry and Microscopic Tensor Properties in Magnetic Resonance Spectroscopy. *Adv. Magn. Res.* **1974**, *6*, 183–257, doi:10.1016/B978-0-12-025506-1.50010-8.

[64] Bak, M.; Rasmussen, J. T.; Nielsen, N. C. SIMPSON: A general simulation program for solid-state NMR spectroscopy. *J. Magn. Reson.* **2000**, *147*, 296–330, doi:10.1006/jmre.2000.2179.

[65] Andrew, E.R. Magic angle spinning in solid state n.m.r. spectroscopy. *Philos. Trans. R. Soc. A* **1981**, *299*, 505–520, doi:10.1098/rsta.1981.0032.

[66] Brunner, E.; Fenzke, D.; Freude, D.; Pfeifer, H. The influence of homonuclear dipolar interaction on the residual linewidths of MAS NMR spectra. *Chem. Phys. Lett.* **1990**, *169*, 591–594, doi:10.1016/0009-2614(90)85653-T.

[67] Giuseppetti, G.; Tadini, C. Reexamination of the crystal structure of phosgenite, $Pb_2Cl_2(CO_3)$. *Tscher. Mineral. Petr. Mitt.* **1974**, *21*, 101–109, doi:10.1007/BF01081262.

[68] Momma, K.; Izumi, F. *VESTA 3* for three-dimensional visualization of crystal, volumetric and morphology data. *J. Appl. Cryst.* **2011**, *44*, 1272-1276, doi:10.1107/S0021889811038970.

[69] Indris, S.; Heitjans, P.; Uecker, R.; Bredow, T. Local electronic structure in a $LiAlO_2$ single crystal studied with ^{7}Li NMR spectroscopy and comparison with quantum chemical calculations. *Phys. Rev. B* **2006**, *74*, 245120, doi:10.1103/PhysRevB.74.245120.

[70] Bräuniger, T.; Groh, B.; Moudrakovski, I.L.; Indris, S. Local electronic structure in γ-$LiAlO_2$ studied by single-crystal ^{27}Al NMR and DFT calculations. *J. Phys. Chem. A* **2016**, *120*, 7839–7846, doi:10.1021/acs.jpca.6b07286.

[71] Greer, G.J.; Michaelis, V.K.; Katz, M.J.; Leznoff, D.B.; Schreckenbach, G.; Kroeker, S. Characterising lone-pair activity of lead(II) by ^{207}Pb solid-state NMR spectroscopy: Coordination polymers of $[N(CN)_2]^-$ and $[Au(CN)_2]^-$ with terpyridine ancillary ligands. *Chem. Eur. J.* **2011**, *17*, 3609–3618, doi:10.1002/chem.201002913.

[72] van Gorkom, L.C.M.; Hook, J.M.; Logan, M.B.; Hanna, J.V.; Wasylishen, R.E. Solid-state lead-207 NMR of lead(II) nitrate: Localized heating effects at high magic angle spinning speeds. *Magn. Reson. Chem.* **1995**, *33*, 791–795, doi:10.1002/mrc.1260331005.

[73] Milder, T.; Ernst, H.; Freude, D. ^{207}Pb NMR detection of spinning-induced temperature gradients in MAS rotors. *Solid State Nucl. Magn. Reson.* **1995**, *5(3)*, 269–271, doi:10.1016/0926-2040(95)01189-1.

[74] Kunwar, A.C.; Turner, G.L.; Oldfield, E. Solid-state spin-echo Fourier transform NMR of ^{39}K and ^{67}Zn salts at high field. *J. Magn. Reson.* **1986**, *69*, 124–127, doi:10.1016/0022-2364(86)90224-6.

[75] Zeman, O.E.O.; Hochleitner, R.; Schmahl, W.W.; Karaghiosoff, K.; Bräuniger, T. Relation between ^{207}Pb NMR chemical shift and the morphology and crystal structure for the apatites $Pb_5(AO_4)_3Cl$, vanadinite (A = V), pyromorphite (A = P), and mimetite (A = As). *Am. Mineral.*, accepted.

[76] Epp, T.; Marks, M.A.W.; Ludwig, T.; Kendrick, M.A.; Eby, N.; Neidhart, H.; Oelmann, Y.; Markl, G. Crystallographic and fluid compositional effects on the halogen (Cl, F, Br, I) incorporation in pyromorphite-group minerals. *Am. Mineral.* **2019**, *104*, 1673–1688, doi:10.2138/am-2019-7068.

[77] Okudera, H. Relationships among channel topology and atomic displacements in the structures of $Pb_5(BO_4)_3Cl$ with B = P (pyromorphite), V (vanadinite), and As (mimetite). *Am. Mineral.* **2019**, *98*, 1573–1579, doi:10.2138/am.2013.4417.

[78] Vinet, N.; Flemming, R.L.; Higgins, M.D. Crystal structure, mosaicity, and strain analysis of Hawaiian olivines using in situ X-ray diffraction. *Am. Mineral.* **2011**, *96*, 486–497, doi:10.2138/am.2011.3593.

[79] Bräuniger, T.; Poupko, R.; Luz, Z.; Gutsche, P.; Meinel, C.; Zimmermann, H.; Haeberlen, U. The dynamic disorder of azulene: A single crystal deuterium nuclear magnetic resonance study. *J. Chem. Phys.* **2000**, *112*, 10858–10870, doi:10.1063/1.481727.

[80] Flis, J.; Manecki, M.; Bajda, T. Solubility of pyromorphite $Pb_5(PO_4)_3Cl$-mimetite $Pb_5(AsO_4)_3Cl$ solid solution series. *Geochim. Cosmochim. Acta* **2011**, *75*, 1858–1868, doi:10.1016/j.gca.2011.01.021.

[81] Antao, S.M. Structural trends for celestite ($SrSO_4$), anglesite ($PbSO_4$), and barite ($BaSO_4$): Confirmation of expected variations within the SO_4 groups. *Am. Mineral.* **2012**, *97*, 661–665, doi:10.2138/am.2012.3905.

[82] Bielecki, A.; Burum, D. P. Temperature dependence of ^{207}Pb MAS spectra of solid lead nitrate: An accurate, sensitive thermometer for variable-temperature MAS. *J. Magn. Reson. A* **1995**, *116*, 215–220, doi:10.1006/jmra.1995.0010.

[83] Hoppe, R. Effective coordination numbers (ECoN) and mean Active ionic radii (MEFIR). *Z. Kristallog. Cryst. Mater.* **1979**, *150*, 23–52, doi:10.1524/zkri.1979.150.1-4.23.

[84] Leciejewicz, J. On the crystal structure of tetragonal (red) PbO. *Acta Crystallogr.* **1961**, *14*, 1304, doi:10.1107/S0365110X61003892.

[85] Hill, R.J. Refinement of the structure of orthorhombic PbO (massicot) by Rietveld analysis of neutron powder diffraction data. *Acta Crystallogr.* **1985**, *C41*, 1281–1284, doi:10.1107/S0108270185007454.

[86] Boucher, M.L.; Peacor, D.R.Z. The crystal structure of alamosite, $PbSiO_3$. *Krist* **1968**, *126*, 98–111, doi:10.1524/zkri.1968.126.1-3.98.

[87] Gavarri, J.R.; Weigel, D.J. Oxydes de plomb. I. Structure cristalline du minium Pb_3O_4, á température ambiante (293 K). *Solid State Chem.* **1975**, *13*, 252–257, doi:10.1016/0022-4596(75)90127-9.

[88] Nelmes, R.J.; Kuhs, W.F. The crystal structure of tetragonal $PbTiO_3$ at room temperature and at 700 K. *Solid State Commun.* **1985**, *54*, 721–723, doi:10.1016/0038-1098(85)90595-2.

[89] Moreau, J.M.; Galez, P.; Peigneux, J.P.; Korzhik, M.V. Structural characterization of $PbWO_4$ and related new phase $Pb_7W_8O_{(32-x)}$. *J. Alloy. Compd.* **1996**, *238*, 46–48, doi:10.1016/0925-8388(95)02175-2.

[90] Nolle, A. ^{207}Pb Magnetic Shielding Anisotropy in $Pb(NO_3)_2$, $PbCO_3$, $PbCrO_4$, $PbMoO_4$ and $PbWO_4$ by Fourier Transform NMR. *Z. Naturforsch.* **1977**, *32a*, 964–967, 10.1515/zna-1977-0909.

[91] Sleight, A.W. Accurate cell dimensions for ABO_4 molybdates and tungstates. *Acta Crystallogr.* **1972**, *B28*, 2899–2902, doi:10.1107/S0567740872007186.

[92] Effenberger, H.; Pertlik, F. Four monazite type structures: Comparison of $SrCrO_4$, $SrSeO_4$, $PbCrO_4$(crocoite), and $PbSeO_4$. *Z. Kristallogr.* **1986**, *176*, 75–83, doi:10.1524/zkri.1986.176.1-2.75.

[93] Basso, R.; Lucchetti, G.; Zefiro, L.; Palenzona, A. Rosiaite, $PbSb_2O_6$, a new mineral from the Cetine mine, Siena, Italy. *Eur. J. Mineral.* **1996**, *8*, 487–492, doi:10.1127/ejm/8/3/0487.

[94] Yoko, T.; Tadanaga, K.; Miyaji, F.; Sakka, S. A ^{207}Pb MAS-NMR study of Pb-containing glasses. *J. Non-Cryst. Solids* **1992**, *150*, 192–196, doi:10.1016/0022-3093(92)90121-Y.

[95] Chevrier, G.; Giester, G.; Heger, G.; Jarosch, D.; Wildner, M.; Zemann, J. Neutron single-crystal refinement of cerussite, $PbCO_3$, and comparison with other aragonite-type carbonates. *Z. Kristallog. Cryst. Mater.* **1992**, *199*, 67–74, 10.1524/zkri.1992.199.1-2.67.

[96] Brusset, H.; Gillier-Pandraud, H.; Mahe, R. Structure cristalline du metaniobate de plomb rhomboedrique. *C. R. Acad. Sci. C* **1966**, *263*, 217–219.

[97] Zhao, P.; Prasad, S.; Huang, J.; Fitzgerald, J.J.; Shore, J.S. Lead-207 NMR Spectroscopic Study of Lead-Based Electronic Materials and Related Lead Oxides. *J. Phys. Chem. B* **1999**, *103*, 10617–10626, doi:10.1021/jp992162r.

[98] Goldschmidt, V.M.; Barth, T.; Lunde, G.V.V. Untersuchung ueber die Kristallstruktur von Sesquioxyden und Verbindungen ABO_3. *DNVA: Mathematics-Natural Sciences Section* **1928**, *1*, 1-165.

[99] Colby, M.Y.; Lacoste, L.J.B. The crystal structure of Cerussite. *Z. Kristallogr.* **1933**, *84*, 299-309, doi:10.1524/zkri.1933.84.1.299.

[100] Minch, R.; Peters, L.; Ehm, L.; Knorr, K.; Siidra, O.I.; Prakapenka, V.; Dera, P.; Depmeier, W. Evidence for the existence of a $PbCO_3$ – II phase from high pressure X-ray measurements. *Z. Kristallogr.* **2010**, *225*, 146-152, doi:10.1524/zkri.2010.1194.

[101] Sahl, K. Verfeinerung der Kristallstruktur von Cerussit, $PbCO_3$. *Z. Kristallogr.* **1974**, *139*, 215-222, doi:10.1524/zkri.1974.139.3-5.215.

[102] Antao, S.M.; Hassan, I. The orthorhombic structure of $CaCO_3$, $SrCO_3$, $PbCO_3$ and $BaCO_3$: linear structural trends. *Canad. Mineral.* **2009**, *47*, 1245-1255, doi:10.3749/canmin.47.5.1245.

[103] Ye, Y.; Smyth, J.R.; Boni, P. Crystal structure and thermal expansion of aragonite-group carbonates by single-crystal X-ray diffraction. *Am. Mineral.* **2012**, *97*, 707-712, doi:10.2138/am.2012.3923.

[104] Termier, P. Cinnabar and Onofrite from Ouen-Shan-Tchiang China. *Bull. soc. franc. min.* **1897**, *20*, 204-210.

[105] Millot, Y.; Man, P. P. Active and passive rotations with Euler angles in NMR. *Concepts Magn. Reson.* **2012**, *40A*, 215–252, doi:10.1002/cmr.a.21242.

[106] Cook, R. B. Connoisseur's Choice: Cerussite, Tsumeb, Namibia. *Rocks & Minerals* **1997**, *72(3)*, 176-180, doi:10.1080/00357529709605035.

[107] Follner, H. Twin Laws Explained by Partitions of Space. *Cryst. Res. Technol.* **1987**, *22(4)*, 509-516, doi:10.1002/crat.2170220412.

[108] Franke, W.; Lenk, K. The morphology of cerussite $PbCO_3$ grown in silica gel and on hydrothermal conditions. *J. Cryst. Growth* **1981**, *51*, 309-313, doi: 10.1016/0022-0248(81)90316-X.

[109] Pogue, J. E. On cerussite twins from the Mammoth Mine, Pinal County, Arizona. *Amer. Jour. Sci.* **1913**, *35*, 90-92, doi:10.2475/ajs.s4-35.205.90.

[110] Eichele, K. HBA 1.7.5. *Universität Tübingen*. 2015. Available online: `http://anorganik.uni-tuebingen.de/klaus/soft/` (accessed on 15 June 2020).

[111] Stoe & Cie. GmbH, *X-Red: data reduction for STADIP and IPDS Version 1.22*, Stoe & Cie. GmbH, Darmstadt, Germany, 2001.

[112] Stoe & Cie. GmbH, *X-Shape: crystal optimization for numerical absorption correction Version 1.06*, Stoe & Cie. GmbH, Darmstadt, Germany, 1999.

[113] Stoe & Cie. GmbH, *X-Area: IPDS control software Version 1.39*, Stoe & Cie. GmbH, Darmstadt, Germany, 2006.

[114] Sheldrick, G.M. A short history of SHELX. *Acta Crystallogr. A* **2008**, *64*, 112-122, doi:10.1107/S0108767307043930.

[115] Gelato, L.M.; Parthé, E. STRUCTURE TIDY - a computer program to standardize crystal structure data. *J. Appl. Cryst.* **1987**, *20*, 139-143, doi:10.1107/S0021889887086965.

[116] Bruker AXS, *APEX 3: software Version 2016.5-0*, Bruker GmbH, Karlsruhe, Germany, 2016.

[117] Zeman, O.E.O.; Moudrakovski, I.L.; Hartmann, C.; Indris, S.; Bräuniger, T. Local Electronic Structure in AlN Studied by Single-Crystal ^{27}Al and ^{14}N NMR and DFT Calculations. *Molecules* **2020**, *25*, 469, doi:10.3390/molecules25030469.

[118] Schulz, H.; Thiemann, K.H. Crystal structure refinement of AlN and GaN. *Solid State Commun.* **1977**, *23*, 815–819, doi:10.1016/0038-1098(77)90959-0.

[119] Silver, A.H.; Kushida, T.; Lambe, J. Nuclear Magnetic Dipole Coupling in Al_2O_3. *Phys. Rev.* **1962**, *125*, 1147–1149, doi:10.1103/PhysRev.125.1147.

[120] Bastow, T.J.; Massiot, D.; Coutures, J.P. ^{14}N NMR in AlN and BN. *Solid State Nucl. Magn. Reson.* **1998**, *10*, 241–245, doi:10.1016/S0926-2040(97)00106-9.

[121] Czernek, J.; Brus, J. Describing the anisotropic ^{133}Cs solid state NMR interactions in cesium chromate. *Chem. Phys. Lett.* **2017**, *684*, 8–13, doi:10.1016/j.cplett.2017.06.026.

[122] Bräuniger, T.; Kempgens, P.; Harris, R.K.; Howes, A.P.; Liddell, K.; Thompson, D.P. A combined ^{14}N/^{27}Al nuclear magnetic resonance and powder X-ray diffraction study of impurity phases in β-sialon ceramics. *Solid State Nucl. Magn. Reson.* **2003**, *23*, 62–76, doi:10.1016/S0926-2040(02)00016-4.

[123] Pyykkö, P. Year-2008 nuclear quadrupole moments. *Mol. Phys.* **2008**, *106*, 1965–1974, doi:10.1080/00268970802018367.

[124] Healy, M.A.; Morris, A. Reference compounds for ^{14}N nuclear magnetic resonance; the relative chemical shifts of aqueous nitrate ion and nitromethane. *Spectrochim. Acta* **1974**, *31A*, 1695–1697, doi:10.1016/0584-8539(75)80111-5.

[125] Jeffrey, G.A.; Parry, G.S.; Mozzi, R.L. Study of the wurtzite-type binary compounds. I. Structures of aluminum nitride and beryllium oxide. *J. Chem. Phys.* **1956**, *25*, 1024–1031, doi:10.1063/1.1743091.

[126] Paszkowicz, W.; Podsiadlo, S.; Minikayev, R. Rietveld-refinement study of aluminium and gallium nitrides. *J. Alloy. Compd.* **2004**, *382*, 100–106, doi:10.1016/j.jallcom.2004.05.036.

[127] Kanhe, N.S.; Nawale, A.B.; Gawade, R.L.; Puranik, V.G.; Bhoraskar, S.V.; Das, A.K.; Mathe, V.L. Understanding the growth of micro and nano-crystalline AlN by thermal plasma process. *J. Cryst. Growth* **2012**, *339*, 36–45, doi:10.1016/j.jcrysgro.2011.11.011.

[128] Wang, J.; Zhao, M.; Jin, S.F.; Li, D.D.; Yang, J.W.; Hu, W.J.; Wang, W.J. Debye temperature of wurtzite AlN determined by X-ray powder diffraction. *Powder Diffr.* **2014**, *29*, 352–355, doi:10.1017/S0885715614000542.

[129] Yin, L.-J.; Zhang, S.-H.; Wang, H.; Jian, X.; Wang, X.; Xu, X.; Liu, M.-Z.; Fang, C.-M. Direct observation of Eu atoms in AlN lattice and the first-principles simulations. *J. Am. Ceram. Soc.* **2019**, *102*, 310–319, doi:10.1111/jace.15912.

[130] Nakahigashi, K.; Ishibashi, H.; Minamigawa, S. Electron density distribution in AlN from powder X-ray diffraction data by the maximum-entropy method. *J. Phys. Chem. Solids* **1993**, *54*, 445–452, doi:10.1016/0022-3697(93)90326-M.

[131] Body, M.; Silly, G.; Legein, C.; Buzare, J-Y.; Calvayrac, F.; Blaha, P. ^{27}Al NMR experiments and quadrupolar parameter ab initio calculations: Crystallographic structure refinement of β-Ba_3AlF_9. *Chem. Phys. Lett.* **2006**, *424*, 321–326, doi:10.1016/j.cplett.2006.04.091.

[132] Cuny, J.; Messaoudi, S.; Alonzo, V.; Furet, E.; Halet, J.-F.; Le Fur, E.; Ashbrook, S.E.; Pickard, C.J.; Gautier, R.; Le Pollès, L. DFT calculations of quadrupolar solid-state NMR properties: Some examples on solid-state inorganic chemistry. *J. Magn. Reson.* **2008**, *29*, 2279–2287, doi:10.1002/jcc.21028.

[133] Chandran, C.V.; Cuny, J.; Gautier, R.; Le Pollès, L.; Pickard, C.J.; Bräuniger, T. Improving sensitivity and resolution of MQMAS spectra: A ^{45}Sc-NMR case study of scandium sulphate pentahydrate. *J. Magn. Reson.* **2010**, *203*, 226–235, doi:10.1016/j.jmr.2009.12.021.

[134] Frank, P. Propagation of Error and the Reliability of Global Air Temperature Projections. *Front. Earth Sci.* **2019**, *7*, 223, doi:10.3389/feart.2019.00223.

[135] Segall, M.D.; Lindan, P.J.D.; Probert, M.J.; Pickard, C.J.; Hasnip, P.J.; Clark, S.J.; Payne, M.C. First-principles simulations: Ideas, illustrations and the CASTEP code. *J. Phys. Condens. Matter* **2002**, *14*, 2717–2744, doi:10.1088/0953-8984/14/11/301.

[136] Yates, J.R.; Pickard, C.J.; Mauri, F. Calculation of NMR chemical shifts for extended systems using ultrasoft pseudopotentials. *Phys. Rev. B* **2007**, *76*, 024401, doi:10.1103/PhysRevB.76.024401.

[137] Perdew, J.P.; Burke, K.; Ernzerhof, M. Generalized gradient approximation made simple. *Phys. Rev. Lett.* **1996**, *77*, 3865–3868, doi:10.1103/PhysRevLett.77.3865.

[138] Monkhorst, H.J.; Pack, J.D. Special points for Brillouin-zone integrations. *Phys. Rev. B* **1976**, *13*, 5188–5192, doi:10.1103/PhysRevB.13.5188.

[139] Tkatchenko, A.; Scheffler, M. Accurate molecular van der Waals interactions from ground-state electron density and free-atom reference data. *Phys. Rev. Lett.* **2009**, *102*, 073005, doi:10.1103/PhysRevLett.102.073005.

[140] Pfrommer, B.G.; Côté, M.; Louie, S.G.; Cohen, M.L. Relaxation of Crystals with the Quasi-Newton Method. *J. Comp. Phys.* **1997**, *131*, 233–240, doi:10.1006/jcph.1996.5612.

[141] Xu, Y.; Bryce, D.L. SCFit: Software for single-crystal NMR analysis. Free *vs* constrained fitting, *Solid State Nucl. Magn. Reson.* **2019**, *102*, 53–62, doi:10.1016/j.ssnmr.2019.07.004.

[142] Zeman, O.E.O.; Kainz, V.; Bräuniger, T. Single-Crystal ^{31}P and ^{7}Li NMR of the Ionic Conductor LiH_2PO_4. *Crystals* **2020**, *10*, 302, doi:10.3390/cryst10040302.

[143] Šušić, M.V.; Minić, D.M. Electric and electrochemical properties of solid LiH_2PO_4. *Solid State Ionics* **1981**, *2*, 309–314, doi:10.1016/0167-2738(81)90032-1.

[144] Kweon, J.J.; Lee, K.W.; Lee, K.-S.; Lee, C.E. Rotating-frame nuclear magnetic resonance study of the superprotonic conduction in LiH_2PO_4. *Solid State Commun.* **2013**, *171*, 5–7, doi:10.1016/j.ssc.2013.07.022.

[145] Kweon, J.J.; Fu, R.; Steven, E.; Lee, C.E.; Dalal, N.S. High Field MAS NMR and Conductivity Study of the Superionic Conductor LiH_2PO_4: Critical Role of Physisorbed Water in Its Protonic Conductivity. *J. Phys. Chem. C* **2014**, *118*, 13387–13393, doi:10.1021/jp501531h.

[146] Oh, I.H.; Lee, K.-S.; Meven, M.; Heger, G.; Lee, C.E. Crystal Structure of LiH_2PO_4 Studied by Single-Crystal Neutron Diffraction. *J. Phys. Soc. Jpn.* **2010**, *79*, 074606, doi:10.1143/JPSJ.79.074606.

[147] Lee, K.-S.; Oh, I.-H.; Kweon, J.J.; Lee, C.E.; Ahn, S.-H. Crystal growth and morphology of LiH_2PO_4. *Mater. Chem. Phys.* **2012**, *136*, 802–808, doi:10.1016/j.matchemphys.2012.08.001.

[148] Eichele, K.; Wasylishen, R.E. ^{31}P NMR study of powder and single-crystal samples of ammonium dihydrogen phosphate: Effect of homonuclear dipolar coupling. *J. Phys. Chem.* **1994**, *98*, 3108–3113, doi:10.1021/j100063a012.

[149] Dawson, D.M.; Moran, R.F.; Sneddon, S.; Ashbrook, S.E. Is the ^{31}P chemical shift anisotropy of aluminophosphates a useful parameter for NMR crystallography? *Magn. Reson. Chem.* **2019**, *57*, 176–190, doi:10.1002/mrc.4788.

[150] Baur, W.H. The Geometry of Polyhedral Distortions. Predictive Relationships for the Phosphate Group. *Acta Cryst.* **1974**, *B30*, 1195–1215, doi:10.1107/S0567740874004560.

[151] Soboleva, L.V.; Smolsky, I.L. Vyrashchivanie monokristallov digidrofosfata litsiya LiH_2PO_4 na osnovanii analiza fazovoj diagrammy Li_2O-P_2O_5-H_2O. *Kristallografiya* **1997**, *42*, 762–764.

[152] Thakur, R.S.; Kurur, N.D.; Madhu, P.K. Swept-frequency two-pulse phase modulation for heteronuclear dipolar decoupling in solid-state NMR. *Chem. Phys. Lett.* **2006**, *426*, 459–463, doi:10.1016/j.cplett.2006.06.007.

[153] Chandran, C.V.; Madhu, P.K.; Kurur, N.D.; Bräuniger, T. Swept-frequency two-pulse phase modulation (SW_f-TPPM) sequences with linear sweep profile for heteronuclear decoupling in solid-state NMR. *Magn. Reson. Chem.* **2008**, *46*, 943–947, doi:10.1002/mrc.2285.

[154] Ripert, V.; Hubert-Pfalzgraf, L. G.; Vaissermann, J. Dehydration of scandium chloride hydrate: synthesis and molecular structures of $ScCl_3(\eta^2$-DME)(MeCN), $ScCl_3$(diglyme) and $[Sc_2(\mu$-$OH)_2(H_2O)_1 0Cl_4 \cdot 2H_2O$. *Polyhedron* **1999**, *18*, 1845–1851, doi:10.1016/S0277-5387(99)00063-7.

[155] Rossini, A.J.; Schurko R.W. Experimental and Theoretical Studies of ^{45}Sc NMR Interactions in Solids. *J. Am. Chem. Soc.* **2006**, *128*, 10391–10402, doi:10.1021/ja060477w.

[156] Bräuniger, T.; Hofmann, A.J.; Moudrakovski, I.L.; Hoch, C.; Schnick, W. A ^{45}Sc-NMR and DFT calculation study of crystalline scandium compounds. *Solid State Sci.* **2016**, *51*, 1–7, doi:10.1016/j.solidstatesciences.2015.11.002.

[157] Rakhmatullin, A.; Polovov, I.B.; Maltsev, D.; Allix, M.; Volkovich, V.; Chukin, A.V.; Boča, M.; Bessada, C. Combined Approach for the Structural Characterization of Alkali Fluoroscandates: Solid-State NMR, Powder X-ray Diffraction, and Density Functional Theory Calculations. *Inorg. Chem.* **2018**, *57*, 1184–1195, doi:10.1021/acs.inorgchem.7b02617.

[158] Ilyukhin, A.B.; Petrosyants, S.P. Synthesis and crystal structure of $[Sc(OH)(H_2O)_5]_2X_4 \cdot 2H_2O$ (X = Cl, Br). *Zh. Neorg. Khim.* **1994**, *39*, 1517–1520.

[159] Pecher, O.; Halat, D.M.; Lee, J.; Liu, Z.; Griffith, K.J.; Braun, M.; Grey, C.P. Enhanced efficiency of solid-state NMR investigations of energy materials using an external automatic tuning/matching (eATM) robot. *J. Magn. Reson.* **2017**, *275*, 127–136, doi:10.1016/j.jmr.2016.12.008.

List of Figures

List of Tables

A Miscellaneous

A.1 List of publications

I Relation between ^{207}Pb NMR chemical shift and the morphology and crystal structure for the apatites $Pb_5(AO_4)_3Cl$, vanadinite (A = V), pyromorphite (A = P), and mimetite (A = As)

Otto E. O. Zeman, Rupert Hochleitner, Wolfgang W. Schmahl, Konstantin Karaghiosoff, and Thomas Bräuniger

Am. Mineral. **2021**, doi:10.2138/am-2020-7368.

Conceptualization, O.E.O.Z, and T.B.; methodology, O.E.O.Z., R.H., and T.B.; formal analysis, O.E.O.Z. and T.B.; investigation, O.E.O.Z., and T.B.; resources, R.H., W.W.S., and T.B.; writing—original draft preparation, O.E.O.Z. and T.B.; writing—review and editing, O.E.O.Z., R.H., W.W.S., K.K., and T.B.; visualization, O.E.O.Z. and T.B.; supervision, T.B. All authors have read and agreed to the submitted version of the manuscript.

II Single-Crystal ^{31}P and ^{7}Li NMR of the Ionic Conductor LiH_2PO_4

Otto E. O. Zeman, Viktoria Kainz, and Thomas Bräuniger

Crystals **2020**, *10*, 302, doi:10.3390/cryst10040302

Conceptualization, O.E.O.Z. and T.B.; methodology, O.E.O.Z. and T.B.; formal analysis, O.E.O.Z. and V.K.; investigation, O.E.O.Z., V.K., and T.B.; resources, T.B.; writing—original draft preparation, O.E.O.Z. and T.B.; writing—review and editing, O.E.O.Z., V.K., and T.B.; visualization, O.E.O.Z. and V.K.; supervision, T.B. All authors have read and agreed to the published version of the manuscript.

III Facile One-step Synthesis of $Zn_{1-x}Mn_xSiN_2$ Nitride Semiconductor Solid Solutions via Solid-state Metathesis Reaction

Otto E. O. Zeman, Fabian O. von Rohr, Lukas Neudert, and Wolfgang Schnick

Z. Anorg. Allg. Chem. **2020**, *646*, 228-233, doi:10.1002/zaac.201900315

Conceptualization, F.O.vR. and W.S.; methodology, O.E.O.Z. and F.O.vR.; formal analysis, O.E.O.Z., F.O.vR., and L.N.; investigation, O.E.O.Z., F.O.vR., and L.N.; resources, W.S.; writing—original draft preparation, O.E.O.Z. and F.O.vR.; writing—review and editing, O.E.O.Z., F.O.vR., L.N., and W.S.; visualization, O.E.O.Z., F.O.vR., and L.N.; supervision, F.O.vR. and W.S. All authors have read and agreed to the published version of the manuscript.

IV Local electronic structure in AlN studied by single-crystal ^{27}Al and ^{14}N NMR and DFT calculations

Otto E. O. Zeman, Igor L. Moudrakovski, Carsten Hartmann, Sylvio Indris, and Thomas Bräuniger

Molecules **2020**, *25*, 469, doi:10.3390/molecules25030469

Conceptualization, O.E.O.Z., C.H., S.I., and T.B.; methodology, O.E.O.Z., I.L.M., S.I., and T.B.; formal analysis, O.E.O.Z. and I.L.M..; investigation, O.E.O.Z., I.L.M., S.I. and T.B.; resources, I.L.M., C.H., S.I. and T.B.; writing—original draft preparation, O.E.O.Z. and T.B.; writing—review and editing, O.E.O.Z., I.L.M., C.H., S.I., and T.B.; visualization, O.E.O.Z., C.H., S.I.; supervision, T.B. All authors have read and agreed to the published version of the manuscript.

V Single-crystal ^{207}Pb-NMR of wulfenite, $PbMoO_4$, aided by simultaneous measurement of phosgenite, $Pb_2Cl_2CO_3$

Otto E. O. Zeman, Jennifer Steinadler, Rupert Hochleitner, and Thomas Bräuniger

Solid State Nucl. Magn. Reson. **2019**, *103*, 17–24, doi:10.1016/j.ssnmr.2019.101620

Conceptualization, O.E.O.Z., R.H., and T.B.; methodology, O.E.O.Z. and T.B.; formal analysis, O.E.O.Z. and J.S.; investigation, O.E.O.Z., J.S., and T.B.; resources, R.H. and T.B.; writing—original draft preparation, O.E.O.Z. and T.B.; writing—review and editing, O.E.O.Z., J.S., R.H., and T.B.; visualization, O.E.O.Z. and J.S.; supervision, T.B. All authors have read and agreed to the published version of the manuscript.

VI Determination of the Full ^{207}Pb Chemical Shift Tensor of Anglesite, $PbSO_4$, and Correlation of the Isotropic Shift to Lead–Oxygen Distance in Natural Minerals

Otto E. O. Zeman, Jennifer Steinadler, Rupert Hochleitner, and Thomas Bräuniger

Crystals **2019**, *9*, 43, doi:10.3390/cryst9010043

Conceptualization, O.E.O.Z., R.H., and T.B.; methodology, O.E.O.Z. and T.B.; formal analysis, O.E.O.Z. and J.S.; investigation, O.E.O.Z. and J.S.; resources, R.H. and T.B.; writing—original draft preparation, O.E.O.Z. and T.B.; writing—review and editing, O.E.O.Z., J.S., R.H., and T.B.; visualization, O.E.O.Z. and J.S.; supervision, T.B. All authors have read and agreed to the published version of the manuscript.

VII NMR interaction tensors of ^{51}V and ^{207}Pb in vanadinite, $Pb_5(VO_4)_3Cl$, determined from DFT calculations and single-crystal NMR measurements, using only one general rotation axis

Otto E. O. Zeman, Constantin Hoch, Rupert Hochleitner, and Thomas Bräuniger

Solide State Nucl. Magn. Reson. **2018**, *89*, 11–20, doi:10.1016/j.ssnmr.2017.12.002

Conceptualization, R.H. and T.B.; methodology, O.E.O.Z. C.H., and T.B.; formal analysis, O.E.O.Z. and T.B.; investigation, O.E.O.Z. and T.B.; resources, C.H., R.H., and T.B.; writing—original draft preparation, T.B.; writing—review and editing, O.E.O.Z., C.H., R.H., and T.B.; visualization, O.E.O.Z. and T.B.; supervision, T.B. All authors have read and agreed to the published version of the manuscript.

VIII Determination of the ^{31}P and ^{207}Pb Chemical Shift Tensors in Pyromorphite, $Pb_5(PO_4)_3Cl$, by Single-Crystal NMR Measurements and DFT Calculations

Otto E. O. Zeman, Igor L. Moudrakovski, Constantin Hoch, Rupert Hochleitner, Wolfgang W. Schmahl, Konstantin Karaghiosoff, and Thomas Bräuniger

Z. Anorg. Allg. Chem. **2017**, *643*, 1635–1641, doi:10.1002/zaac.201700261.

Conceptualization, R.H., W.W.S., K.K., and T.B.; methodology, O.E.O.Z. I.L.M., C.H, and T.B.; formal analysis, O.E.O.Z. and T.B.; investigation, O.E.O.Z., I.L.M. and T.B.;

resources, I.L.M. C.H., R.H., W.W.S., and T.B.; writing—original draft preparation, T.B.; writing—review and editing, O.E.O.Z., I.L.M., C.H., R.H., W.W.S., and T.B.; visualization, O.E.O.Z. and T.B.; supervision, T.B. All authors have read and agreed to the published version of the manuscript.

IX Clarification of Crystal Structure and Characterization of Macroscopic Twinning for Cerussite, $PbCO_3$, by Single-Crystal NMR Spectroscopy

Otto E. O. Zeman, Jennifer Steinadler, Constantin Hoch, Rupert Hochleitner, and Thomas Bräuniger

Submitted manuscript

Conceptualization, O.E.O.Z, C.H., and T.B.; methodology, O.E.O.Z., C.H., and T.B.; formal analysis, O.E.O.Z., J.S., and C.H.; investigation, O.E.O.Z. and J.S.; resources, C.H., R.H., and T.B.; writing—original draft preparation, O.E.O.Z., C.H. and T.B.; writing—review and editing, O.E.O.Z., J.S., C.H., R.H., and T.B.; visualization, O.E.O.Z., J.S., and C.H.; supervision, T.B. All authors have read and agreed to the submitted version of the manuscript.

X Electron-Blocking and Oxygen Evolution Catalyst Layers by Plasma-Enhanced Atomic Layer Deposition of Nickel Oxide

Alexander G. Hufnagel, Ann-Kathrin Henß, Ramona Hoffmann, Otto E. O. Zeman, Sebastian Häringer, Dina Fattakhov-Rohlfing, and Thomas Bein

Adv. Mater. Interfaces **2018**, *5*, 1701531, doi:10.1002/admi.201701531

Conceptualization, A.G.H, A.K.H., and R.H.; methodology, A.G.H, A.K.H., R.H., O.E.O.Z., S.H., and D.F.R.; formal analysis, A.G.H, A.K.H., R.H., and O.E.O.Z.; investigation, A.G.H, A.K.H., R.H., O.E.O.Z., and S.H.; resources, D.F.R. and T.B.; writing—original draft preparation, A.G.H; writing—review and editing, A.G.H, A.K.H., R.H., O.E.O.Z., S.H., D.F.R., and T.B.; visualization, A.G.H and O.E.O.Z.; supervision, D.F.R. and T.B. All authors have read and agreed to the published version of the manuscript.

A.2 List of presentations

Oral presentations

I Determination of the Full ^{207}Pb Chemical Shift Tensor of the Natural Mineral Phosgenite ($Pb_2Cl_2CO_3$) and Wulfenite ($PbMoO_4$) by Single-Crystal NMR Spectroscopy Only

Otto E. O. Zeman and Thomas Bräuniger

34^{th} Central European NMR Meeting, Valtice (Czech Republic), March 31 – April 03, 2019.

O.E.O.Z. awarded 1. Place *Josef Dadok Prize*

II NMR-Kristallographie: Zwillingsbestimmung von Cerussit, $^{207}PbCO_3$

Otto E. O. Zeman and Thomas Bräuniger

4. Obergurgl-Seminar für Festkörperchemie, Obergurgl (Austria), January 29 – February 01, 2019.

III Einkristall-NMR-Spektroskopie von Vanadinite [$^{207}Pb_5(^{51}VO_4)_3Cl$], Pyromorphit [$^{207}Pb_5(^{31}PO_4)_3Cl$], and Mimetesit [$^{207}Pb_5(^{75}AsO_4)_3Cl$]

Otto E. O. Zeman and Thomas Bräuniger

3. Obergurgl-Seminar für Festkörperchemie, Obergurgl (Austria), January 23 – 26, 2018.

Poster presentations

I Relation between ^{207}Pb NMR chemical shift and the morphology and crystal structure for the natural minerals $Pb_5(AO_4)_3Cl$, vanadinite (A = V), pyromorphite (A = P), and mimetite (A = As)

Otto E. O. Zeman, Rupert Hochleitner, Wolfgang, W. Schmahl and Thomas Bräuniger

40^{th} FGMR Annual Discussion Meeting, Leipzig (Germany), September 10 – 13, 2018.